GRAVITY WAVE GENERATION AND MOMENTUM DEPOSITION IN THE ATMOSPHERE

MAHTAB MAJDZADEH

A DISSERTATION SUBMITTED TO
THE FACULTY OF GRADUATE STUDIES
IN PARTIAL FULFILLMENT OF THE REQUIREMENTS
FOR THE DEGREE OF
DOCTOR OF PHILOSOPHY

GRADUATE PROGRAM IN
EARTH AND SPACE SCIENCE
YORK UNIVERSITY
TORONTO, ONTARIO

JULY 2017

Abstract

The first part of this study investigates gravity wave parameterization in the middle atmosphere, focusing on internal waves with a broad spectrum of phase speeds. A column model based on CIRA wind and temperature profiles is employed to assess the characteristics of the Hines Doppler-spread(1997) and Warner-McIntyre-Scinocca(2001) nonorographic drag parameterizations for internal gravity waves. The Alexander-Dunkerton(1999) variant of Warner-McIntyre-Scinocca scheme is also briefly considered.

This study goes into more detail than previous comparisons by performing a spectral analysis of the momentum deposition and drag, and by examining the ability of each scheme to reproduce saturation. Comparisons with pure critical level filtering are also made, and it is found that Hines DSP mainly constitutes an enhancement to critical level absorption, while the Warner-McIntyre-Scinocca scheme produces substantially different wave drag profiles. We find several undesirable characteristics in the drag produced by the Hines scheme. For typical midlatitude profiles, it produces an abrupt onset of large accelerations that are confined to a relatively narrow layer. It is also unable to reproduce wave spectra consistent with observed saturation at high vertical wavenumbers.

The second part of this study investigates the generation mechanisms of the gravity waves over Newfoundland and Labrador (NL). We performed a series of simulations for a selection of the strongest peak events using WRF model to further investigate

the characteristics and generation mechanisms of gravity wave peak events over NL. We studied three different peak events, 2003, 2008 and 2014.

We showed that gravity wave events in the winter hotspot region over NL can have both topographic and jet streak sources. In the cases we examined, one source of waves was the Torngat range on the northern coast of Labrador. However, the other two wave sources were in fact outside the hotspot region, and a combination of advection and propagation caused those packets to enter the hotspot in the middle atmosphere. We have demonstrated that topographic wave packets, which are normally assumed to remain stationary over the source, can in fact be advected far downstream from the source.

Dedication

To the loving memory of my father, Dr. S.E. Majdzadeh, whose lifelong pursuit of learning has been the greatest inspiration in my life.

Acknowledgements

I would like to offer my most heartfelt gratitude to the people whose support, insight and contribution greatly assisted me throughout the course of my doctoral studies.

First and foremost, I would like to extend my sincerest thanks and appreciation to my mentor and supervisor Professor Gary P. Klaassen for giving me the opportunity to carry out this research project. His unconditional support, profound knowledge and meticulous suggestions have been invaluable to this research. It has been a great privilege to work under his guidance.

My appreciation goes to Professor Yongsheng Chen. This research project could not have been completed without the support that I received from Professor Chen and his group. His expertise and vision helped me greatly during the critical years of my studies.

I am grateful to my Supervisory Committee, Professor James A. Whiteway and Professor George Zhu. I benefited greatly from Professor Whiteway's comments and suggestions. Professor Zhu's support has been a great asset to this project.

I would like to take this opportunity to express my deepest gratitude to Professor John C. McConnell. He was a great scientist, a remarkable person and an inspiration to all his students.

Thanks to the members of ESSE graduate program and to my peers, in particular, Jianyu(Richard) Liang, Sopan Kurkute and Sangay Bhutia for their help, support and friendship.

I am grateful for the funding I received towards my PhD through Dr. Diane Michelangeli Memorial Scholarship.

Special thanks to Dr. Lars Hoffmann of Jülich Supercomputing Centre (JSC), who kindly provided us with a time series of AIRS temperature variance over Newfoundland and Labrador.

I would also like to thank Calcul Québec and Compute Canada for providing computational resources for this project. Computations were made on the supercomputer "Mammoth-Mp2" from "Université de Sherbrooke", managed by Calcul Québec (www.calculquebec.ca) and Compute Canada (www.computecanada.ca). The operation of this supercomputer is funded by the Canada Foundation for Innovation (CFI), the ministère de l'Économie, de la science et de l'innovation du Québec (MESI) and the Fonds de recherche du Québec - Nature et technologies (FRQ-NT).

Finally, thanks to my son, Alireza, a wonderful young man who makes me proud and gives me hope and motivation every day.

Contents

List of Tables

List of Figures

Chapter 1

Introduction

1.1 Gravity Waves

Atmospheric gravity waves are horizontally and vertically propagating waves which can be treated as small departures from a stably stratified background state in atmosphere. The zonal-mean wind and temperature structure of the middle atmosphere is largely determined by the balance between radiative driving and gravity wave drag (Holton 1983). Gravity waves are generated by lower atmospheric sources, e.g., flow over irregularities at the Earth's surface such as mountains and valleys, uneven distribution of diabatic heat sources associated with convective systems, and atmospheric processes such as jet streams and fronts.

Gravity waves can be categorized based on their restoring forces. The restoring force for high and medium frequency internal gravity waves (which for simplicity are referred to as *gravity waves*) is the buoyancy force, while the restoring force for low frequency internal gravity waves, which are known as *inertia gravity waves*, is a combination of buoyancy and rotation or Coriolis forces.

Neglecting Coriolis forces for the moment, a vertically displaced air parcel oscillates adiabatically around its equilibrium level under the influence of the restoring

buoyancy force, which is due to stable stratification of the atmosphere. The vertically directed buoyancy force per unit mass is $F_b = -N^2\delta z$, where δz is the vertical displacement. The oscillation frequency is given by the Brunt-Väisälä frequency N:

$$N^2 = -\frac{g}{\bar{\rho}}\frac{d\bar{\rho}}{dz} \qquad \text{(In a Boussinesq or incompressible fluid)} \quad (1.1)$$

$$N^2 = \frac{g}{\overline{T}}(\frac{d\overline{T}}{dz} + \frac{g}{c_p}) = g\frac{d(ln\bar{\theta})}{dz} \qquad \text{(In a compressible fluid, like atmosphere)} \quad (1.2)$$

Here $\bar{\rho}(z)$ is the mean density, $\overline{\mathrm{T}}(z)$ is the mean temperature, g is the gravitational acceleration and c_p is the specific heat at constant pressure. Noting the fact that parcel displacements are adiabatic and $\bar{\theta}$ is the mean potential temperature, the buoyancy frequency is therefore a measure of static stability in the atmosphere. For slantwise oscillations along a surface at an angle α with respect to the vertical, the displacement $\delta s = \delta z/\cos\alpha$ and the component of F_b parallel to the surface is $-N^2\delta z\cos\alpha = -N^2 cos^2\alpha\delta s$ and the oscillation frequency is $N\cos\alpha$ (Holton 2004).

Following Fritts and Alexander (2003, hereafter FA03) and Dutton (1986), we assume wave perturbations of the form $exp[i(kx + ly + m_c z - \hat{\omega}t]$ about a hydrostatic isothermal basic state at rest, with wavenumber components (k, l, m_c) where m_c is possibly complex, and intrinsic frequency $\hat{\omega}$. After substituting into the linearized inviscid compressible equations of motion, one obtains a complex fourth order *dispersion relation*, possessing two gravity wave modes and two acoustic wave modes. By putting $m_c = m - i/2H$, where m is real, one may obtain propagating solutions for which k, l and $\hat{\omega}$ are real. Putting the speed of sound $c_s \to \infty$ eliminates the two acoustic modes and yields the gravity wave dispersion relation for a compressible

fluid:

$$\hat{\omega}^2 = \frac{N^2(k^2+l^2) + f^2(m^2 + \frac{1}{4H^2})}{k^2+l^2+m^2+\frac{1}{4H^2}} \tag{1.3}$$

where we note that $|m_c|^2 = m^2 + 1/4H^2$. Here H is the scale height given by $H = \frac{RT}{g}$, where R is the gas constant for dry air. The Brunt-Väisälä frequency and scale height are related by:

$$\frac{1}{H} - \frac{N^2}{g} = \frac{g}{{c_s}^2} \tag{1.4}$$

In equation (1.3), the term $\frac{1}{4H^2}$ represents the *compressibility effect*. Typically $H \approx 7$ km, so this term is only important when vertical wavelengths exceed ≈ 30 km. Note that the wave form has become $exp[i(kx+ly+mz-\hat{\omega}t)+\frac{z}{2H}]$. The exponential growth with height is countered by the background density variation $\bar{\rho} = \rho_\circ e^{-z/H}$, so that the vertical momentum flux $\bar{\rho}\overline{u'w'}$ remains constant. Since the intrinsic frequency, $\hat{\omega}$, is the frequency relative to the background wind $\bar{\mathbf{U}} = (\bar{u}, \bar{v}, 0)$, the observed or ground-based frequency ω is given by:

$$\omega = \hat{\omega} + k\bar{u} + l\bar{v} \tag{1.5}$$

If we define the total wave vector $\boldsymbol{\kappa} = (k, l, m)$, then the intrinsic phase velocity vector is:

$$\hat{\mathbf{c}} = \frac{\hat{\omega}\boldsymbol{\kappa}}{|\boldsymbol{\kappa}|^2} = \frac{\hat{\omega}}{|\boldsymbol{\kappa}|^2}(k, l, m) \tag{1.6}$$

Here $\hat{\mathbf{c}}$ is the speed of lines of constant phase $\Phi = kx + ly + mz - \omega t$, in the direction of $\boldsymbol{\kappa}$ and relative to the background flow. The observed phase speeds relative to the

ground are given by:

$$c_x = \hat{c}_x + \bar{u} \qquad c_y = \hat{c}_y + \bar{v} \qquad c_z = \hat{c}_z \tag{1.7}$$

The intrinsic speeds of constant phase lines in the (x, y, z) directions are given by:

$$\hat{c}_x = \frac{\hat{\omega}}{k} \qquad \hat{c}_y = \frac{\hat{\omega}}{l} \qquad \hat{c}_z = \frac{\hat{\omega}}{m} \tag{1.8}$$

It should be mentioned that since (k, l, m) is a vector, equation 1.8 clearly shows that $\hat{c}_x$, $\hat{c}_y$ and $\hat{c}_z$ cannot form the components of a vector. Instead, the phase speed vector is given by equation 1.6. The wave group velocity, $\mathbf{c_g}$ is the velocity at which a group of waves or wave packet propagates. In fact wave energy propagates at the group velocity. The intrinsic group velocity vector $\hat{\mathbf{c}}_\mathbf{g}$ is the gradient of ω over the wavenumber components and can be written as:

$$\hat{\mathbf{c}}_\mathbf{g} = (\hat{c}_{gx}, \hat{c}_{gy}, \hat{c}_{gz}) = (\frac{\partial \omega}{\partial k}, \frac{\partial \omega}{\partial l}, \frac{\partial \omega}{\partial m}) \tag{1.9}$$

and therefore:

$$c_{gx} = \bar{u} + \frac{k(N^2 - \hat{\omega}^2)}{\hat{\omega}(k^2 + l^2 + m^2 + \frac{1}{4H^2})} \qquad c_{gy} = \bar{v} + \frac{l(N^2 - \hat{\omega}^2)}{\hat{\omega}(k^2 + l^2 + m^2 + \frac{1}{4H^2})}$$
$$c_{gz} = \frac{-m(\hat{\omega}^2 - f^2)}{\hat{\omega}(k^2 + l^2 + m^2 + \frac{1}{4H^2})} \tag{1.10}$$

We note that for the case $\bar{u} = \bar{v} = 0$ and $1/4H^2 \to 0$, we have $\hat{\mathbf{c}}_\mathbf{g} \cdot \boldsymbol{\kappa} = 0$, i.e., the group velocity is orthogonal to the wave vector.

The dispersion relation (1.3) can also be written as:

$$m^2 = \frac{(k^2 + l^2)(N^2 - \hat{\omega}^2)}{(\hat{\omega}^2 - f^2)} - \frac{1}{4H^2} \tag{1.11}$$

By requiring m^2 to be positive (i.e. for real m), we find the acceptable range for the intrinsic frequency of gravity waves to be: $|f| < \hat{\omega} < N$. The left hand inequality shows that the Coriolis parameter, f, is the lowest frequency possible for gravity waves, while the right hand inequality is a consequence of stratification. The limit $\hat{\omega} \to f$ corresponds to $m \to \infty$ (zero vertical wavelength), and represents a critical level. The limit $\hat{\omega} \to N$ yields $m \to 1/2H$ corresponding to a vertical wavelength of $4\pi H \approx 88$ km. This long wavelength limit represents internal reflection at a turning level, where the group velocity changes sign. Fritts and Alexander (2003) show that short horizontal wavelengths < 10 km are more easily reflected and are therefore unlikely to be able to propagate into the middle atmosphere. Models describing gravity wave propagation in various parts of the spectrum often make approximations that simplify the dispersion relation. Considering the allowable range for intrinsic frequency, gravity waves can be categorized in three different frequency regimes:

High Frequency Waves ($\hat{\omega} \gg f$) **:**

For high frequency waves, the rotation terms in equation (1.3) can be neglected, so that the dispersion relation for waves with $m \gg 1/4H^2$ can be written as:

$$\hat{\omega}^2 = \frac{N^2(k^2 + l^2)}{k^2 + l^2 + m^2} = N^2 \cos^2\alpha \tag{1.12}$$

where α is the angle between lines of constant phase and the vertical. Horizontal and vertical components of group velocity (c_{gh} and c_{gz}) for these waves are:

$$(c_{gh}, c_{gz}) = (\overline{U}_h, 0) \pm \frac{Nm}{{\kappa_h}^2 + m^2} \frac{(m, -\kappa_h)}{\sqrt{{\kappa_h}^2 + m^2}} \tag{1.13}$$

where $\overline{U}_h = \overline{\mathbf{U}} \cdot \hat{\boldsymbol{\kappa}}_\mathbf{h}$ is the horizontal wind in the direction of propagation and the horizontal wavenumber $\kappa_h = \pm\sqrt{k^2 + l^2}$. As mentioned earlier, the intrinsic group velocity is parallel to lines of constant phase and perpendicular to the direction of phase propagation.

Medium Frequency Waves ($N \gg \hat{\omega} \gg f$) **:**

Applying the hydrostatic approximation and neglecting compressibility and rotation effects yields a much simpler dispersion relation of the form:

$$\hat{\omega} = N \left| \frac{\boldsymbol{\kappa}_h}{m} \right| \qquad\qquad \hat{c}_h = \pm \frac{N}{|m|} \tag{1.14}$$

where $\hat{c}_h$ is the horizontal intrinsic phase speed. As we can see, the intrinsic frequency and the vertical wavelength are both proportional to the intrinsic phase speed $\hat{c}_h$.

When the observed horizontal phase speed $\mathbf{c_h} \to \overline{\mathbf{U}}_\mathbf{h}$ at any level ($\overline{\mathbf{U}}_\mathbf{h}$ is the horizontal background wind vector), then $\hat{\boldsymbol{c}}_h = \mathbf{c_h} - \overline{\mathbf{U}}_\mathbf{h} \to 0$ and the vertical wavenumber $m \to \infty$[1]. This is known as a *critical level*. From equation 1.14, a critical level corresponds to vanishing the intrinsic phase speed and the vertical wavelength λ_z reduces to zero, i.e., vertical wave propagation ceases. With the rotation term (f) included, the intrinsic phase speed $\hat{c_h}$ does not vanish completely but instead becomes very

[1]Alternatively a critical level occurs when the projection of $\overline{\boldsymbol{U}}_\boldsymbol{h}$ on the horizontal direction of wave propagation $\hat{\boldsymbol{\kappa}}_h$ approaches c_h, i.e. $\overline{\boldsymbol{U}}_\boldsymbol{h} \cdot \hat{\boldsymbol{\kappa}}_\boldsymbol{h} \to c_h$.

small as $\hat{\omega} \to f$. This is an important physical process that needs to be considered in gravity wave drag parameterizations and as we will see later in this study, this process is a wave filtering mechanism for the middle atmosphere.

Low Frequency Waves ($\hat{\omega} \sim f$) **:**

Low frequency gravity waves are called *inertia gravity waves*. Since the propagation of these waves are influenced by the rotation of the earth, Coriolis terms must be retained in the dispersion relation. For these waves the wave vector is nearly vertical (i.e., $\alpha \to \frac{\pi}{2}$) and $|m| \gg \sqrt{k^2 + l^2}$. In this limit the dispersion relation reduces to:

$$\hat{\omega}^2 = N^2 \frac{{\kappa_h}^2}{m^2} + f^2 \qquad\qquad \hat{c}_h^2 = \frac{N^2}{m^2} + \frac{f^2}{{\kappa_h}^2} \tag{1.15}$$

Holton (2004) shows that the vertical to horizontal group speed ratio is:

$$\left| \frac{\hat{c}_{gz}}{\hat{c}_{gh}} \right| = \left| \frac{\kappa_h}{m} \right| = \frac{(\hat{\omega}^2 - f^2)^{\frac{1}{2}}}{N} \tag{1.16}$$

which becomes small as $\hat{\omega} \to f$. This demonstrates that inertia gravity wave groups have relatively slow vertical propagation and relatively fast horizontal propagation speeds. Equation(1.16) follows from (1.15) and:

$$\hat{c}_{gh} = \frac{\kappa_h}{\hat{\omega}} \frac{N^2}{m^2} \qquad , \qquad \hat{c}_{gz} = -\frac{{\kappa^2}_h}{\hat{\omega}} \frac{N^2}{m^3} \tag{1.17}$$

1.2 Gravity Wave Sources and Propagation

Gravity waves are generated in several ways, including topography, convection, wind shear and geostrophic adjustment. Here we give a brief review of the most significant generation mechanisms for gravity waves.

1.2.1 Topographic Gravity Waves

Flow over topography is an important source of gravity waves (Fritts and Alexander, 2003; Kim et. al., 2003). Since topographic waves are generated by stationary obstacles, they are stationary in the Earth frame, i.e. their observed horizontal phase speeds, c_h are generally near zero since the sources are stationary. Mountain waves have been well studied, numerically and observationally, and are arguably the best understood source mechanism. GCM parameterizations generally include topographic schemes, as gravity wave drag is an important contributor to the upper-troposphere lower-stratosphere circulation in midlatitudes (McFarlane 1987).

Topographic waves typically have horizontal wavelengths of ten to hundreds of kilometers, with small to breaking amplitudes and momentum fluxes ranging between 0.01 to 0.5 Pa in the upper troposphere and lower stratosphere.(Fritts and Alexander, 2003).

1.2.2 Convective Gravity Waves

Vertically propagating gravity waves generated by convection are known to provide an important contribution to the momentum budget of the middle atmosphere. Thermal forcing associated with latent heat release and deep convection interacts with the

overlying stably stratified layer to produce gravity waves. Unlike topographic waves, convectively-generated waves may have a broad range of phase speeds, frequencies, vertical and horizontal scale. Observations of high-frequency waves in the stratosphere have shown a close correspondence with deep convective clouds (Fritts and Alexander, 2003). Such waves have large vertical group velocities, so they are only observed for a short duration and at short horizontal distances from the convective source. Low frequency gravity wave packets on the other hand, generally travel large horizontal distances from their sources, so they may not be easily linked to clouds or other convective systems. These wave components have short vertical wavelengths and much slower vertical group velocities, so their contribution to the momentum flux in the upper stratosphere and mesosphere is difficult to quantify but may be less than that of the high frequency waves (Alexander and Holton, 2004).

Observational studies of momentum flux show significant variability. Local magnitude of $\bar{\rho}\overline{u'w'}$ are estimated to be between 0.03 to 0.2 Pa, with long-term averages of $1 - 5 \times 10^{-3}$ Pa (Fritts and Alexander, 2003; Vincent and Alexander, 2000).

1.2.3 Jet Streams, Fronts and Gravity Wave Generation

Jet streaks are associated with enhanced vertical wind shear in baroclinic systems and are thought to be a significant energy source for gravity waves. These jet-front gravity waves typically have vertical wavelengths of $4 - 10$ km, periods of $0.5 - 4$ h, amplitudes of $0.5 - 15$ hPa (pressure perturbations at the surface), and phase speeds of $15 - 35$ ms^{-1} (Uccellini and Koch 1987; Plougonven and Zhang 2014).

Several observational studies have highlighted the generation of gravity wave activity in the vicinity of jets and fronts (e.g., Fritts and Nastrom, 1992; Eckermann

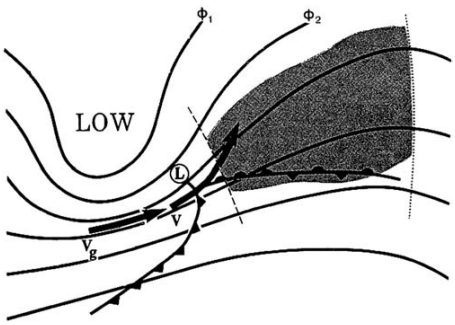

Figure 1.1: One of the flow configurations identified by Uccelini and Koch (1987). Lines of geopotential in the upper troposphere, surface fronts and intense gravity wave activity are indicated. The area of wave activity (shaded region) appears to be bounded by the jet axis and the inflection axis to the west (dashed line), a $300hPa$ ridge axis to the east (dotted line), and the surface frontal boundary to the south.(After Koch and O'Handley, 1997; Plougonven and Zhang, 2014).

and Vincent, 1993; Plougonven et al., 2003). In addition, numerous case studies have analyzed the occurrence of strong gravity wave events in the vicinity of a jet/front system. Uccellini and Koch (1987, hereafter UK87), reviewed thirteen case studies of mesoscale wave disturbances and showed that many of these wave events are associated with a surface low pressure system upstream of the area of wave activity and a distinct frontal boundary extending northeast from the surface low (figure 1.1). This synoptic setting involves an upper level trough, in which the jet streak is propagating towards the ridge axis. Gravity waves are generated predominantly in the left exit region of the jet streak, as shown in figure 1.1. While UK87 were primarily interested in horizontally propagating (i.e., ducted) waves, many subsequent studies have applied their paradigm to vertically propagating packets.

1.3 Wave Dissipation Mechanisms

Wave dissipation can be separated into two components: The first is *critical level filtering* and the second is *nonlinear dissipation*. Upward-propagating waves that do not meet critical levels eventually attain sufficiently large amplitudes that nonlin-

ear effects, such as instabilities or wave-wave interactions become important. These nonlinear processes result in momentum deposition, and are thought to be responsible for the formation of the so-called universal saturated gravity wave spectrum (VanZandt, 1982; Smith et al. 1987). Saturation occurs when wave amplitudes stop growing with height, i.e. when potential growth is balanced by dissipation. In other cases, nonlinear effects may be strong enough to obliterate some wave components. In such situations, the momentum flux $\bar{\rho}\overline{u'w'}$ decreases with altitude and momentum is transferred from the wave to the background flow.

1.3.1 Critical Level Dissipation

Some form of critical level filtering by the background wind is applied in all schemes. A critical level, z_C is the altitude where $c = \bar{U}(z_C)$, i.e. the level where the horizontal phase speed is equal to the mean horizontal wind speed. The dispersion relation for hydrostatic[2] wave dynamics in the absence of rotation may be written:

$$m^2 = \frac{N^2}{(c-\bar{U})^2} = \frac{k^2 N^2}{\hat{\omega}^2} \tag{1.18}$$

where c is the phase speed, m is the vertical wavenumber, $\hat{\omega}$ is the intrinsic frequency, k is the horizontal wavenumber projected onto the azimuth ϕ and $\bar{U}$ is the magnitude of the projection of the background wind velocity onto direction ϕ. From equation 1.18, the definition of critical level corresponds to vanishing intrinsic phase speed, where $m \to \infty$ and the vertical wavelength λ_z reduces to zero.

It was shown in Bretherton's study (1966) that a wave packet approaches the

[2]Gravity waves with $m^2 \gg k^2$ have $\frac{N^2}{k^2(c-\bar{U})^2} \gg 1$ and $\hat{\omega}^2 \ll N^2$ and are termed hydrostatic.

critical level for the dominant wavenumber and frequency for the packet, but does not reach it in any finite time. It would not be reflected or transmitted, but effectively absorbed, i.e. gravity waves deposit their momentum to the mean flow just below the critical level. This process filters a significant portion of one azimuth of the wave spectrum as it propagates upward through the middle atmosphere. As the process is reasonably well-understood and supported by theory, modelling and observational studies, all gravity wave drag schemes include some representation of critical level dissipation.

1.3.2 Nonlinear Dissipation

Upward-propagating waves that do not meet critical levels eventually attain sufficiently large amplitudes as the ambient density decreases exponentially with height and nonlinear effects, such as instabilities or wave-wave interactions become important. These processes have been reviewed by Fritts and Alexander (2003) and result in momentum deposition. Saturation occurs when wave amplitudes stop growing with height. According to observational evidence, vertical wavenumber spectra of horizontal wind perturbations show a high $-m$ tail of m^{-3} form which is more or less independent of height (VanZandt, 1982; Smith and Fritts, 1987).

As shown in figure 1.2, vertical wavenumber spectra at large m are consistent in shape and amplitude throughout the atmosphere. Since the power spectral density does not exceed $N/2m^3$, we can conclude that these waves are saturated, i.e., their potential growth is balanced by dissipation. There have been several very different proposals for the nonlinear dissipation that leads to wave saturation and/or obliteration (see Fritts and Alexander, 2003), but there is as yet no generally accepted

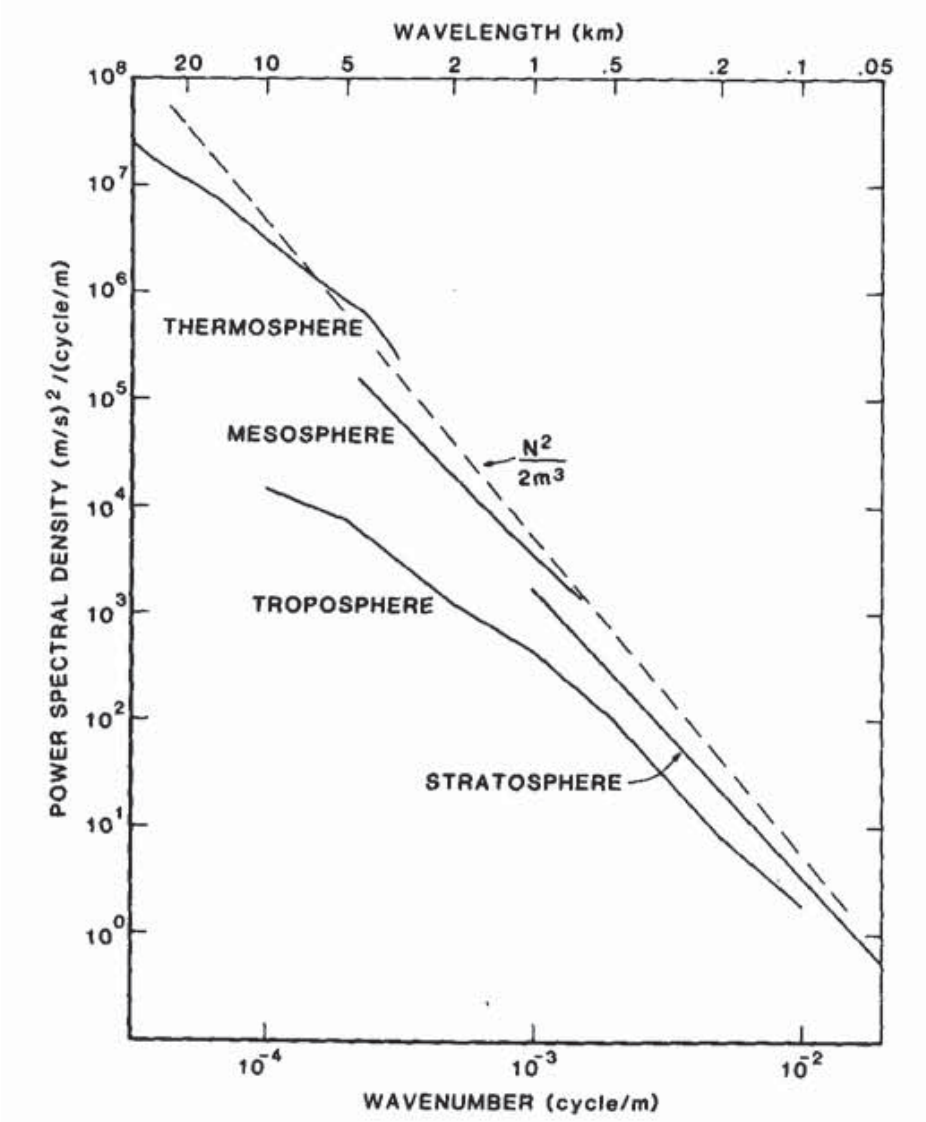

Figure 1.2: Spectra of horizontal velocity versus vertical wavenumber as a function of altitude (After Smith and Fritts, 1987).

theory.

1.4 Gravity Wave Drag

The dissipation of gravity waves produces a wave-induced force in the atmosphere, termed as *gravity wave drag* (GWD), that affects both short and long term weather systems. The body forces exerted on the flow by gravity waves can either accelerate or decelerate atmospheric winds and therefore have a major role in driving the atmospheric circulation and structure, specially in middle atmosphere between 10 to 110 km altitude. Gravity wave drag on the mean flow produced by wave dissipation is represented by the divergence of the wave's momentum flux or *E-P flux*. For a background flow where $v_\circ = w_\circ = 0$, $\bar{u} = \bar{u}(z)$ and density $\bar{\rho} = \bar{\rho}(z)$, *Eliassen and Palm*'s first theorem states that:

$$\overline{p'w'} = -\bar{\rho}(\bar{u} - c)\overline{u'w'} \tag{1.19}$$

where $\overline{p'w'}$ is related to the vertical energy flux[3] associated with the wave, c is the horizontal phase speed and $\bar{\rho}\overline{u'w'}$ is the vertical flux of momentum carried by the wave (Reynold's stress). For an upward moving wave $\overline{p'w'} > 0$, so the wave carries westerly momentum when $c > \bar{u}$ and easterly momentum when $c < \bar{u}$. Thus when a wave does deposit momentum to the mean flow, it tends to drag the mean flow toward it's own phase speed (Lindzen, 1973,1990).

[3]Hines and Reddy (1967) showed that the energy flux is given by $\overline{p'w'} - \bar{\rho}(\overline{u'w'})\bar{u}$.

Eliassen and Palm's second theorem is given by:

$$\frac{\partial}{\partial z}(\bar{\rho}\overline{u'w'}) = 0 \tag{1.20}$$

This equation tells us that in the absence of thermal forcing, critical levels (i.e. $\bar{u}-c = 0$) and damping, no momentum flux is deposited or extracted from the basic flow, i.e. $\bar{\rho}\overline{u'w'}$ remains constant. (Lindzen, 1990). Thus, for a 2D, steady and linear case in the absence of critical levels and dissipation, the E-P flux, $-\bar{\rho}\overline{u'w'}$ is conserved. This is consistent with the discussion in section 1.1, where it was shown that in an isothermal atmosphere gravity wave, velocity fluctuations tend to grow exponentially in amplitude as the background density $\bar{\rho}$ decreases exponentially with height.

Ignoring the rotation effect, the GWD on the background flow is then given by the divergence (or in this case the vertical derivative) of the wave's E-P flux: i.e. $\frac{\partial \bar{u}}{\partial t} = -\frac{1}{\bar{\rho}}\frac{\partial}{\partial z}(\bar{\rho}\overline{u'w'})$. This is zero prior to saturation or breaking, i.e. $\bar{\rho}\overline{u'w'}$ is constant for conservative wave propagation as indicated by (1.20). This means that a steady undamped gravity wave induces no force on the mean state. In the case that wave is being dissipated, the magnitude of its flux is not constant and decreases with height and the wave dissipation exerts a mean force on the atmosphere (GWD).

1.5 Gravity Wave Drag Parameterization

Gravity waves with scales in the range of $\sim 10-1000$ km horizontally and ~ 100 m-30 km vertically, have important dynamical effects in the middle atmosphere and their dissipation generally occurs at even smaller scales. These gravity wave processes cannot be adequately resolved by current general circulation models (GCMs) and their

effects on the large-scale circulation must be parameterized.

Early numerical models produced unrealistic simulations of some atmospheric phenomenon, such as systematic strong westerlies in northern hemisphere in the troposphere and lower stratosphere known as *westerly biases*, as first noted by Palmer et al., 1986. It is now generally accepted that the westerly bias in models can be partially corrected with a suitable orographic GWD parameterization.

The middle atmosphere zonal winds in the earliest numerical models were simulated to be much stronger than observed (gray arrows in figure 1.3). Hamilton (1996) showed that applying thermal wind balance to radiative equilibrium temperatures in the middle atmosphere produced zonal wind speeds of over 30 m/s near the mesosphere. A missing drag force generated by breaking subgrid scale gravity waves was needed to reduce the winds to the observed values. Since there isn't sufficient data available to assimilate in the middle atmosphere, heights $\sim$ 50-90 km are excluded in many modern NWP models.

The stratosphere (z=10 km to 50 km), needs to be included in long-term forecasting of more than one week, due to the downward force induced by upper level GWD to the lower atmosphere (Kim et. al. 2003, see figure 5). Global NWP models are currently including most of the stratosphere to improve the modeling of satellite radiance and to provide initial states for the forecast models (Kim et.al., 2003).

As we discussed earlier, in the absence of dissipation, the gravity wave momentum flux densities, $\bar{\rho}\overline{u'w'}$, are conserved and therefore the gravity wave velocity fluctuations (e.g. $u'(x,z,t)$) tend to grow exponentially in amplitude as the background density $\bar{\rho}$ decrease exponentially with height. Thus, waves can attain large amplitude as they propagate to higher altitudes and may either saturate or break when nonlinear effects

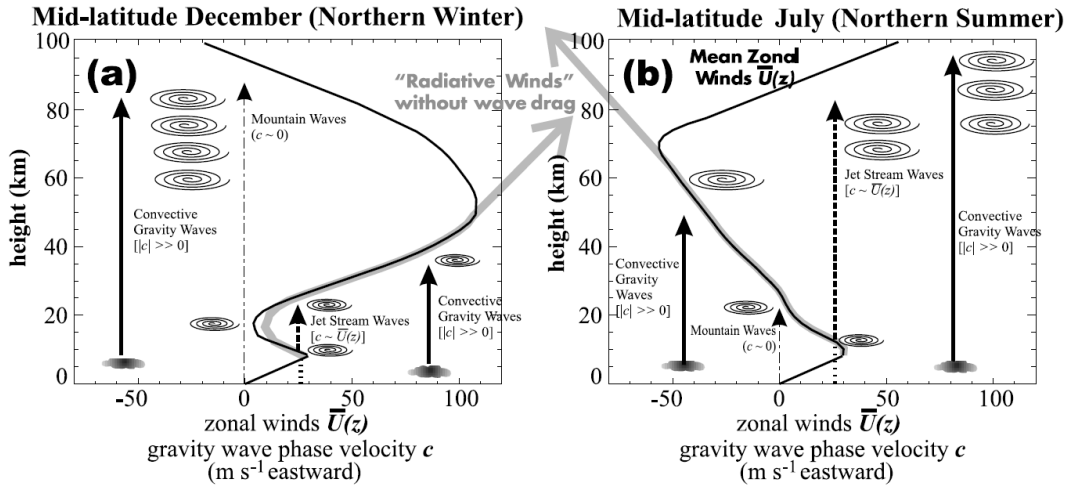

Figure 1.3: Black curve represents observed winds and gray curve shows radiative winds that would result from a model without wave drag parameterization during northern (a) winter and (b) summer. Gravity wave sources with different phase speeds, c, and wave breaking are shown. Gravity waves with different sources ascend while c remains constant, until they break or reach the critical level where $c_h = \bar{U}_h(z_C)$. After *Kim et al.*, 2003.

become important. As discussed in more detail in section 1.3, when gravity waves approach a critical level z_c, their intrinsic phase speed $|\hat{c}|$ and vertical wavelength λ_z vanish and their momentum in absorbed into the background flow. This *critical level filtering* of gravity waves is important in all GWD parameterizations. Ground base gravity wave speeds c are assumed constant in GWD parameterizations, under the assumption that horizontal variations in the background wind profile $\bar{U}(z)$ can be neglected. It is then relatively straight forward to identify the waves that reach their critical level.

Stationary gravity waves ($c = 0$) and also westward propagating gravity waves ($c < 0$) in north hemisphere winter (figure 1.3a) do not encounter critical levels and can propagate to high altitudes in the middle atmosphere. On the other hand, all except the fastest eastward propagating gravity waves ($c > 0$) encounter critical

levels in the eastward stratospheric jet and dissipate. In the absence of eastward phase speed waves, the stationary and westward phase speed waves in mesosphere, where $c - \bar{U}(z) < 0$, produce wave breaking in this region that drags the winds to the west. Otherwise, the presence of eastward phase speed waves would cancel this westward drag in the mesosphere. Note that orographic gravity waves breaking in the lower stratosphere will generate drag that tends toward the zero wind line (figure 1.3a).

The reverse situation occurs in northern hemisphere summer (figure 1.3b). Mountain waves and westward convective gravity waves are absorbed by the strong westward stratospheric jet, while the eastward convective waves and jet stream waves reach the mesosphere. This demonstrates that nonorographic gravity wave drag parameterization is critical for the extratropical middle atmosphere.

In order to parameterize these subgrid scale processes (GWD) in GCMs, one needs to specify the gravity wave sources and also an absorption mechanism which causes damping or obliteration of waves and deposition of their momentum to the mean flow.

1.5.1 Nonorographic Gravity Wave Drag Parameterizations

As we have seen, the drag exerted by nonorographic[4] gravity waves is critical in the upper stratosphere and mesosphere, where it prevents the formation of excessively strong zonal winds. Modern GCMs often contain independent parameterizations for orographic and nonorographic waves, primarily because the sources for the former are much better known than those of the latter. It is important to recognize that many so-called nonorographic parameterizations (including those considered in the present

[4]The sources of nonorographic gravity waves are nonstationary and so induce waves with non-zero horizontal phase speeds.

study) also include stationary waves, although the launch amplitudes are not tied to orography.

The source of nonorographic gravity waves can be specified by imposing a *launch spectrum* in the troposphere or lower stratosphere that is typically independent of time and geographic location. For reasons of efficiency, the effects associated with the propagation of waves in the horizontal are often neglected and the effects of vertical propagation are grossly simplified. Instead, as a first approximation, waves are assumed to be steady over the course of a model time step, so that changes in the spectrum and associated mean flux maybe calculated vertically in a column. However, some proposed parameterization schemes do not use column models, but rather do full ray tracing. These schemes are relatively time consuming and beyond the scope of this thesis, the focus of the current study will be on column models.

1.6 Outline of Thesis

Gravity waves play an important role in determining the general circulation of the atmosphere. Two of the least well understood aspects concern the generation of gravity waves (e.g. by synoptic scale disturbances) and the representation of their subgrid scale effects in global general circulation models. This study addresses both of these aspects.

Chapter 2 investigates gravity wave parameterization in the middle atmosphere, focusing on internal waves with a broad spectrum of phase speeds. We explore the underlying similarities and differences between Hines Doppler-Spread (1997), Warner and McIntyre (2001), Alexander and Dunkerton (1999) parameterizations, and the

extent to which they can be constrained by measurements of saturated wave spectra. We use these parameterizations to examine the evolution of the wave spectrum and drag as a function of phase speed and height. We employ a column model of gravity wave drag based on the COSPAR International Reference Atmosphere (CIRA, Fleming et al. 1990) wind and temperature data. The column model is based on fixed mean zonal wind and temperature profiles. Using this methodology, we identify the differences in GWD that are only due to dissipation mechanisms and launch spectra.

Chapter 3 will focus on the generation mechanisms of gravity waves, specifically the gravity wave hotspot over Newfoundland and Labrador. Hoffmann, Xue and Alexander (2013) first introduced global gravity wave hotspots and were able to categorize most of them in terms of their source mechanisms (i.e. orographic and convective sources). The peak event over Newfoundland and Labrador was among the unclassified hotspots. Chapter 3 shows the results of a series of simulations for a selection of strongest peak events using the Weather Research and Forecast (WRF) model, and investigates the characteristics and generation mechanisms of gravity wave peak events over Newfoundland.

Chapter 2

An Analysis of the Hines and Warner-McIntyre-Scinocca Nonorographic Gravity Wave Drag Parameterizations

2.1 Introduction

Lindzen (1981) and Holton (1982, 1983) clearly established the necessary role of nonorographic gravity waves in maintaining the observed zonal winds in the mesosphere. Since that time, several drag parameterizations for nonorographic gravity waves have been proposed, including Medvedev and Klaassen (1995), it's thermospheric variant by Yigit and Medvedev (2008), Hines Doppler-spread (1997), Alexander and Dunkerton (1999, hereafter AD), and Warner-McIntyre (2001, hereafter WM01). The latter is a more computationally efficient hydrostatic version of the non-hydrostatic parameterization proposed by Warner and McIntyre (1996, hereafter WM96).

While WM01 employed piecewise continuous spectra and saturation conditions, Scinocca (2003, hereafter S03) has developed a discretized implementation of the Warner-McIntyre scheme. Since WM01 and S03 represent different approximations

to essentially the same momentum deposition scheme, we will refer to both as the "WM scheme". Both the Hines and WM schemes have been employed in various middle atmosphere models. Manzini et al. 1997, Mayr et al. (1998a, 1998b, 2001, 2010, 2011), Fomichev et al. (2002), McLandress et al. (2006), Jockel et al. (2006), Schmidt et al. (2006) have all used Hines DSP, while Scaife et al. (2002), Warner et al. (2005), Scinocca et al. (2008) and Orr et al. (2010) have employed the Warner-McIntyre scheme.

Charron et al. (2002, hereafter CMW02) compared momentum deposition and drag profiles for the Hines and WM schemes based on CIRA86 winds and temperatures at 70° N in January and July. In the first set of comparisons, the WM launch spectrum was adjusted to match that recommended by Hines; in particular WM's value of the vertical wavenumber of spectral peak, $m^* = 2\pi/2$ km, was adjusted to match Hines' value of $2\pi/0.5$ km. When similar launch spectra were specified for the two schemes, WM was found to deposit momentum lower in the atmosphere than Hines, and to produce at least an order of magnitude less drag in the mesosphere. For both schemes, energy dissipation rates in the winter mesosphere were found to be within the range of measurements derived by Lubken (1997) from high-resolution rocket soundings.

For summer, Lubken found energy dissipation rates onset abruptly at altitudes greater than 80 km (near the mesopause). The Hines scheme agreed well with Lubken's sudden onset of dissipation above 80 km for the summer case, while WM with the same launch spectra did not. When the WM launch spectrum amplitude was increased by an order of magnitude, it matched the Hines and Lubken dissipation rates above 80 km reasonably well, but produced dissipation rates that were an order

of magnitude too large below that altitude.

CMW02 also found that profiles of wave-induced force produced by WM are smoother than those of the Hines Doppler-spread. One key aspect is that the saturation threshold of the WM scheme is set to the amplitude of the high-m portion of the *launch spectrum*; the latter amplitude is a free parameter of the scheme and in most if not all studies, it is not normally set to values consistent with atmospheric observations (see Appendix B of McLandress and Scinocca, 2005). This aspect is clearly the source of the increased momentum deposition produced by WM at lower altitudes.

McLandress and Scinocca's (2005, hereafter MS05) compared Hines and WM schemes (including the "AD" variant of WM) both in a column model based on CIRA winds and a middle atmosphere GCM. It should be noted however that in the AD variant of WM, the threshold amplitude is based on WM criteria rather than the overturning threshold proposed by Alexander and Dunkerton (1999). With the same launch spectra specified for each scheme, MS05's column model for June and July at 50° S confirmed CMW02's finding that the Hines' scheme produced momentum deposition and significantly stronger drag at higher altitudes. Taking an approach different from that of CMW02, they introduced a parameter C^* into the WM and AD schemes to adjust the saturation level of those parameterizations. The value $C^* = 1$ corresponds to the original WM scheme, which matches the saturation threshold to the one at launch altitude at high vertical wavenumbers m. They showed that increasing C^* to 50 for WM and 200 for AD brought the altitude of momentum deposition into rough agreement with that produced by the Hines scheme. This result underscores the fact that wave-breaking and/or saturation thresholds play a crucial role in

drag parameterizations.

MS05 also did GCM experiments showing that once the value of C^* was tuned to deposit momentum in the same altitude range as Hines, the resulting WM and AD simulations yielded zonal wind and momentum deposition fields that were "essentially indistinguishable" from Hines (their figure 10). They concluded that "significant differences between the various nonlinear dissipation mechanisms have little or no impact on the GCM response". This is because it is only the net drag that influences the GCM simulation. Since MS05 adjusted the WM, AD and Hines parameterizations to give similar momentum deposition profiles, they effectively removed the most significant differences between the forcing produced by the schemes. It is important to note that momentum deposition profiles produced by GWD parameterizations should not be tuned to match other schemes, but rather should be adjusted to be consistent with measurements, although such measurements are admittedly sparse.

Hines' Doppler-spread theory is based on Lagrangian wave theories (e.g. Hines 2001) which assume that waves are conservative, linear and sinusoidal in the Lagrangian frame, yet nonlinear when transformed to the Eulerian frame. Klaassen and Sonmor (2006) and Klaassen (2009a,b) tested the foundation of those Lagrangian wave theories, and demonstrated that the Hines picture of wave-wave interactions (Doppler-spreading) was based on a physically flawed theoretical model that involves singular Lagrangian to Eulerian transformations that violate both conservation of mass and thermodynamic energy. This immediately raises the question of why the Hines Doppler-spread parameterization has been able to produce reasonable middle atmosphere circulations. In this chapter, we will address this question by performing an in-depth analysis of the characteristics of the momentum deposition and drag

produced by the Hines and WM gravity wave drag schemes, as well as that produced by pure critical level deposition.

2.2 Column Model for Gravity Wave Drag

The present study employs a column model of gravity wave drag based on that of S03 (http://www.cccma.bc.ec.gc.ca/~jscinocca). For computational convenience, the model assumes hydrostatic nonrotating waves obeying the dispersion relation:

$$c - U = \pm N/m = \pm\hat{\omega}/k \tag{2.1}$$

where c is the observed horizontal phase speed, N is the Brunt-Väisälä frequency, $\hat{\omega}$ is the intrinsic frequency, k and m are the horizontal and vertical wavenumbers respectively, and U is the magnitude of the projection of the background horizontal wind in the azimuthal direction ϕ. For the purposes of this study, only eastward and westward azimuths are considered.

2.2.1 Desaubies Form of the Launch Spectrum

The spectral density of the total wave energy per unit mass in each azimuth ϕ at launch altitude is assumed to have the generalized Desaubies form (Fritts and VanZandt 1993):

$$\hat{E}(m, \hat{\omega}, \phi) = C \left(\frac{m}{m_*}\right)^s \frac{N^2 \hat{\omega}^{-p}}{1 + \left(\frac{m}{m_*}\right)^{s+t}} \tag{2.2}$$

Although this form of equation 2.2 has become accepted in both oceanographic and atmospheric applications and agrees reasonably well with statistically averaged

measurements of wave spectra, it must be noted that there is evidence indicating that the internal wave spectrum in the middle atmosphere does not take such a separable form in the presence of even moderate background flows (Gardner et al. 1993).

In Eq.(2.2), m_* is a characteristic vertical wavenumber corresponding to the local maximum spectral density, and C is an amplitude. The spectrum is proportional to m^{-t} for m large compared to m_*, with measurements constraining t to a value near 3. According to Fritts and VanZandt (1993), acceptable values for p lie in the range $(1 \leq p \leq \frac{5}{3})$. The parameter s determines the spectral shape at low m, but is not well-constrained by observations; commonly accepted values are in the range $s = 0$ to 1. We will adopt MS05's values of $t = 3$, $s = 1$, $m_* = 2\pi/2$ km and $p = \frac{3}{2}$ in all GWD calculations. These parameters represent a reasonable fit to the shape of the so-called "universal" gravity wave spectrum, which is roughly independent of location and season. For the purposes of S03's gravity wave drag parameterization, the value of C is a free parameter specifying the amount of upward momentum flux in each azimuth.

Gravity wave drag exerted on the mean flow is given by the divergence of the horizontally-averaged momentum flux (e.g. Fritts and Alexander 2003). The launch momentum flux density is obtained from $E(m, \hat{\omega}, \phi)$ by the group velocity rule (WM96):

$$\rho \hat{F}(m, \hat{\omega}, \phi) = \rho c_{gz} \frac{k}{\hat{\omega}} \hat{E}(m, \hat{\omega}, \phi) \tag{2.3}$$

where ρ is the basic state density and c_{gz} is the vertical group velocity ($c_{gz} = \partial\hat{\omega}/\partial m$). For hydrostatic waves, $|c_{gz}| = \hat{\omega}/m$, so Eq. (2.3) simplifies to:

$$\rho\hat{F}(m,\hat{\omega},\phi) = \rho\frac{k}{m}\hat{E}(m,\hat{\omega},\phi) \tag{2.4}$$

In the present case of interest, U and N may vary significantly with height, but not with horizontal position. Under these circumstances the horizontal wavenumber k and the ground-based horizontal phase speed c remain invariant during vertical wave propagation through background wind shear, while according to Eq. (2.1), m and $\hat{\omega}$ do not. During conservative wave propagation, the spectral element $(dmd\hat{\omega}d\phi)$ varies, so the momentum flux density $\rho\hat{F}(m,\hat{\omega},\phi)$ also changes so as to keep $\rho\hat{F}(m,\hat{\omega},\phi)dmd\hat{\omega}d\phi$ invariant. For the purpose of calculating momentum deposition, it is more convenient to work in a frame where the momentum flux density of the upward-propagating waves remains invariant in the absence of wave dissipation. For this reason, S03 chose to transform from $(m,\hat{\omega})$-space to $(c,\hat{\omega})$-space and then integrate over $\hat{\omega}$. The transformation is given by:

$$\rho F(c,\hat{\omega},\phi) = J_2\rho\hat{F}(m,\hat{\omega},\phi) = J_2\rho\frac{k}{m}\hat{E}(m,\hat{\omega},\phi) \tag{2.5}$$

where c is the horizontal phase speed in the direction ϕ and the Jacobian J_2 is

$$J_2 = \frac{\partial(m,\hat{\omega},\phi)}{\partial(c,\omega,\phi)} = \frac{m^2}{N} \tag{2.6}$$

Using the dispersion relation to replace the factor k/m by $\hat{\omega}/N$ in (2.4), and substituting from (2.2), the expression for $\rho F(c,\hat{\omega},\phi)$ becomes:

$$\rho F(c,\hat{\omega},\phi) = \rho C \left(\frac{m}{m_*}\right)^s \frac{m^2}{1+\left(\frac{m}{m_*}\right)^{(s+t)}}\ \hat{\omega}^{(1-p)} \tag{2.7}$$

$$= \rho C m_*^t \left(\frac{c-U}{N}\right)^{t-2} \frac{1}{1+\left[\frac{m_*(c-U)}{N}\right]^{(s+t)}}\ \hat{\omega}^{(1-p)} \tag{2.8}$$

where we have also used the fact that the dispersion relation (2.1) provides a one-to-one relation between m and c.

The dependence of the momentum flux on the non-conserved variable $\hat{\omega}$ may be removed by integration, as it is done in WM01 and S03. The momentum flux at launch altitude is non-zero only for the restricted range of frequencies $f^2 \leq \hat{\omega}^2 \leq N_\circ^2$ for which nonhydrostatic waves are allowed to propagate. Here $N_\circ \equiv N(z_\circ)$ where $z_\circ$ is the launch altitude. Introducing the subscript L in ρF_L and C_L to emphasize that this represents the momentum flux at launch level $z = z_0$, and setting $U = U_0 = U_0(z)$, the result of the integration of equation 2.8 over $\hat{\omega}$ is:

$$\rho\overline{F_L}(c,\phi) = \rho C_L m_*^t \left[\frac{N_\circ^{2-p} - f^{2-p}}{2-p}\right] \left(\frac{c-U_\circ}{N_\circ}\right)^{t-2} \frac{1}{1+\left[\frac{m_*(c-U_\circ)}{N_\circ}\right]^{(s+t)}} \tag{2.9}$$

It should be noted that the integration step has only introduced an additional constant factor in the numerator. It is convenient to cast (2.9) into the form:

$$\rho\overline{F}_L(\tilde{c},\phi) = \rho A_L \left(\frac{\tilde{c}}{N_\circ}\right)^{t-2} \frac{1}{1+\left[\frac{m_*\tilde{c}}{N_\circ}\right]^{(s+t)}} \tag{2.10}$$

where we have introduced the launch-relative phase speed $\tilde{c} = c - U_\circ$ and collected all constants into $A_L = C_L m_*^t \left[N_\circ^{2-p} - f^{2-p}\right]/(2-p)$. Applying MS05's values of $t = 3$, $s = 1$ and $p = 3/2$, we obtain the launch spectrum:

$$\rho \overline{F}_L(\tilde{c}, \phi) = \rho A_L \left(\frac{\tilde{c}}{N_\circ}\right) \frac{1}{1 + \left[\frac{m_* \tilde{c}}{N_\circ}\right]^4} \tag{2.11}$$

along with $A_L = 2 C_L m_*^t \left[N_\circ^{1/2} - f^{1/2}\right]$.

2.2.2 S03's Version of WM Dissipation

The WM parameterization (WM96, WM01, Scinocca (2002, hereafter S02), S03) is not based on an explicit physical mechanism for wave dissipation; instead it assumes wave spectra do not exceed a specific threshold based on the universal shape of vertical wavenumber and frequency spectra of atmospheric perturbations; any momentum flux that exceeds the threshold due to wave growth with height is deposited to the mean flow.

The wave energy density at saturation is taken to be:

$$\hat{E}_S(m, \hat{\omega}, \phi) = C_S \left(\frac{m}{m_*}\right)^{-t} N^2 \, \hat{\omega}^{-p} \tag{2.12}$$

where we depart slightly from S03 by allowing the saturation amplitude C_S to differ from the amplitude C_L of the launch spectrum. The exponent t represents the slope of the high-m spectral tail. The value $t = 3$ is in general agreement with statistical averages of both atmospheric and oceanic wave spectra. The corresponding momentum flux density is:

$$\rho \hat{F}_s(m, \hat{\omega}, \phi) = \rho c_{gz} \frac{k}{\hat{\omega}} \hat{E}_s(m, \hat{\omega}, \phi) \tag{2.13}$$

Following steps similar to those in the derivation of (2.8), the corresponding momentum flux density, transformed from $(m, \hat{\omega}, \phi)$ to $(c, \hat{\omega}, \phi)$ is:

$$\rho \hat{F}_s(c, \hat{\omega}, \phi) = \rho C_s m^2 \left(\frac{m}{m_*} \right)^{-t} \hat{\omega}^{1-p} \tag{2.14}$$

$$= \rho C_s \, {m^t}_* \left(\frac{c - U}{N} \right)^{t-2} \hat{\omega}^{1-p} \tag{2.15}$$

Again the $\hat{\omega}$ dependence may be removed by integration, with the limits at launch altitude being $f^2 \leq \hat{\omega}^2 \leq N_\circ^2$. At higher altitudes, S03 states that the intrinsic frequency $\hat{\omega}$ may be Doppler-shifted outside that interval. Therefore, S03 defines the formal limits for the integration as $\hat{\omega}_{low} \leq \hat{\omega} \leq \hat{\omega}_{hi}$. Treating $\hat{\omega}$ and m as independent variables, integrating (2.15) with respect to $\hat{\omega}$ yields

$$\rho \overline{F}_S(c, \phi) = \rho C_S I(z; p) \, {m^t}_* \left(\frac{c - U}{N} \right)^{t-2} \tag{2.16}$$

where $I(z; p)$ contains the result of the integration over $\hat{\omega}$:

$$I(z; p) = \int_{\hat{\omega}_{low}(z)}^{\hat{\omega}_{hi}(z)} \hat{\omega}^{1-p} d\hat{\omega} = \frac{\hat{\omega}_{hi}^{2-p}(z) - \hat{\omega}_{low}^{2-p}(z)}{2 - p} \tag{2.17}$$

S03 obtains the limits $\hat{\omega}_{low}$ and $\hat{\omega}_{hi}$ from the relation:

$$\hat{\omega}(z) = k[c - U(z)] \tag{2.18}$$

Since k and c are invariant for waves propagating in a horizontally homogeneous

medium, the intrinsic frequency at any altitude z can be related to its value at launch altitude $z_\circ$ by:

$$\hat{\omega}(z) = \hat{\omega}(z_\circ)\left[\frac{c - U(z)}{c - U(z_\circ)}\right]. \tag{2.19}$$

Consequently, S03 obtains:

$$\hat{\omega}_{low}(z) = f\left[\frac{c-U}{c-U_\circ}\right] \qquad \text{and} \qquad \hat{\omega}_{hi}(z) = N_\circ\left[\frac{c-U}{c-U_\circ}\right] \tag{2.20}$$

where $N_\circ = N(z_\circ)$ and $U_\circ = U(z_\circ)$. With this result, (2.17) may be written as:

$$I(z;p) = \left(\frac{c-U}{c-U_\circ}\right)^{2-p}\left[\frac{N_\circ^{2-p} - f^{2-p}}{2-p}\right] \tag{2.21}$$

Substituting (2.21) into (2.16) gives:

$$\rho\overline{F}_S(c,\phi) = \rho A_S\left(\frac{c-U}{N}\right)^{t-2}\left(\frac{c-U}{c-U_\circ}\right)^{2-p} \tag{2.22}$$

where $A_S = C_S m_*^t\left[N_\circ^{2-p} - f^{2-p}\right]/(2-p)$. Using $m = N/(c-U)$ from the dispersion relation, and introducing the launch-relative variables $\tilde{c} = c - U_\circ$ and $\tilde{U} = U - U_\circ$, this becomes:

$$\rho\overline{F}_S(\tilde{c},\phi) = \rho A_S\left(\frac{N}{\tilde{c}-\tilde{U}}\right)^{2-t}\left(\frac{\tilde{c}-\tilde{U}}{\tilde{c}}\right)^{2-p} \tag{2.23}$$

Putting $t = 3$ and $p = 3/2$, S03 obtains the following formula for the saturation limit with altitude:

$$\rho\overline{F}_S(\tilde{c},\phi) = \rho A_S\left(\frac{\tilde{c}-\tilde{U}}{N}\right)\left(\frac{\tilde{c}-\tilde{U}}{\tilde{c}}\right)^{1/2} \tag{2.24}$$

where $A_S = 2C_S m_*^t\left[N_\circ^{1/2} - f^{1/2}\right] = 2C_S m_*^3\left[N_\circ^{1/2} - f^{1/2}\right]$.

The saturation condition for each spectral element of the launch spectrum is given by:

$$\rho\overline{F}_L(\tilde{c},\phi) \leq \rho\overline{F}_S(\tilde{c},\phi) \tag{2.25}$$

The inequality (2.25) limits the total integrated momentum flux by removing a part of the solution in each model layer which is equal to the amount of momentum deposited to the flow in the current azimuth due to saturation.

It should be recognized that while the shape of the WM saturation threshold follows that of the universal spectrum, its amplitude is not necessarily taken to be consistent with measurements of saturated waves in the atmosphere. Rather it is set equal to the amplitude of the Desaubies launch spectrum, i.e. $A_S = A_L$. This prevents the abrupt deposition of arbitrary amounts of momentum at the first model level above launch altitude.

According to MS05 (see Appendix B), most if not all studies have set the launch amplitude A_L to a value well below the generally accepted range of saturated atmospheric waves. To assess the impact of having A_L below the observed range, MS05 introduced an additional constant factor C^* into their S03/WM saturation condition [their equation (4)]. In their nomenclature, $C^* = A_S/A_L$. MS05 reported that values of $C^* = 10$ to 30 were consistent with measurements of saturated atmospheric waves. According to WM96, WM01, CMW02, Scinocca et al. (2008), Orr et al. (2010), most modelers are using $C^* = 1$ for operational model simulations.

At this juncture, we wish to point out an unsettling aspect of S03's saturation threshold (2.24). For waves with phase speed less than horizontal background wind (i.e. $\tilde{c} < \tilde{U}$), the factor $\left[(\tilde{c}-\tilde{U})/\tilde{c}\right]^{1/2}$ is imaginary and is dealt with in the S03's program by taking the square root of the absolute value of $[(\tilde{c}-\tilde{U})/\tilde{c}]^{1/2}$. This un-

physical property can be traced back to S03's assumption that the intrinsic frequency $\hat{\omega}$ of a propagating wave may be Doppler shifted outside the interval $f^2 \leq \hat{\omega}^2 \leq N^2$. According to the nonhydrostatic rotating dispersion relation:

$$\hat{\omega}^2 = \frac{f^2 m^2 + N^2 k^2}{k^2 + m^2} \tag{2.26}$$

the intrinsic frequency is clearly constrained by $f^2 \leq \hat{\omega}^2 \leq N^2$, with the left limit corresponding to a critical level and the right limit corresponding to reflection. Certainly the hydrostatic non-rotating dispersion relation:

$$\hat{\omega}^2 = \frac{N^2 k^2}{m^2} \tag{2.27}$$

employed by S03 permits $0 \leq \hat{\omega}^2 \leq \infty$, but allowing that broad range of $\hat{\omega}$ leads to S03's potentially imaginary saturation threshold. We therefore suggest there is no physical basis for permitting $\hat{\omega}$ to wander over the full range allowed by (2.27). If instead one integrates $\hat{\omega}^{1-p}$ over the range f to N, one obtains:

$$I(z;p) = \int_f^N \hat{\omega}^{1-p} d\hat{\omega} = \frac{N^{2-p} - f^{2-p}}{2-p} \tag{2.28}$$

instead of (2.21) and:

$$\rho \overline{F}_S(\tilde{c}, \phi) = \rho A_S \left(\frac{\tilde{c} - \tilde{U}}{N} \right)^{t-2} \tag{2.29}$$

$$\rho \overline{F}_S(\tilde{c}, \phi) = \rho A_S \left(\frac{\tilde{c} - \tilde{U}}{N} \right) \tag{2.30}$$

instead of (2.23) and (2.24) respectively.

Here $A_S = C_S m_*^t \left[N^{1/2} - f^{1/2}\right] = C_S m_*^3 \left[N^{1/2} - f^{1/2}\right]$. Since the primary purpose of this chapter is to assess the behaviour of S03 and Hines schemes, we will not consider this modification of S03 scheme further.

2.2.3 Hines Doppler-spread Dissipation

Hines (1991b) Doppler Spread Theory (DST), maintains that nonlinear interactions between waves produce a net Doppler spreading of the wave spectrum to higher vertical wavenumbers. Waves with vertical wavenumbers greater than some imposed maximum value, were assumed to be obliterated as a result of critical level interactions.

The Doppler spread parameterization (Hines 1997 DSP) simplifies the DST by assuming that nonlinearity within the wave field may be modelled by enhancing the Doppler shifting by the background horizontal wind U, with an rms measure of the wave induced horizontal wind perturbations, u_{rms}. As a result, critical level filtering extends to additional wavenumbers and frequencies. Following Hines, the total wind is enhanced according to:

$$U_{tot}(z) = \bar{U}(z) + u_{rms}(z) = \bar{U}(z) + \Phi_1 \sigma(z) + \Phi_2 \sigma_T(z) \tag{2.31}$$

where σ is the rms wind for waves directed into the current azimuth, σ_T is the rms wind of all waves and Φ_1 and Φ_2 are adjustable tuning parameters. Following H97, MS05 use $\Phi_1 = 1.5$ and $\Phi_2 = 0.3$. DSP obliterates waves when their Doppler shifted m exceeds m_{max}, a third tuning parameter.

2.2.4 Alexander-Dunkerton-Warner-McIntyre Dissipation (AD-WM)

The Alexander and Dunkerton, 1999 (AD99) parameterization scheme assumes that nonlinear dissipation may be modeled by depositing all of the launch momentum flux of a spectral element at the altitude of the initial onset of instability. This differs from the Lindzen (1981) scheme which assumes that waves saturate at the onset of instability. AD99 use the Lindzen (1981) convective overturning criterion to determine the onset of instability but invokes obliteration instead of saturation. In principle, any dissipation criterion could be used for this purpose.

MS05 modified the WM scheme to accommodate the AD99 proposal that instabilities obliterate gravity waves rather than causing them to saturate. Thus, for altitudes and phase speeds where the launch momentum flux ρF_L exceeds the saturation threshold ρF_S given in (2.24), ρF_L is not reset to ρF_S (as in the WM parameterization) but is rather set to zero. While the AD-WM scheme does not produce the same drag as the original Alexander-Dunkerton parameterization, it will yield some insights into the possible consequences of assuming wave obliteration as opposed to saturation.

We should note that all GWD schemes (e.g. WM, AD and Hines), include some representation of critical level dissipation. However, we will demonstrate that there are significant differences between the WM and Hines representations of critical layer absorption.

2.2.5 The Method of Solution:

S02's scheme works as follows:

• The azimuthal dependence of the launch spectrum is represented by a number n_ϕ of equally spaced azimuths.

• The launch spectrum $\rho\overline{F_L}(\tilde{c},\phi)$ in each azimuth, is discretized in horizontal phase speed $\tilde{c}$ by a fixed number of spectral elements $n_{\tilde{c}}$.

• The total integrated E-P flux directed into each azimuth at launch, $\rho {F_L}^{total}(\phi) = \int \overline{F_L}(\tilde{c},\phi)d\tilde{c}$, is one of the most important and free parameters of the new scheme and is used to normalize $\rho\overline{F_L}(\tilde{c},\phi)$.

• Dissipative processes are represented by the application of the saturation condition (2.24), or by a substitute mechanism like Hines or AD, etc.

• This scheme produces two profiles of net eastward and northward vertical E-P fluxes. The zonal and meridional wind accelerations induced by the dissipation of nonorographic gravity waves are represented by the vertical divergence of these two fluxes.

2.2.6 Zonal Background Winds and Launch Spectrum

All of our calculations are based on representative midlatitude southern hemisphere (50° S) summer (January) and winter (June) CIRA profiles from COSPAR International Reference Atmosphere, CIRA. (Fleming et al. 1990). Profiles of CIRA mean zonal wind and temperature for January/June at 50° S are shown in figure 2.1. This figure shows that, unlike the tropospheric jets, the zonal middle atmosphere jets change direction with season, with westerly winds in the winter and easterly winds in the summer.

Critical level filtering by the background zonal wind at altitudes below the jet maximum occurs for eastward traveling waves in winter up to $c = 80$ m/s, and

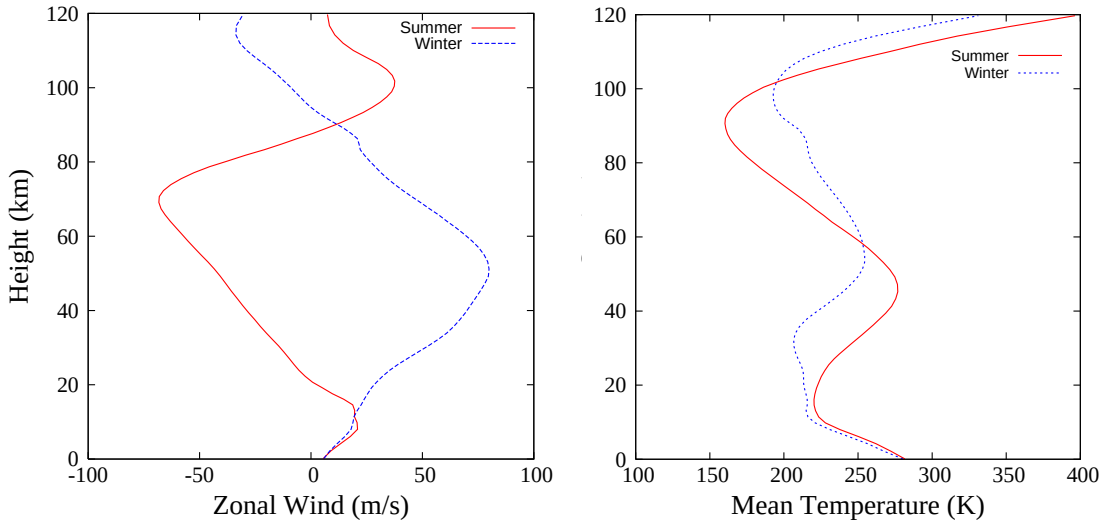

Figure 2.1: Profiles of mean zonal wind (left) and temperature (right) for January/June at 50° S from input CIRA data

westward traveling waves up to $c = -68$ m/s in summer. It means that waves with $c > 80$ m/s in winter and $c < -68$ m/s in summer can't meet critical levels, so will eventually break at very high altitudes.

Above z=87 km in summer and 95 km in winter, the zonal wind changes sign and there is a possibility of additional critical level filtering of waves that have propagated from the lower stratosphere, e.g. westward waves in winter and eastward waves in summer. This is only possible if these waves haven't already dissipated at lower levels by saturation or breaking mechanisms present in the gravity wave drag scheme.

Waves are launched in the eastward and westward azimuths, from an altitude of 17.5 km (83.2 hPa). By way of comparison, MS05 considered launch levels at the surface and 16 km (100 hPa), while S03 used 15 km (125 hPa). The launch momentum flux spectrum ($\rho\overline{F_L}$) with observed and launch-relative phase speeds for

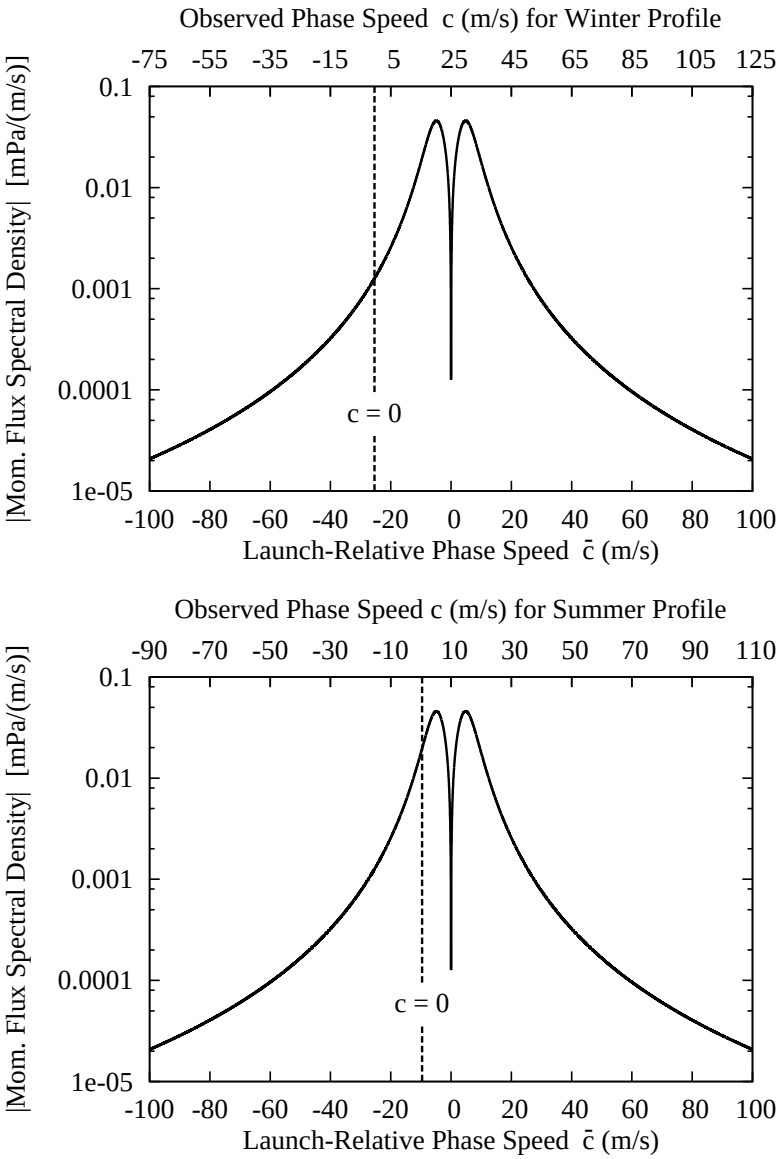

Figure 2.2: Launch spectra for winter and summer profiles vs. observed (c) and launch-relative ($\tilde{c}$) phase speeds. Owing to the log axis, the absolute value of the momentum flux spectral density is plotted. The actual momentum flux has the same sign as $\tilde{c} = c - u_0$.

each season are shown in figure 2.2.

S03 and MS05 employed a range of launch relative phase speeds from $|\tilde{c}| = 0.25$ to 2000 m/s and applied a nonuniform grid with 1000 intervals to provide increased resolution at small vertical wavelengths. We note the $\tilde{c} = 2000$ m/s is well outside the observed range of physical gravity wave phase speeds and corresponds to an excessively large vertical wavelength $\lambda_z = 2\pi c/N \approx 628$ km.

2.2.7 Profiles of Wave Drag

Gravity wave drag calculated for different phase speed intervals using CIRA winter profiles is illustrated in figure 2.3. This figure shows that waves with launch-relative phase speeds $|\tilde{c}| > 100$ m/s only produce significant drag above 105 km for Hines and 90 km for WM. Thus these waves dissipate and don't play a role in the middle atmosphere ($z \lesssim 85$ to 90 km)[1]. Since the S03/MS05 approach includes many unnecessary wave components, hereafter in all the calculations we use a uniform grid of 400 phase speeds for 0.25 m/s $\leq \tilde{c} \leq$ 100 m/s, which is sufficient to represent drag up to altitudes of 90 to 100 km. Although a smaller number of phase speed grid points would be acceptable, a grid with 400 points is chosen to provide a smoother spectral analysis for the Hines scheme in particular.

The total drag profile panels for no background wind are shown in Figure 2.4. As in all cases to be shown, similar *universal* wave spectra are launched at an altitude of $\sim$ 17.5 km. Note that the drag produced by the Hines scheme (a) is considerably stronger than that produced by WM (b). For example, the drag at z=100 km for Hines is $\sim \pm 200$ m/s/day, while it is an order of magnitude less ($\sim \pm 25$ m/s/day) for WM. Hines drag also shows strong fluctuations from level to level, a characteristic

[1]Waves with $\tilde{c} = 100$ m/s correspond to a vertical wavelength of $\lambda_z = 2\pi\tilde{c}/N \approx 30$ km.

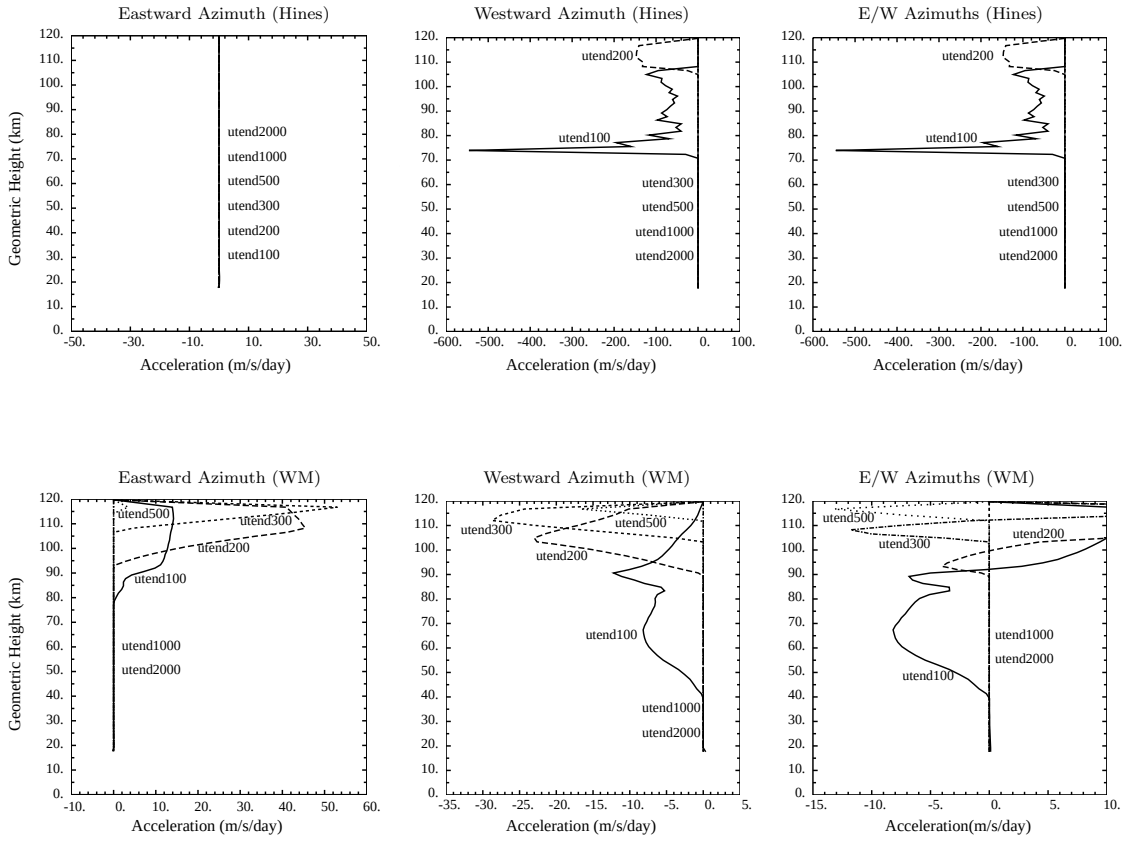

Figure 2.3: Drag (u-tendency) vs altitude z for WM and Hines schemes with CIRA winter profiles (June 50° S) for various phase speed intervals: utend100 ($\tilde{c}$ = 0 to 100 m/s), utend200 ($\tilde{c}$ = 100 to 200 m/s) utend300 ($\tilde{c}$ = 200 to 300 m/s), utend500 ($\tilde{c}$ = 300 to 500 m/s). Drag utend1000 ($\tilde{c}$ = 500 to 1000 m/s) and utend2000 ($\tilde{c}$ = 1000 to 2000 m/s) does not appear in the altitude range shown.

that could cause potential numerical issues in a GCM. We note that MS05 claim these oscillations can be removed by an iterative procedure to refine values of σ and σ_T. Of course, such iterations would increase the overall computational time for the Hines scheme, and so this extra step is not generally implemented in operational GCMs.

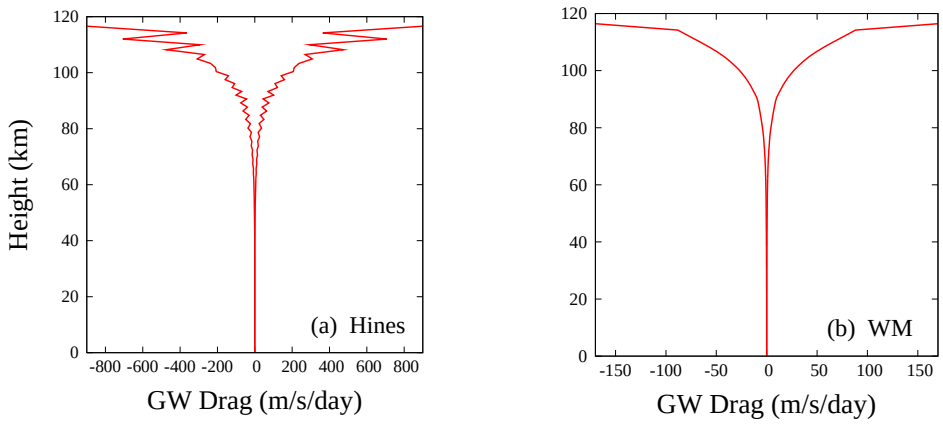

Figure 2.4: Gravity wave drag calculated for a windless atmosphere with (a) Hines and (b) WM GWD schemes with the same launch spectra. The launch level is located near 16 km, with total momentum flux eplaunch $= 7.2 \times 10^{-4}$ Pa and $m_* = 0.003$ rad/m.

Total drag profiles with winter and summer CIRA data and with similar launch spectra are shown in figure 2.5. Comparing the drag values in those plots, we can see that the Hines scheme produces a large amount of drag over a very narrow altitude range in both winter and summer profiles. Such highly localized forcing is not an ideal way to exert drag on the broad middle atmosphere jets. One expects drag to be distributed over a broad range of levels near and above the jet maximum. In contrast, WM produces considerably smaller amounts of drag spread over a large range of altitudes. While these total drag profiles are useful, more detailed information about each scheme can be gained by examining momentum flux spectra and drag contours as a function of phase speed and height.

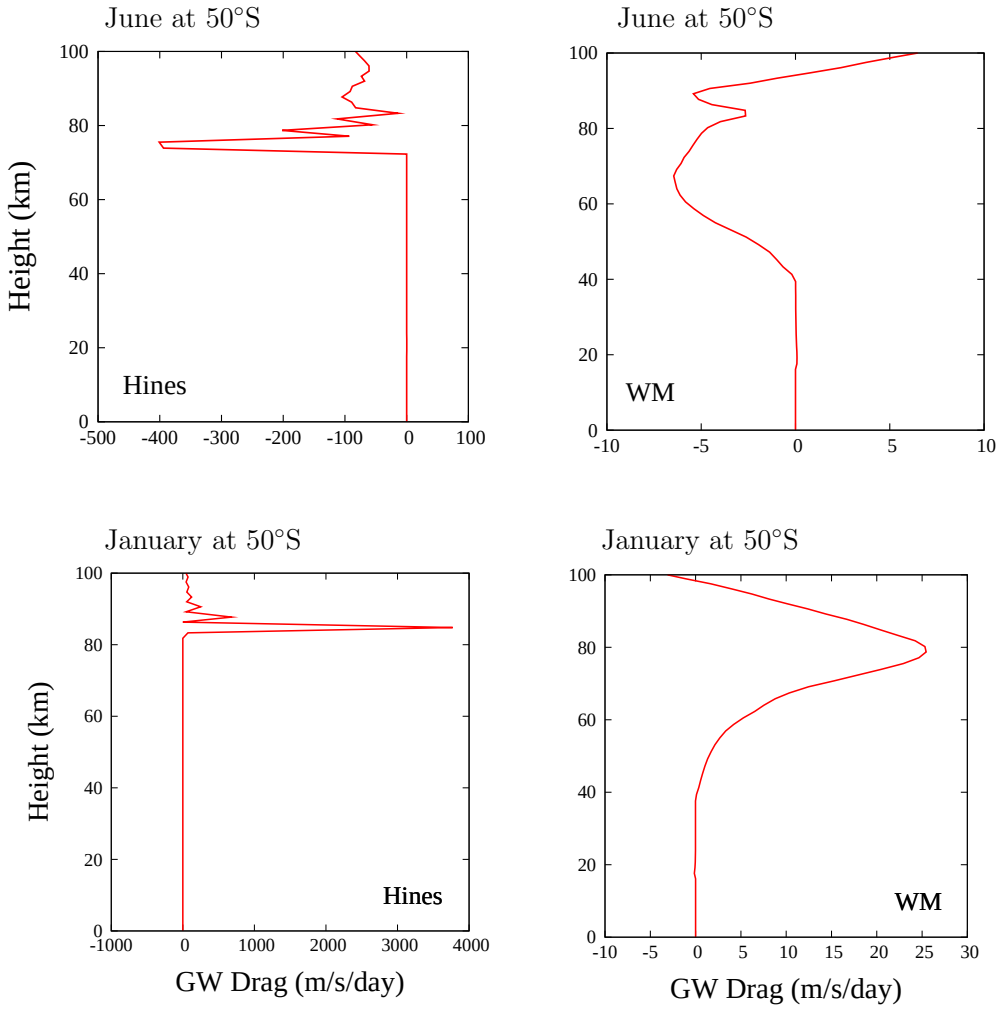

Figure 2.5: Gravity wave drag calculated with winter and summer CIRA profiles for Hines (left) and WM (right). The launch level is located near 16km, with the same launch spectra as in figure 2.4.

2.2.8 Momentum Flux Spectra for Various Altitudes

The Momentum Flux (MF) spectra at various levels are shown in figure 2.6 and 2.7 for Hines and WM respectively. Since momentum flux is conserved for stable non-interacting waves, any reduction in MF must be due to saturation or critical level

effects. The change in MF corresponds to the amount of momentum deposited by gravity wave to the background flow as a consequence of gravity wave dissipation.

As shown in figure 2.6 for the Hines scheme with winter CIRA winds, the critical level filtering of gravity waves is evident at $z = 19.2$ km. Here $\tilde{U} = 1.8$ m/s, so eastward waves with 0 m/s$< \tilde{c} <$1.8 m/s have been dissipated by critical level filtering. At higher altitudes eastward waves with larger $\tilde{c}$ continue to meet critical levels, with most of the eastward MF being deposited by $z = 35$ km. The MF deposition by westward waves begins just below $z = 73.9$ km, where the launch relative background wind $\tilde{U} \sim 12.3$ m/s ($\bar{U} \sim 37$ m/s), well below their lowest critical level near $z \sim 79$ km. At $z = 75.5$ km, waves with $\tilde{c} = -9$ to 0 m/s, (16 m/s$< c <$ 25 m/s) have been obliterated. This is due to Hines dissipation mechanism, in which nonlinear Doppler spreading is assumed to obliterate waves before their critical levels are reached. Virtually all of the westward momentum flux is obliterated by $z = 95$ km.

As shown in Figure 2.7 for WM with winter CIRA winds, the critical level filtering of eastward gravity waves by the background wind is also evident at $z = 19.2$ km. Interestingly, WM deposition at low $\tilde{c}$ does not show the sharp cut-off characteristic of critical level obliteration. The "curve" seen at the low-$\tilde{c}$ end of the spectrum is in fact due to waves exceeding their saturation threshold as they approach critical levels. This is because the WM/S03 saturation curve is proportional to $(\tilde{c}-\tilde{u})^{\frac{3}{2}}$, which vanishes at the critical layer. Thus WM/S03 includes some dissipation of waves at altitudes below their critical levels, rather than the abrupt obliteration in the Hines scheme. At altitude $z = 45.2$ km, where the background wind $\tilde{U} = 50.5$ m/s, just below the jet maximum, one can see momentum deposition of westward waves with

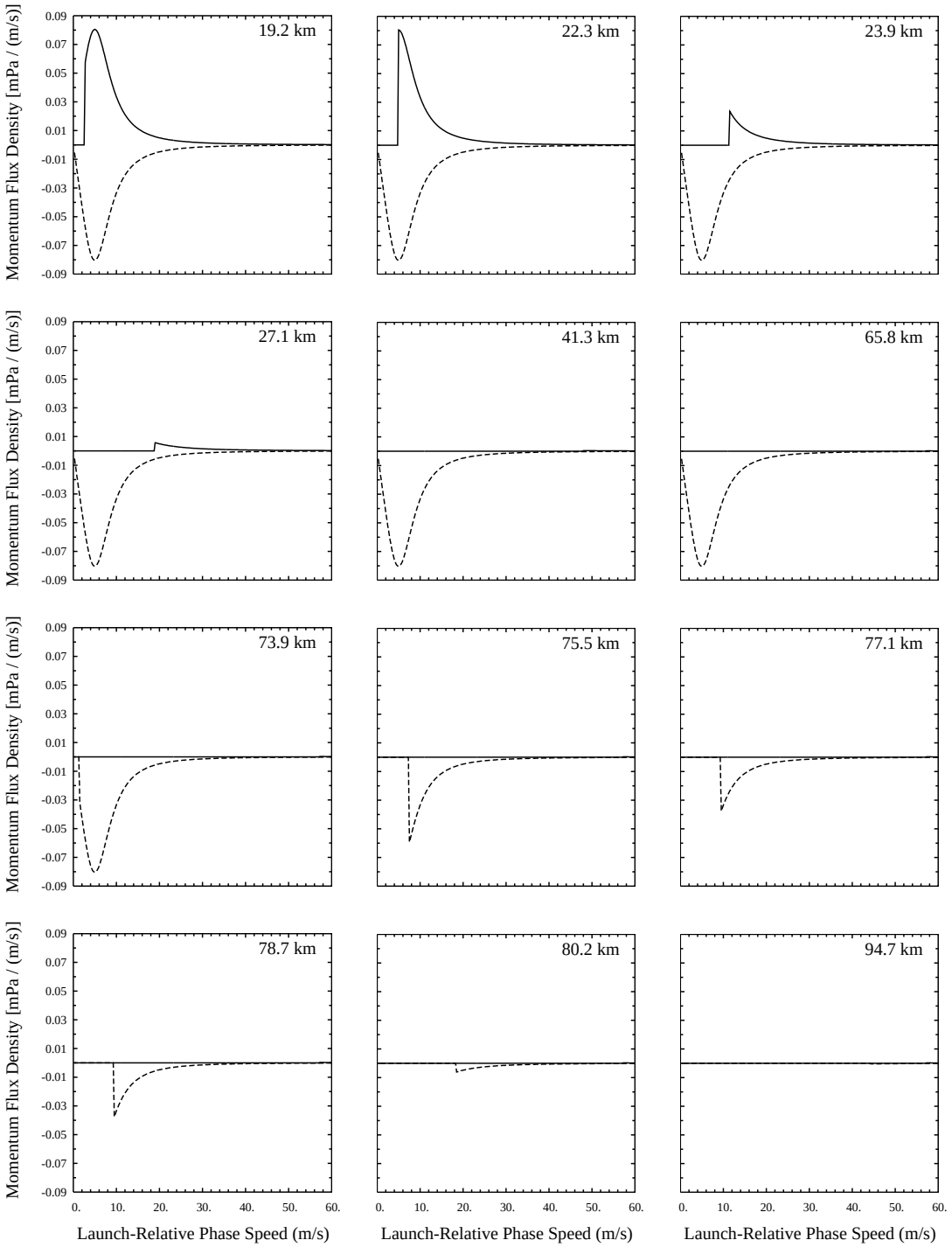

Figure 2.6: Eastward (solid) and westward (dashed) components of the momentum flux vs launch-relative phase speed $\tilde{c} = c - u_0$, at various altitudes for the Hines scheme with CIRA winter profiles (June 50S), for which $u_0 = 25.4$ m/s.

$\tilde{c} = -8$ to -4 m/s where they have exceeded the WM saturation threshold. This nonlinear deposition begins at lower altitudes than the Hines Mechanism.

2.2.9 Drag Contours in $\tilde{c} - z$ Space

The drag contours in $\tilde{c}-z$ space shown in figure 2.8 reveal which waves are breaking at which levels. Owing to the enhanced critical-level nature of Hines dissipation, the drag at any level is produced by a relatively narrow band of phase speeds. This leads to large amounts of drag being exerted in an oscillatory manner, a property which can cause problems in numerical models. In contrast, WM shows smaller amounts of drag deposited over a wider range of altitudes. In the windless cases, Figure 2.8(a) and (b), the eastward drag exactly balances the westward drag, so there is no net forcing of the zonal wind.

For the CIRA cases, high altitude drag for WM and Hines is predominantly in the azimuth opposite to the middle atmosphere jet. Interestingly, WM also shows somewhat smaller amounts of high altitude drag in the same azimuth as the jet, whereas such drag is too small to appear in the Hines plot. This same-azimuth drag is associated with saturating waves whose phase speeds are too large to meet critical levels at lower altitudes.

2.2.10 Momentum Deposition in $\tilde{c} - z$ Space

Momentum deposition contours in the $\tilde{c} - z$ plane are shown in figure 2.9 for the Hines and WM schemes and both seasons. These plots again demonstrate the altitudes at which specific wave components dissipate, but since momentum deposition includes weighting by density, one can clearly see both schemes produce narrow bands

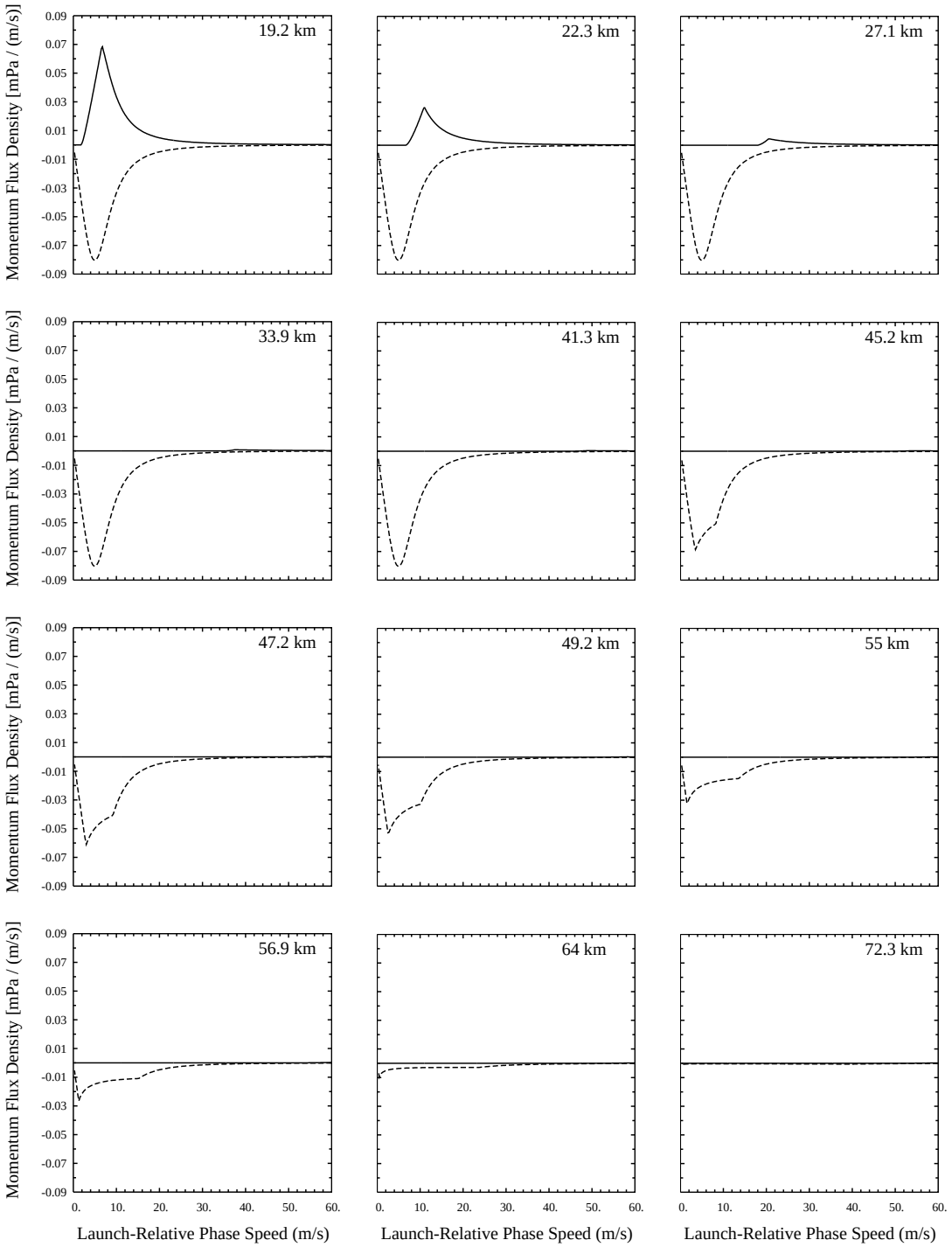

Figure 2.7: Eastward (solid) and westward (dash) components of the momentum flux vs launch-relative phase speed $\tilde{c} = c - u_0$, at various altitudes for the WM scheme with CIRA winter profiles (June 50° S), for which $u_0 = 25.4$ m/s.

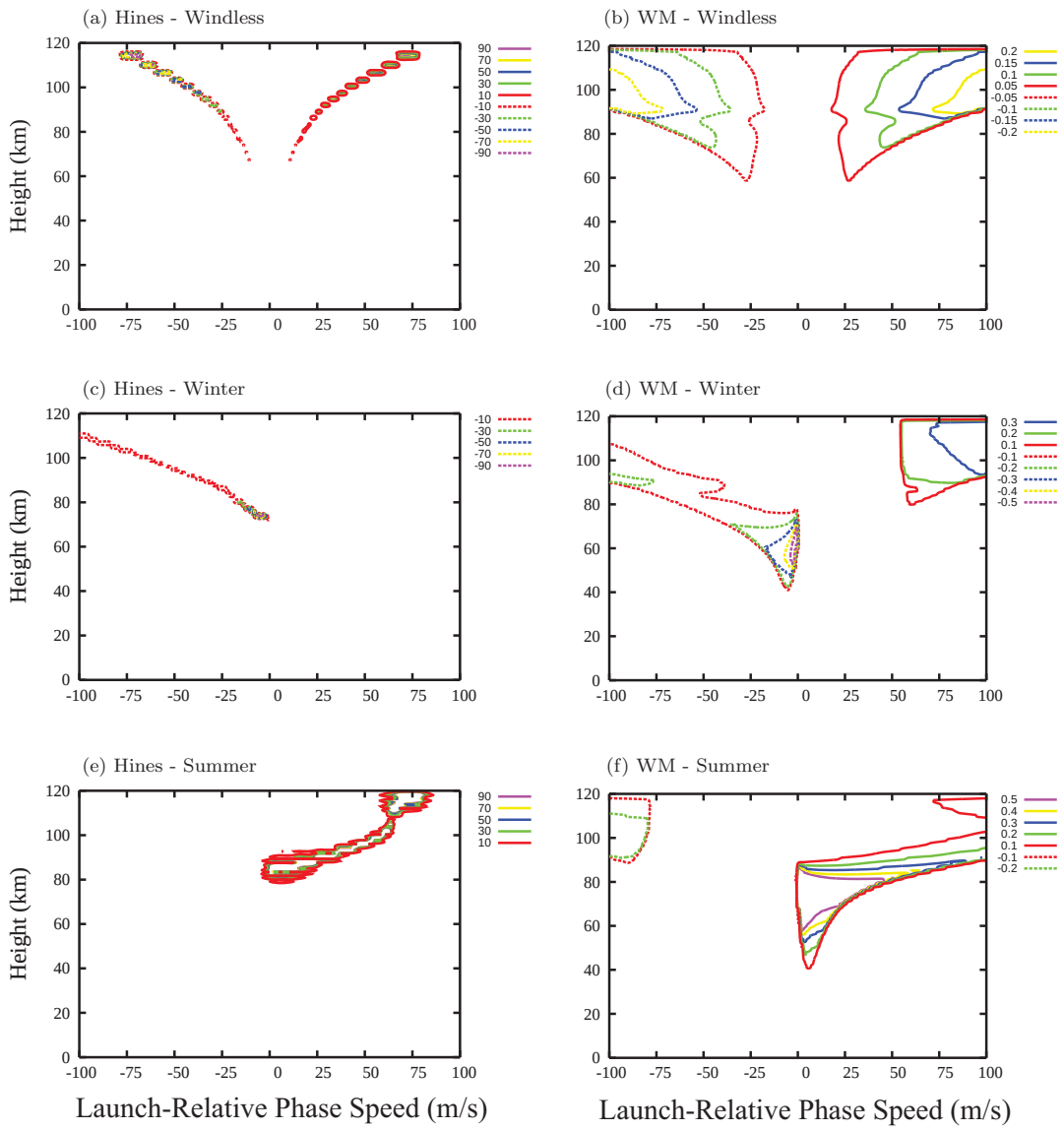

Figure 2.8: Gravity wave drag spectral density (/day) as a function of height calculated for windless atmosphere and with winter and summer CIRA profiles for Hines and WM. The horizontal axis is the launch-relative phase speed $\tilde{c} = c - u_0$. A uniform phase speed grid has been used with phase speed interval $dc = 0.25$ m/s. The launch level is located near 17.5 km, with $m_* = 0.003$ rad/m, and total launch momentum flux eplaunch $= 7.2 \times 10^{-4}$ Pa.

of momentum deposition as waves propagating through the jets in the stratosphere encounter their critical levels. At higher altitudes, Hines nonlinear dissipation produces similar narrow bands of momentum deposition, since it is based on spectrum-induced critical levels. In contrast, WM shows smaller amounts of drag deposited over a wider range of altitudes, typically with many wave components dissipating at each altitude. For the CIRA cases, WM also shows some high altitude acceleration in both azimuths (the summer case has momentum deposition smaller than the momentum contour level). While the Hines scheme does produce high altitude acceleration in the same azimuth as the jet, it is much higher than in the WM case, and too small to appear in the contour plot.

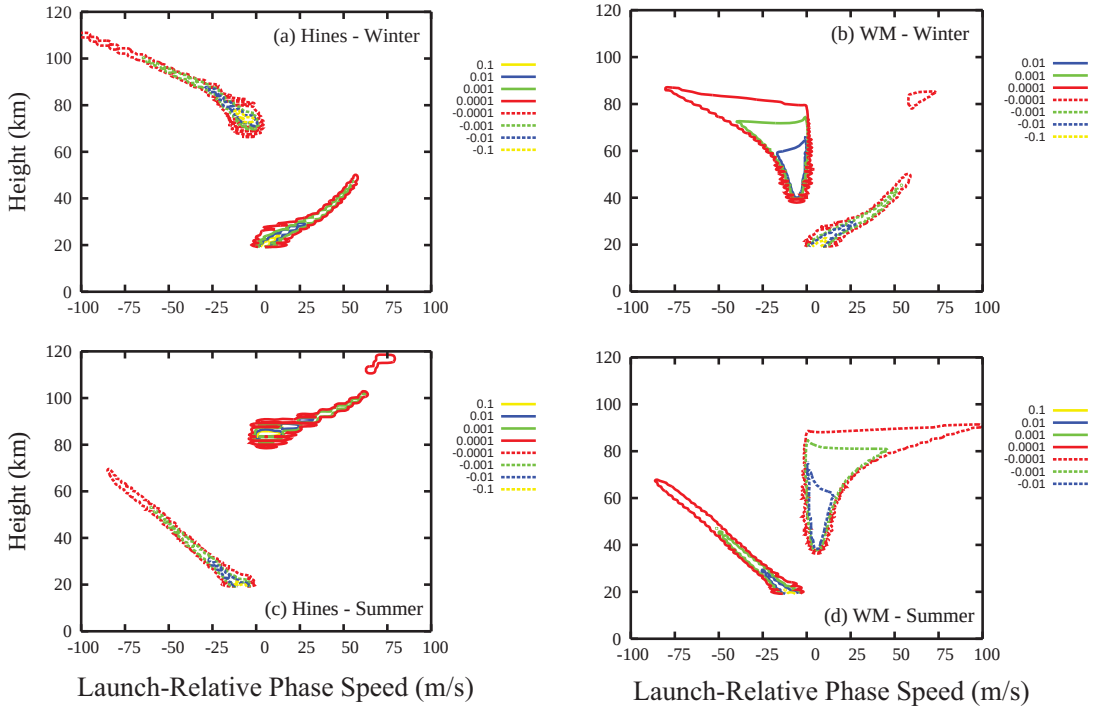

Figure 2.9: Momentum deposition spectral density (10^{-7} (Pa/m)/(m/s)) as a function of height calculated for with winter and summer CIRA profiles for Hines and WM mechanisms. The launch level is located near 17.6 km. A uniform grid has been used for contour plotting with phase speed interval of c=0 to 100 m/s and $dc = 0.25$ m/s.

2.2.11 Evolution of $\langle u'w' \rangle$ Spectra

In order to investigate whether the Hines, WM and AD GWD schemes are consistent with measurements of saturated wave spectra, it is useful to consider the evolution of $\langle u'w' \rangle$ spectra vs. height, since constant $\langle u'w' \rangle$ indicates saturation. On the other hand, the covariance $\langle u'w' \rangle$ of nondissipating waves grows with altitude, so plotting spectra of $\langle u'w' \rangle$ for various heights will show whether or not the waves present in the GWD scheme are saturating or not. There are two types of spectra to consider: those with respect to launch-relative phase speed and those with respect to vertical wavenumber. Since the launch-relative phase speed, $\tilde{c} = c - u_0$, is conserved as the wave components propagate upward, those spectra yield useful information about critical level deposition. On the other hand, vertical wavenumber spectra incorporate the effects of Doppler shifting by the background wind, according to the dispersion relation $m = \frac{N}{c-\bar{u}} = \frac{N}{\tilde{c}-\tilde{u}}$. Since m varies as the wave components propagate upward, m-spectra yield information about the shape of the spectrum at high-m that are not always evident from $\tilde{c}$-spectra. In particular, m-spectra are routinely used by experimentalists to demonstrate saturation at high values of m.

The spectral density of $\langle u'w' \rangle$ vs launch-relative phase speed for the windless case is shown in figure 2.10. First we note that there can be no critical level dissipation in this case due to the absence of a mean background wind and minimum $|\tilde{c}| = 0.25$ m/s. It should also be noted that the $\langle u'w' \rangle$ range is significantly higher for Hines and the case with no nonlinear dissipation than it is for the WM and AD cases. The case of no nonlinear dissipation [figure 2.10(d)], shows the $\langle u'w' \rangle$ spectrum simply growing with altitude, as expected. For the WM case [figure 2.10(b)] one clearly sees saturation starting at lower values of $\tilde{c}$ (corresponding to high m). As the spectrum

propagates upward, a wider phase-speed range is limited by the WM-S03 threshold for saturation. In other words, WM-S03 dissipation enforces a specific saturation envelope, and the $\langle u'w' \rangle$ spectra never exceed that envelope.

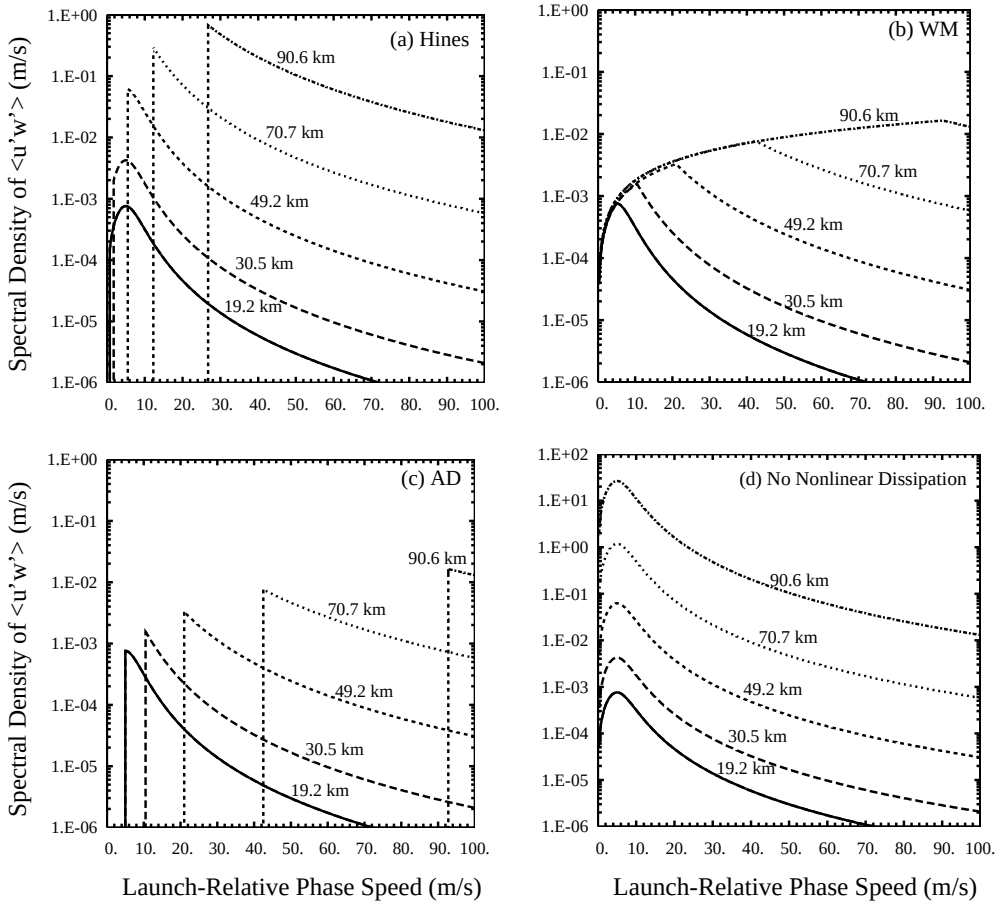

Figure 2.10: Spectral density of $\langle u'w' \rangle$ vs launch-relative phase speed $\tilde{c} = c - u_0$ at various altitudes, for a windless atmosphere $u_0 = 0$ m/s. (a) Hines, (b) WM, (c) AD and (d) No Nonlinear Dissipation.

For both Hines and AD however [figure 2.10(a),(c)], there is clearly no saturation. Instead, as the waves propagate upward, increasingly larger portions of the spectrum are completely wiped out. This is because Hines nonlinear dissipation acts like an enhanced form of critical level obliteration. Even though there is no mean wind in

this case, Hines treats the u_{rms} of the waves as an additional mean wind. Thus the Hines spectra do not saturate at lower values of $\tilde{c}$ as they do for WM. Instead, when the rms wind associated with the wave spectrum attains an rms value sufficient to produce Hines' hypothesized Doppler spreading, waves are obliterated from the low-$\tilde{c}$ side. For example, at z=90.6 km, the Doppler spread is about 27 m/s, so all waves from $\tilde{c}$=0 to 27 m/s are removed from the spectrum.

For AD, the low-$\tilde{c}$ chopping of the spectrum is considerably more pronounced than in the case of Hines. This is because the MS05 version of AD obliterates and deposits the wave momentum flux when the wave amplitudes exceed the specific WM-S03 saturation level. Consequently, obliteration for AD occurs over a much wider range of phase speeds than for the Hines DSP scheme. In other words, the MS05 variant of AD behaves like a more aggressive version of the Hines scheme. For example, at z=90.6 km, AD obliterates all waves up to c=93 m/s, compared to 27 m/s for Hines.

The spectral density of $\langle u'w' \rangle$ vs. vertical wave number m for the windless case is shown in figure 2.11. The case without nonlinear dissipation [figure 2.11(d)] shows that the amplitude of the high-m tail grows as the waves propagate upward. Of course this is not consistent with atmospheric measurements, which indicate that the high-m portion of the spectrum saturates. Obviously an appropriate nonlinear dissipation mechanism is required to produce saturation. The WM scheme in figure 2.11(b) does exhibit saturation at high m, as $\langle u'w' \rangle$ never exceeds a specific line with slope of about -3.3 (as determined from the graph). This saturation behaviour is not surprising, since the WM-S03 dissipation mechanism is based on empirical measurements of wave saturation. Note that the $m^{-3.3}$ shape of $\langle u'w' \rangle$ differs somewhat from the m^{-3} form of kinetic energy spectra ($\langle u'u' \rangle$).

In contrast, for Hines DSP [figure 2.11(a)], the high-m tail is progressively obliterated by the Doppler-spread mechanism as the wave spectrum propagates upward. Note that the high-m tail is entirely obliterated for altitudes above ≈ 51 km. Again, it is seen that the obliteration for waves in the tail is even more pronounced for the MS05 version of the AD mechanism [figure 2.11(c)], since all waves that exceed the WM-S03 saturation threshold are obliterated. In this case the high-m tail is completely obliterated for altitudes of about 30.5 km and higher.

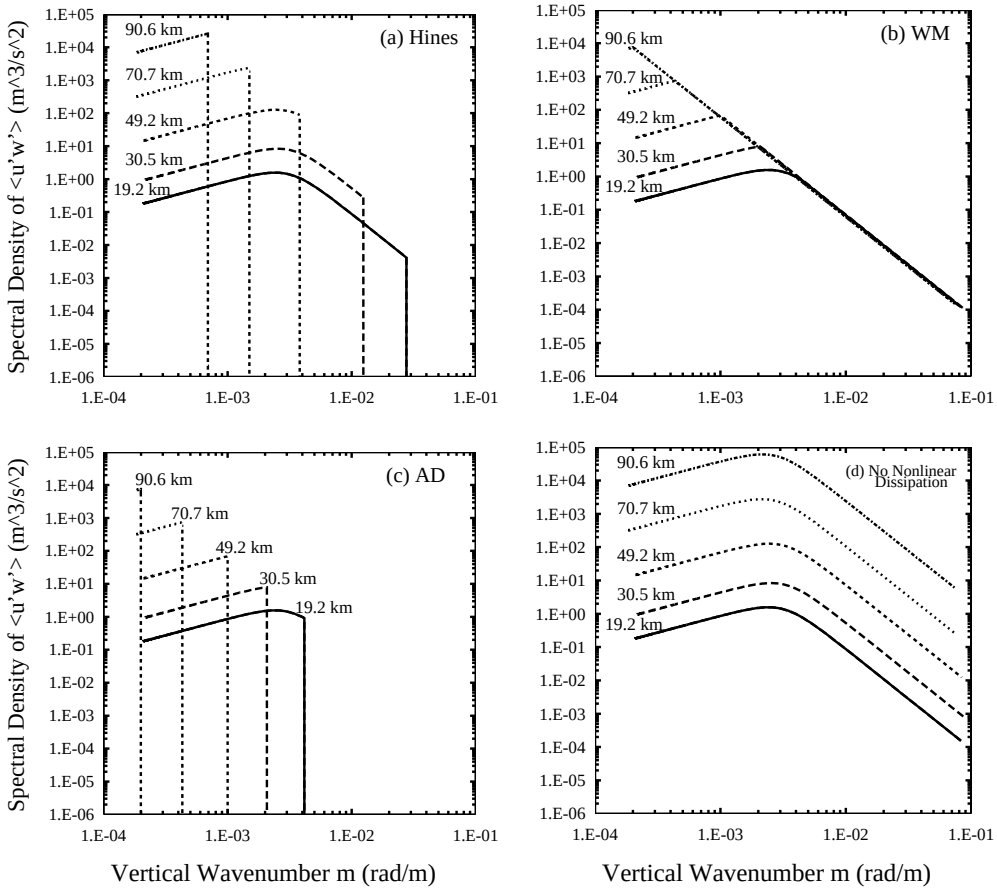

Figure 2.11: Spectral density of $\langle u'w' \rangle$ vs vertical wave number, m, at various altitudes. Windless atmosphere for (a) Hines, (b) WM, (c) AD and (d) No Nonlinear Dissipation.

It is clear that for this windless case, both Hines and the AD variant of WM drastically erode the spectrum, leaving nothing that is even close to compatible with the universal saturated m^{-3} spectral tail seen in measurements of middle atmosphere waves. Since WM's nonlinear dissipation is modeled on saturation, it produces a saturated tail, although the amplitude is lower than observations.

CIRA winds affect the wave spectrum through critical level interactions. For example, the winter eastward jet filters out a large portion of the eastward wave spectrum ($\tilde{c}$ = 0 to 54.5 m/s) at altitudes between 17.6 km (launch) and 51.2 km, while westward waves freely propagate to higher altitudes. The summer westward jet filters out westward waves from $\tilde{c}$ = 0 to -77.9 m/s at altitudes between launch and 69.1 km. Since the launch-relative phase speed of wave components is conserved, those spectra are most useful for demonstrating critical level effects, while vertical wavenumber spectra are needed to evaluate saturation effects in the presence of a mean wind.

figure 2.12(a) shows the effect of CIRA midlatitude winter winds on eastward gravity wave spectra for the WM scheme. Eastward waves meet critical levels below the altitude of the jet maximum (about 51 km). The spectra at 19.2, 30.5 and 49.2 show progressively greater amounts of critical level obliteration until all waves with $\tilde{c} < 54.5$ m/s (the launch-relative maximum wind speed of the jet) are filtered out. For phase speeds $\tilde{c} > 54.5$ m/s, waves continue to propagate upward unimpeded by further critical-level interactions. When they reach altitudes above 70.7 km, WM-S03 saturation comes into play. At z=90.6 km, waves with $\tilde{c}$ = 54.5 m/s to 89 m/s have clearly exceeded the WM-S03 saturation threshold.

figure 2.12(d) shows a similar process occurs for westward waves for the CIRA

summer wind profile. Since the jet maximum has $\tilde{u} = -78$ m/s at z=69 km, all westward waves with $|\tilde{c}| < 78$ m/s are obliterated by critical levels by the time the spectrum reaches z=70.7 km. The spectrum at z=90.6 km has clearly exceeded the WM-S03 saturation threshold.

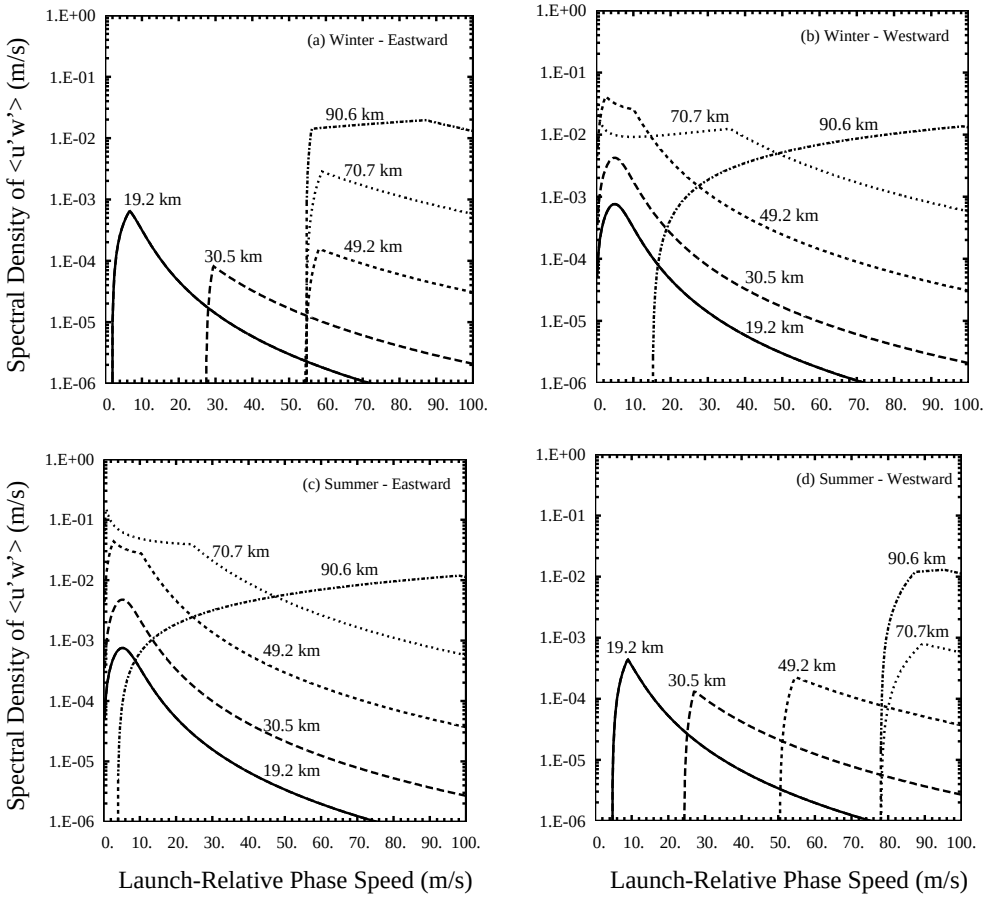

Figure 2.12: Eastward and westward components of spectral density of $\langle u'w' \rangle$ vs launch-relative phase speed $\tilde{c} = c - u_0$, at various altitudes. WM scheme with CIRA winter and summer profiles [June ($u_0 = 25.4$ m/s) and January ($u_0 = 9.6$ m/s) at 50° S.]

figure 2.12(b) shows that westward waves in winter begin to experience WM-S03 saturation at altitudes just below 49.2 km. Critical level obliteration begins at z=81

km, where the launch relative zonal wind changes sign. When the spectrum has reached z=90.6 km, westward waves with $|\tilde{c}| < 15.1$ m/s have been removed from the spectrum. figure 2.12(c) for the Summer-Eastward case is very similar, with saturation commencing just below z=49.2 km. In this case the launch-relative zonal wind changes sign at z=90 km, and all waves with $\tilde{c} < 3.8$ m/s are filtered out by critical levels. In both the winter-westward and summer-eastward cases, the shape of the spectrum at z= 90.6 km is a combination of saturation and critical level effects (all waves from $\tilde{c} = 0$ to 100 m/s have saturated).

In order to assess the shape of the high-m tail for WM, we refer to the m-spectra presented in figure 2.13. These figures show the effect of Doppler shifting on the spectrum, according to the dispersion relation $m = N/(\tilde{c} - \tilde{u})$, when $\tilde{c}$ approaches $\tilde{u}$, m becomes large and the wave component approaches critical level conditions. This particular Doppler shifting process can have the effect of extending the spectrum in vertical wavenumber space. On the other hand, when $\tilde{c}$ and $\tilde{u}$ are in opposite azimuths, m values may become small and the spectrum may be compressed in wavenumber space.

figure 2.13 shows m-spectra for the WM scheme. Consider first the Winter-Eastward (a) and Summer-Westward (d) cases. For altitudes below and just above the jet maxima (z=51 km for Winter-Eastward and z=69 km for Summer-Westward), the m-spectra show a long spectral tail with $m^{-3.3}$ shape, similar to that found in the no wind case for WM dissipation. However, unlike the no wind case, the amplitudes of the spectral tails vary by a factor of 7 or more for the different altitudes. Moreover, at altitudes above the jet maximum, Doppler shifting due to the background wind steadily decreases, and additionally, all waves with $\tilde{c} < 54.5$ m/s (winter) or 77.9 m/s

(summer) have been removed by critical levels. As a consequence of these two effects, the spectral tail tends to be severely truncated at altitudes sufficiently far above the jet maximum.

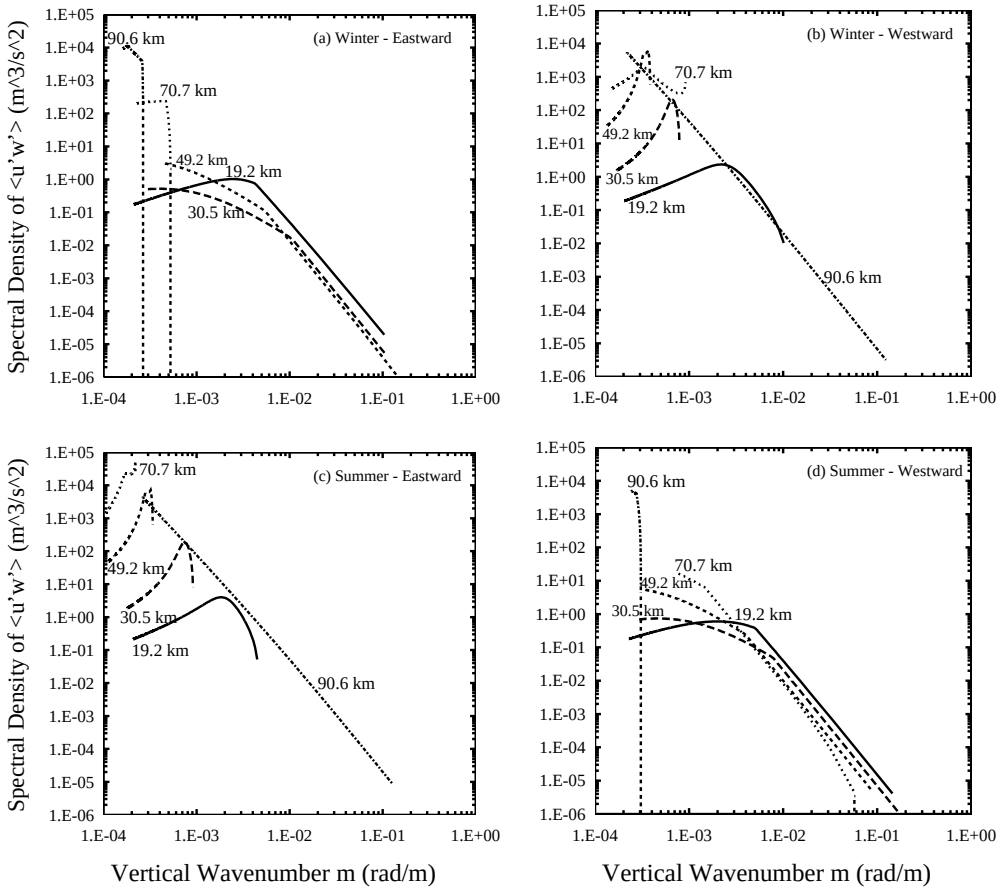

Figure 2.13: Eastward and westward components of spectral density of <u′w′> vs vertical wave number, m, at various altitudes for WM scheme with CIRA winter and summer profiles (June and January 50° S).

As specific examples of the effect of Doppler shifting, consider the summer westward and winter eastward spectra [figure 2.13(d),(a)] at z=70.7 km. The summer westward spectrum at z=70.7 km is significantly Doppler shifted to high m, while the corresponding winter eastward spectrum is not. This can be explained as follows.

For the summer westward case, that altitude is just barely above the jet maximum, yielding a smallest intrinsic phase speed of $\tilde{c}-\tilde{u} = 0.2$ m/s; this corresponds to a large maximum vertical wavenumber of 6×10^{-2} m^{-1}. In contrast, for the winter westward case, the corresponding spectrum has been drastically compressed in wavenumber space. For winter, the altitude 70.7 km is about 20 km above the jet maximum. Thus the smallest remaining phase speed in the spectrum after critical level filtering (54.5 m/s) has been Doppler shifted to 34.8 m/s, yielding a rather small maximum vertical wavenumber of about 5.3×10^{-4} m^{-1}. It is worth pointing out that the launch-relative mean CIRA wind reverses direction at altitudes of 81 km (winter) and 90 km (summer); above those altitudes, Doppler shifting tends to compress the spectrum even further, as is evident for both winter and summer spectra at z=90.6 km.

The Summer-Eastward and Winter-Westward cases for WM [figure 2.13(b),(c)] show a saturated $m^{-3.3}$ covariance spectrum only for the altitude z=90.6 km. At all other altitudes, the waves propagate in the opposite azimuth to the background wind, and the spectra have been compressed. In summary, figure 2.13 demonstrates that even though WM-S03 imposes a saturation condition consistent with atmospheric observations of wave spectra, it does not necessarily produce spectra of saturated form when the waves propagate in an azimuth opposite to the background wind.

figure 2.14 shows the evolution of wave $\tilde{c}$-spectra with height for the Hines scheme with CIRA midlatitude winds. At first glance, the winter eastward and summer westward $\tilde{c}$-spectra [figure 2.14(a),(d)] appear roughly similar to those produced by the WM scheme. The main differences are as follows.

The Hines critical level obliteration is abrupt, while WM-S03 critical level absorp-

tion is more gradual, with some dissipation evident for waves a few m/s away from the critical threshold. Hines critical level absorption is also hastened by u_{rms}. For example, at altitudes above the jet maximum, all waves up to $\tilde{c} = 57$ m/s have been obliterated for the winter eastward case, whereas only waves up to 54.5 m/s encounter critical levels in the WM scheme. In the summer westward case, Hines obliterates waves up to $\tilde{c}$=84 m/s whereas critical levels only dissipate waves up to 78 m/s in the WM scheme.

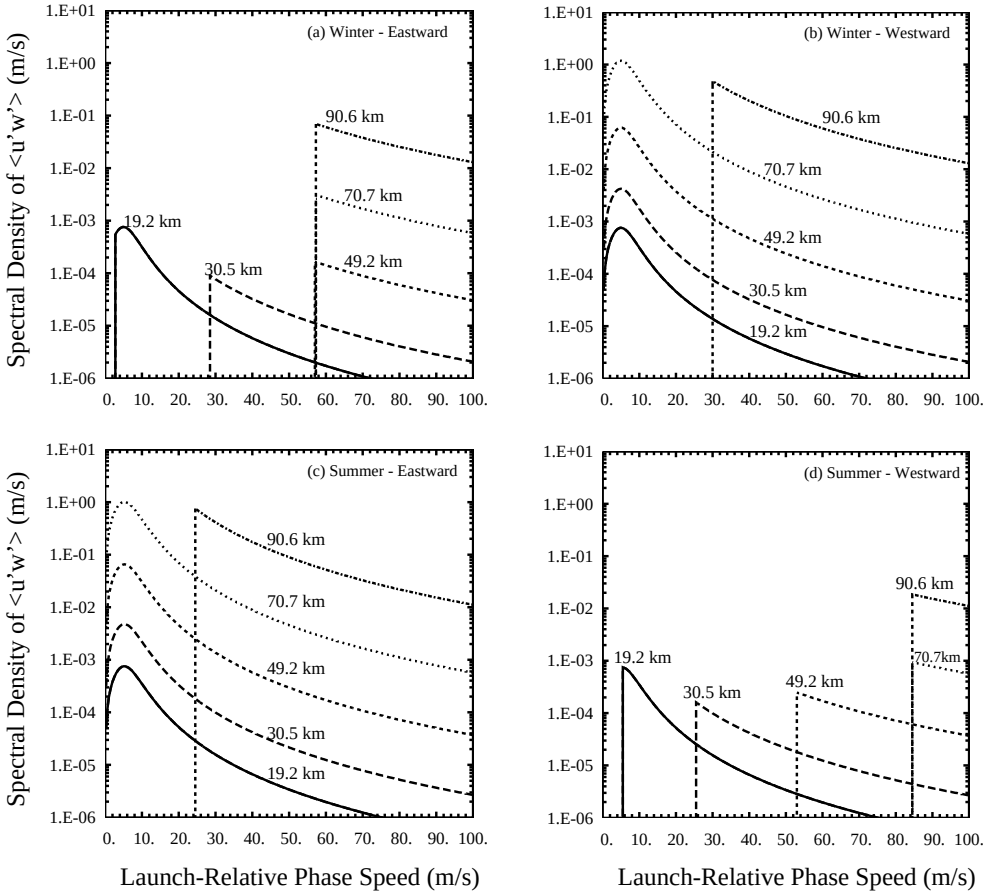

Figure 2.14: Eastward and westward components of spectral density of <u′w′> vs. launch-relative phase speed $\tilde{c} = c - u_0$, at various altitudes. Hines scheme with CIRA winter and summer profiles [June ($u_0 = 25.4$ m/s) and January ($u_0 = 9.6$ m/s) at 50° S].

At altitudes above 70.7 km, waves are also dissipated by saturation in the WM-S03 scheme, while they aren't in the Hines scheme. In the winter westward and summer eastward cases [figure 2.14(b),(c)], the waves do not encounter critical levels below the wind reversal altitude. The Hines spectrum at z=90.6 km shows dramatically enhanced critical level obliteration compared to WM. For example for winter westward at z=90.6 km, Hines has obliterated all waves up to $\tilde{c}$=30 m/s, while the critical levels in WM-S03 filter only waves up to $\tilde{c}$=15.1 m/s.

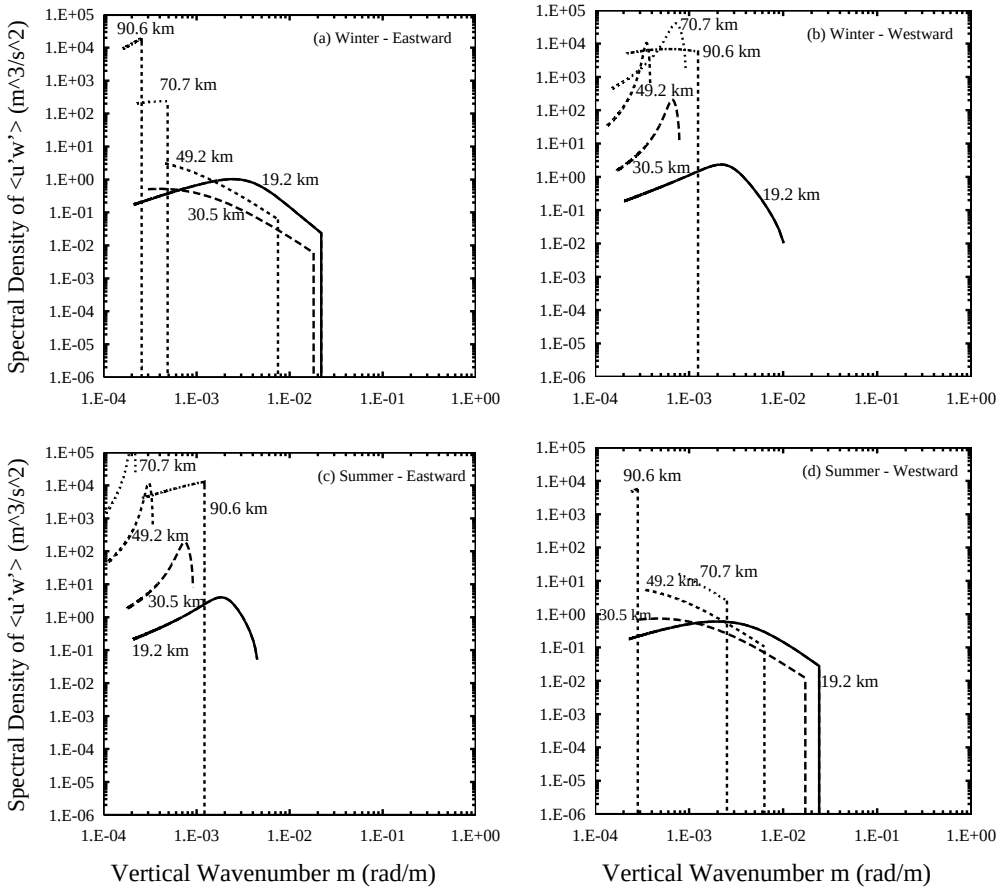

Figure 2.15: Eastward and westward components of spectral density of $<u'w'>$ vs vertical wave number, m, at various altitudes for Hines with CIRA winter and summer profiles (June and January 50° S).

In the summer eastward case the corresponding values are $\tilde{c} = 24$ m/s for Hines vs. $\tilde{c} = 3.8$ m/s for WM-S03. The WM-S03 saturation condition produces dissipation in the spectra at z=49.2 and 70.7 km, whereas Hines produces no dissipation at these lower levels.

For CIRA midlatitude background wind profiles, the vertical wavenumber spectra in Fg. 2.15 demonstrate that Hines DSP does not produce $m^{-3.3}$ spectral tails at any altitude, for any azimuth or season. WM produced such tails at least at some altitudes. Similar results to WM are obtained for the MS05 variant of AD dissipation, but are not shown here in the interest of brevity. Further discussion and conclusions will be presented in Chapter 4.

Chapter 3

Gravity Wave Generation over Newfoundland and Labrador in Winter

3.1 Introduction

Hoffmann et al. (2013) used radiance measurements obtained from the Atmospheric Infrared Sounder (AIRS) aboard NASA's Aqua satellite to detect gravity wave peak events, where the local brightness temperature variances significantly exceed background levels. The satellite is in a sun-synchronous polar orbit at altitude 705 km with a period of 99 minutes, which crosses the equator at 1:30 A.M. local time (descending pass) ans 1:30 P.M. local time (ascending pass). AIRS measures infrared thermal emissions of atmospheric constituents in the nadir and sublimb observation geometry. Sublimb scans are performed using a rotating mirror across the track. There are 90 footprints in each across-track scan, which covers 1765 km or $\pm 48.95^{\circ}$ in scan angle. The distance between two scans along the track is 18 km. AIRS measurements have been continuously provided since September 2002. Major advantages of the AIRS data are the good horizontal resolution and the long time series of observations, however, the vertical resolution is rather coarse.

Hoffmann et. al. (2013) gathered AIRS data into a $0.5° \times 0.5°$ longitude-latitude grid (roughly 50 km by 50 km). In the latitude range from 82° S to 82° N there are typically 10 to 16 footprints in each grid box per day. Their analysis covers nine years (2003 to 2011) of AIRS observations, during which, measurement dropouts of more than a day occur only from 29 October to 18 November 2003 and from 9 to 26 January 2011. Observations from 6 A.M. to 6 P.M. local time are classified as daytime and observations from 6 P.M to 6 A.M. are considered as nighttime data.

The AIRS spectral measurements cover the wavelength ranges 3.74 to 4.61 μm, 6.20 to 8.22 μm, and 8.8 to 15.4 μm. A diffraction grating disperses the scene radiance onto 17 linear arrays of HgCdTe detectors, providing a total of 2378 radiance channels (Hoffmann et. al., 2010). Hoffmann's analysis is based on average brightness temperatures from 42 AIRS channels in the 4.3 μm CO_2 fundamental band. The brightness temperature variance measurements at 4.3 μm are used to detect gravity waves. At this wavelength, due to strong absorption bands of CO_2, the atmosphere becomes optically thick in the stratosphere, and tropospheric emissions from clouds or interfering species like water vapor do not influence the measurements.

The brightness temperature perturbations are calculated by taking a fourth-order polynomial fit for each scan. Each polynomial fit is limited to data from 90 footprints for the full scan. The stratospheric gravity waves are identified based on local variances that are calculated from the brightness temperature perturbations. According to Hoffmann et. al. (2013), the observed temperature variances (${\sigma_A}^2$) have two main components, ${\sigma_A}^2 = {\sigma^2}_{GW} + {\sigma^2}_N$, the contributions due to gravity waves (${\sigma^2}_{GW}$) and instrument noise (${\sigma^2}_N$). They use a variance filter to distinguish gravity wave disturbances from instrument noise. The algorithm used to detect gravity wave hotspots

was the same as the one used in Hoffmann and Alexander (2010), but with a different variance threshold which varies with respect to latitude, month, and time of day[1].

Monthly peak event frequencies were calculated for the whole measurement period and then averaged for different seasons (November to February, March and April, May to August, September and October), giving each month equal weight to homogenize the results. The gravity waves detected by this algorithm are in the altitude range from 20 to 65 km with vertical wavelengths larger than roughly 15 km and horizontal wavelengths from 50 to 1000 km^2. This means the AIRS observations are limited to $\lambda_z > 15$ km, whereas the peak of the stratospheric gravity wave spectrum is found at shorter vertical wavelengths, e.g., $\lambda_z \approx 2$ to 6 km over AIRS altitude range (Fritts and VanZandt, 1993). This long wavelength is due to the broad vertical weighting functions used in the temperature retrievals from AIRS radiance measurements (infrared nadir soundings).

When the peak event frequency of a specific region exceeded 5%, Hoffmann et. al. (2013) considered the location to be a gravity wave hotspot. The hotspots were classified according to source mechanisms for gravity waves, in particular with respect to orographic and convective generation. AIRS radiances at 8.1 μm were used to detect any simultaneous deep convective events (i.e. high cold cloud tops), including deep convection in the tropics and mesoscale convective systems at middle latitudes. Since this was a global scale study, the brightness temperature thresholds were based on a monthly-mean zonal-mean tropopause temperature climatology derived from NCAR/NCEP reanalysis to allow for variations with latitude and season.

[1]The variance threshold used in their study at 50° N in December for ascending orbit is ≈ 0.1 K^2 (night) and for descending orbit (day) is ≈ 0.2 K^2.

[2]Note that the upper horizontal wavelength limit depends on the lower vertical wavelength limit.

Although Hoffmann and his collaborators were able to reproduce well-known hotspots of gravity waves and identify the source mechanism for many of the hotspots as either orographic or convective sources, 1-2 % of the hotspot areas including the peak event over Newfoundland and Labrador during the winter time remained unclassified (see figure 3.1). This chapter therefore investigates the generation mechanisms of gravity waves over Newfoundland and Labrador in winter.

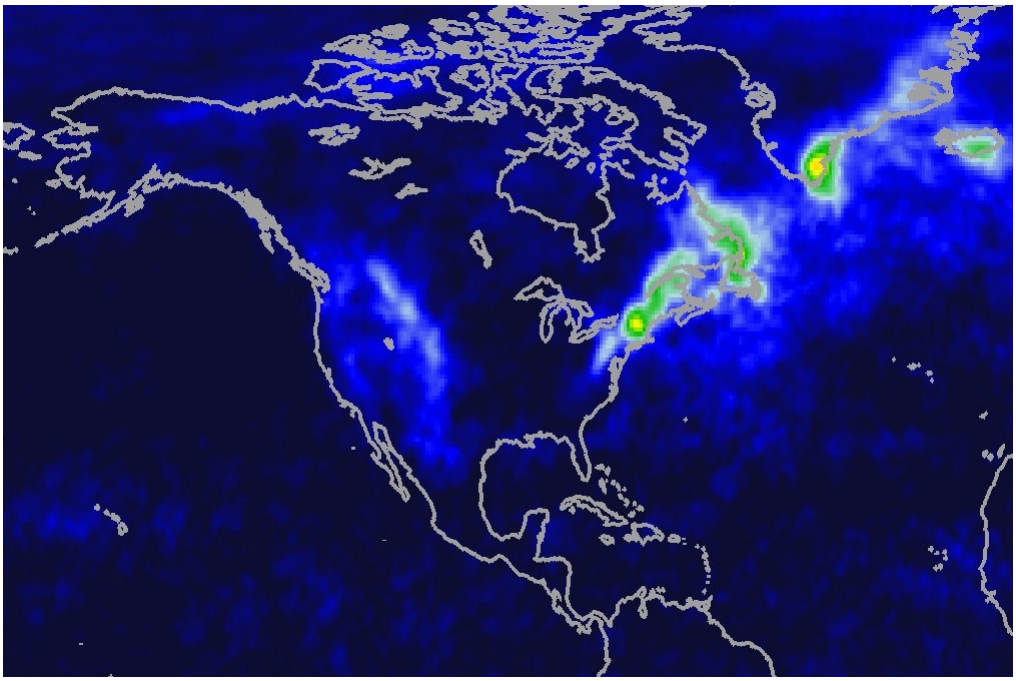

Figure 3.1: Peak event frequencies of gravity waves over North America at night as obtained from AIRS observations during the winter time 2003 to 2011 (After *Hoffmann et al.*, 2013).

Note that the hotspots over the Appalachians and Greenland were classified as orographic but surprisingly, there are relatively low frequencies over the Rockies. This suggests there may be more than topography playing a role in the generation of wintertime gravity waves over the Appalachians and Greenland. For example, the North American East Coast winter storm track may be playing a role. It is also

possible that many gravity wave emission events over the Rockies may have vertical wavelengths that are too short to be seen by AIRS. Hoffmann et. al. (2013) did find a prominent orography gravity wave hotspot over the U.S. Rockies in the summer. This seasonal difference may be due in part to the mid-latitude jet stream being located further south during the summer.

For the reference purposes, it is useful to compare heights for the various mountain ranges. The Long Range mountains in Newfoundland reach heights of only 800 m, while the highest peaks in the Torngats (northeast Labrador) reach 1500 to 1650 m. The highest Appalachian mountains attain heights of about 1600 m (Main), 1920 m (Mew Hampshire), 1750 m (Virginia) and 2040 m (North Carolina). While the peaks in the Colorado Rockies are higher, ranging from 2400 to 4350 m, it should be recognized that the surrounding foothills are at elevations from 1400 to 1600 m.

We obtained a time series of 12 years of AIRS data over the Newfoundland and Labrador region (area shown in figure 3.2) from Dr. Hoffmann and identified the events with the largest gravity wave activity. We then selected three of the strongest peak events and examined the synoptic situation with North American Regional Reanalysis (NARR) data that extends to 100 hPa ($\sim$ 16 km) and has 0.3° (32 km) horizontal resolution at the lowest latitude. In each case, we found evidence of upper level jet streaks passing along the coast of North America suggesting a possible baroclinic wave generation mechanism similar to figure 1.1. However, it should be noted that the surface flows were very different in these three cases. We then performed a series of simulations using the Weather Research and Forecast (WRF) model to further investigate the characteristics and generation mechanisms of those gravity wave peak events over Newfoundland.

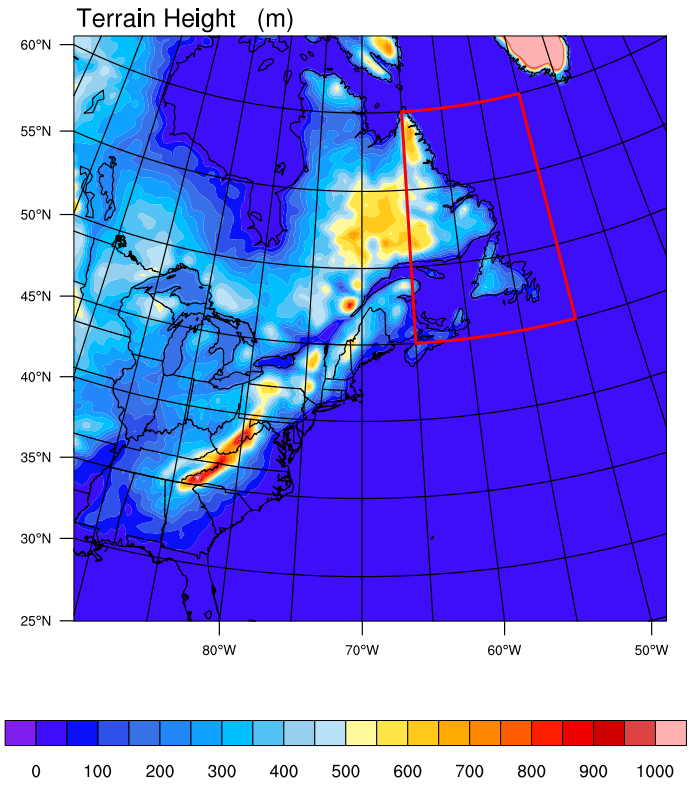

Figure 3.2: The lat-lon box over Newfoundland and Labrador, in which the AIRS time series were extracted.

The initial and boundary conditions for the simulations are provided from either NCEP FNL (Final) Operational Global Analysis data or ECMWF (European Centre for Medium-Range Weather Forecasts) ERA Interim data, both of which have coarser horizontal resolution but greater vertical extent than NARR data. We study three particularly strong peak wintertime events, 2003, 2008 and 2014. Although in all those cases we found significant jet stream development in upper levels during the times of peak events, the surface flow in each case is different and therefore leads to a different mechanism for gravity wave generation. In order to identify each individual source, we ran a few test simulations, eliminating each potential source (convection and

topography) from the model, and compared the results with the original simulations.

3.2 Numerical Simulations of Mid-latitude Baroclinic Generation of gravity wave (Literature Review)

Numerical models have been helpful in the investigation of gravity wave generation mechanisms by synoptic scale flows. While a few idealized simulations have been performed to study the generation of mesoscale gravity waves during the life cycle of idealized baroclinic jet-front systems, there have been relatively few real case studies. This section will review some of the idealized and real case simulations.

3.2.1 Idealized Simulations

O'Sullivan and Dunkerton (1995) made one of the first attempts to simulate inertia gravity waves initiated from an idealized baroclinic case. They used a slightly modified version of the 3D, global, hydrostatic primitive equation model of Young and Villere (1985), which is a spectral transform model with finite differencing in the vertical with no topography or moisture. The model had a horizontal resolution of 1° (110 km) and the vertical coordinate was uniformly spaced in log pressure with $\Delta z = 700$ m up to 35 km (51 levels). They used the Lagrangian Rossby number ${R_o}^{(L)}$ which is the ratio of parcel acceleration to Coriolis acceleration ($|d\mathbf{V}/dt|/f|\mathbf{V}|$) to estimate the flow imbalance[3]. Their results showed that an upper level jet distorted by baroclinic

[3]note that $d\mathbf{V}/dt \approx -f\hat{z} \times \mathbf{V_a}$, where $\mathbf{V_a}$ is the ageostrophic component of the wind.

instability, radiates low frequency gravity waves in the jet stream exit region.

Zhang (2004, hereafter Z04) studied the generation of mesoscale gravity waves via a developing baroclinic system using extremely high-resolution simulations (up to $\Delta x = 3.3$ km and $\Delta z = 180$ m) in a multiply nested mesoscale model. In his control simulation (CNTL) with the MM5 model, he employed three model domains (D1, D2, D3) with 90, 30, and 10 km horizontal grid spacing, respectively, and 60 vertical layers with 360m vertical spacing (top at 21.6km). The initial condition was an idealized balanced two-dimensional (2D) baroclinic jet with constant potential vorticity below and above a specified tropopause. A localized, three-dimensional, balanced perturbation of moderate amplitude was added to the base state to represent the early phase of typical mid-latitude cyclogenesis. To study the characteristics of simulated mesoscale gravity waves, Z04 examined the evolution of the horizontal velocity divergence during the baroclinic wave life cycle. A packet of mesoscale gravity waves with a vertical wavelength of 2.5 km and a predominant horizontal wavelength of about 150 km was found. The gravity waves originated from the upper-tropospheric jet-front system and in the left exit region of the upper-level jet streak and persisted for more than 24 hours. This is in agreement with the scenario proposed by UK87.

Wei and Zhang (2014), addressed the general role of moisture and heating in the generation of gravity waves in idealized baroclinic systems. Their work is complementary to the dry simulations of Z04. They performed a series of cloud-permitting simulations with the WRF model (version 3.4), with increasing moisture content. The domain was 4000 km in the zonal (x) direction, 8020 km in the meridional (y) direction, and 22 km in the vertical (z) direction ($\Delta x = \Delta y = 10$ km and $\Delta z = 300$ m on average with 70 vertical layers). They used periodic boundary conditions in x and

rigid boundaries in direction y. To prevent artificial wave reflection from the model top, Rayleigh damping was applied to the vertical velocity in the upper 5 km of the model domain. Moist processes were parameterized with the Lin et al. (1983) microphysics scheme. While no specific convection scheme was mentioned, models with $\Delta x = \Delta y = 10$ km generally do employ convective parameterizations. Radiation, surface fluxes, and friction were all neglected.

The model was initialized with a balanced 2D baroclinic jet, similar to that of Simmons and Hoskins (1978), and its most unstable perturbation. The procedure for creating the initial balanced jet is similar to that used by Z04 and Wang and Zhang (2007). The initial moisture field follows Tan et. al. (2004) and Zhang et. al. (2007). They showed that the dry experiment with no moisture or convection produces gravity waves that are consistent with past modeling studies, e.g. Z04. Increasing the moisture content leads to progressively stronger moist convection and stronger gravity wave generation.

Idealized dry and moist simulations both show relatively short, but well-defined dominant vertical wavelengths for baroclinic generation. These simulations have a rather low model lid ($\sim$22 km or less), with the top 5 to 7 km being reserved for a wave-absorbing layer. It is unclear to what extent AIRS satellite measurements, which are confined to vertical wavelengths $\lambda_z > 15$ km, might register a response to a wave packet with such a short dominant vertical wavelength. On the other hand, a larger vertical domain might produce longer wavelengths, e.g., possibly as a result of Doppler Shifting by strong upper stratospheric winds. As a result, these simulations do not fully explain the long vertical wavelengths found by AIRS satellite measurements which are confined to $\lambda_z > 15$ km.

3.2.2 Previous Case Studies

There have been relatively few *real* case simulations of baroclinic systems generating gravity waves. In particular, gravity waves over the North Atlantic region have not been investigated in detail. One relevant study was performed by Wu and Zhang (2004, hereafter WZ04) for the December-February periods over the North Atlantic region during a strong gravity wave event on 19-21 January 2003. This particular gravity wave event had been previously observed by Microwave Limb Sounder(MLS), but the wave excitation mechanisms and propagation properties remained unclear due to MLS height and sampling limitations (WZ04). The simulations were carried out with the MM5 model, using ECMWF data on a $2.5^\circ \times 2.5^\circ$ grid for initial and boundary conditions. They used a 300 by 200 model domain with 30 km horizontal resolution and 90 equally spaced layers in the vertical, with the model lid at 10 hPa ($z \approx 32$ km). WZ04 compared Advanced Microwave Sounding Unit-A (AMSU-A) observations to simulations from MM5 model to investigate the causes and properties of the North Atlantic gravity waves.

WZ04 simulation results for 1800 UT on 19 January 2003 are shown in figure 3.3 (Note that $z > 20$ km has been excluded owing to the presence of a damping layer there). They found gravity wave emission in the lower stratosphere, in the region south of the Newfoundland hotspot. Interestingly, this event precedes a moderate peak in AIRS measurements of the Newfoundland and Labrador hotspot area by about 12 hours, even though the wave source was outside the hotspot region.

The top plot on figure 3.3 is the 80 hPa horizontal divergence overlaid with the shaded upper tropospheric (300 hPa) jet streak and the bottom plot shows a vertical cross section through the center of the wave packets and along the direction of wave

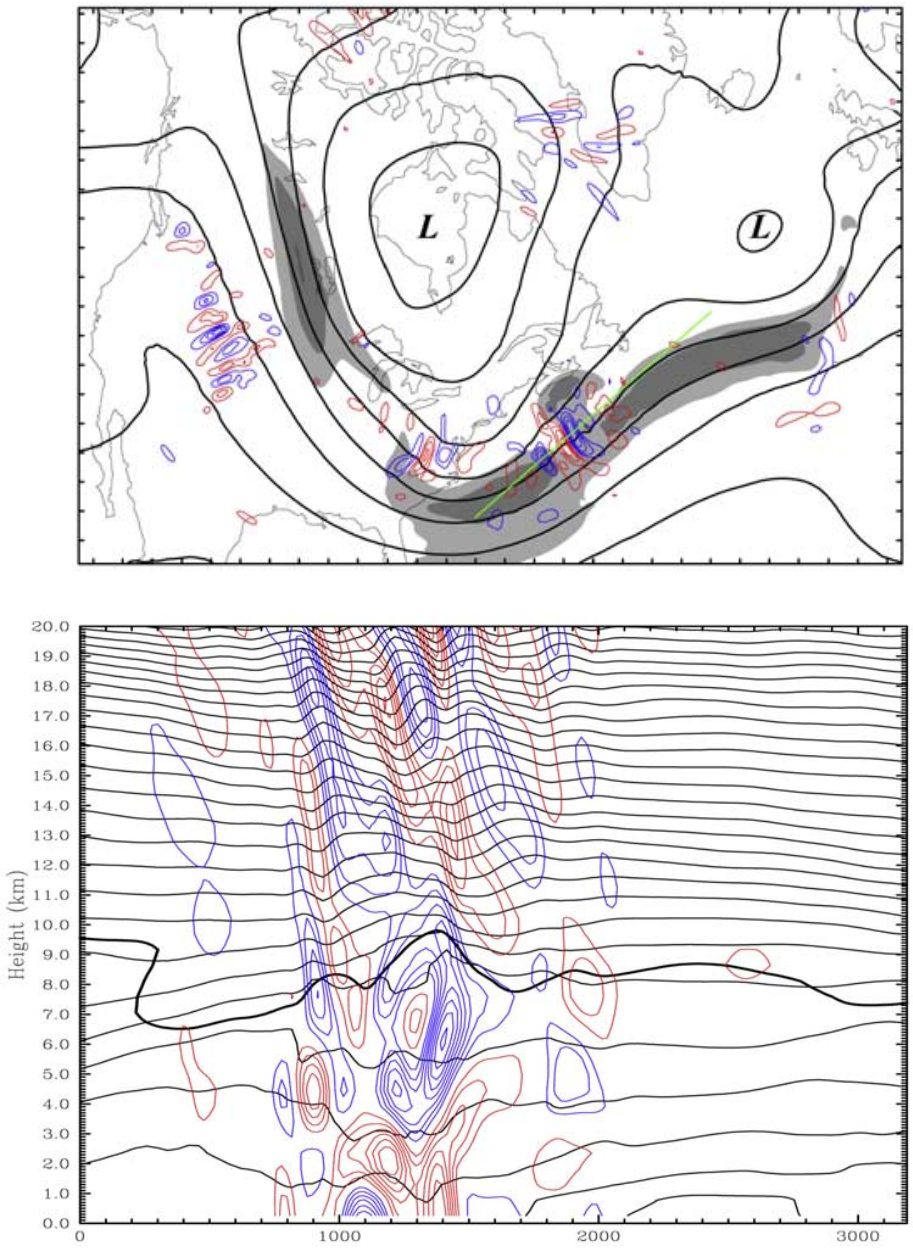

Figure 3.3: Top: 80-hPa horizontal divergence (every 3×10^{-5} s^{-1}; blue, positive; red, negative), the 300-hPa geopotential heights (every 20 decameter), and horizontal wind speed (shaded) from the MM5 simulations of WZ04 at 1800 UT on 19 January. The green straight line indicates where the cross section for the bottom plot is located. Bottom: Vertical cross section of horizontal divergence (every 3×10^{-5} s^{-1}; blue, positive; red, negative) and potential temperature (black curves, every 8° K) of gravity waves on January 19 at 1800 UT. Dark thick curve denotes the dynamic tropopause (After WZ04).

propagation. WZ04 reported waves with horizontal wavelengths of approximately 300-500 km and vertical wavelength of 7-15 km in the upper troposphere. Note that the vertical wavelengths generated in WZ04's MM5 simulation are either at or somewhat below the limit of what is detectable by satellite measurements (The AMSU-A satellite is only sensitive to longer vertical wavelengths > 10 km and AIRS is only sensitive to $\lambda_z > 15$ km).

3.3 Simulations of Gravity Wave Peak Events over Newfoundland and Labrador

3.3.1 Selection of Wintertime Events

After obtaining a time series of 12 years of AIRS data over the Newfoundland and Labrador region from Dr. Hoffmann of "Jülich Supercomputing Centre", we identified two wintertime events with gravity wave activity over a temperature variance threshold of 1.1 K^2. A third case (January 2003) with a peak below this threshold (0.67 K^2) was selected for benchmarking purposes against WZ04 results (see table 3.1). In order to fully understand the potential wave generation mechanisms, we studied the synoptic features of a few of these major gravity wave peak events over Newfoundland and Labrador region, utilizing maps produced from the North American Regional Reanalysis (NARR) database. The NARR model uses the high resolution National Center for Environmental Prediction (NCEP) Eta Model together with the Regional Data Assimilation System (RDAS). The grid resolution is 349×277 which gives approximately 0.3° (32 km) resolution at the lowest latitude. Currently NARR

output includes 8 times daily data at 29 pressure levels (top at 100 hPa or $z \approx 16$ km).

NARR data was used to identify developing lows and tropopause level jet streaks that might provide a source for gravity waves. It was also used to verify the synoptic development in the WRF simulations. The relatively low data lid precludes the possibility of using NARR data to identify baroclinically or convectively-generated gravity wave packets, since wave amplitudes are generally too low at these altitudes. Relevant NARR plots will be provided with each WRF simulation.

Peak Event Year	**Date**	**Time**	**Variance (K^2)**
2003	**Jan 19**	**06:32:10 UT**	**0.428042**
	Jan 19	**17:22:17 UT**	**0.424677**
	Jan 20	**06:24:47 UT**	**0.672707**
	Jan 20	**17:12:12 UT**	**0.168116**
	Jan 21	**06:30:01 UT**	**0.313298**
	Jan 21	**17:21:36 UT**	**0.240471**
2008	**Dec 22**	**06:31:19 UT**	**0.578187**
	Dec 22	**17:23:17 UT**	**0.399499**
	Dec 23	**06:38:23 UT**	**1.15292**
	Dec 23	**17:24:00 UT**	**0.958011**
	Dec 24	**06:29:00 UT**	**1.45305**
2014	**Jan 30**	**06:26:53 UT**	**0.722941**
	Jan 30	**17:18:17 UT**	**0.942626**
	Jan 31	**06:36:21 UT**	**1.41708**
	Feb 31	**17:23:34 UT**	**1.13554**
	Feb 01	**06:26:17 UT**	**1.11597**
	Feb 01	**17:16:12 UT**	**0.614139**

Note: The 2003 case was chosen to benchmark the performance of the WRF model.

Table 3.1: List of selected wintertime peak events measured by AIRS over Newfoundland hotspot region. Universal time 06:30 is 1.5 hours after local midnight, while 17:20 is 20 minutes after local noon.

3.3.2 Weather Research and Forecasting Model

The Weather Research and Forecasting (WRF) Model is a community mesoscale numerical weather prediction (NWP) system which is widely used for atmospheric research and operational forecasting in both regional and global configurations (Skamarock et. al., 2008)[4]. WRF allows researchers to generate atmospheric simulations supported by reanalysis data sets or other model output as well as idealized initial conditions. WRF provides a computationally-efficient dynamical core based on open-source Fortran 95 that supports efficient parallel computing, along with representations of a wide range of physical processes.

The physics components in the WRF model include radiation, boundary layer and land-surface parameterization, convective parameterizations, subgrid eddy diffusion, and microphysics. For many physical processes there are multiple options available. Since the horizontal resolution is 30 km for this study, it is not possible to explicitly resolve convective processes and their direct role in gravity wave forcing. Instead a convective parameterization is used to modify atmospheric heat and moisture, cloud tendencies and surface rainfall. The parameterized heating can provide forcing for gravity waves in the model.

The convective (cumulus) parameterization we used in our simulations is Kain-Fritsch scheme (both new and old versions, cu_physics options 1 and 99 respectively). Option 99 allowed the highest model lid. Other options were tested but produced system aborts. These errors were likely due to the cumulus parameterization scheme attempting calculations at high altitudes, for which it was not designed.

[4]See also ARW User's Guide V3.8 (January 2017): http://www2.mmm.ucar.edu/wrf/users/docs/user_guide_V3.8/ARWUsersGuideV3.8.pdf

Simulation /Year	Model Top	$\Delta X \times \Delta Y$	NX× NY× NZ	Δt	Wave Absorb Layer	Data Set	Convection Scheme	Microphysics	Area With No Topography
FNL10 /2003	10.hPa ≈29 km	30km× 30km	300× 200 × 90	120s	7 km	NCEP FNL	Kain-Fritsch Scheme	WSM 3-Class Simple Ice Scheme	
ERA10 /2003	10. hPa ≈29 km	30km× 30km	300× 200 × 90	90 s	7 km	ECMWF ERA Interim	Kain-Fritsch Scheme	WSM 3-Class Simple Ice Scheme	
ERA1.5 /2003	1.5 hPa ≈ 42 km	30km× 30km	300× 200 × 90	90 s	7 km	ECMWF ERA Interim	Old Kain-Fritsch Scheme	WSM 3-Class Simple Ice Scheme	
ERA1.5 Dry/2003	1.5 hPa ≈ 42 km	30km× 30km	300× 200 × 90	90 s	7 km	ECMWF ERA Interim	No Cumulus	No Microphysics	
ERA1.5 Flat/2003	1.5 hPa ≈ 42 km	30km× 30km	300× 200 × 90	90 s	7 km	ECMWF ERA Interim	Kain-Fritsch Scheme	WSM 3-Class Simple Ice scheme	40° N-60° N 80° W-50° W
ERA1.5 /2008	1.5 hPa ≈ 42 km	30km× 30km	300× 200 × 90	90 s	7 km	ECMWF ERA Interim	Kain-Fritsch Scheme	WSM 3-Class Simple Ice Scheme	
ERA1.5 Dry/2008	1.5 hPa ≈ 42 km	30km× 30km	300× 200 × 90	90 s	7 km	ECMWF ERA Interim	No Cumulus	No Microphysics	
ERA1.5 Flat1/2008	1.5 hPa ≈ 42 km	30km× 30km	300× 200 × 90	90 s	7 km	ECMWF ERA Interim	Kain-Fritsch Scheme	WSM 3-Class Simple Ice Scheme	40° N-60° N 80° W-50° W
ERA1.5 Flat2/2008	1.5 hPa ≈ 42 km	30km× 30km	300× 200 × 90	90 s	7 km	ECMWF ERA Interim	Kain-Fritsch Scheme	WSM 3-Class Simple Ice Scheme	35° N-60° N 85° W-50° W
ERA1.5 /2014	1.5 hPa ≈ 42 km	30km× 30km	300× 200 × 90	90 s	7 km	ECMWF ERA Interim	Kain-Fritsch Scheme	WSM 3-Class Simple Ice Scheme	
ERA1.5 Dry/2014	1.5 hPa ≈ 42 km	30km× 30km	300× 200 × 90	90 s	7 km	ECMWF ERA Interim	No Cumulus	No Microphysics	
ERA1.5 Flat/2014	1.5 hPa ≈ 42 km	30km× 30km	300× 200 × 90	90 s	7 km	ECMWF ERA Interim	Kain-Fritsch Scheme	WSM 3-Class Simple Ice Scheme	35° N-60° N 85° W-50° W

Note that ***flat*** means no topography in the region indicated, ***dry*** retains water vapor but turns off condensation and convective parameterizations.

Table 3.2: List of WRF simulations

The old Kain-Fritsch scheme (Kain and Fritsch 1990, 1993) is taken from the MM5 model. It is a simple cloud model, which includes detrainment, entrainment, updraft and downdraft and estimates the effects of latent heat release on the model. This version only includes deep convection. The modified version of the Kain-Fritsch scheme (KF-Eta, 2000) is based on the old Kain and Fritsch, but has been modified based on testing within the Eta model. As with the original KF scheme, it utilizes a simple cloud model with moist updrafts and downdrafts, including the effects of detrainment, entrainment, and relatively crude microphysics. Some of the changes include imposing a minimum entrainment rate and allowing shallow (non precipitating) convection.

Microphysics parameterization provides atmospheric heat and moisture tendencies, microphysical rates and surface rainfall. The Microphysics parameterization we used in our simulations is WSM 3-class scheme (mp_physics=3). This microphysics scheme (Hong, Dudhia and Chen, 2004) is a 3-class microphysics with ice and includes ice processes below 0° C and ice sedimentation.

3.3.3 Simulation Plan

The Wu and Zhang (2004) case study of gravity wave generation off the coast of New England described in section 3.2.2 was performed with MM5 model lid at 10 hPa ($z \approx 32$ km). We use this 2003 case to benchmark the performance of the WRF model, using NCEP FNL (Final) Operational Global Analysis data (see case FNL10/2003 in Table 3.2 for simulation details). FNL data are available on 1° by 1° (approximately 100×100 km) grids at six hour intervals, at the surface and 26

pressure levels from 1000 hPa to 10 hPa [5]. The results will be compared in section 3.4.

In order to study the wave characteristics at altitudes above $\approx$ 26 km, we repeated the simulations using ECMWF ERA-Interim data for initial and boundary conditions. ERA-Interim is a continually updated global atmospheric reanalysis, beginning in 1979. The resolution of ERA-Interim data set is approximately 80 km$\times$80 km on 60 vertical levels from the surface up to 0.1 hPa[6].

In order to investigate the characteristics and generation of gravity waves near Newfoundland and Labrador, we carried out a series of simulations for the selected hotspot peak events in winter 2003, 2008 and 2014, utilizing the WRF model with ERA-Interim data (see table 3.1). In order to identify each individual source for gravity wave peak events, we ran a few test simulations, eliminating potential sources (convection and topography), and compared the results with the original simulations. A list of all the simulations is summarized in table 3.2.

3.4 Winter 2003

3.4.1 Benchmark Numerical Simulations Using FNL Data

The time series for 2003 peak event over Newfoundland and Labrador region is shown in figure 3.4 with the second strongest temperature variance measured on Jan 20 2003, 0600 UT and was selected for comparison with WZ04's results. The mean sea level pressure and 250 hPa maps for 2003 peak event, produced from the North American Regional Reanalysis (NARR) database are shown in figures 3.5 and 3.6.

[5]See: https://rda.ucar.edu/datasets/ds083.2/ for more details

[6]For more details see: http://www.ecmwf.int/en/research/climate-reanalysis/era-interim

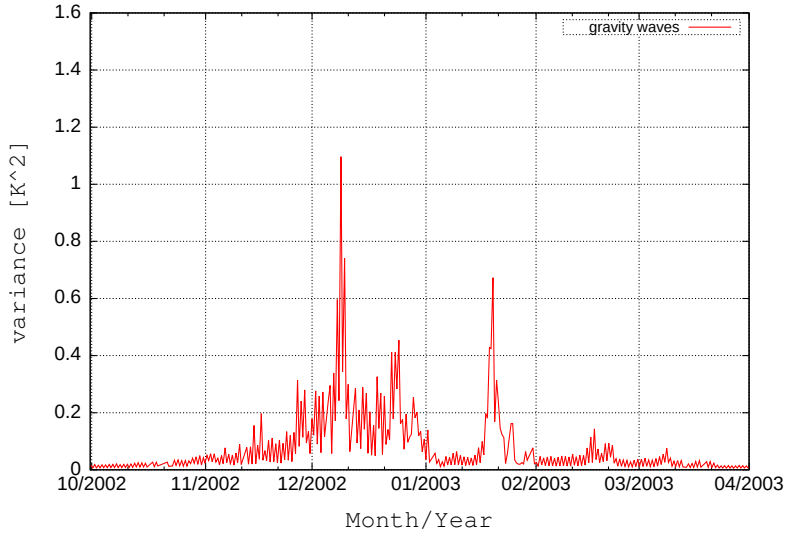

Figure 3.4: Time series for gravity wave peak event over Newfoundland and Labrador during 2002-2003 winter. The temperature variance of the second strongest peak measured by AIRS is 0.672707 K^2 and occurs on Jan 20 2003, 0600 UT. The time considered by WZ04 is the third strongest peak of winter 2003 event (0.424677 K^2), which occurs 12 hours earlier on Jan 19 2003, 1800 UT.

The NARR data in Figs 3.5 and 3.6 show the surface and upper level flow during the 24 hours preceding the maximum variance observed in the AIRS hotspot data. The surface flow in Figure 3.5 shows an intense quasi-stationary low to the east of the hotspot region, SE of Greenland. The surface and upper level fields show a trough moving rapidly across Southern Ontario and New England in conjunction with a much weaker quasi-stationary low situated over Northern Hudson Bay. This rapidly moving trough produces surface flows (figure 3.5) that are, for a few hours, perpendicular to the Appalachian and Labrador coastal mountains, and potentially capable of generating topographic gravity waves.

The upper level flow (figure 3.6) shows a series of strongest streaks moving off the coast of North America. There are associated with the development of a relatively weak but deepening low moving up the East coast. As we shall soon see, the jet

streak associated with this deepening low is responsible for the generation of gravity waves near the tropopause.

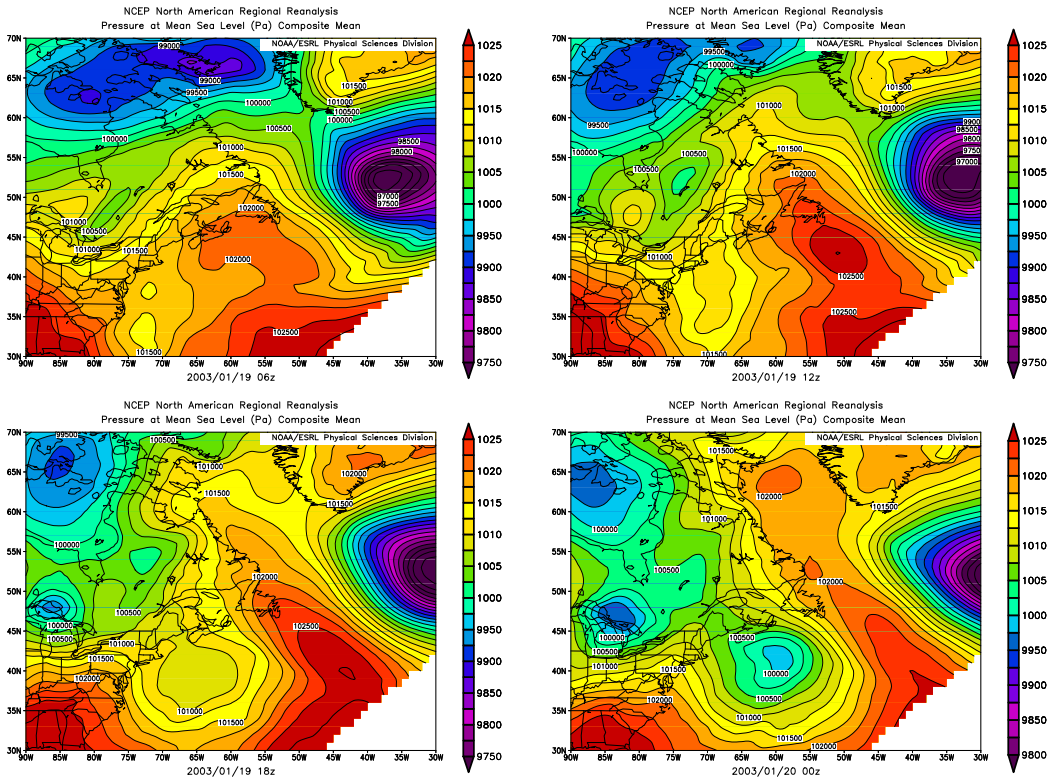

Figure 3.5: Mean Sea Level Pressure (Pa) plots every 6 hours from January 19, 2003 at 06 UT to January 20, 2003 at 00 UT (preceding the gravity wave peak event by 24 to 6 hours). Taken from North American Regional Reanalysis (NARR) dataset. Note the NARR Cylindrical Equidistant projection differs from Lambert Conformal projection used for WRF.

As mentioned in section 3.2.2, WZ04 performed a real case simulation of gravity wave event over the North Atlantic region on 19-21 January 2003. They used an older mesoscale model (MM5). Although this is not one of the strongest events for the selected hotspot region, simulating this event allows a direct comparison to validate the model against earlier modeling results before attempting to simulate stronger peaks.

It must be noted that it is only possible to evaluate large scale features against reanalysis data. Although FNL and Interim reanalysis data are available up to 10 hPa and 0.1 hPa respectively, their horizontal resolution is only 1 degree (110 km) and 0.703 degree (80 km). Since mesoscale gravity waves typically have horizontal wavelengths smaller than 400 km, these can't be expected to be well-resolved in FNL and and ERA-Interim data. Hence we need to use a high resolution model to simulate the waves.

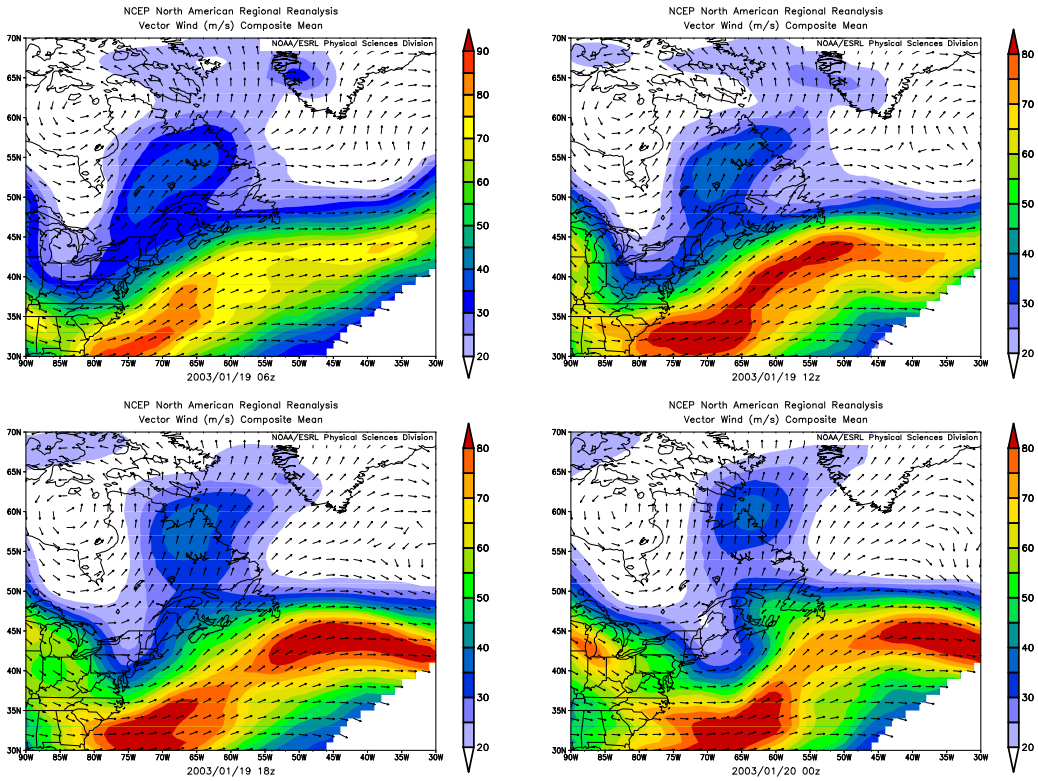

Figure 3.6: NARR 250 hPa Vector Wind (m/s) plots at the same times as Figure 3.5. Arrows show wind direction, while colour contours show the horizontal wind speed in m/s. Note the upper level jet streaks off the East Coast of North America.

In our benchmark simulations for the 2003 case (FNL10/2003, see table 3.2), the WRF model domain has 300×200 grid points with 30-km horizontal grid spacing

and 90 vertical layers up to 10 hPa ($z \approx 32$ km). This produces resolutions of $\Delta x = \Delta y = 30$ km, $\Delta t = 120$ s and $\Delta z = 350$ m on average. The same resolution and vertical extent were used by WZ04. The initial and boundary conditions for the simulations are provided from NCEP FNL (Final) Operational Global Analysis data. Thus, the initial and boundary conditions have better resolution than WZ04, who used ECMWF data with ~ 250 km horizontal resolution.

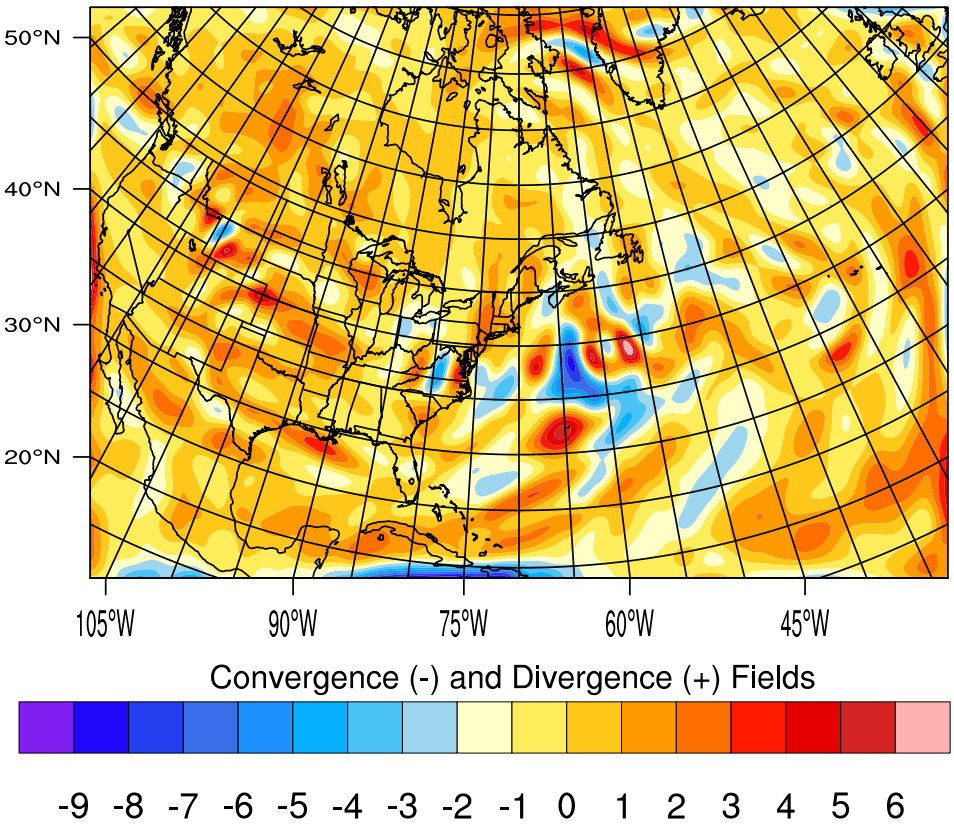

Figure 3.7: Divergence (10^{-5} s^{-1}) map at 80-hPa. From WRF simulations at 1800 UT on 19 January, 2003. To be compared with WZ04, see figure 3.3.

The model is initialized at 0000 UT on 19 January 2003 and integrated up to 0000 UT on 21 January 2003. The upper 7 km of the model domain contains a wave absorbing layer (with damp_opt=3, implicit vertical velocity damping and damping

coefficient=0.4 s^{-1}, which is somewhat stronger than the default 0.2 s^{-1}). The model domain includes all North America to avoid boundaries over the continent. As in WZ04, no model nesting has been used.

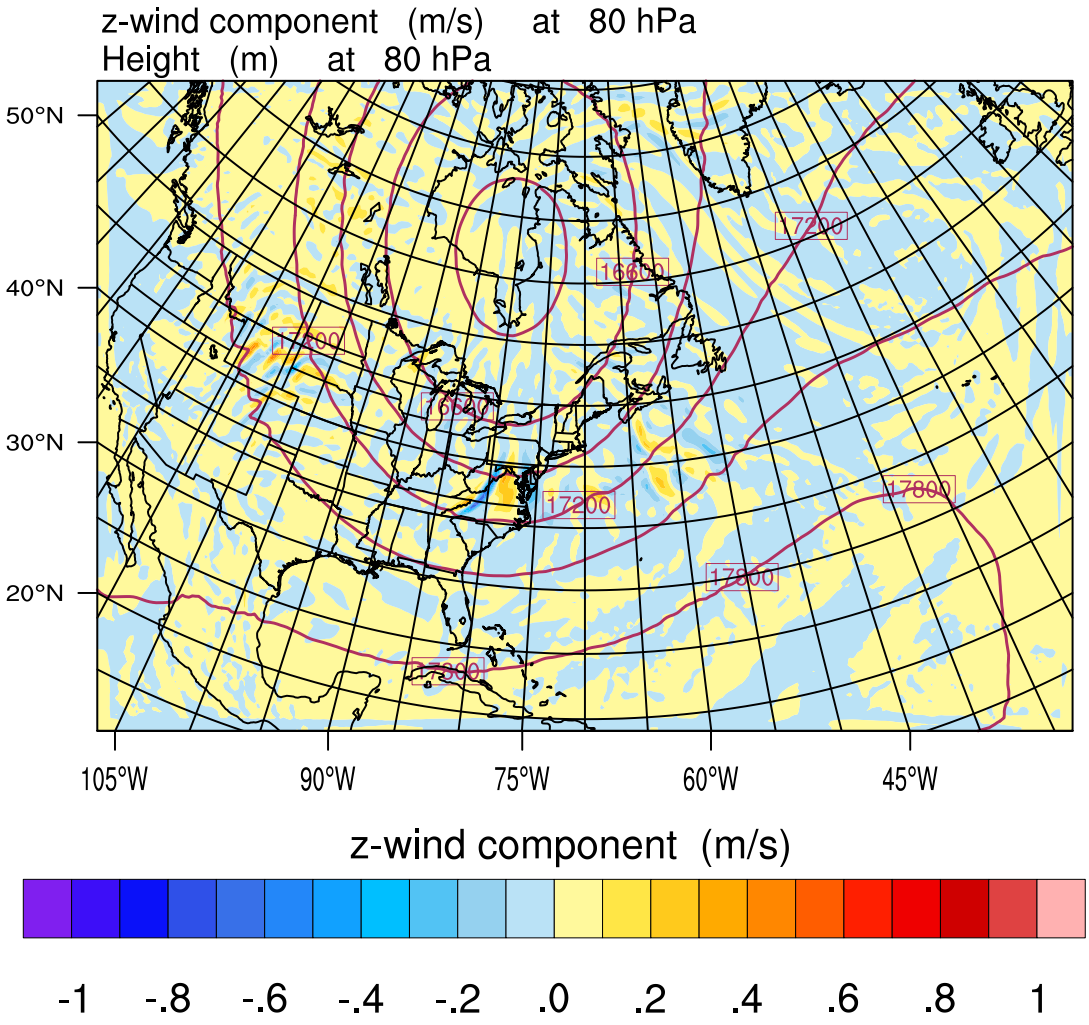

Figure 3.8: Vertical velocity overlaid with geopotential height contours at 80-hPa(m/s). From WRF simulations at 1800 UT on 19 January, 2003.

We note that WZ04 used divergence plots to isolate and identify wave activity in their MM5 simulations, but did not calculate temperature perturbations for direct comparison with the AMSU satellite data. In this benchmark section we will therefore

focus on divergence fields to facilitate comparison with WZ04. Our WRF simulations at 1800 UT on 19 January 2003 are shown in figures 3.7, 3.8 and 3.9 and may be compared with WZ04's results (see figure 3.3). The 80 hPa map of divergence in Figure 3.7 shows a relatively weak wave packet produced by flow perpendicular to the Appalachians in the northeast USA, as well as a much stronger wave packet situated over the ocean directly to the south of Nova Scotia. The location and amplitude of these packets agree well with WZ04's results.

Figure 3.8 shows vertical velocity (a good indicator of waves in the strongly stable stratosphere), overlaid with geopotential height contours for the same time as figure 3.7. The geopotential height also agrees well with WZ04 (figure 3.3, note that the horizontal domain on map projection are different). It is the stronger gravity wave packet over the ocean that is of primary interest to us, since WZ04 identified it as being produced by a localized baroclinic jet streak at the 300 hPa level.

Figure 3.9 shows a vertical cross section of divergence along a line perpendicular to the phase fronts of the wave packet over the ocean. The vertical location and phase tilt of the packet agrees well with WZ04 (figure 3.3), although one should note the limited vertical extent of WZ04's plot ($z < 20$ km). At around z=25 km (above the wave source region), the horizontal wavelength of these waves is $\lambda_h \approx 220$ km ($\kappa_h = 2.85 \times 10^{-5}$ m^{-1}) and the vertical wavelength is $\lambda_z \approx 4.2$ km ($m = 1.5 \times 10^{-3}$ m^{-1}) with somewhat longer wavelengths evident at lower altitudes. Assuming $f = 10^{-4}$ s^{-1} and N ~ 0.02 s^{-1} in (1.15), we estimate the intrinsic frequency to be $\hat{\omega} \sim 3.9 \times 10^{-4}$ s^{-1} and intrinsic phase speed is $\hat{c}_h \sim -14$ m/s. One can also see areas where the vertical wavelength is as large as 6 km. This compares reasonably well with WZ04's MM5 simulations, although they estimated their horizontal wavelength to be

somewhat larger (300-500 km). Our estimate of their vertical wavelength (between $z = 10$ and 20 km) is 4-7 km, which compares well with our values. Our extreme divergence values (1.2 to 1.5×10^{-4} s^{-1}) at 80 hPa also agree with WZ04.

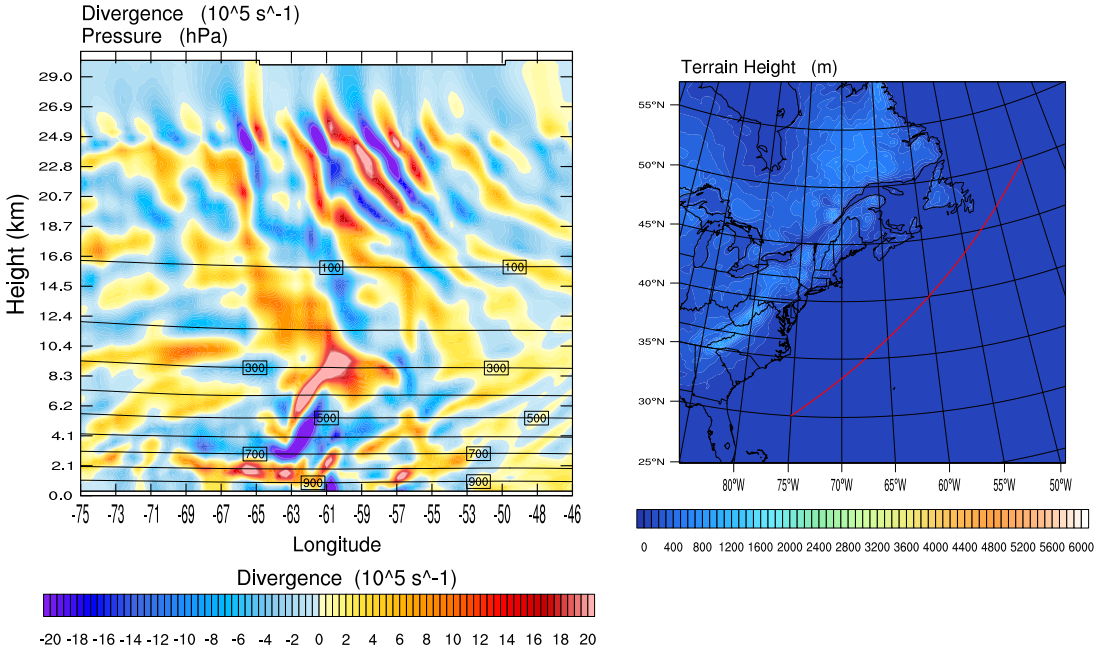

Figure 3.9: Divergence (10^{-5} s^{-1}) cross section on January 19, 2003 at 1800 UT. The red line on the right indicates where the cross section is plotted. To be compared with WZ04, see figure 3.3. Note that levels above $z \approx 24$ km are affected by the damping layer.

Figure 3.10 shows the divergence cross section map over the area closer to Newfoundland. Waves are present in the cross section, but are much weaker and not as strong or as well organized as over the ocean. This confirms that topography is not a strong source for the waves that AIRS sees over the Newfoundland/Labrador hotspot.

The divergence plots at 0600 UT on January 20 for 80 hPa and 35 hPa are shown in figure 3.11. From figure 3.11, we can see the wave packet is propagating towards northeast as it ascends in the atmosphere, i.e., the wave group is moving toward and into the hotspot region as it propagates upward. Now that we have demonstrated

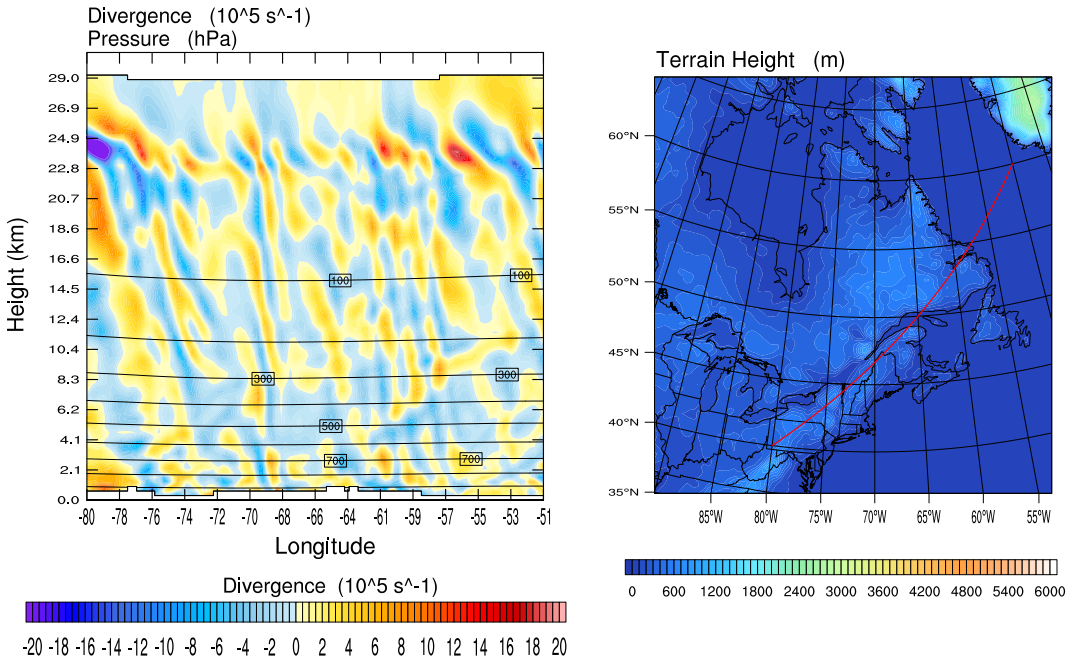

Figure 3.10: Divergence (10^{-5} s^{-1}) cross section at 0600 UT on January 20, 2003 . The red line on the right indicates where the cross section is plotted. Note that levels above $\sim$ 24 km are affected by the damping layer.

reasonable agreement with WZ04 results for Jan 19 at 1800 UT, we can follow the wave packet development leading up to the 2003 peak event over Newfoundland and Labrador at 0600 UT on January 20.

3.4.2 Numerical Simulations Using ECMWF ERA Interim Data

As mentioned in section 3.3, we increased the vertical extent of the model by performing simulations based on ECMWF ERA-Interim data. The horizontal resolution of ERA-Interim data set is coarser than FNL data, being approximately 80 km$\times$80 km, but extends to much higher altitudes, having 60 vertical levels from the surface up to 0.1 hPa. Several attempts made to run WRF model with lids above 1hPa

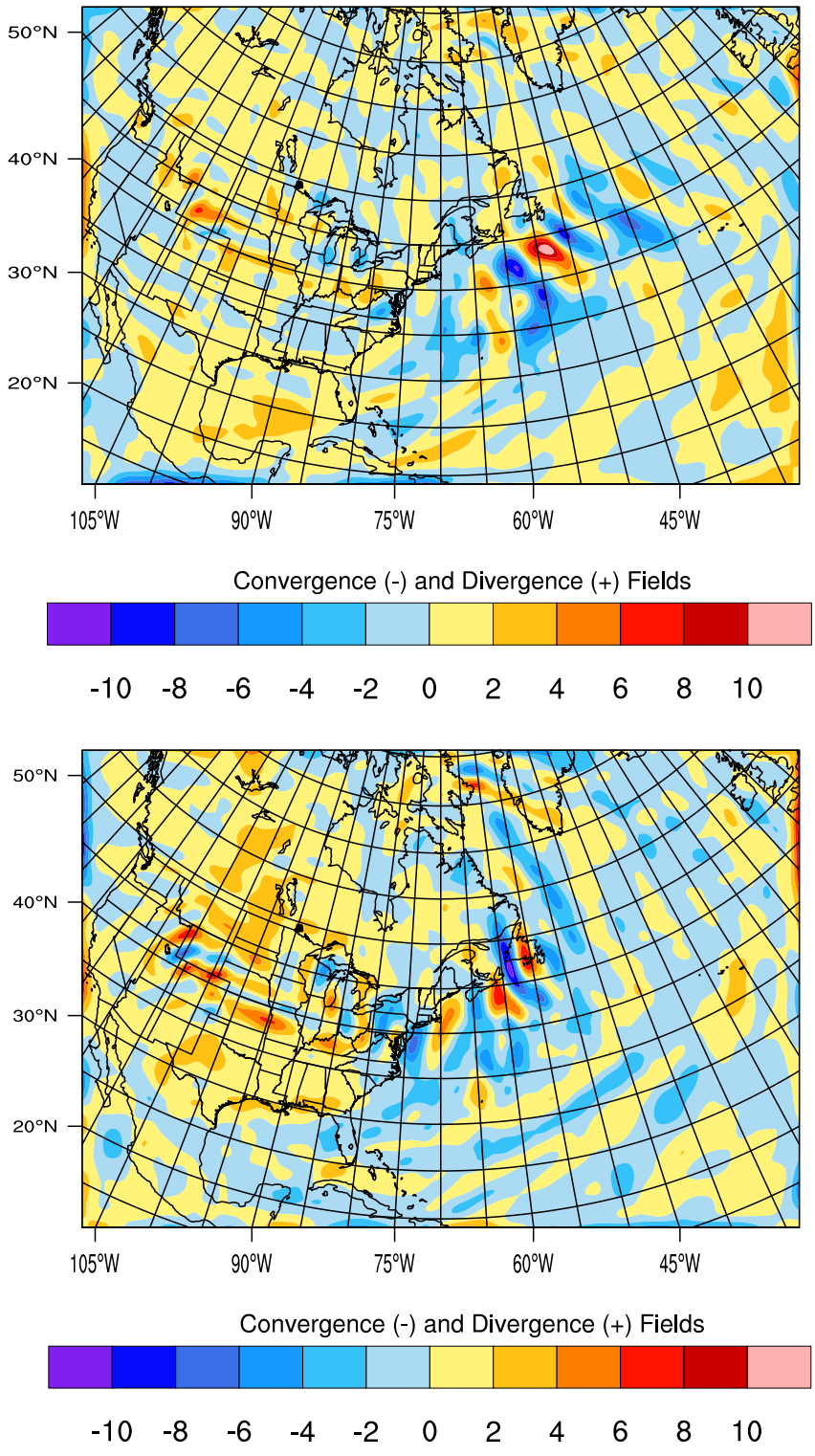

Figure 3.11: Divergence (10^{-5} s^{-1}) map at 80 hPa (top) and at 35 hPa (bottom) from WRF simulations at 0600 UT on 20 January, 2003.

and more than 90 vertical levels, but unfortunately the simulations terminated with errors. The errors appear to be associated with extremely small water vapor mixing ratios at high altitudes. The largest vertical domain that could be obtained was 90 vertical levels with a lid at 1.5 hPa ($\approx$ 43 km). The sponge layer extends from 36 to 43 km.

Since ERA Interim data has coarser resolution compared to FNL data (80 km vs. 30 km), we performed a WRF simulation (ERA10 in Table 3.2) with ERA Interim data limited to a top level of 10 hPa. This was done in order to check the sensitivity of simulations to horizontal resolution of the initial and boundary conditions. The model used 6-hourly ERA Interim data interpolated to pressure levels and was initialized at 0000 UT on 19 January 2003 and integrated up to 0000 UT on 21 January 2003.

The results of sensitivity tests for 1800 UT on 19 January 2003 are shown at 6 hour intervals in figures 3.12 and 3.13. Those figures show divergence cross section plots from WRF FNL10 and ERA10 simulations, along the red line shown on the bottom plot. As we can see, the results of two simulations compare well, showing very similar wave patterns both over the ocean and land. It can be seen in figure 3.12 that the wave packet over the ocean may have slightly larger amplitude and slightly longer horizontal wavelength in the ERA10 simulation.

We performed another set of simulations with ERA Interim data, extending the vertical domain with ERA Interim data to 1.5 hPa, but retaining the same horizontal domain[7]. For those simulations (ERA1.5), our WRF model domain employs 300×200 grid points with 30-km horizontal grid spacing and 90 vertical layers up to 1.5 hPa ($z \approx 43$ km) see table 3.2). The model is then initialized at 0000 UT on 19 January

[7]Note that for ERA1.5/2003, cu-physics = 1 (Kain-Fritsch scheme, 2004) produced a simulation abort, so we used cu-physics = 99 (Kain-Fritsch scheme, 1990)

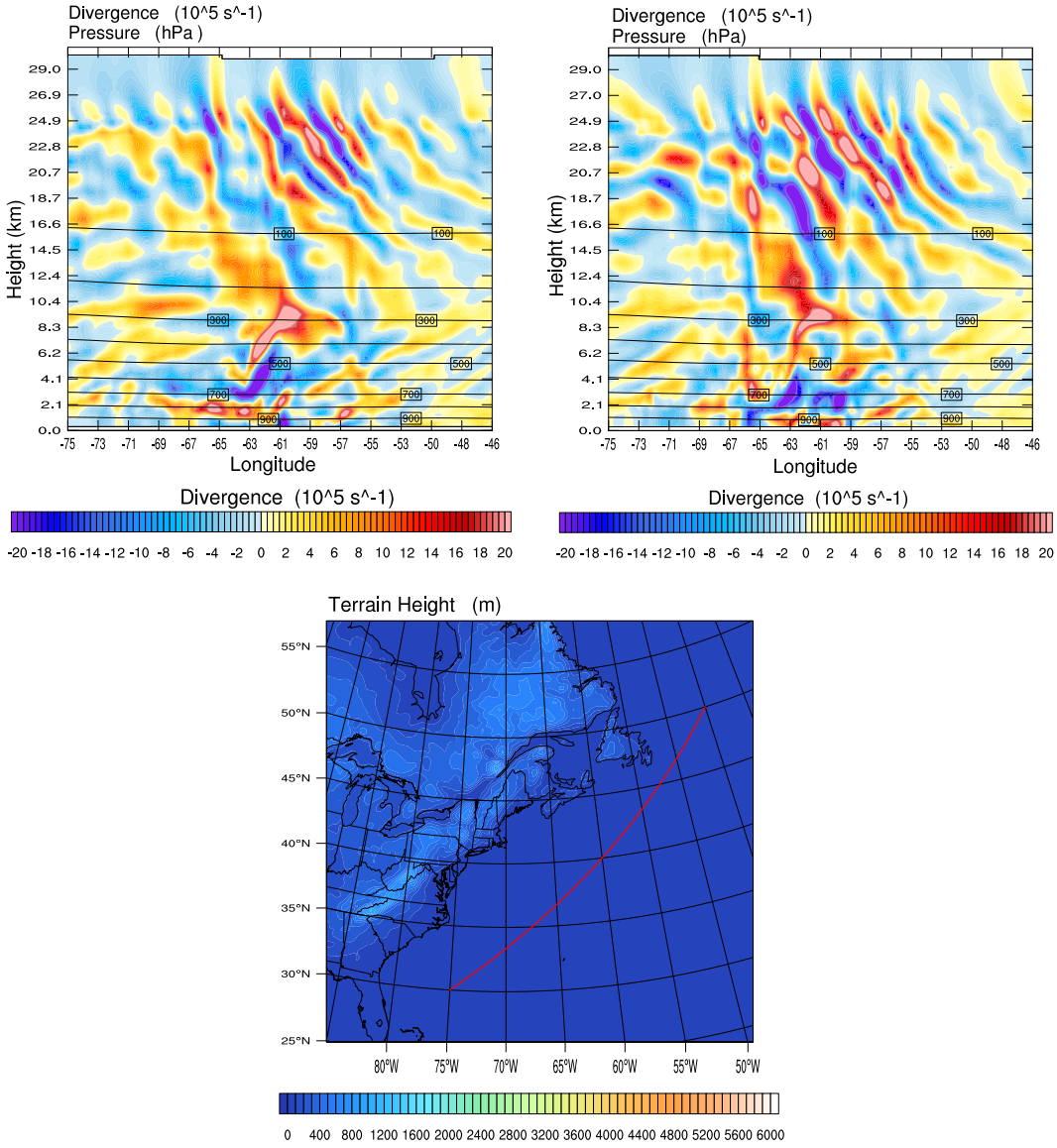

Figure 3.12: Divergence (10^{-5} s^{-1}) cross section on January 19, 2003 at 1800 UT up to 10 hPa from WRF simulations using FNL data (left, FNL10 in Table 3.2) and ECMWF ERA Interim data (right, ERA10 in Table 3.2). The red line on the bottom figure indicates where the cross section is plotted.

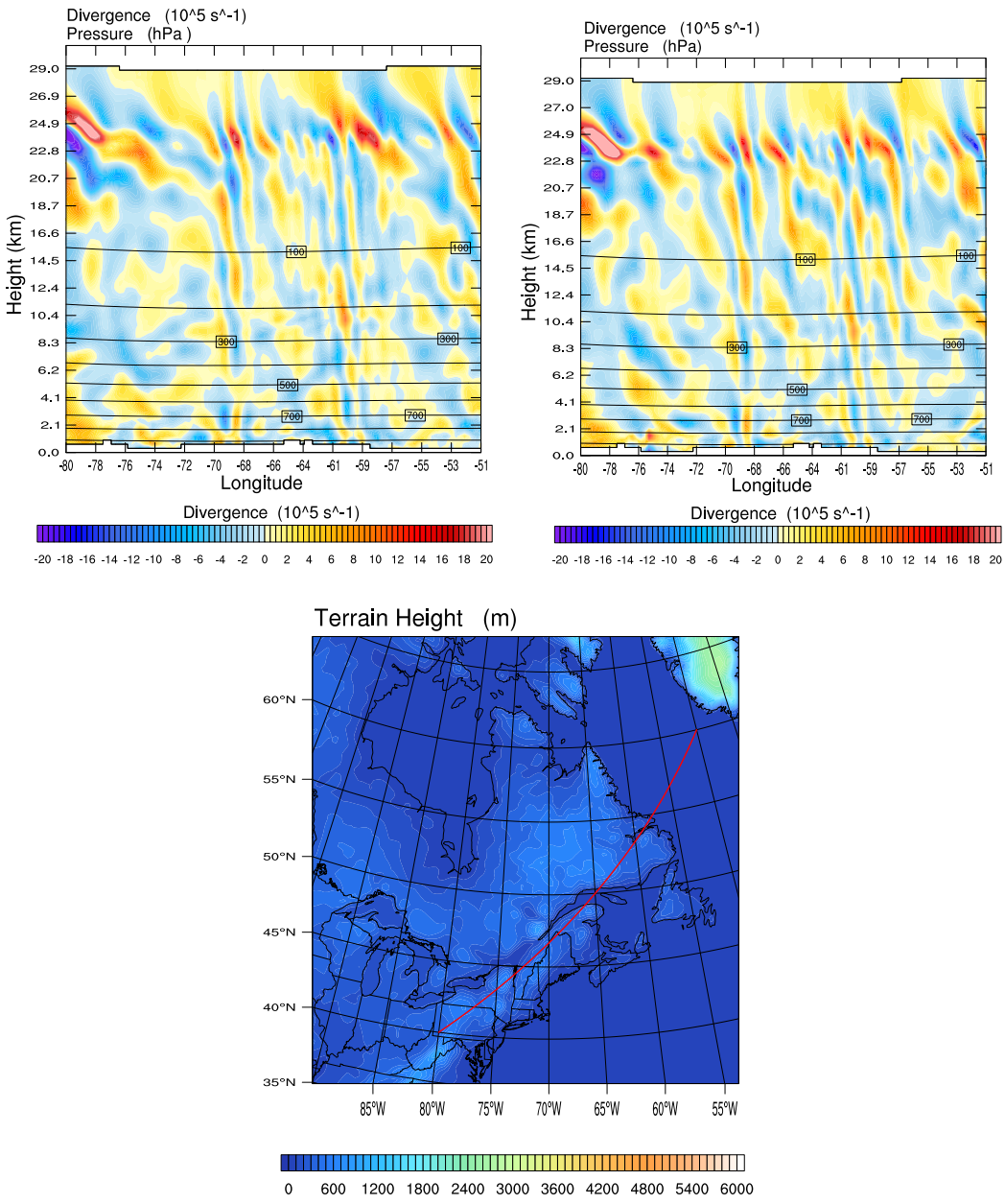

Figure 3.13: Divergence (10^{-5} s^{-1}) cross section on January 19, 2003 at 1800 UT up to 10 hPa from WRF simulations using FNL data (left, FNL10 in Table 3.2) and ECMWF ERA Interim data (right, ERA10 in Table 3.2). The red line on the bottom figure indicates where the cross section is plotted.

2003 and integrated up to 0000 UT on 21 January 2003. The upper 7 km of the model domain contains a wave absorbing layer (with dampcoef = 0.4).

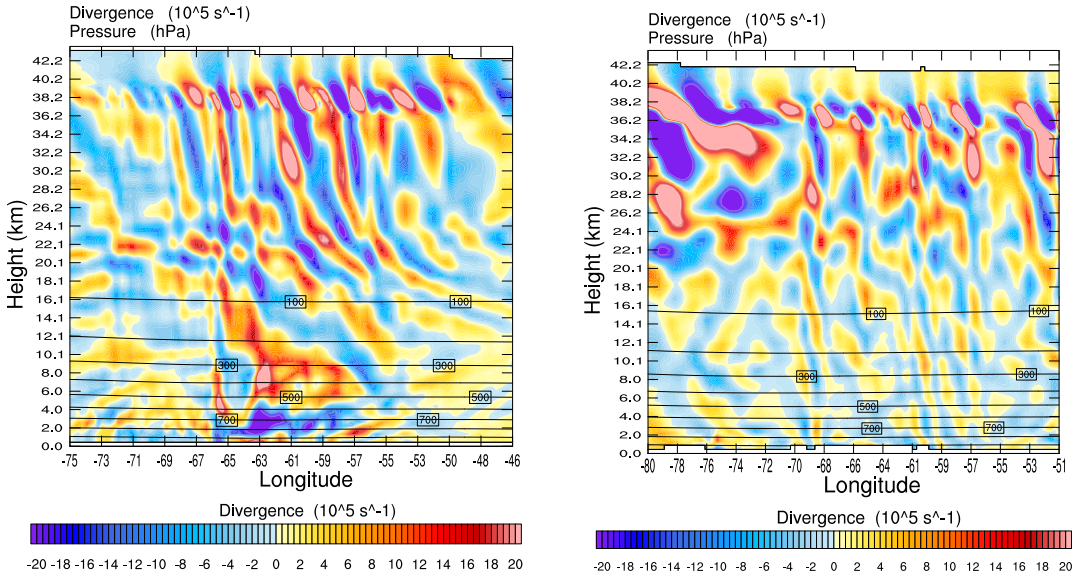

Figure 3.14: Divergence (10^{-5} s^{-1}) cross section on January 19, 2003 at 1800 UT up to 1.5 hPa over the ocean (left, ERA1.5 and along the red line in figure 3.12) and land (right, ERA1.5 and along the red line in figure 3.13). From WRF simulations using ECMWF ERA Interim data. Note altitudes $z \gtrsim 36$ to 43 km correspond to the sponge layer.

Figure 3.14 shows the vertical cross section of divergence over the ocean and land from WRF simulations (ERA1.5) on 19 January 2003. We can see a similar wave pattern to that in figures 3.12 and 3.13 at levels below 26 km. Note that divergence is artificially enhanced by the onset of damping of vertical velocity in the sponge layer (upper 7 km)[8], so divergence values above z≈ 35 km are not to be interpreted physically.

Figure 3.15 shows sea level pressure contours overlaid on temperature at sea level over the period Jan 19, 1200 UT to Jan 20, 0600 UT (the time of the peak hotspot event). As in figure 3.5, there is a strong quasi-stationary low southeast of Green-

[8]Since vertical velocity w decreases rapidly near the top, i.e., $w \to 0$, divergence must be large, since $\nabla.\mathbf{u_h} \sim -\frac{\partial w}{\partial z}$.

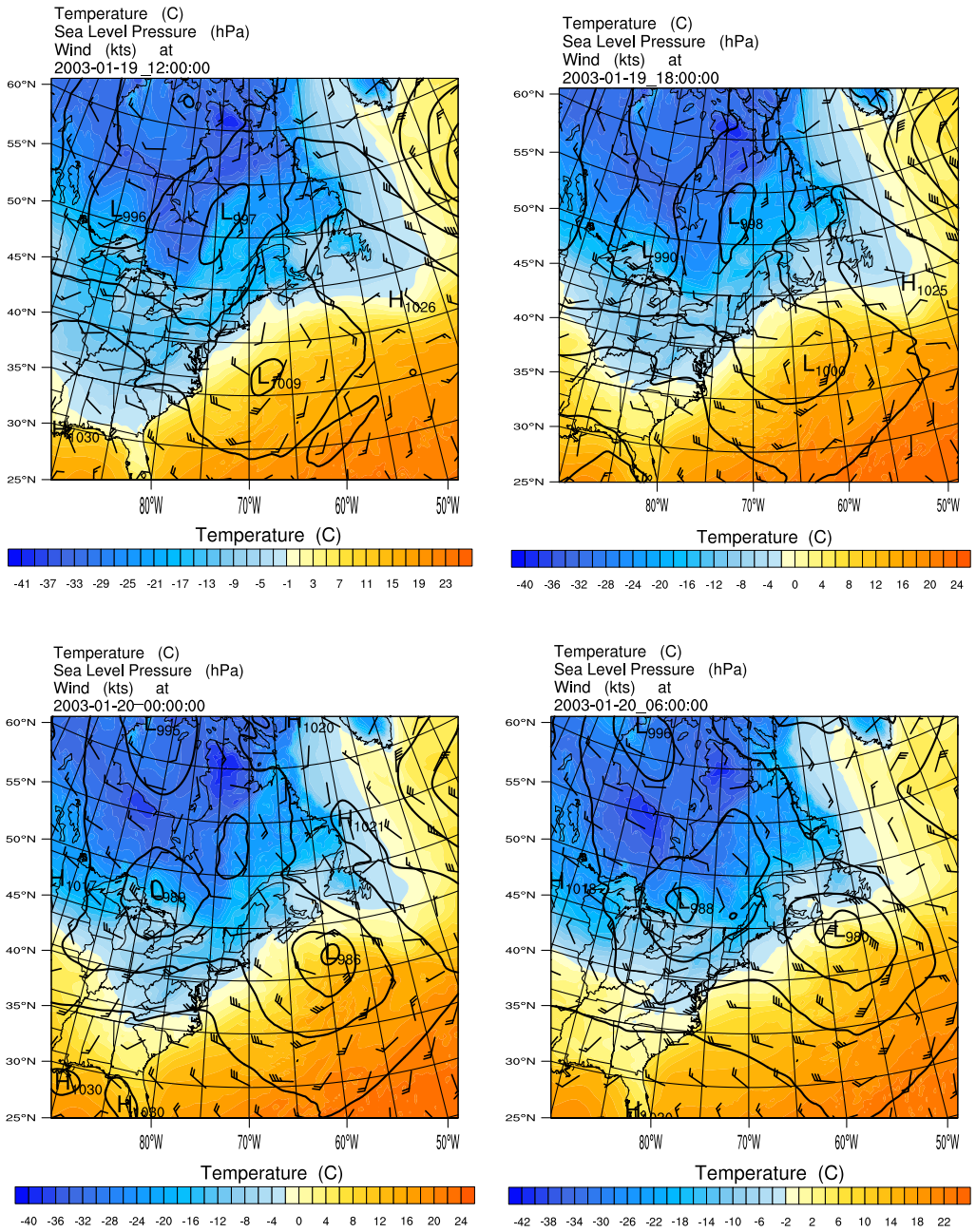

Figure 3.15: Sea level pressure contours (hPa), temperature (°K) and wind-barbs (kts), every 6 hours from January 19, 2003 at 1200 UT to January 20, 2003 at 0600 UT. From WRF simulations using ECMWF ERA Interim data (Note: 1kt $\approx$ 0.51 m/s).

land. A low develops over 500 km off the coast of the southern USA (Carolinas) and gradually deepens from 1009 to 980 hPa as it moves up the coast along the jet stream (figure 3.6), which coincides with the climatological winter East Coast storm track. The low remains well offshore and relatively weak. The surface flow over the continent remains relatively weak and for Jan 19 is roughly perpendicular to the Appalachian mountain ridge. As noted by WZ04, this produces some relatively weak topographic waves, but these waves don't propagate into the hotspot region.

As we shall see, the jet streak associated with the low developing in the East Coast storm track generates much stronger waves. Although these waves are generated over the ocean south of the hotspot, we will demonstrate that they propagate northward and westward as they ascend into the stratosphere, so that they enter the Newfoundland/Labrador hotspot region.

In order to study wave characteristics, we make a conventional assumption that waves represent small scale local departures from a smooth or slowly varying background state. The perturbation of any field variable can then be estimated by the difference between its local value and the smooth or slowly varying background state. In order to estimate the background state we evaluated two techniques. The first applies a 4th order polynomial fit over a section of the domain, while the second applies a 20-point moving average. Both methods have been used in prior studies to calculate perturbations in various fields, e.g., Hoffmann et. al., 2013 uses a 4th order polynomial fit to calculate brightness temperature perturbations[9], while Wu (2004) uses a 3rd order polynomial fit to calculate the radiance residual across the satellite scan. The typhoon modeling study of Kim and Chun (2010) use a 20×20 point

[9]AIRS radiance perturbations, defined as the difference from a fourth-order polynomial fit in scan angle that removes the scan angle dependent radiance.

running average to calculate the background state. Their horizontal resolution (27 km) is similar to ours (30 km). This procedure smooths oscillations with wavelengths shorter than about 300 km.

For each grid point, the 20-point running average method averages each variable at +/-10 grid points along the cross section horizontal direction. For each variable, e.g. v, at the boundaries we average v_0 to v_{n+10} for grid points $n < 10$, and for grid points $n > n_{max} - 10$, we average v_{n-10} to $v_{n_{max}}$. For pressure level maps, the variable average has been calculated along latitudes and longitudes, i.e., for each grid point we calculated variable average of +/-10 grid points along latitudes and +/-10 grid points along longitudes). The calculations on boundaries follow the same rule as the cross section plots.

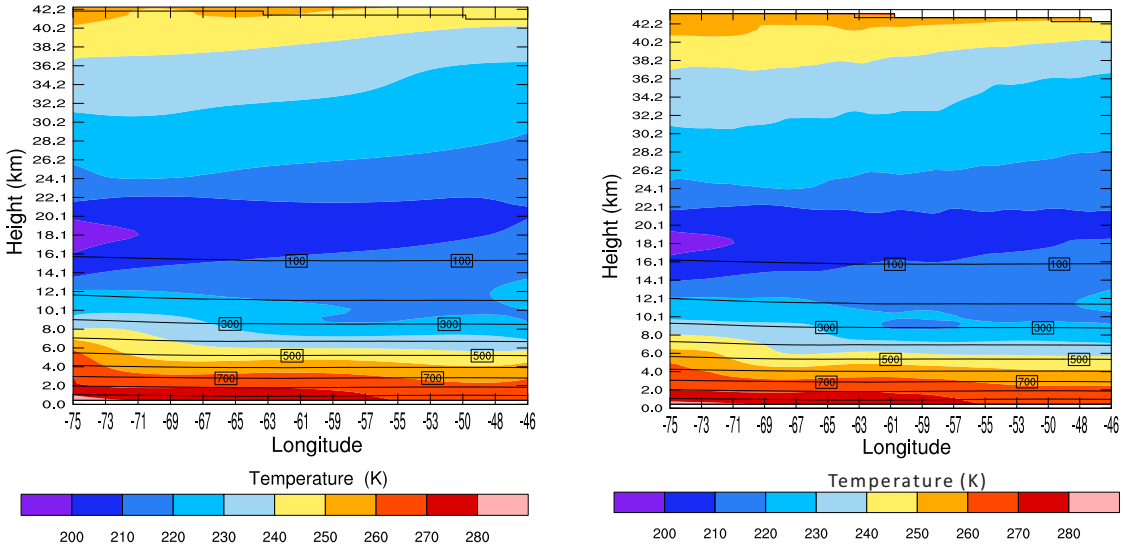

Figure 3.16: Average temperature (°K) cross section on January 19, 2003 at 1800 UT up to 1.5 hPa over the ocean, using 4th order polynomial fit (left) and 20 grid point average (right). From WRF simulations using ECMWF ERA Interim data.

Figure 3.16 shows average temperature cross section on January 19, 2003 at 1800 UT over the ocean using 4th order polynomial fit (left) and 20-point moving

average (right). As we can see, the results of two averaging methods are very similar. These plots show a strong temperature lapse rate in the troposphere, followed by a much weaker lapse rate in the lower stratosphere. Temperature reaches a minimum at altitudes around 18 km. At higher altitudes, temperature increases slowly with height. Estimates of the stratification using $N^2 = \frac{g}{T}(\frac{dT}{dz} + \frac{g}{c_p})$ show static stability increasing from values of $N \approx 0.012$ s^{-1} in the troposphere, to values of about 0.018 s^{-1}in the stratosphere and about 0.022 s^{-1} in the upper stratosphere.

$dT/dz + g/c_p$	$\bar{T}(^\circ K)$	**N (s^{-1})**
Troposphere 4° **K/km**	**260**	**0.012**
Lower Stratosphere 7° **K/km**	**210**	**0.018**
Upper Stratosphere 11° **K/km**	**230**	**0.022**

Table 3.3: Typical static stability values in troposphere and stratosphere.

Perturbation temperature cross section plots for January 19, 2003 at 1800 UT are shown in figure 3.17. The methods we used to calculate average temperature are the same as figure 3.16; 4th order polynomial fit for the plot on the left and 20-point moving average for the plot on the right. These cross sections are plotted over the ocean (the red line in figure 3.12). As we can see in figure 3.17, the two methods produce similar results, with T' values ranging between -5° K to 5° K. The wave features in these plots compare well with the divergence plots, (ERA1.5 in figure 3.14, left, and FNL10 in figure 3.12, left) horizontal wavelength of 200 km$\leq \lambda_x \leq$ 450 km, and the vertical wavelength of 4 km $\leq \lambda_z \leq$ 16 km.

The horizontal and vertical wavenumber are 1.4×10^{-5} m$^{-1} \leq k \leq 3.1 \times 10^{-5}$ m^{-1} and 3.9×10^{-4} m$^{-1} \leq m \leq 1.6 \times 10^{-3}$ m^{-1} respectively. The buoyancy frequency is $N \approx 0.022$ s^{-1} and $f(50^\circ N) = 1.1 \times 10^{-4}$ s^{-1}, giving intrinsic frequency 4.5×10^{-4} s$^{-1} \leq \hat{\omega} \leq 7.9 \times 10^{-4}$ s^{-1} and intrinsic phase speed -15 m/s$\leq \hat{c} \leq -56$ m/s. The

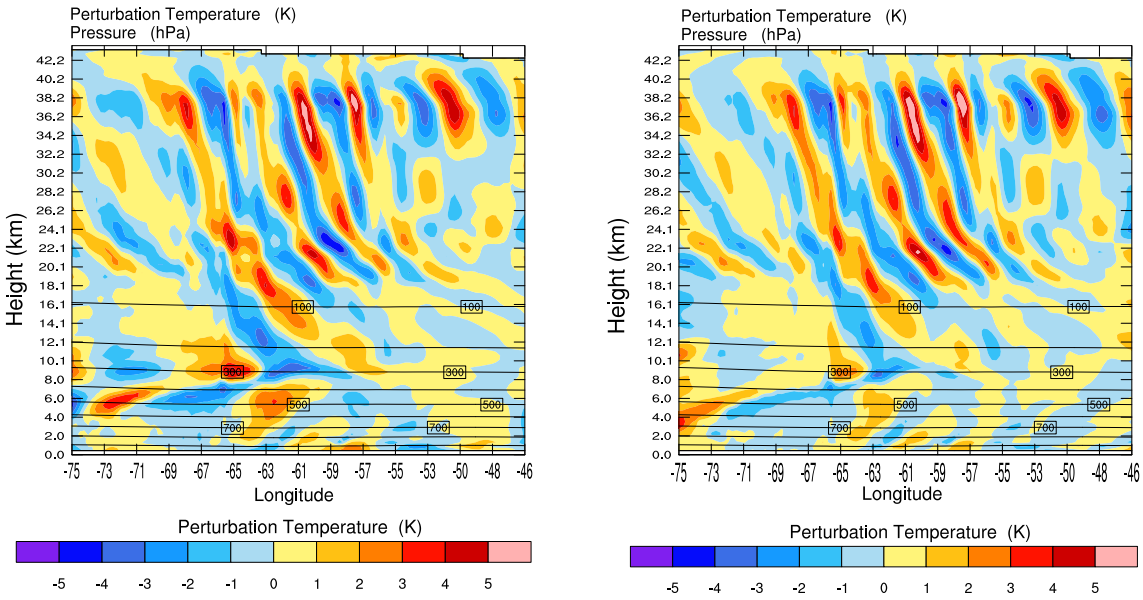

Figure 3.17: Perturbation Temperature (°K) cross section on January 19, 2003 at 1800 UT up to 1.5 hPa over the ocean (ERA1.5), using 4th order polynomial fit (left) and 20 grid point average (right). From WRF simulations using ECMWF ERA Interim data. Note, altitudes 36 km$< z <$ 43 km correspond to the sponge layer.

vertical group speed c_{gz} ranges from 0.25 m/s (short λ_z) to 2.0 m/s (large λ_z), so the time for the packet to travel 20 km vertically is between 3 to 22 hours with longer vertical wavelengths traveling more quickly.

Figure 3.18 shows the progression of the wave packet temperature perturbations with time over the ocean, every 6 hours from January 19, 2003 at 1200 UT to January 20, 2003 at 1200 UT. The packet begins forming on January 19, at 1200 UT and gains strength over the next 24 hours. The wave packet becomes stronger and more organized closer to the AIRS data peak, January 20, 2003 at 0600 UT. After that time the packet begins to move out of the chosen cross section

Figure 3.19 shows perturbation temperature field (°K) at 50 hPa, 30 hPa, 10 hPa and 5 hPa. In order to reveal more details about the wave packet movement and propagation, these plots are zoomed into a smaller area close to Newfoundland. At

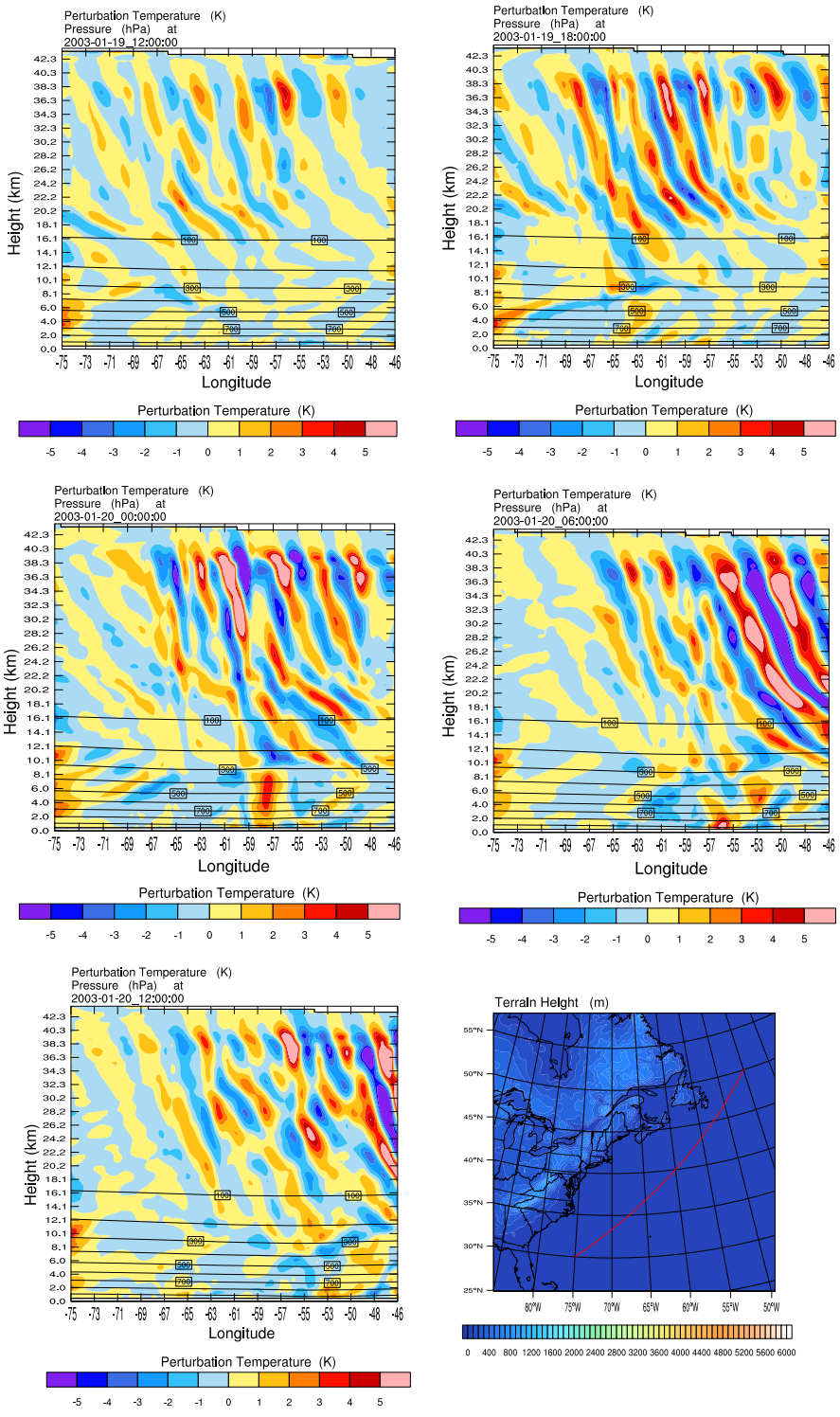

Figure 3.18: Perturbation temperature (°K) cross section over the ocean (along the red line shown in the last figure), every 6 hours from January 19, 2003 at 1200 UT to January 20, 2003 at 1200 UT, using 20 point average. From WRF simulations using ECMWF ERA Interim data. Note, altitudes 36 km$< z <$ 43 km correspond to the sponge layer.

50 hPa, a wave packet is present over the ocean to the southwest of Nova Scotia. Also, we can see the wave packet is propagating towards the north (i.e., it tilts toward the hotspot region and away from the cross section) as it propagates upward.

The northward tilt of the wave packet with height can also be seen in the horizontal wind speed perturbation $(u'^2 + v'^2)^{\frac{1}{2}}$ plots at different pressure levels (figure 3.20).

The wave packet structure and progression in these plots follow the same pattern as in temperature perturbation plots (figure 3.19). It illustrates that the wave packet is also propagating towards the north, roughly parallel to the wave fronts, as it ascends through the middle atmosphere, i.e., it is propagating into the hotspot region identified by Hoffmann et. al., 2013. This packet, which originates in a baroclinic disturbance near the tropopause and outside the hotspot region, eventually enters the hotspot region at higher altitudes, due to advection by the background wind.

Figure 3.21 shows hodographs for chosen points along the cross section line over the ocean. Each ellipse represents one vertical wavelength. According to the polarization relations for rotating hydrostatic waves (Gill, 1982), for which $m^2 \gg k^2$, the ratio $\frac{|u'|}{|v'|} \approx \frac{\hat{\omega}}{f}$, where u' and v' are zonal wind and meridional perturbation wind components, $\hat{\omega}$ is the wave intrinsic frequency and f is the Coriolis parameter. Thus the ratio between the major and minor axes of the ellipse gives the non-dimensional frequency $\frac{\hat{\omega}}{f}$ and can also be used to determine the ratio between vertical and horizontal wavelength, since $\frac{\hat{\omega}}{f} = [1 + \frac{k^2 N^2}{m^2 f^2}]^{\frac{1}{2}}$. As the wave frequency decreases toward f, the ellipses become increasingly circular (at $\hat{\omega} = f$ they are perfectly circular). As the wave frequency increases, the hodographs become more elliptical, eventually becoming straight lines. The direction of the major axis represents the direction of wave propagation in the horizontal plane. Zhang et. al (2004), found a large variation

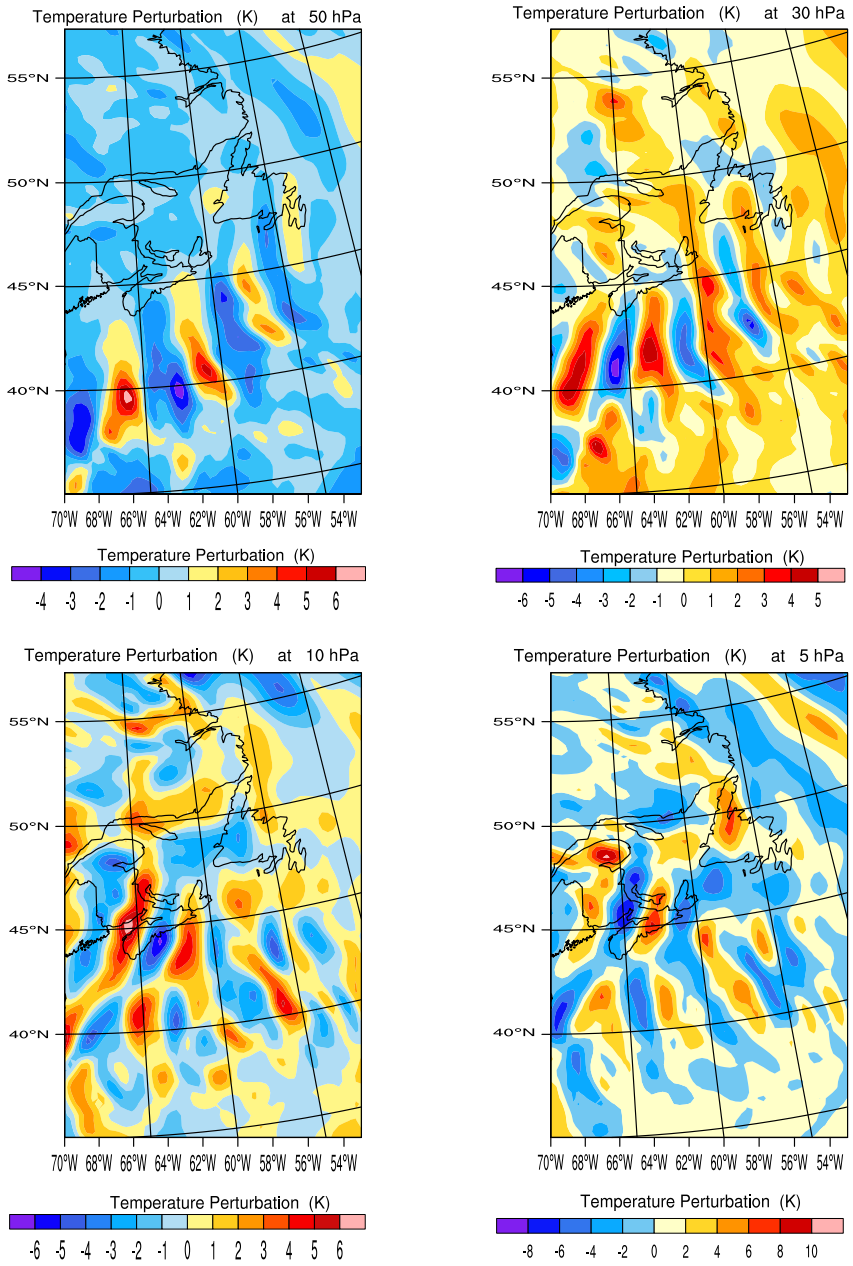

Figure 3.19: Perturbation temperature (°K) at 50 hPa(19 km), 30 hPa(22 km), 10 hPa(28.5 km) and 5 hPa(32 km) on January 19, 2003 at 1800 UT, using 20 point average. From WRF simulations using ECMWF ERA Interim data.

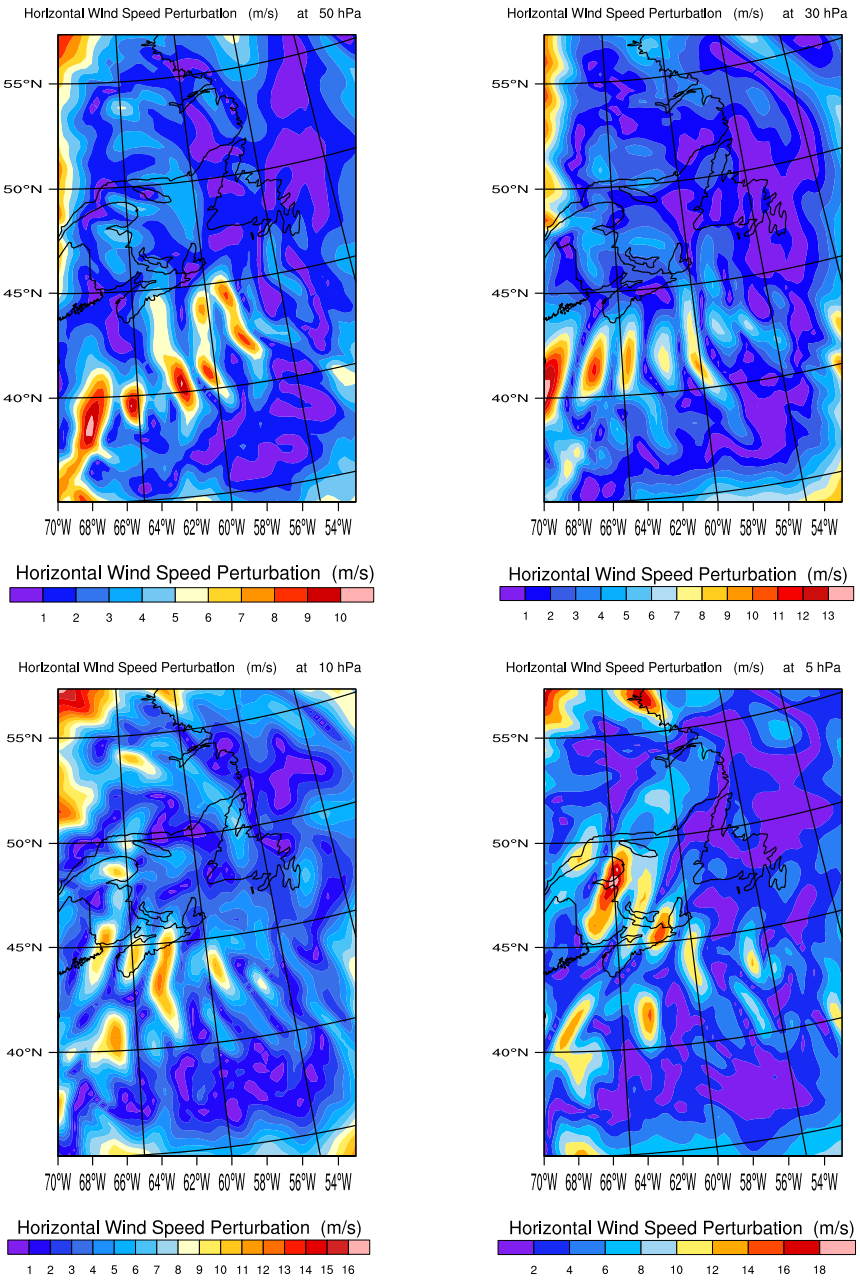

Figure 3.20: Horizontal wind speed perturbation $(u'^2 + v'^2)^{\frac{1}{2}}$ (m/s) at 50 hPa, 30 hPa, 10 hPa and 5 hPa on January 19, 2003 at 1800 UT (12 hours before the peak event), using 20 grid point average. From WRF simulations using ECMWF ERA Interim data.

in wave properties using this method. This is likely due to the effects of vertical wind shear as well as variations in N^2. Nevertheless, a hodograph analysis can sometimes yield useful results if the vertical wavelength is small enough.

Hodographs on the left side of figure 3.21 are in the lower stratosphere. The nearly circular shape indicates wave frequencies are close to f. In contrast, the elliptical shapes on right side indicate the wave frequencies are higher at higher altitudes in the middle stratosphere. This is supported by T' and divergence cross-sections in figure 3.17, where we can see the phase lines are less steep in lower levels ($z < 20$ km) and steeper in upper levels ($z > 20$ km). It is evident that the wave frequency in the stratosphere is close to f. i.e., close to the forcing frequency provided by the unbalanced motions associated with the synoptic scale jet streak. As the packet ascends into the upper stratosphere it is Doppler shifted to higher frequencies by the increasing background wind, i.e., as the projection of background wind on $\boldsymbol{\kappa_h}$ increases with height, so does the intrinsic frequency.

The hodographs on the right are for the layer 30 hPa to 10 hPa. For these upper layers, from the ratio of the major to minor axis, we estimate $\frac{\hat{\omega}}{f}$ to be between 4 to 6, which agrees well with earlier estimates ($f(50^\circ \text{ N})$=1.1 $\times 10^{-4}$ s^{-1} and 4.5×10^{-4} s^{-1} $\leq \hat{\omega} \leq 7.9 \times 10^{-4}$ s^{-1}). The direction of wave propagation $\boldsymbol{\kappa}$ projected in the horizontal plane is given by the direction of the major axis of the ellipse, which in this case is 10° to the north of zonal. The wave vector can also be found by forming a line perpendicular to the phase fronts in figure 3.19 and 3.20. At 30 hPa (22 km) it can be seen that $\boldsymbol{\kappa_h}$ is indeed about 10° to the north of zonal, which agrees well with the hodograph results.

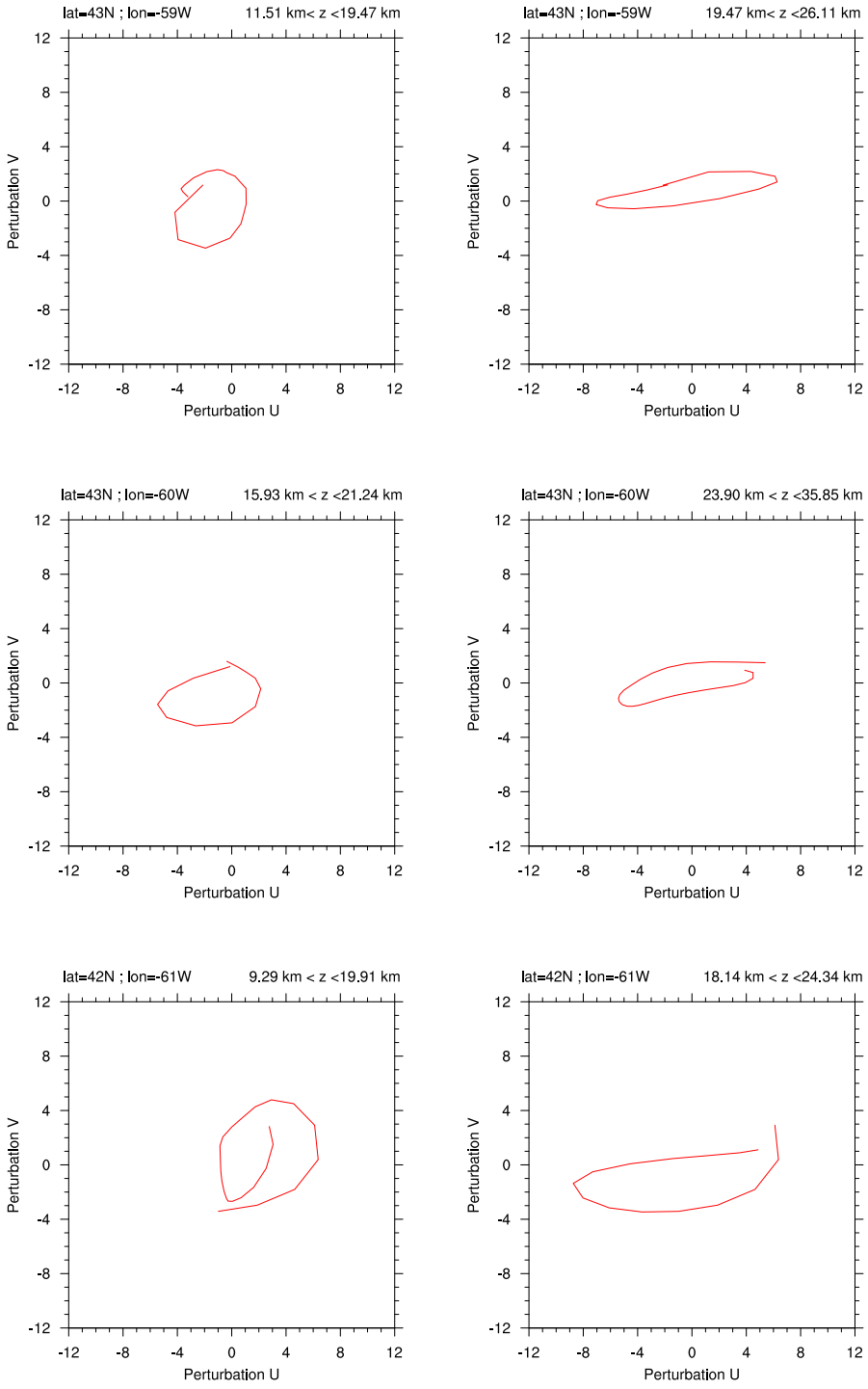

Figure 3.21: Hodographs for chosen points across the cross section line over the ocean on January 19, 2003 at 1800 UT. From WRF simulations using ECMWF ERA Interim data. The left side is for the lower stratosphere, while the right is for the middle stratosphere.

3.4.3 Numerical Simulations Without Topography

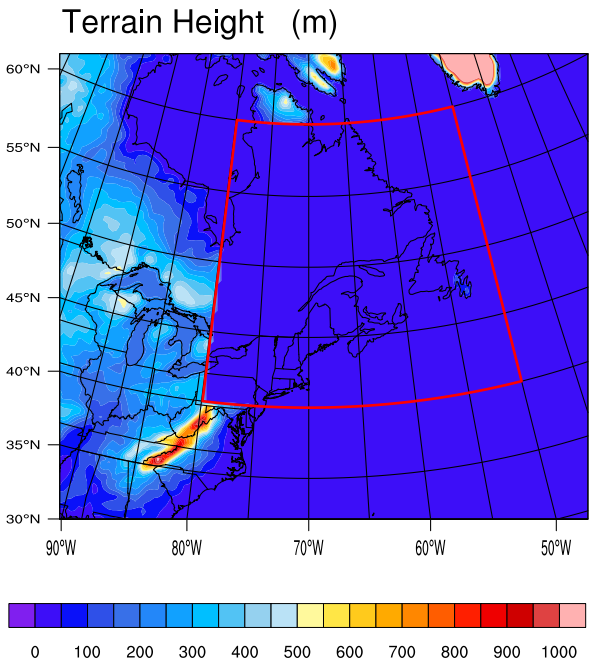

Figure 3.22: The area which the topography has been removed from the land. From WRF simulations using ECMWF ERA Interim data.

To determine the effect of topography on generation of these wave packets, we performed an additional simulation without topography (ERA1.5-flat/2003) in the area bounded by longitudes 80° W to 50° W and latitudes 40° N to 60° N (the area is shown in figure 3.22).

The bottom row of figure 3.23 shows that removing topography does not alter the development or propagation of the wave packet generated by the baroclinic jet streak off the coast of North America. Also note that the plot for Jan 19, 2003 1800 UT shows a wave packet present over the Appalachian mountain range. This agrees with the findings of WZ04 (see figure 3.3). This packet appears in both simulations (with and without topography), because Appalachians were not removed (figure 3.22). This topographic packet dissipates at later times because the flow direction changes.

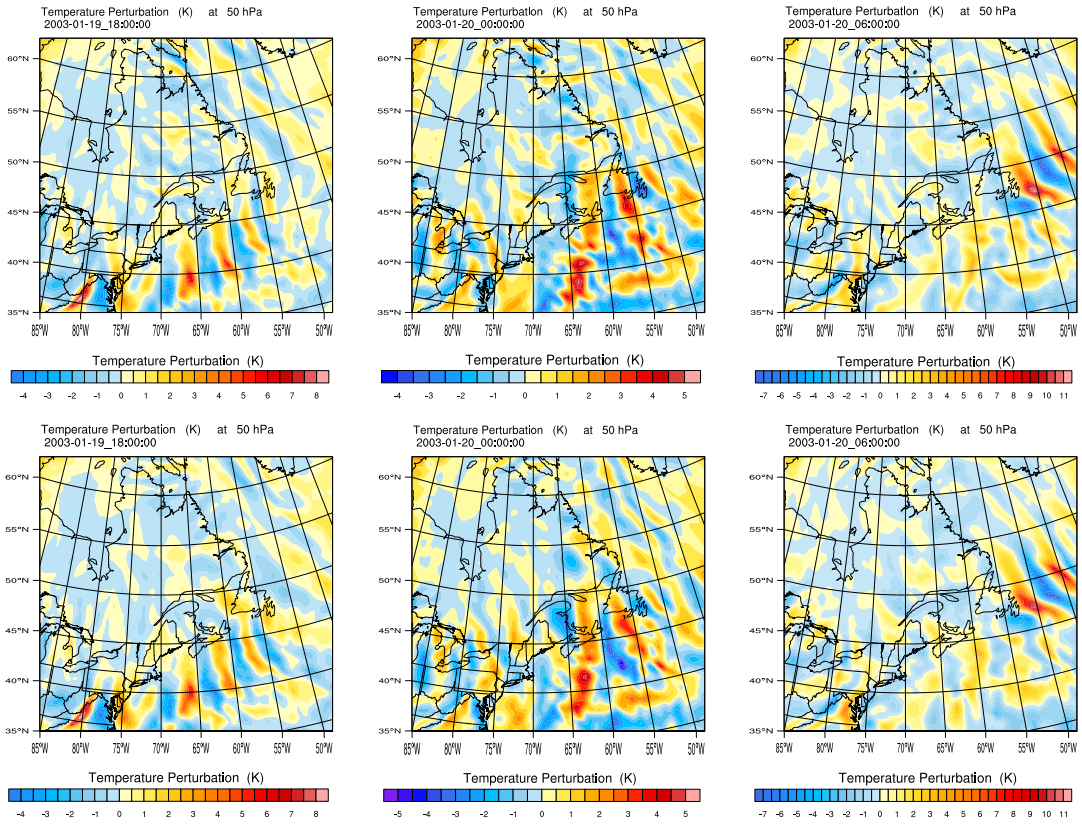

Figure 3.23: Temperature perturbation (° K) at 50 hPa, every 6 hours from January 19, 2003 at 1800 UT to January 20, 2003 at 0600 UT. Mean temperature has been removed using running 20 grid point (600 km) averages. Plots are zoomed into a smaller area close to Newfoundland. Top row: with topography (ERA1.5/2003), bottom row: topography in figure 3.22 is removed (ERA1.5-Flat/2003). From WRF simulations using ECMWF ERA Interim data.

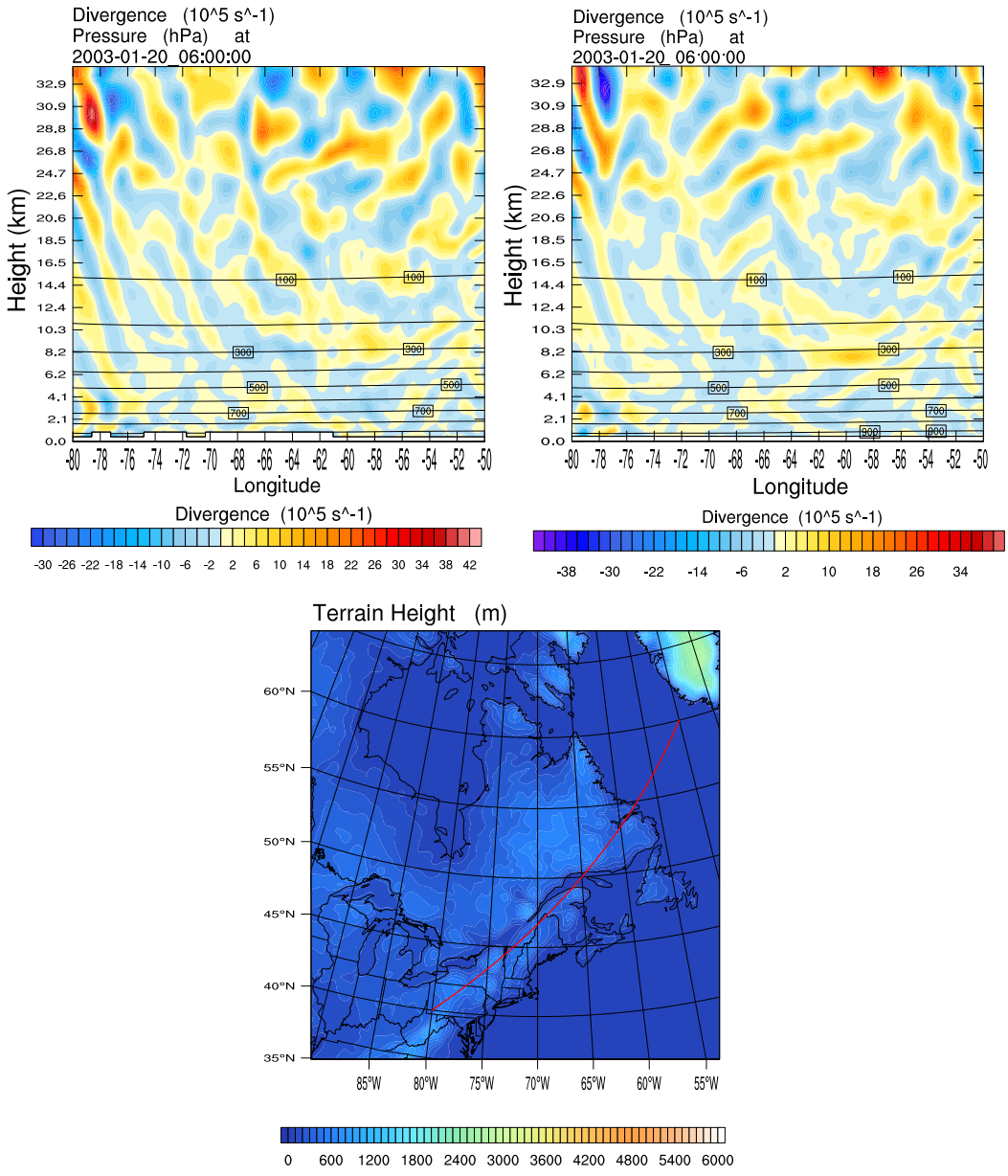

Figure 3.24: Divergence (10^{-5} s^{-1}) cross section every on January 20, 2003 at 0600 UT, with topography (ERA1.5/2003, left) and without topography (ERA1.5-Flat/2003, right). The red line indicates where the cross section has been plotted. The vertical extent of the profiles has been limited to just below the sponge layer. From WRF simulations using ECMWF ERA Interim data.

Figure 3.24 shows the divergence cross section over the land, with and without topography. The cross section over the land with topographic forcing only shows very weak and disorganized small-scale disturbances compared to those in the ocean cross sections, and they are virtually identical to the no-topography case, so we conclude that these weak disturbances are not topographic in origin.

3.4.4 Numerical Simulations Without Convective Parameterizations

We performed an additional simulation without convective parameterizations, i.e. cumulus and microphysics parameterizations were turned off (ERA1.5-dry/2003). Figure 3.25 compares the evolution of temperature perturbations in ERA1.5-dry/2003 (bottom row) with those in ERA1.5/2003 (top row). Both simulations were started on Jan 19 0000 UT, allowing sufficient time for latent heating to affect the development of the East coast low.

On Jan 19 1800 UT, the gravity wave packet in the dry simulation is clearly weaker and less well-organized than in the simulation with convective parameterizations. On Jan 20 0000 UT, the wave packet have similar strength but different location and structure. On Jan 20 0600 UT, the dry packet is again much weaker than the moist one, and is clearly behind the moist packet.

Clearly the latent heat release associated with moist convection is affecting the development of the low and its gravity wave generation (see figure 3.26). These results are generally consistent with the effects of moisture on idealized baroclinic wave simulations of Wei and Zhang, 2014 (WZ14). Those authors performed simulations of gravity wave generation in an idealized baroclinic wave with varying amounts of

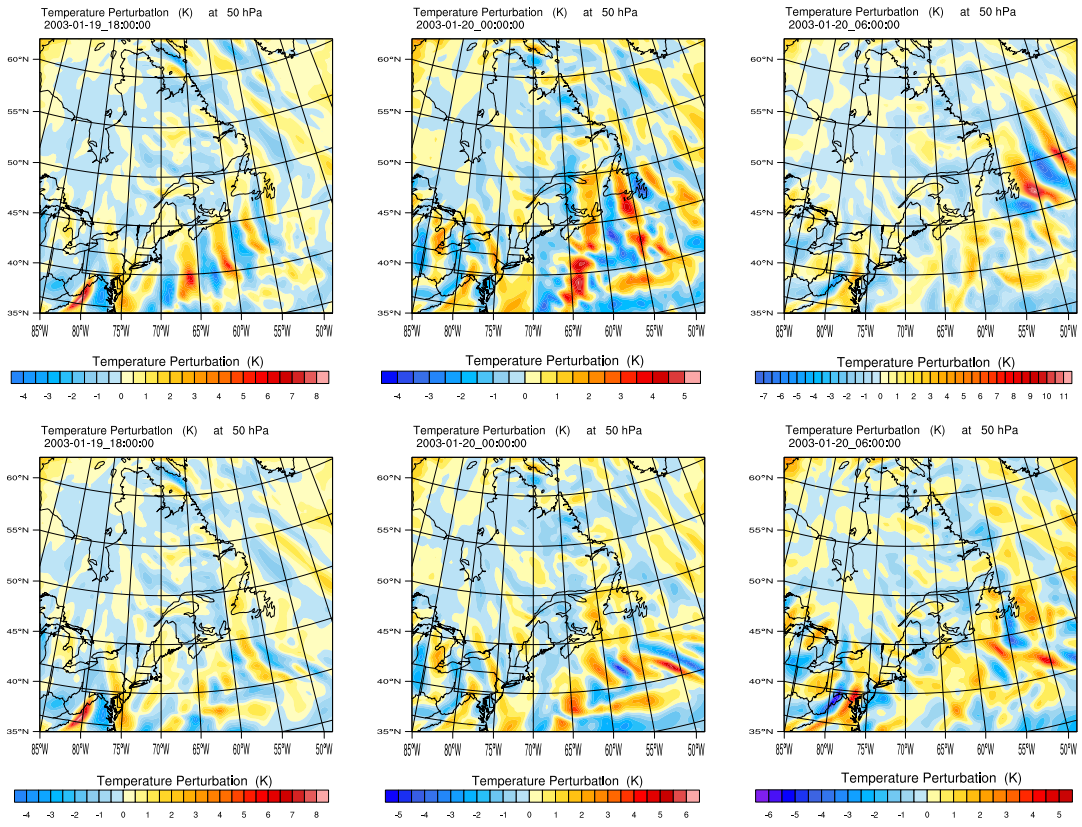

Figure 3.25: Temperature perturbation (°K) at 50 hPa, every 6 hours from January 19, 2003 at 1800 UT to January 20, 2003 at 0600 UT. Mean temperature has been removed using running 20 grid point (600 km) averages. Plots are zoomed into a smaller area close to Newfoundland. Top row: with moisture (ERA1.5/2003), bottom row: without moisture (ERA1.5-Dry/2003). From WRF simulations using ECMWF ERA Interim data.

moisture using the WRF model with the horizontal resolution of 10 km, average vertical resolution of about 300 m and model top at $z = 22$ km, with the top 5 km being devoted to a Rayleigh damping layer. They showed wave modes can appear earlier and become stronger in the presence of significant latent heating.

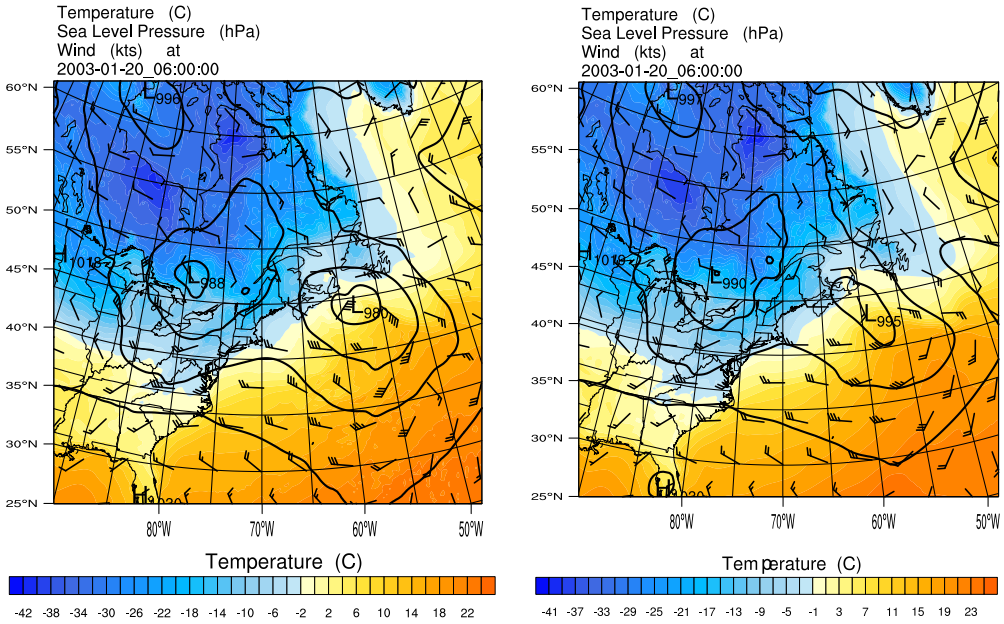

Figure 3.26: Sea level pressure contours (hPa), temperature (°K) and wind-barbs (kts), with moisture (ERA1.5/2003, left) and without moisture (ERA1.5-Dry/2003, right), on January 20, 2003 at 0600 UT. From WRF simulations using ECMWF ERA Interim data.

3.5 Winter 2008

3.5.1 Numerical Simulations Using ECMWF ERA Interim Data

As shown in figure 3.27 the strongest peaks in the time series for 2008 occur on Dec 23 and Dec 24 at 06 UT (1.1 K^2 and 1.4 K^2 respectively). Both peaks may

correspond to a single extended event since measurements are made at 12 hour intervals. Figure 3.28 and 3.29 show maps from the North American Regional Reanalysis (NARR) database from 12 hours preceding the first peak to 6 hours afterward. In figure 3.28, we can see a strong southwesterly jet streak laying off the coast of North America, while figure 3.29 shows a deep quasi-stationary low southeast of Greenland. These features are very similar to the 2003 case shown in figures 3.5 and 3.6. However there are significant differences from the 2003 case.

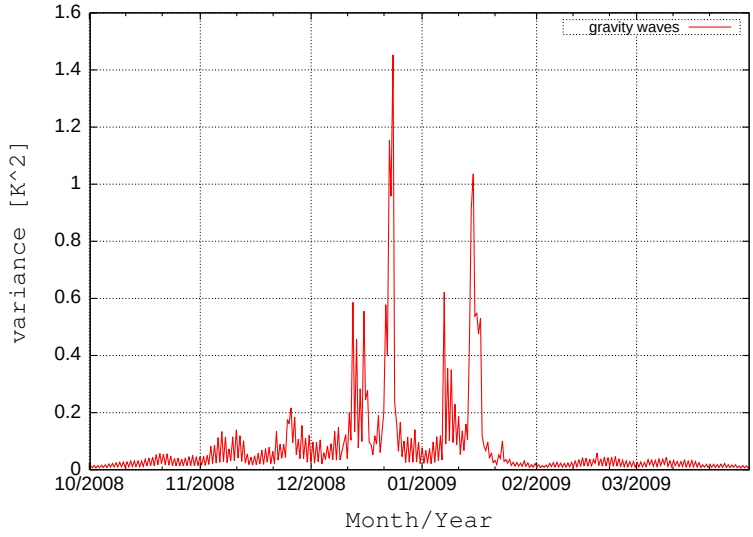

Figure 3.27: Time series for gravity wave peak event over Newfoundland and Labrador during 2008-2009 winter(the strongest peaks on Dec 23 2008, 0600 UT and Dec 24 2008, 0600 UT).

Both cases also have a second quasi-stationary low over Hudson Bay, with a third low moving up the coast of North America, along the 250 hPa jet stream. However, the development of the Hudson Bay and East Coast lows is dramatically different in the two cases. In 2003, the Hudson Bay low gradually weakens, while the initially weak East Coast low intensifies leading up to the event. In 2008, the Hudson Bay low is initially weak and intensifies, while East Coast low is fully mature as it travels up

the coast. It does not significantly deepens until it begins to merge with the Greenland low, around the time of the first hotspot gravity wave peak. In 2003, the flow over the Eastern US was dominated by a rapidly moving trough associated with a fourth low north of the Great Lakes. In 2008, the surface flow over the Eastern US is dominated by a combination of the intensifying low over Hudson Bay, the very strong low off the East Coast, and a high pressure centre originally located over Oklahoma. This combination sets up a surface flow that is nearly perpendicular to the East Coast.

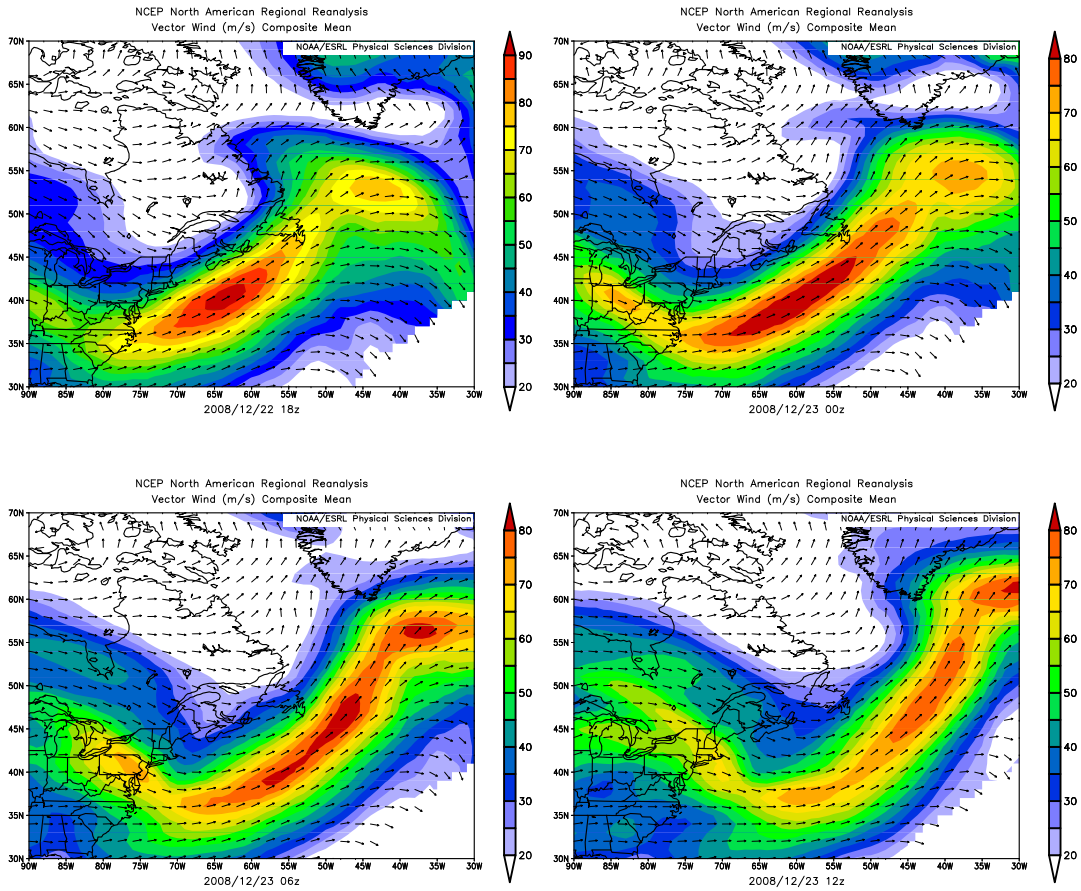

Figure 3.28: 250hPa Vector Wind (m/s) plots every 6 hours from December 22, 2008 at 1800 UT to December 23, 2008 at 1200 UT. Taken from North American Regional Reanalysis (NARR) dataset.

Figure 3.30 shows the surface synoptic flow for Dec 22 at 1200 UT to Dec 24 at

1200 UT, from WRF simulations using ECMWF ERA Interim data (ERA1.5/2008). A strong low is located over the Maritimes on Dec 22 1200 UT. The combination of the Maritime and Hudson Bay lows with the Oklahoma high, produces a flow perpendicular to the New England Coast, i.e. up over the Appalachian mountains and down to the sea. Such a flow configuration is expected to launch topographic waves with wave fronts parallel to the coast. This offshore flow pattern exists for several hours before the gravity wave peak event and provides enough time for waves to propagate well into the stratosphere, provided no critical levels are encountered.

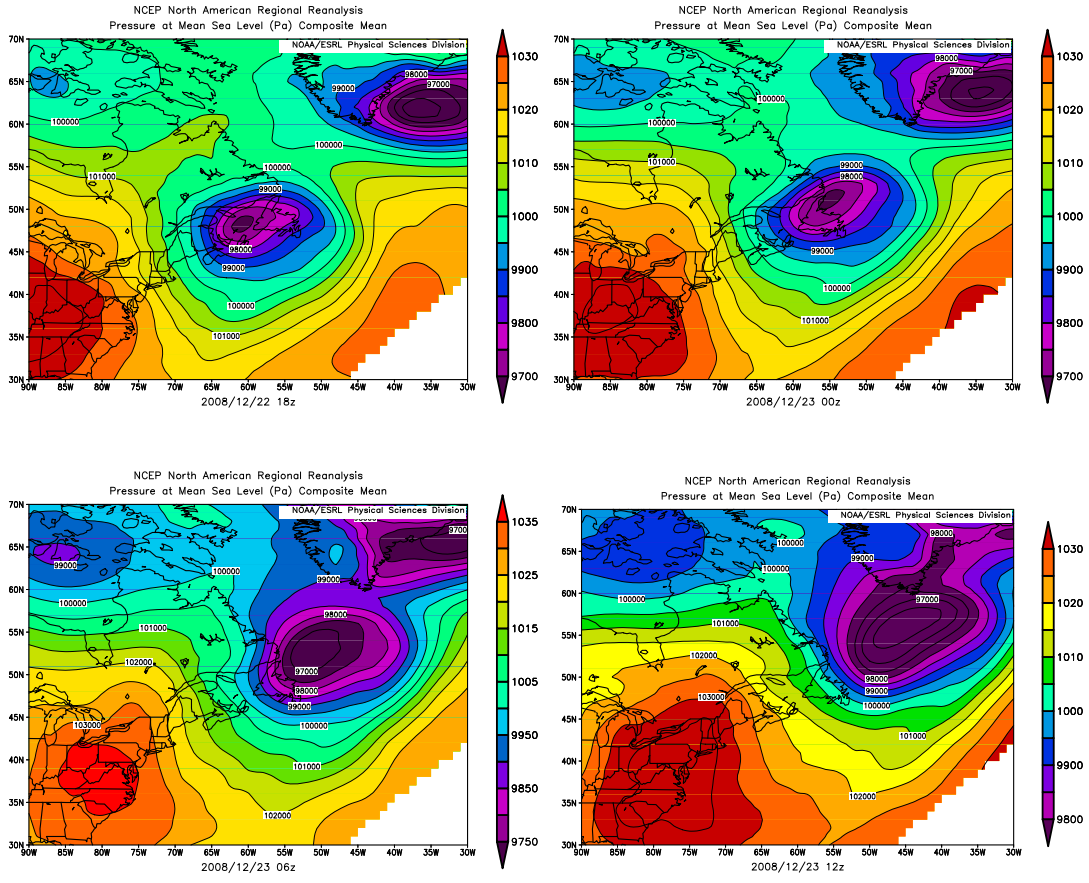

Figure 3.29: Mean Sea Level Pressure (Pa) plots every 6 hours from December 22, 2008 at 1800 UT to December 23, 2008 at 1200 UT. Taken from North American Regional Reanalysis (NARR) dataset.

Indeed, all along the Appalachians, which range from Tennessee and North Carolina to New Hampshire and Vermont, we see large short-wave distortions in WRF's surface isobars that are significantly more pronounced than those in NARR (figure 3.29). By Dec 23 0600 UT and 1200 UT, the Low has moved to the north of NFLD, while the high has moved over the Virginias. There is still a strong flow perpendicular to the Canadian Coast, but the surface flow to the south is now parallel to the Appalachian ridge and would no longer be expected to launch topographic gravity waves.

In the final stages shown in figure 3.30, as the Hudson Bay low deepens and the East Coast low merges with the Greenland low, the surface flow over Northeastern Canada shifts towards the northeast (i.e., from southwest), so that it is perpendicular to the Labrador coast. This type of flow is also expected to launch topographic gravity waves.

Figure 3.31 shows the evolution of the 50 hPa perturbation field over the same region as the surface flow in figure 3.30 (Note that figure 3.31 starts 6 hours later than figure 3.30). December 22 at 1800 UT shows a strong tropospheric wave packet has developed over the Appalachians from North Carolina to Pennsylvania. This is a response to the southeastward surface flow, which is perpendicular to the mountain ridge. As the East Coast low and Oklahoma high progress up the coast, the inter-vortex southeastward surface flow moves with them, and the topographic gravity wave response follows this surface forcing. However, by Dec 23 at 1200 UT, the southeastward surface flow has moved past the northern range of the Appalachians, so there is no more topographic forcing. At this time, the packet is cut off from its source and what remains in the lower stratosphere will propagate according to

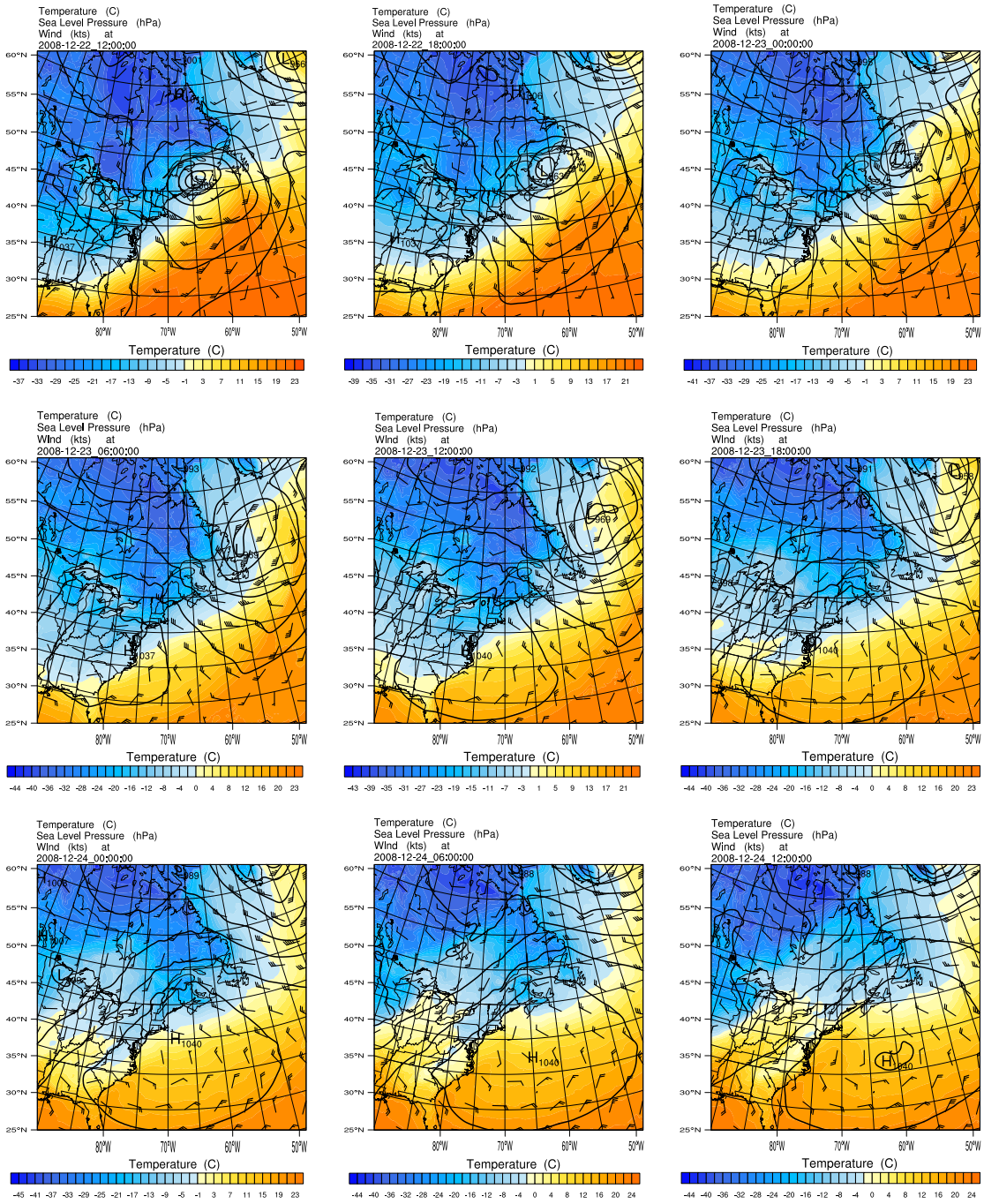

Figure 3.30: Sea level pressure contours (hPa), temperature (°K) and wind-barbs (kts), every 6 hours from December 22, 2008 at 1200 UT to December 24, 2008 at 1200 UT. From WRF simulations using ECMWF ERA Interim data (ERA1.5/2008).

standard group velocity rules, which include advection by the difference between the horizontal background wind and the horizontal intrinsic phase speed perpendicular to the ridge.

The background flow is along the geopotential height contours shown in figures 3.32 (50 hPa) and 3.33 (5 hPa). As the packet moves into the Atlantic Provinces on Dec 23 at 1200 UT, the 50 hPa flow is somewhat to the north of eastward, but as the packet progresses westward and northward, the background flow shifts increasingly toward the north. This is consistent with the movement of the packet after Dec 23 at 1200 UT.

Figure 3.33 shows that there is some backing of the wind with height, i.e., the 5 hPa flow over the Atlantic Provinces is consistently northeastward (directed along the coast) at all times during this period. Figure 3.34 shows the temperature perturbation field at 5 hPa ($z \approx 37$ km). Even on Dec 22 at 1800 UT (12 hours before the hotspot gravity wave peak) there is some gravity wave activity in the hotspot region. The strength of the gravity wave temperature perturbations increases dramatically, almost doubling by Dec 23 at 1800 UT (which is midway between the two AIRS measurements that correspond to the peak gravity wave variance).

Figures 3.31 (50 hPa) and 3.34 (5 hPa) also show a stationary wave packet appearing along the coast of Labrador on Dec 23 at 1800 UT. This corresponds to the time at which the surface flow in figure 3.30 becomes perpendicular to the Labrador Coast. These topographic waves represent another source of temperature variance for the AIRS gravity wave peak events.

Figure 3.35 shows 5 hPa (35 km) temperature perturbations zoomed into an area that is just a bit larger than the hotspot region shown in figure 3.1 for the 18 hour

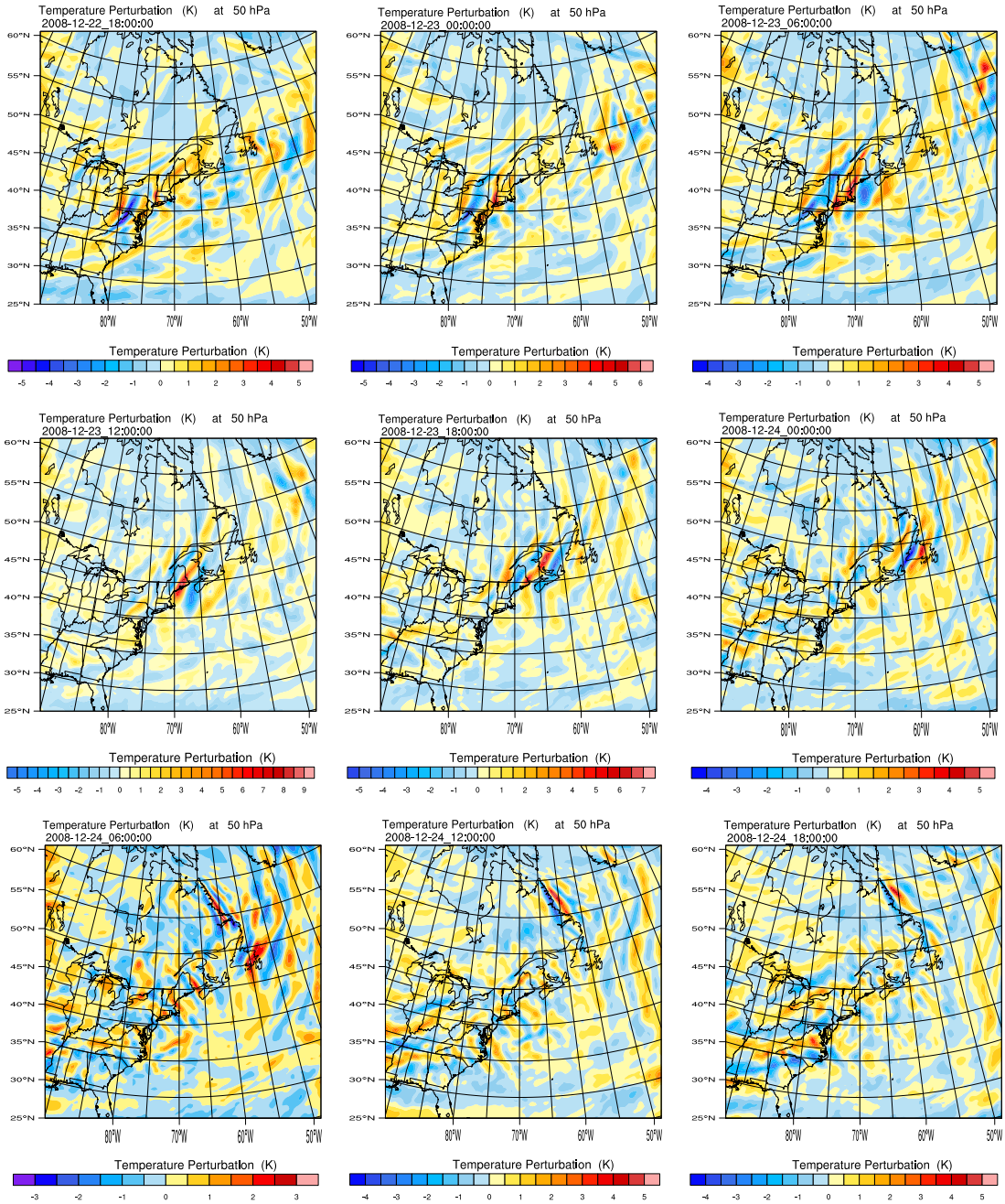

Figure 3.31: Temperature perturbation (°K) at 50 hPa, every 6 hours from December 22, 2008 at 1800 UT to December 24, 2008 at 1800 UT, using 20 grid point average. From WRF simulations using ECMWF ERA Interim data (ERA1.5/2008). Note this figure starts 6 hours later than figure 3.30.

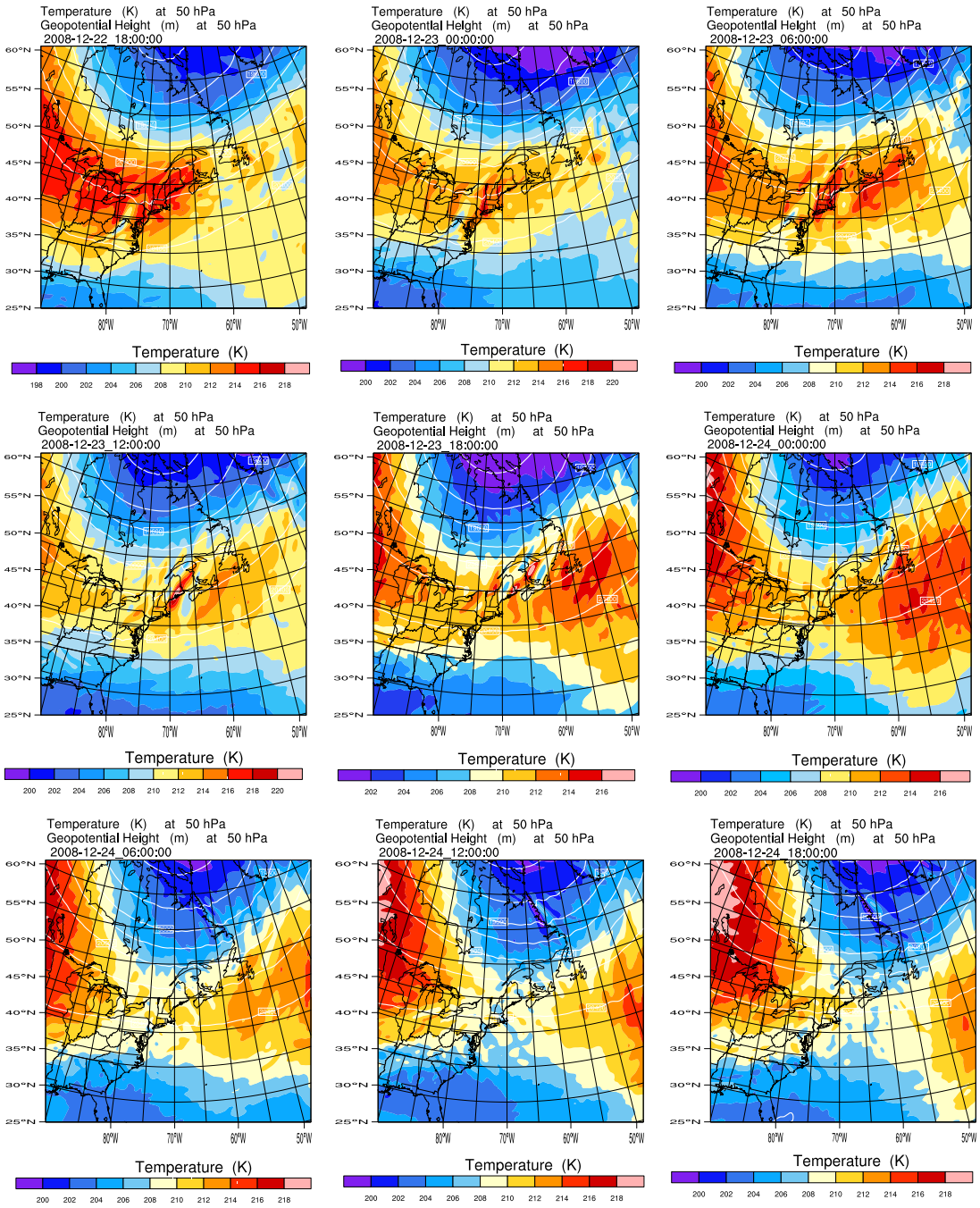

Figure 3.32: Geopotential height contours (m), horizontal wind speed (m/s) and wind-barbs (m/s) at 50 hPa, every 6 hours from December 22, 2008 at 1800 UT to December 24, 2008 at 1800 UT. From WRF simulations using ECMWF ERA Interim data (ERA1.5/2008).

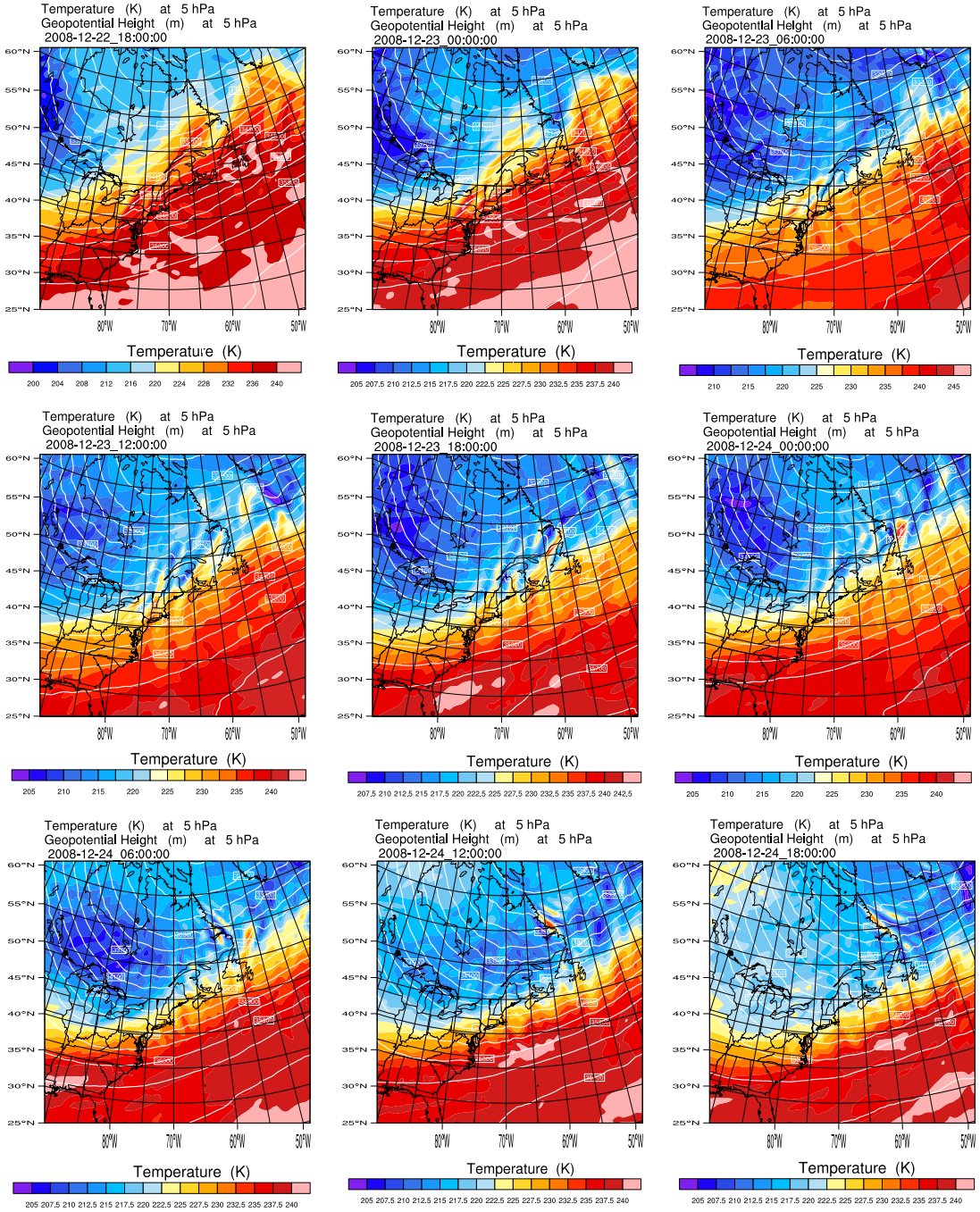

Figure 3.33: Geopotential height contours (m), horizontal wind speed (m/s) and wind-barbs (m/s) at 5 hPa, every 6 hours from December 22, 2008 at 1800 UT to December 24, 2008 at 1800 UT. From WRF simulations using ECMWF ERA Interim data (ERA1.5/2008).

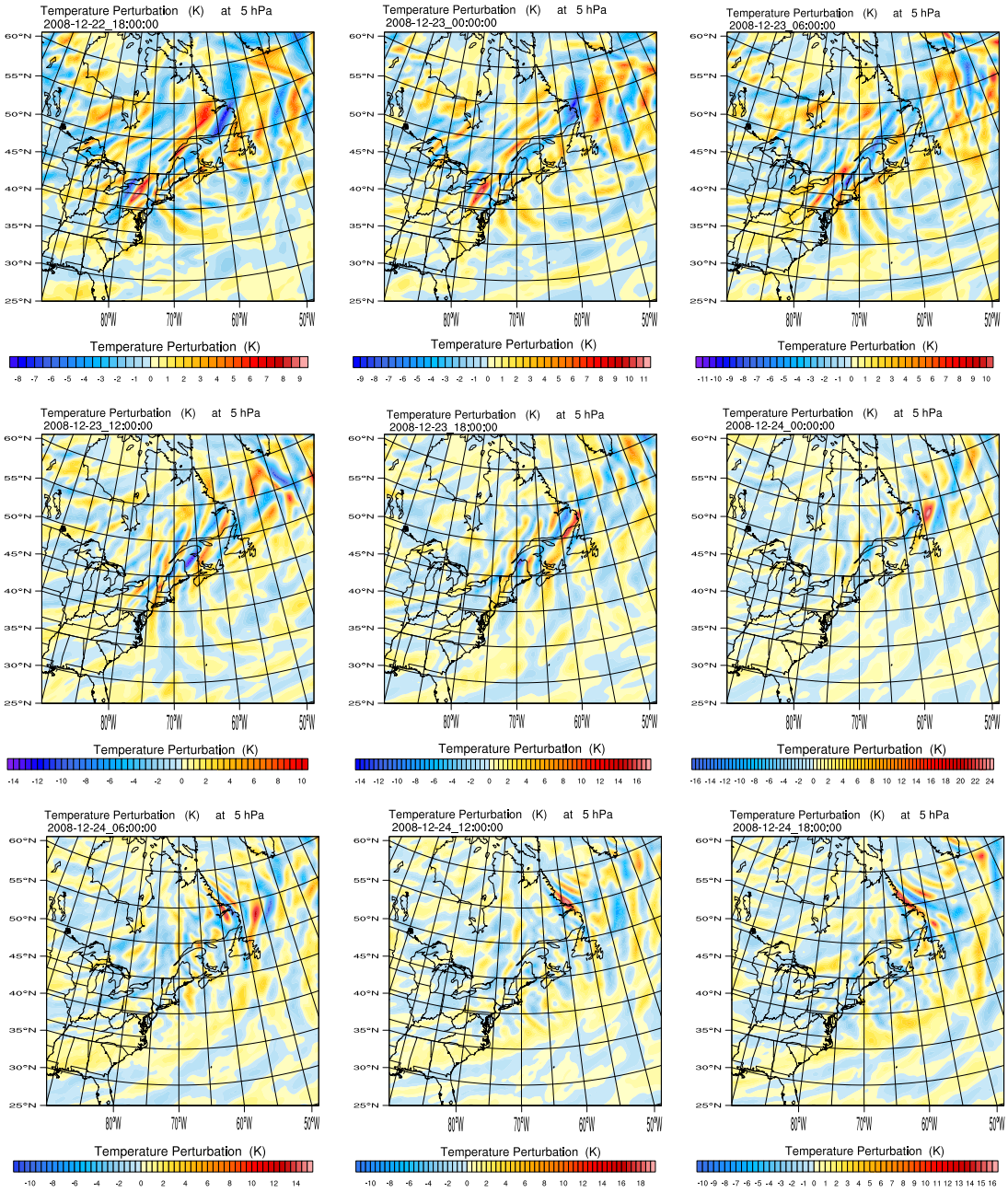

Figure 3.34: Temperature perturbation (°K) at 5 hPa, every 6 hours from December 22, 2008 at 1800 UT to December 24, 2008 at 1800 UT, using 20 grid point average. From WRF simulations using ECMWF ERA Interim data (ERA1.5/2008).

period between the two strongest AIRS variance peaks. As we have shown, the wave packet on Dec 23 at 1800 UT which propagates northeastward over the next 18 hours, originates over the Appalachians.

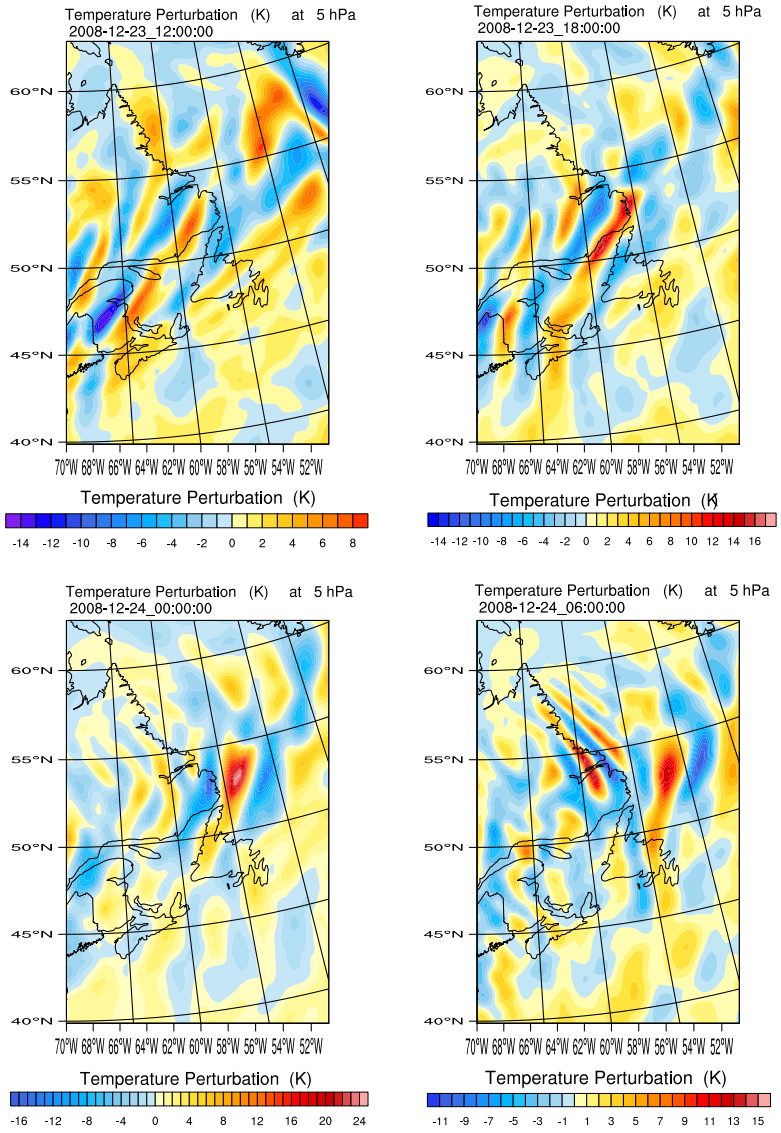

Figure 3.35: Temperature perturbation (°K) at 5 hPa, every 6 hours from December 23, 2008 at 1200 UT to December 24, 2008 at 0600 UT, using 20 grid point average. Plots are zoomed into a smaller area close to Newfoundland. From WRF simulations using ECMWF ERA Interim data (ERA1.5/2008).

A quasi-stationary wave packet also appears over the Labrador Coast on December 24 at 0600 UT and remains active for about 12 hours before dissipating. This clearly demonstrates that there are two sources of gravity waves entering the Newfoundland/Labrador hotspot during the period in which AIRS registers a peak in gravity wave activity. Evidently, one of the packets originates from earlier topographic wave activity over the Appalachians. To our knowledge, this is the first time a topographic wave packet has been shown to affect a region of the atmosphere thousands of kilometers away from the topographic source. Consequently, we will perform tests to confirm the forcing mechanism for the hotspot peaks.

3.5.2 Numerical Simulations Without Topography and Convection

Figure 3.36 shows the evolution of wave patterns in the perturbation temperature field at 50 hPa (20 km) over Eastern North America at 6 hour intervals from December 23 1800 UT to December 24 0600 UT. The top row in figure 3.36 has convective parameterization and full topography.

In order to determine the generation mechanism for these wave packets, we performed two additional simulations, shown in the middle and bottom rows. The middle row has removed the convective parameterization. Since the wave patterns are similar to the case with convective parameterization, we conclude that convective processes associated with the low pressure system are not responsible for the generation of these waves.

The bottom row has removed topography from the area bounded by longitudes 80° W to 50° W and latitudes 40° N to 60° N (area A, shown in figure 3.37, ERA1.5

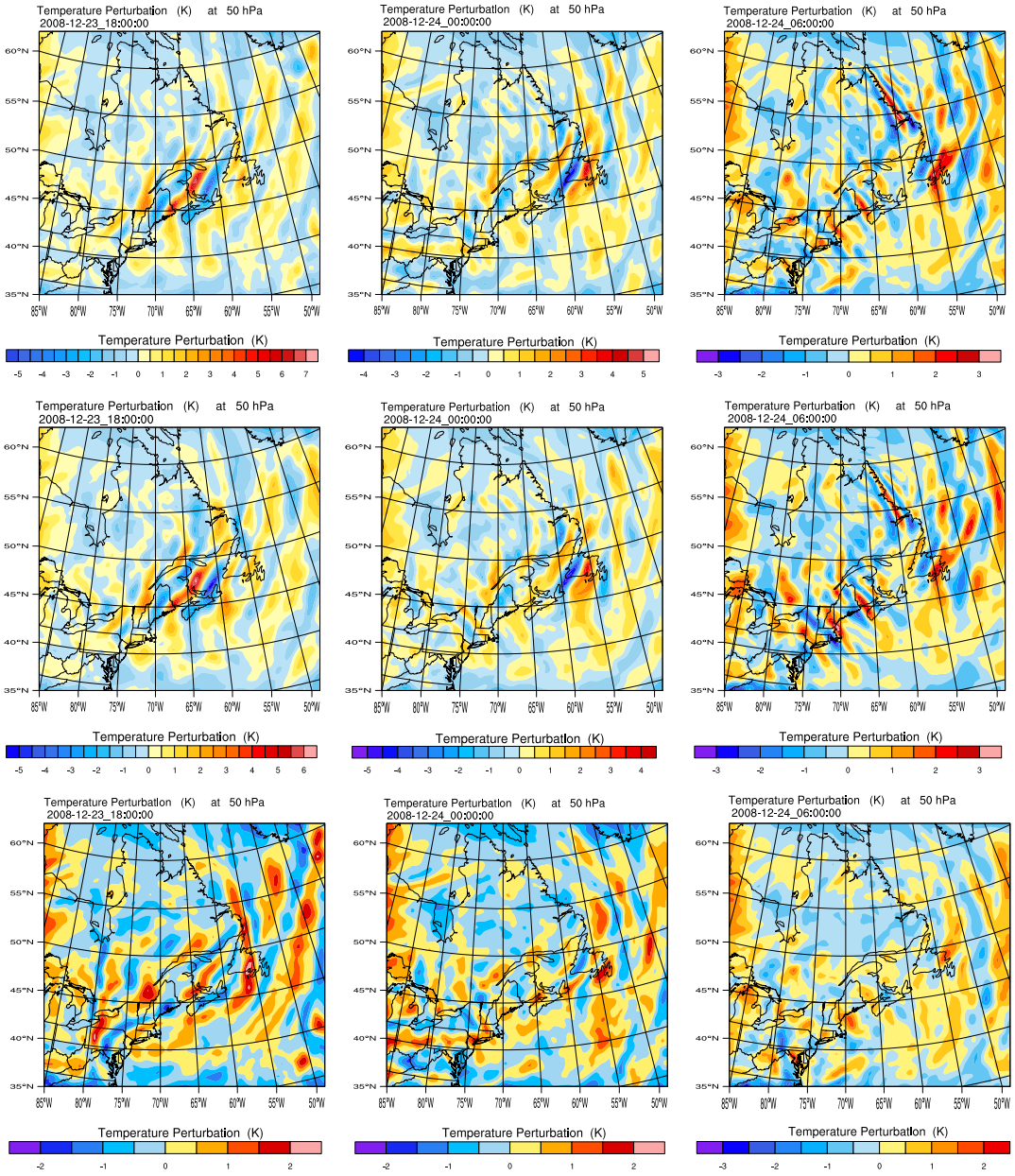

Figure 3.36: Temperature perturbation (°K) at 50 hPa, every 6 hours from December 23, 2008 at 1800 UT to December 24, 2008 at 006 UT, using 20 grid point average. Plots are zoomed into a smaller area close to Newfoundland. Top row: with moisture and topography (ERA1.5/2008), middle row: without moisture (ERA1.5 Dry/2008), bottom row: topography has been removed from area A shown in figure 3.37 (ERA1.5 Flat1/2008). From WRF simulations using ECMWF ERA Interim data.

Flat1/2008). This removes the New England section of the Appalachians but retains the southern part of the range. The left (inflow) boundary of the region was chosen to pass through Hudson and James Bay and the relatively low-elevation area in Southern Ontario. We do see a modest amount of topographic wave generation at this inflow boundary, but it is sufficiently far away from the hotspot region so that the results are not affected.

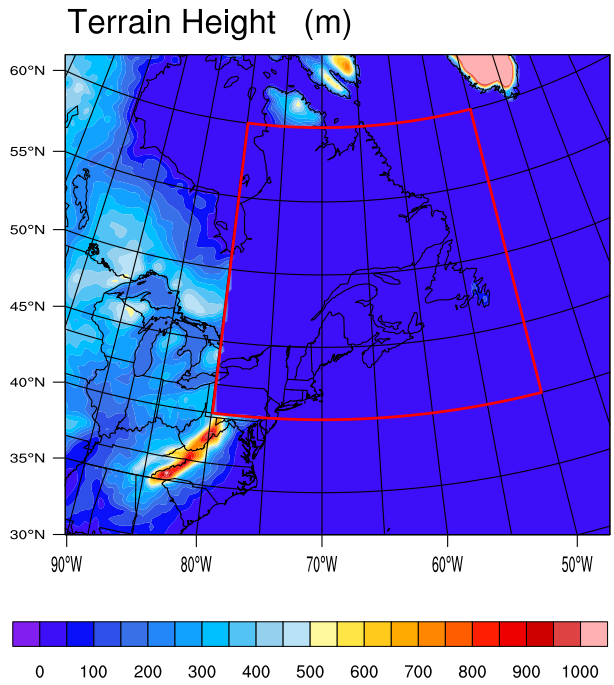

Figure 3.37: Area A: The area which the topography has been removed from the land. From WRF simulations using ECMWF ERA Interim data (ERA1.5 Flat1/2008).

In this simulation, the wave packet off the coast of Labrador is not present on Dec 24 0600 UT. This proves that this particular wave packet has been generated by the coastal topography. Also note that removing topography has reduced the strength of the first wave packet by about 65%. This is because part of the topographic source has been removed (Let the Appalachians south of Pennsylvania remain). This

demonstrates that the southern Appalachians are responsible for a significant part of the gravity wave activity in the hotspot region. Same results can be seen in 5 hPa temperature perturbation zoomed plots, figure 3.38.

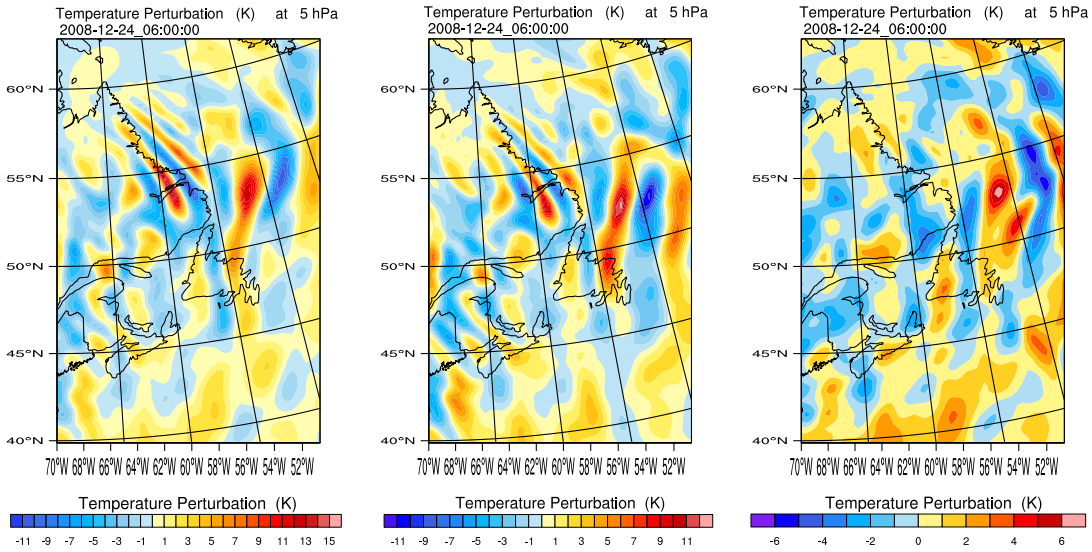

Figure 3.38: Temperature perturbation (°K) at 5 hPa on December 24, 2008 at 0600 UT, using 20 grid point average. Plots are zoomed into a smaller area close to Newfoundland. Left: with moisture and topography (ERA1.5/2008), middle: without moisture (ERA1.5 Dry/2008), right: topography has been removed from area A shown in figure 3.37 (ERA1.5 Flat1/2008). From WRF simulations using ECMWF ERA Interim data.

Figure 3.40 shows cross-sections over land (over the red line in figure 3.39) for the divergence field for the period of Dec 23 1800 UT to Dec 24 0600 UT. The cross section passes through Maine, New Brunswick and Newfoundland. It allows us to calculate wave parameters such as horizontal and vertical wavelengths.

All of the waves have horizontal wavelengths λ_h much larger than their vertical wavelengths λ_z, so we may use the dispersion relation (1.15). Table 3.4 shows that the horizontal wavelengths are between 350 and 420 km, while vertical wavelengths are between 7.5 and 10.3 km. The intrinsic frequencies are between 3.9×10^{-4} and 5.4×10^{-4} s^{-1}, horizontal phase speeds between -24 and -34 m/s, and vertical groups

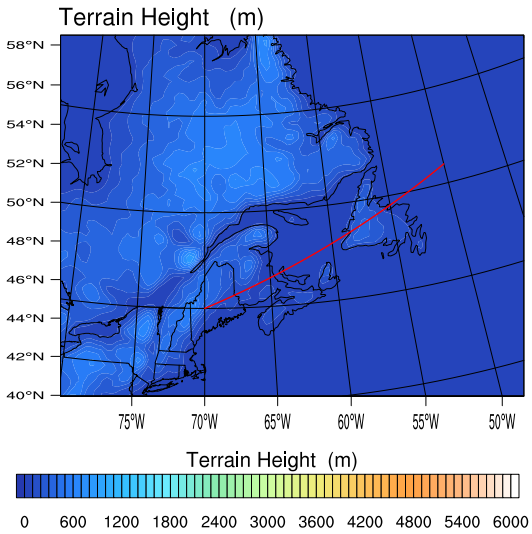

Figure 3.39: The red line on the figure indicates where the cross section on figure 3.40 is plotted (over the land). From WRF simulations using ECMWF ERA Interim data.

speeds between 0.47 and 0.85 m/s. The horizontal phase speed is negative, indicating that it is opposite to the south-westerly mean horizontal flow, as would be expected for topographic gravity waves.

	λ_h(km)	λ_z (km)	N (s^{-1})	f (s^{-1})	$\hat{\omega}$ (s^{-1})	$\lvert\hat{c}_h\rvert$(m/s)	c_{gz}(m/s)
Dec 23 12 UT 68W, 45N	400	8.0	0.019	1.03×10^{-4}	3.9×10^{-4}	25	0.47
Dec 23 18 UT 65W, 47N (upper layer)	420	10.3	0.020	1.07×10^{-4}	5.0×10^{-4}	34	0.79
Dec 23 18 UT 65W, 47N (lower layer)	350	7.5	0.019	1.07×10^{-4}	4.2×10^{-4}	24	0.47
Dec 24 00 UT 57W, 48.5N	370	10.3	0.019	1.09×10^{-4}	5.4×10^{-4}	32	0.85

Table 3.4: Gravity wave parameters calculated for the case ERA 1.5/2008. The direction of horizontal phase propagation at 50 hPa is northeastward in all cases. See figure 3.31 and the top row of figure 3.40. This is the packet being advected from Appalachians to the hotspot.

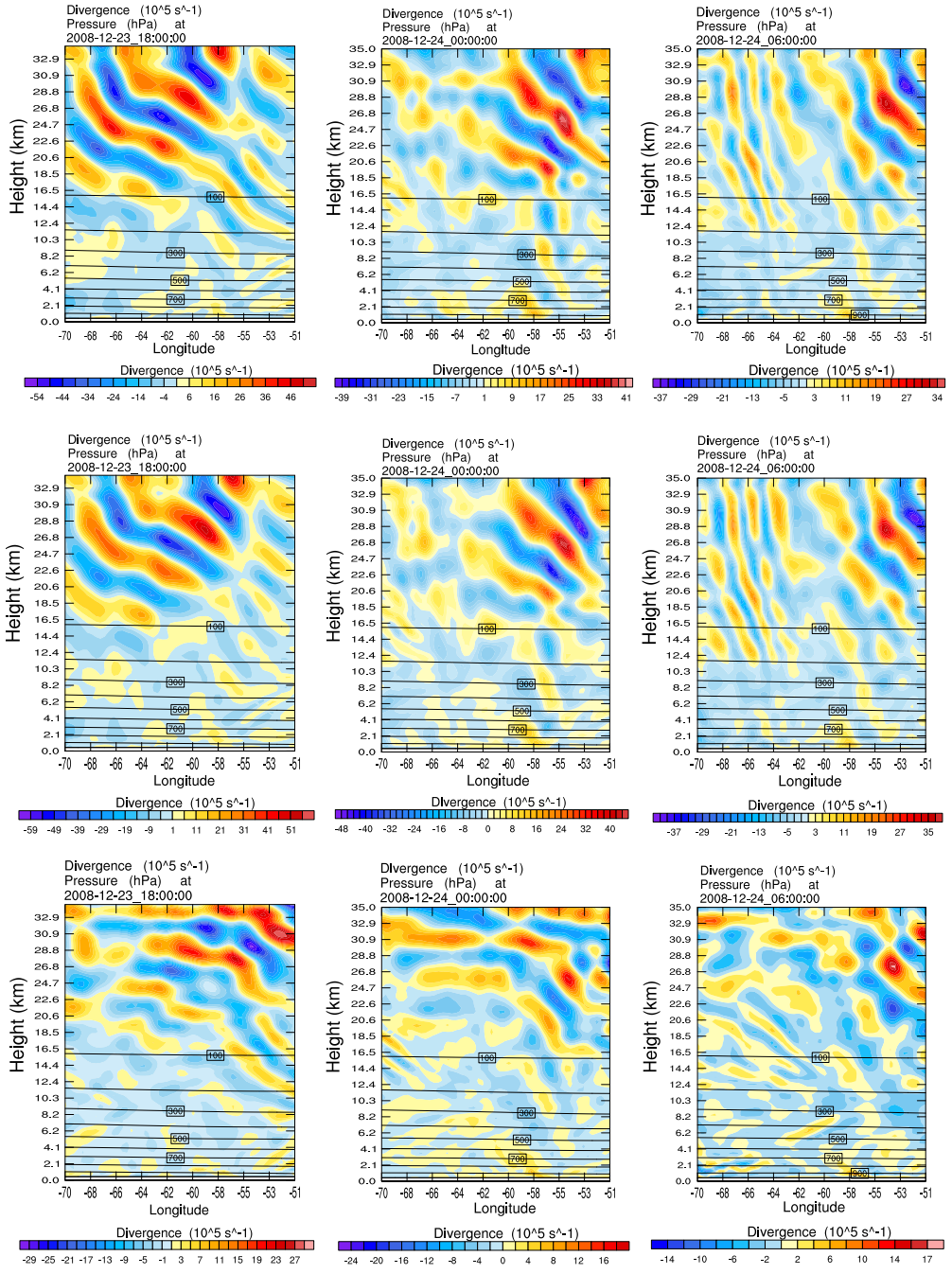

Figure 3.40: Divergence (10^{-5} s^{-1}) cross section every 6 hours from December 23, 2008 at 1800 UT to December 24, 2008 at 006 UT. Top row: with moisture and topography (ERA1.5/2008), middle row: without moisture (ERA1.5 Dry/2008), bottom row: with topography removed from area A shown in figure 3.37 (ERA1.5 Flat1/2008). The vertical extent of the profiles have been limited to just below the sponge layer. From WRF simulations using ECMWF ERA Interim data.

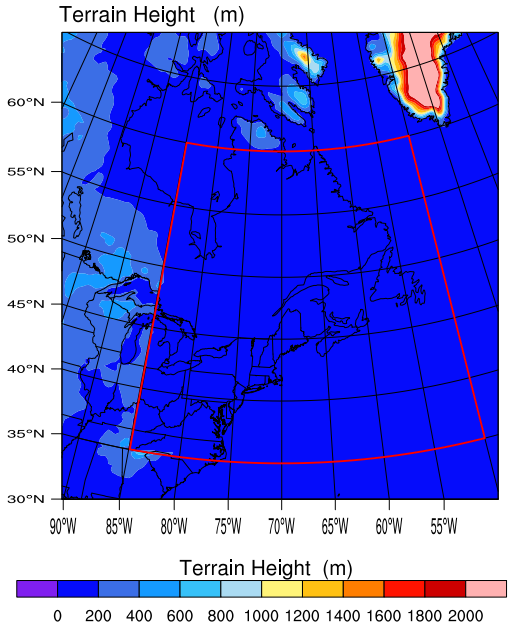

Figure 3.41: Area B, which the topography has been removed from the land. From WRF simulations using ECMWF ERA Interim data (ERA1.5 Flat2/2008).

The second row in figure 3.40 shows the 2008 simulation EAR1.5 Dry/2008, which the cumulus parameterization and condensation have been turned off. In this case the simulation is virtually identical to the simulation in the top row, indicating that moist processes are not involved in the formation of the gravity wave packet. The third row shows the 2008 simulation without topography, ERA1.5-flat1/2008. In this case the wave packet has been almost entirely eliminated at lower levels. What little remains is due to wave generation by topography in the southern U.S. which was not removed. This shows, under the right circumstances, the Appalachian mountains generate topographic gravity wave packets that may be advected great distances up the coast line as they propagate upward. These circumstances are associated with the wintertime East Coast storm track and may therefore be a regular occurrence.

In order to further investigate the effects of topography on the generation of gravity

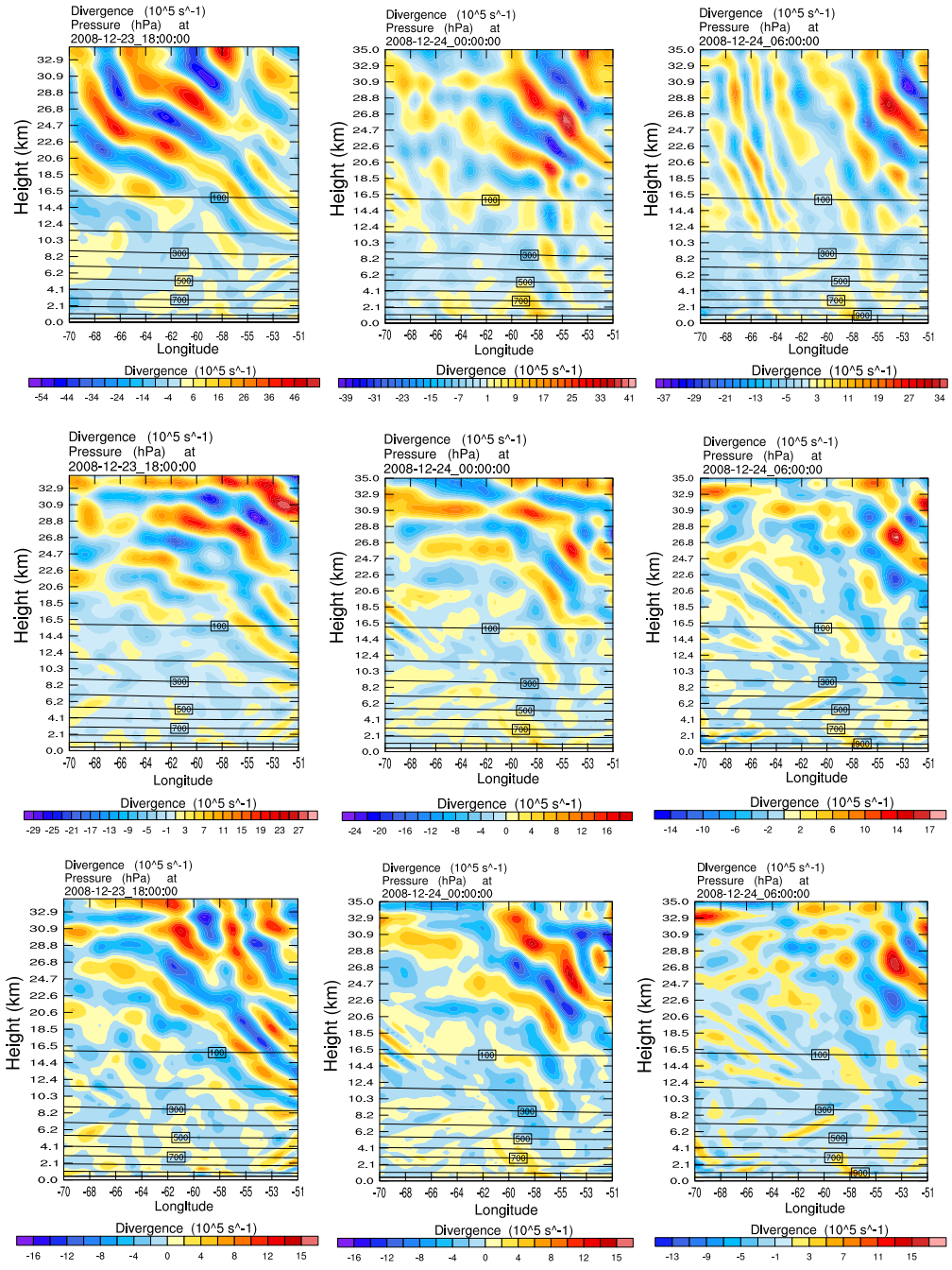

Figure 3.42: Divergence (10^{-5} s^{-1}) cross section every 6 hours from December 23, 2008 at 1800 UT to December 24, 2008 at 006 UT. Top row: with convection and topography (ERA1.5/2008), middle row: topography has been removed from area A, shown in figure 3.37 (ERA1.5 Flat1/2008), bottom row: topography has been removed from area B shown in figure 3.41 (ERA1.5 Flat2/2008). From WRF simulations using ECMWF ERA Interim data.

waves, we performed another series of simulations (ERA1.5 Flat2/2008), removing the topography from a larger area bounded by longitudes 85° W to 50° W and latitudes 35° N to 60° N (Area B, shown in figure 3.41). Figure 3.42 shows cross-sections over the same line as figure 3.40, for the divergence field for the period of Dec 23 1800 UT to Dec 24 0600 UT. As we can see, removing the topography from a larger area leads to further elimination of the wave packet.

3.6 Winter 2014

3.6.1 Numerical Simulations Using ECMWF ERA Interim Data

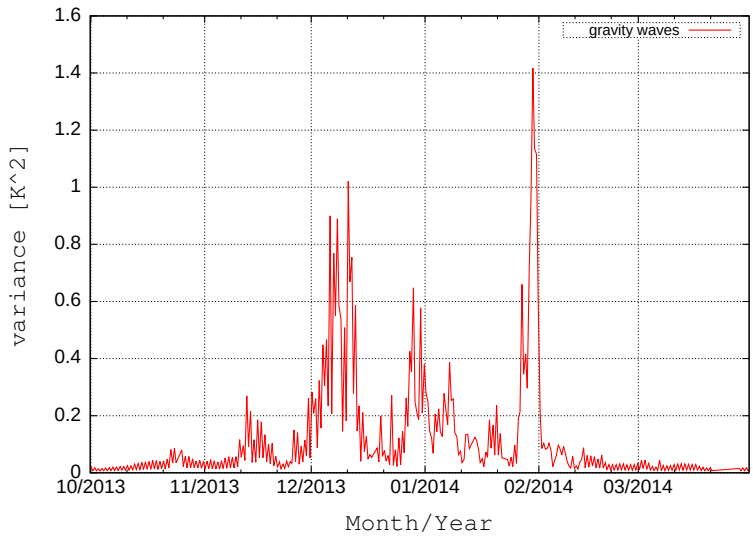

Figure 3.43: Time series for gravity wave peak event over Newfoundland and Labrador during 2013-2014 winter(the strongest peak on Jan 31 2014, 0600 UT).

As shown in figure 3.43, the strongest peak in the Time Series for 2014 occur on Jan 31 2014, 0600 UT (1.4 K^2). Strong variance signals (> 1 K^2) were also found on

Feb 1, 2014, 0600 UT. This is a relatively strong and persistent event compared to others in the record. Synoptic flow patterns from the North American Regional Reanalysis (NARR) database for the 2014 peak event are shown in figures 3.44 and 3.45 respectively. At 250 hPa (figure 3.44), we can see a jet streak with wind speeds of 90 to 100 m/s, just off the coast of the continent. This feature looks very similar to the 2003 and 2008 cases.

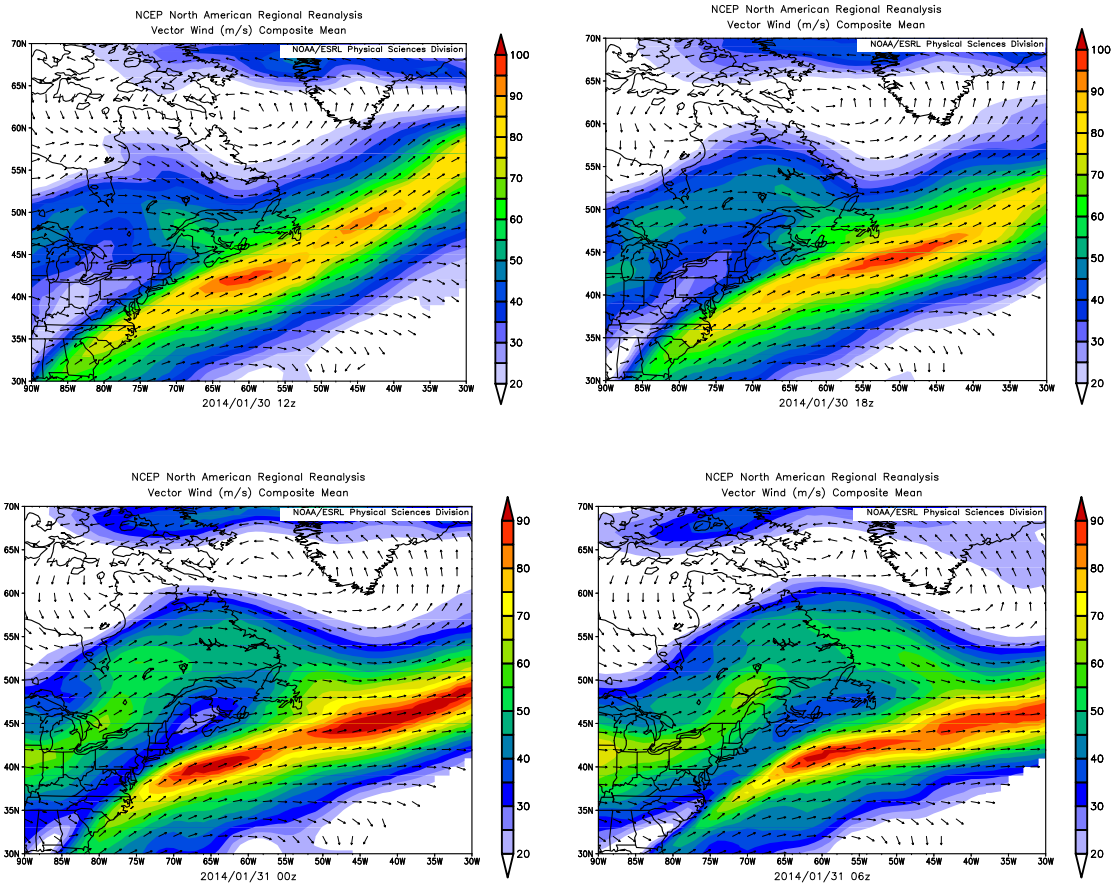

Figure 3.44: 250hPa Vector Wind (m/s) plots every 6 hours from January 30, 2014 at 1800 UT to January 31, 2014 at 0600 UT. Taken from North American Regional Reanalysis (NARR) dataset.

As in the 2008 case, we see a persistent quasi-stationary low southeast of Greenland, and a weaker low developing over Hudson Bay. Whereas the 2008 case had a

strong low moving up the East Coast, and 2003 had a strong trough moving eastward across the USA, 2014 has a strong ridge moving from Quebec to the Atlantic province. The ridge is associated with a high pressure centre, east of Atlantic Provinces. The sea level pressure contours indicate the flow near the Appalachians is parallel to the mountain ridge and relatively weak. In contrast, the surface flow over Labrador is strong and becomes perpendicular to the coastal range just before the gravity wave peak event. These flow conditions support topographic gravity wave emission only from the Labrador Coast.

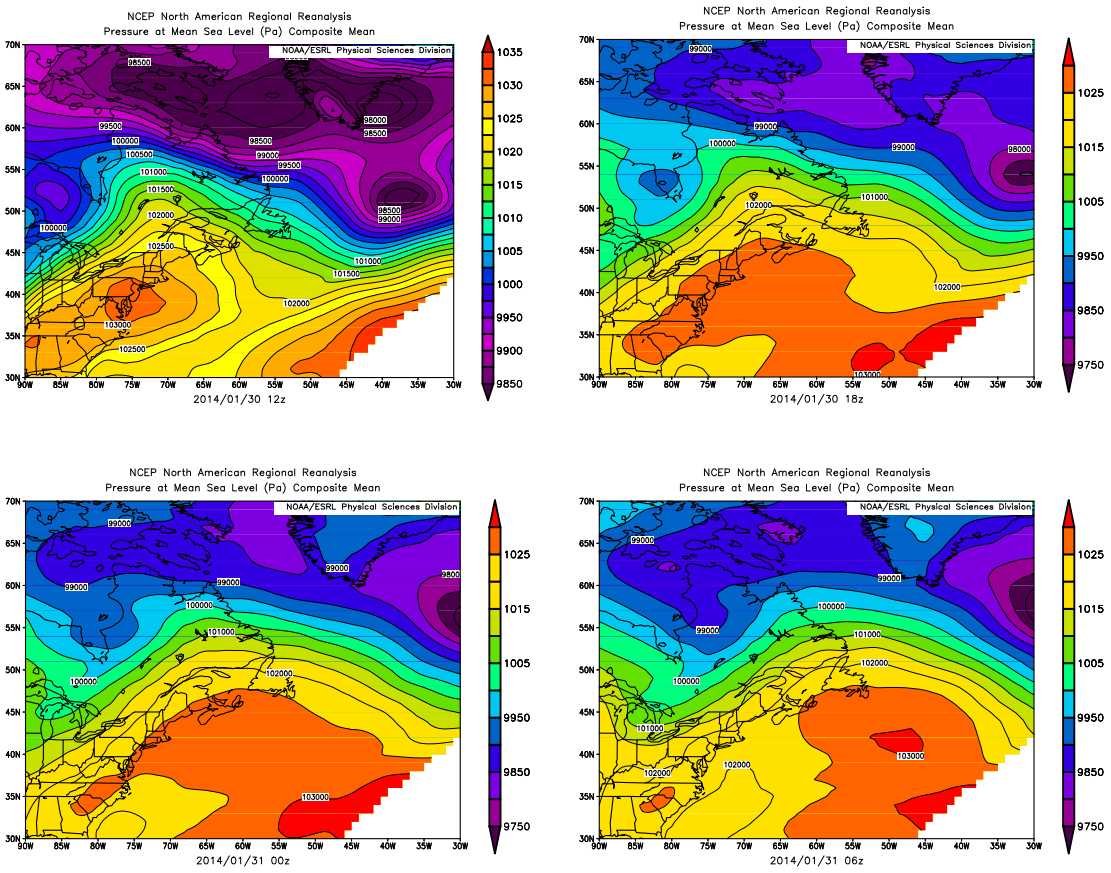

Figure 3.45: Mean Sea Level Pressure (Pa) plots every 6 hours from January 30, 2014 at 1800 UT to January 31, 2014 at 0600 UT. Taken from North American Regional Reanalysis (NARR) dataset.

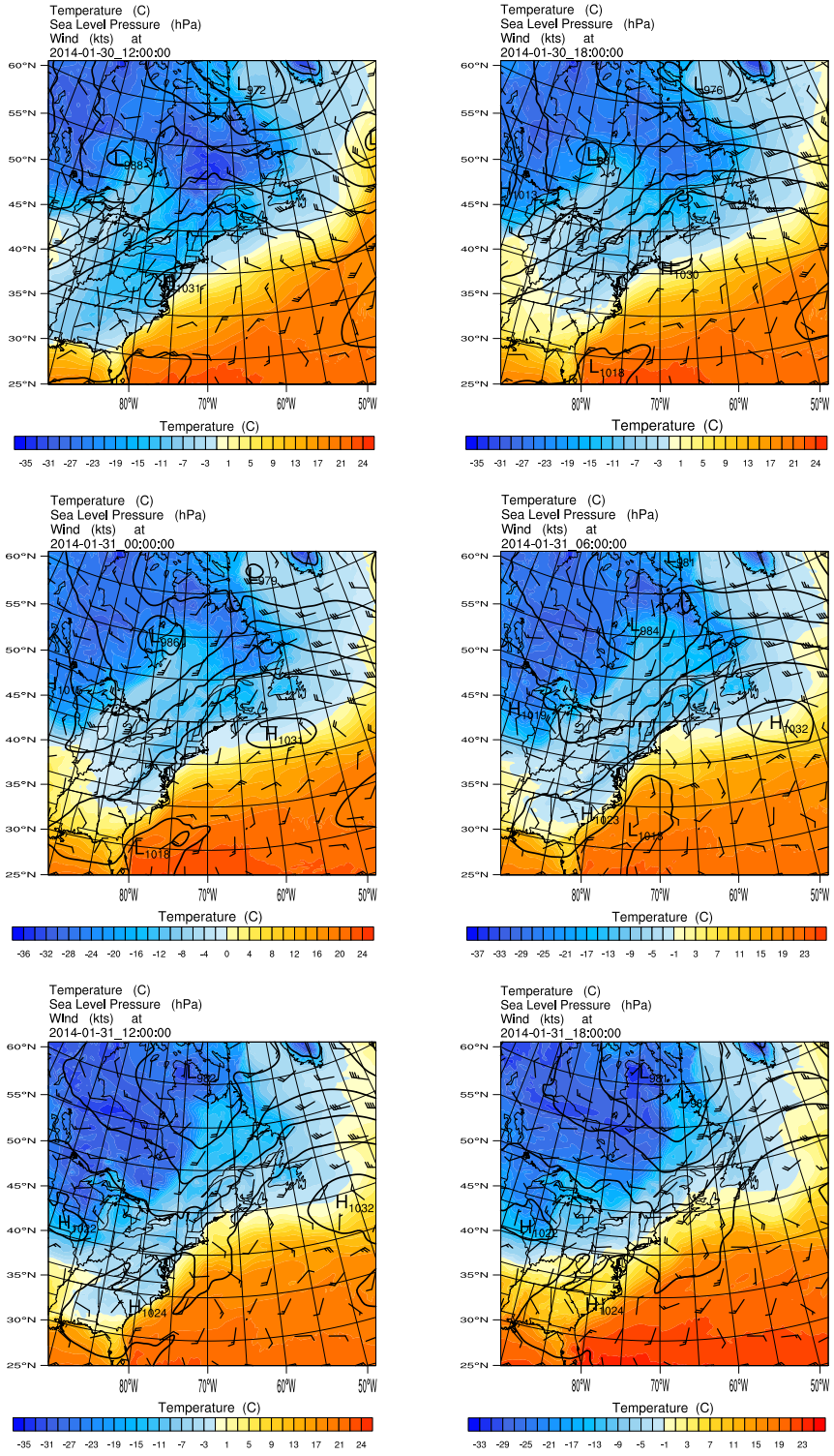

Figure 3.46: Sea level pressure contours (hPa), temperature (°K) and wind-barbs (kts), every 6 hours from January 30, 2014 at 1200 UT to January 31, 2014 at 1800. From WRF simulations using ECMWF ERA Interim data (ERA1.5/2014).

Figure 3.46 shows the surface (1000 hPa) synoptic flow from January 30, 2014 at 1200 UT to January 31, 2014 at 1800 UT, from WRF simulations using ECMWF ERA Interim data (ERA1.5/2014). The main features agree well with the NARR data in figure 3.45. The flow near the Appalachians is parallel to the mountain range and relatively weak. There is a ridge over Newfoundland and Labrador and a strong surface flow between the Hudson Bay low and the East Coast high, that becomes perpendicular to the coastal range of Labrador just before the gravity wave peak event.

The 50 hPa temperature perturbation field in figure 3.47 shows a topographic gravity wave packet has developed along the Labrador Coast on January 31 at 0000 UT, just 6 hours before the hotspot gravity wave peak measured by AIRS. This topographic gravity wave event persists until January 31 at 1200 UT and is also evident in the 5 hPa perturbation temperature field (figure 3.48).

After that time, the northeastward surface flow that was producing the gravity wave is pushed southeastward by the movement of the Hudson Bay low and the East Coast high. However, figure 3.48 shows that strong gravity wave activity persists in the hotspot region at 5 hPa (January 31 at 1800 UT to February 01 at 0600 UT), even after the gravity wave surface forcing has stopped. This is consistent with AIRS measurements which indicate strong gravity wave activity in the 20 to 65 km altitude range during that period. This behaviour is expected owing to the finite vertical group speed, e.g., a packet traveling at $c_g \approx 0.4$ m/s takes about 12 hours to travel 17 km in the vertical. Figure 3.47 also shows the development of a wavepacket with phase lines parallel to the US Coast during the period of Jan 30 at 1800 UT to Jan 31 at 0600 UT, but this packet does not appear at higher altitudes (figure 3.48), nor

does it enter the hotspot region.

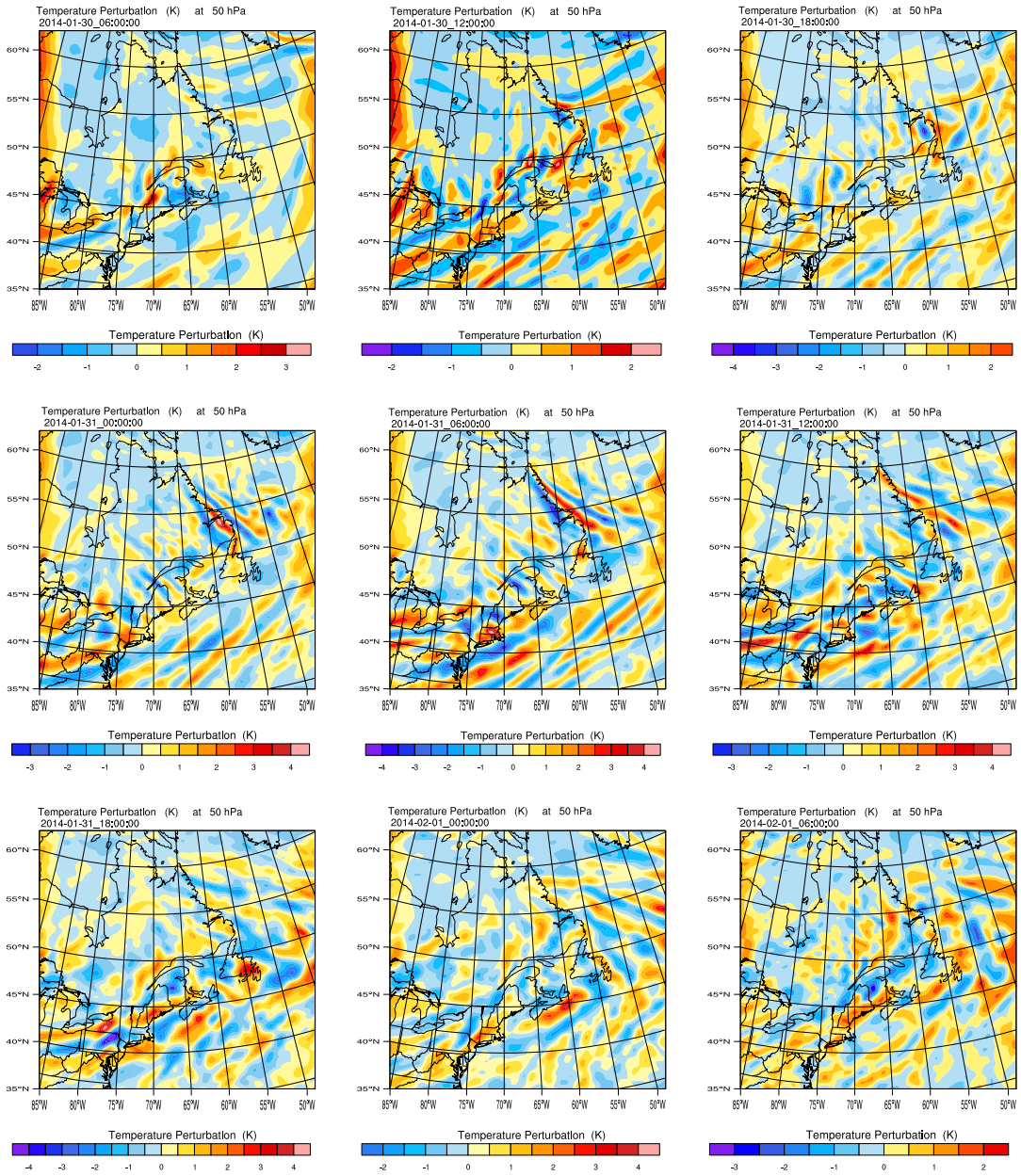

Figure 3.47: Temperature perturbation (°K) at 50 hPa, every 6 hours from January 30, 2014 at 0600 UT to February 01, 2014 at 0600 UT, using 20 grid point average. From WRF simulations using ECMWF ERA Interim data (ERA1.5/2014).

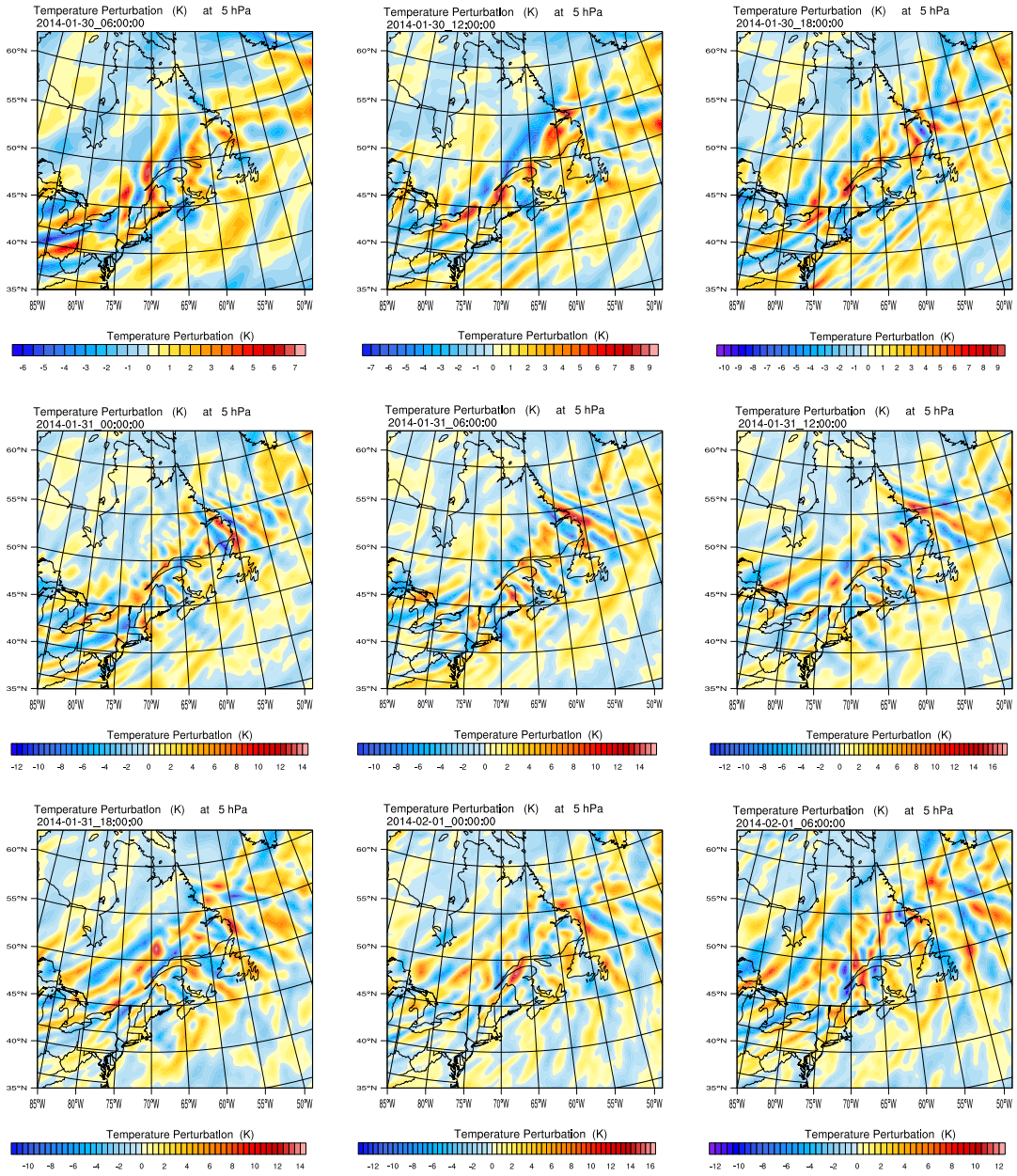

Figure 3.48: Temperature perturbation (°K) at 5 hPa, every 6 hours from January 30, 2014 at 0600 UT to February 01, 2014 at 0600 UT, using 20 grid point average. From WRF simulations using ECMWF ERA Interim data (ERA1.5/2014)

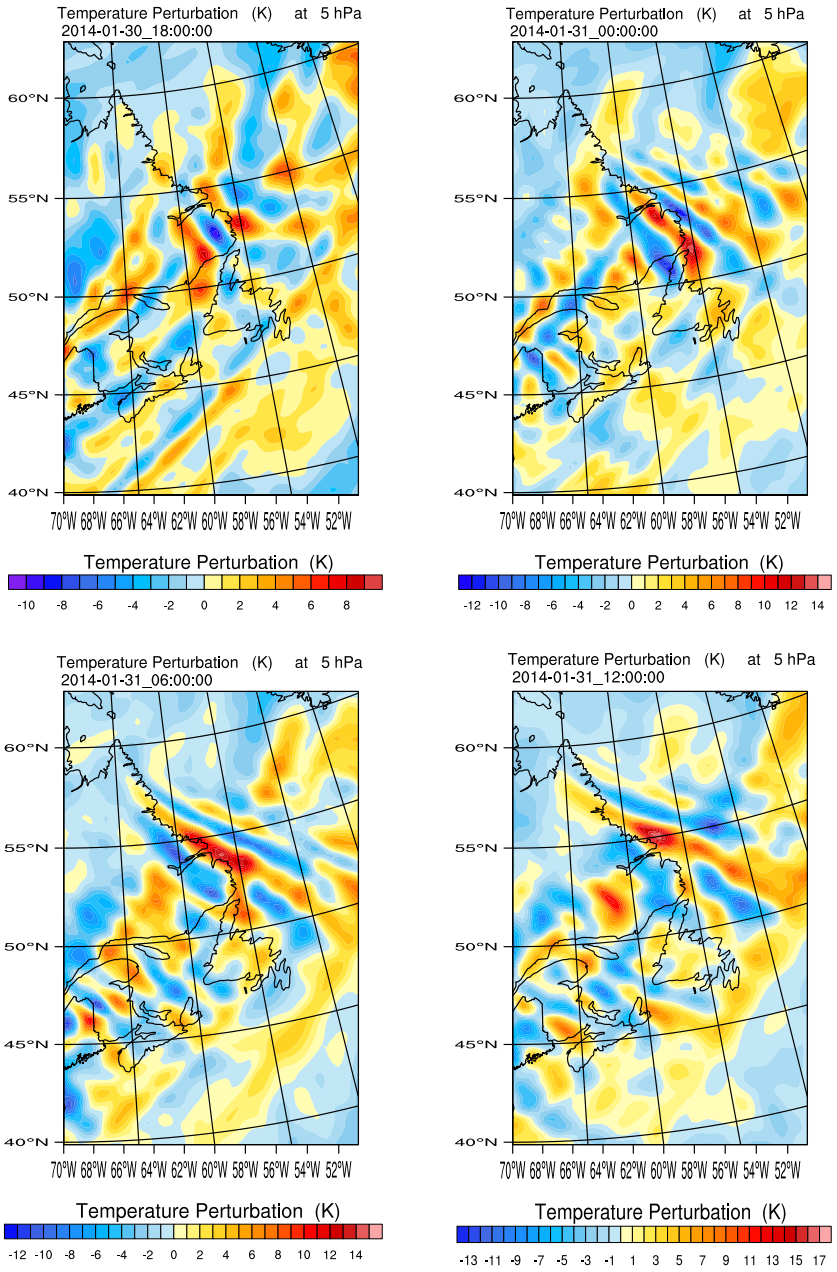

Figure 3.49: Temperature perturbation (°K) at 5 hPa, every 3 hours from January 30, 2014 at 1800 UT to January 31, 2014 at 1200 UT, using 20 grid point average. Plots are zoomed into a smaller area close to Newfoundland. From WRF simulations using ECMWF ERA Interim data (ERA1.5/2014).

We can see greater detail in the evolution of the wavepackets in the 5 hPa (32 km) perturbation temperature maps (figure 3.49). A wavepacket is forming on January 31 at 0000 UT over the Labrador Coast, and the topographic forcing remains active for about 24 hours before the surface flow changes. This clearly demonstrates that there are topographic waves entering the Newfoundland/Labrador hotspot during the period in which AIRS registers a peak in gravity wave activity.

3.6.2 Numerical Simulations Without Topography and Convection

Figure 3.50 shows the temperature perturbation at 50 hPa, every 6 hours from January 30, 2014 at 1800 UT to January 31, 2014 at 1200 UT. Simulations with convective parameterization and full topography (ERA1.5/2014) are shown in the first row (repeating part of figure 3.47). These plots show topographic gravity waves along the Labrador Coast and another wavepacket parallel to the US and Maritime provinces. The middle row of figure 3.50 has removed the convective parameterization (ERA1.5 Dry/2014). Since the Labrador Coast wave patterns in this case are similar to the case with convective parameterization, we conclude that convective processes are not responsible for the generation of these waves. However, the removal of convective parameterization has significantly weakened the wavepacket parallel to the US/Maritime Coast, so we can conclude that convective activity is the forcing mechanism for these waves. This band corresponds to a strong precipitating squall line as shown in figure 3.51. As noted earlier, this wavepacket does not penetrate into the upper stratosphere.

The bottom row (ERA1.5 Flat/2014) has removed topography from the area

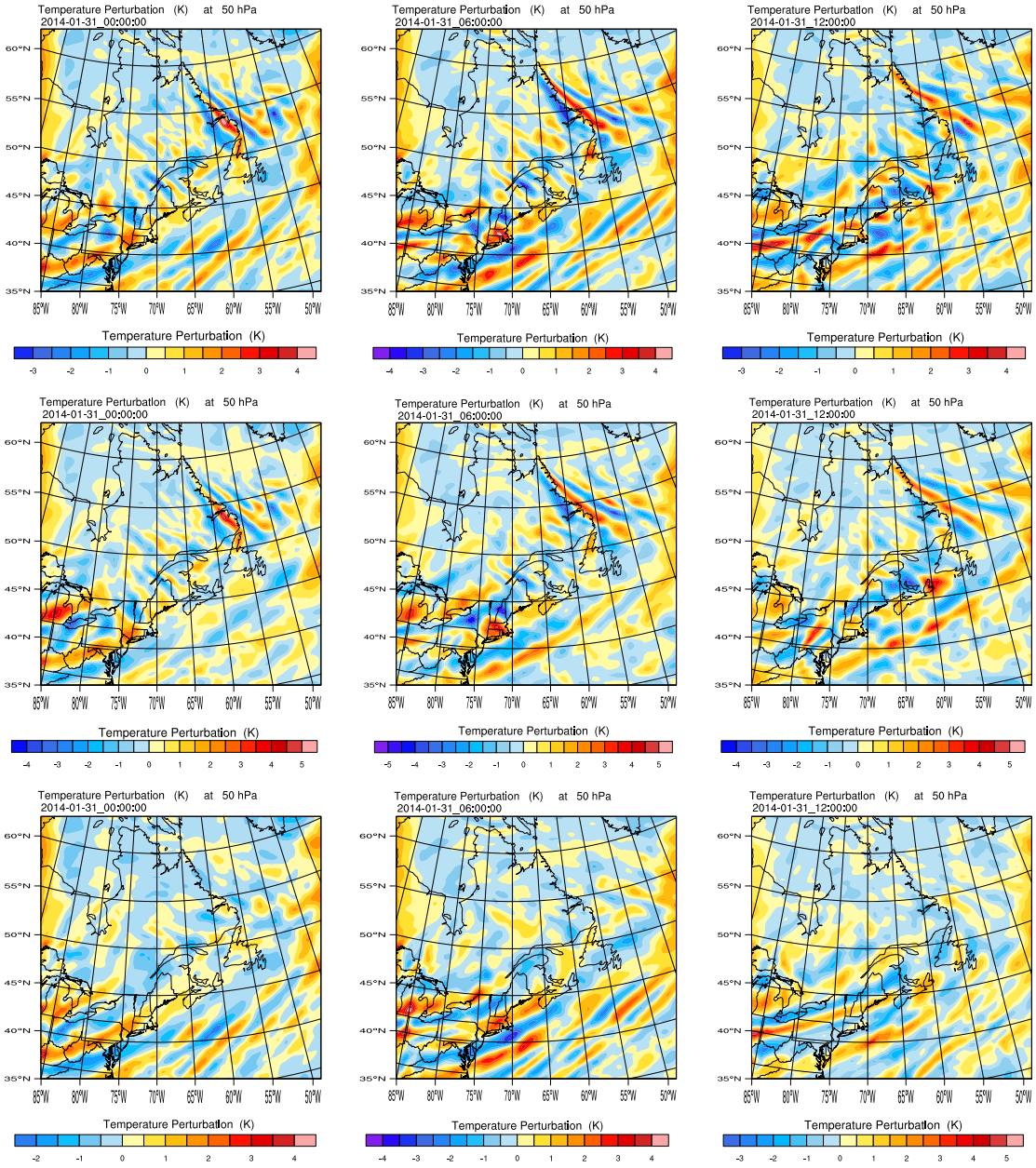

Figure 3.50: Temperature perturbation (°K) at 50 hPa ($z \approx 20$ km), every 6 hours from January 31, 2014 at 0000 UT to January 31, 2014 at 1200 UT, using 20 grid point average. Plots are zoomed into a smaller area close to Newfoundland. Top row: with convection and topography (ERA1.5/2014), second row: without convection (ERA1.5 Dry/2014), third row: topography has been removed from the area shown in figure 3.52 (ERA1.5 Flat/2014). From WRF simulations using ECMWF ERA Interim data.

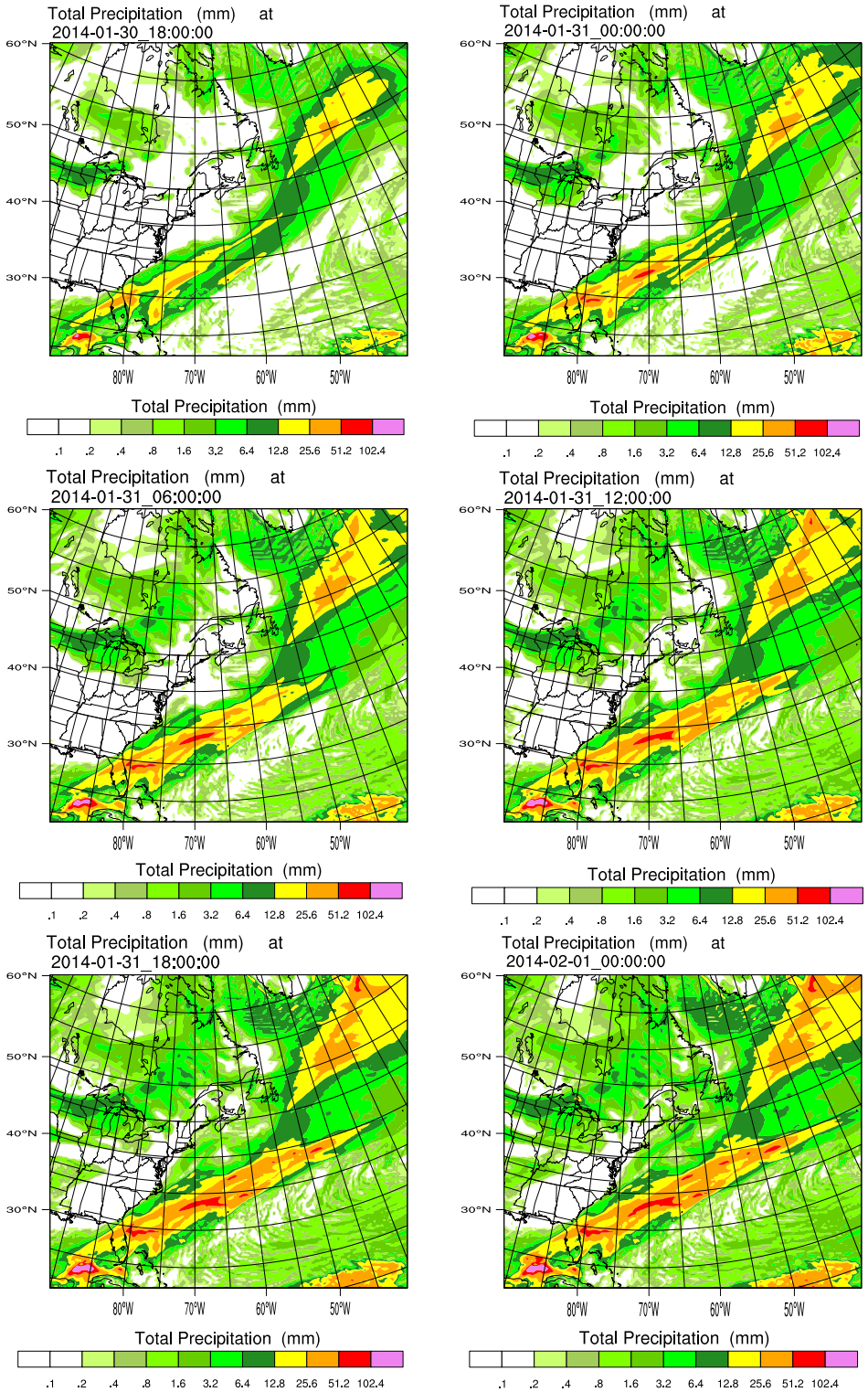

Figure 3.51: Total precipitation (mm) every 6 hours from January 30, 2014 at 1800 UT to February 01, 2014 at 0000 UT. From WRF simulations using ECMWF ERA Interim data (ERA1.5/2014).

shown in figure 3.52, including much of Eastern Canada and the U.S. In the case with no topography the wave packet off the coast of Labrador is not present. This shows that this wave packet has been generated by the local coastal topography in Labrador.

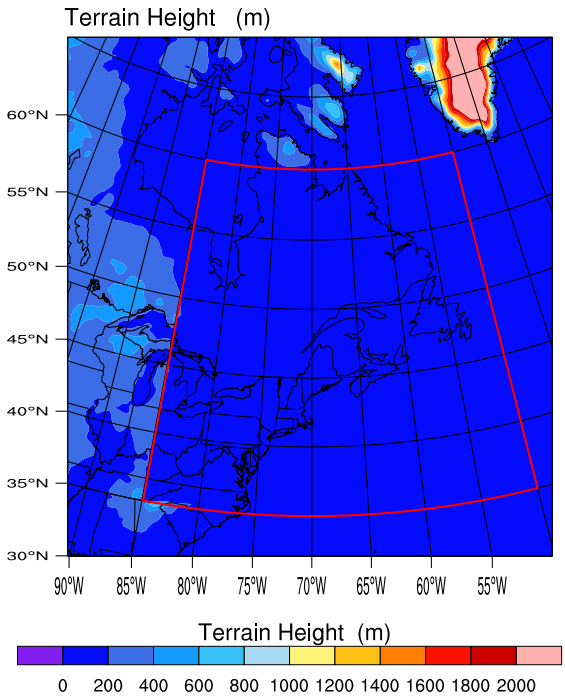

Figure 3.52: Area B, which the topography has been removed from the land. From WRF simulations using ECMWF ERA Interim data.

Figure 3.54 shows divergence field cross section along the line shown in figure 3.53. The top row of figure 3.54 has both convective parameterization and topography. We can see significant wave activity over the coast of Labrador (at 55° W), in the hotspot region during the gravity peak event. The peak divergence occurs in the middle frame on January 31 at 0600 UT, exactly the time AIRS records maximum temperature variance.

For the simulations of the second row in figure 3.54 the cumulus parameterization

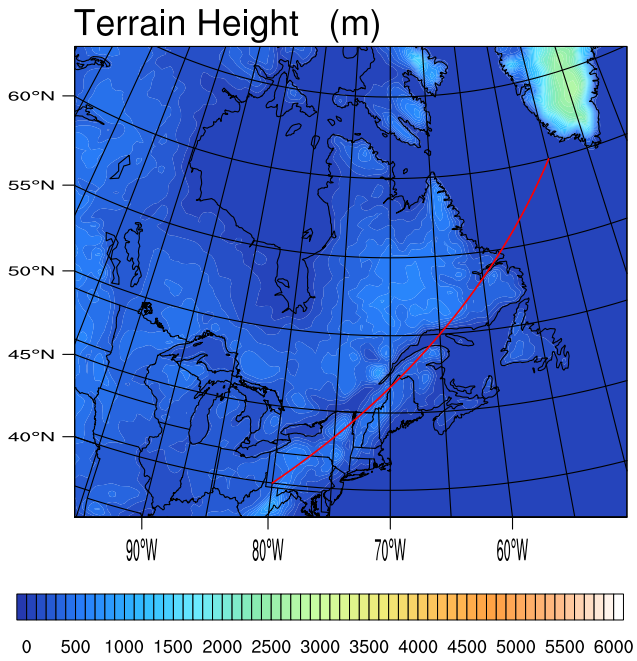

Figure 3.53: The red line on the figure indicates where the cross section on figure 3.54 is plotted. From WRF simulations using ECMWF ERA Interim data.

and condensation have been turned off (ERA1.5 Dry/2014). Since these simulations are identical to the simulation on the top row, we can conclude that moist processes are not involved in this particular formation of the gravity wave packet. The third row shows the results of the simulations without topography(ERA1.5 Flat/2014). In this case the wave packet has been almost entirely eliminated. This proves that the wave packet has been generated by the coastal topography over the Labrador Coast.

Since that flow remains perpendicular to the coastal range (including the Torngats), the topographic waves have zero ground-based phase speeds. From the top row of figure 3.54 we calculate wave parameters for January 31, at 0000 UT. The horizontal wavelengths, λ_h (along the cross-section), are between 250 and 350 km, while vertical wavelength, λ_z, is 5.7 km. All of the waves have horizontal wavelengths λ_h much larger than their vertical wavelengths λ_z, so we may use the rotating hy-

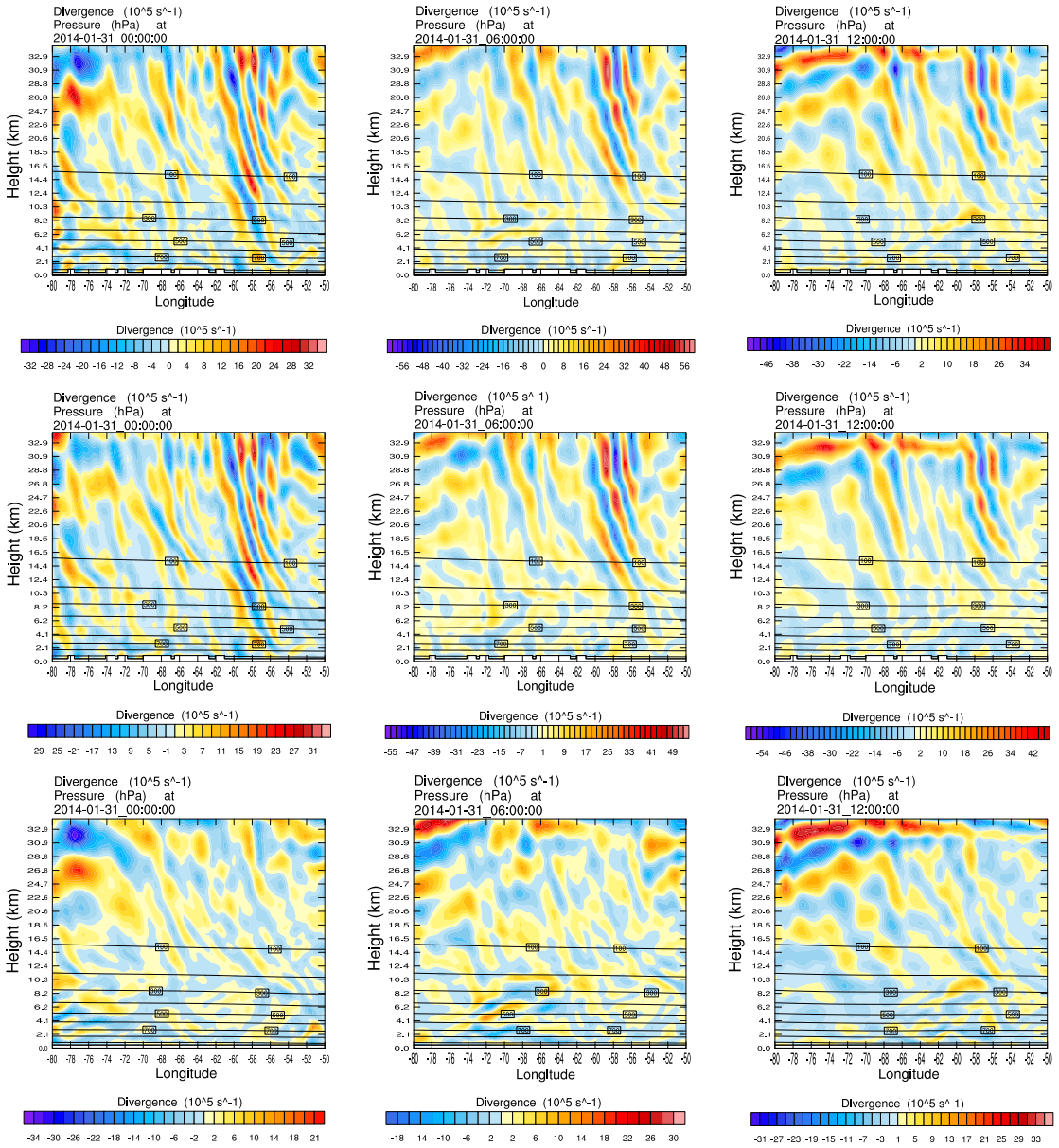

Figure 3.54: Divergence (10^{-5} s^{-1}) cross section along the red line shown in figure 3.53, every 6 hours from January 31, 2014 at 0000 UT to January 31, 2014 at 1200 UT. Top row: with convection and topography (ERA1.5/2014), second row: without convection (ERA1.5 Dry/2014), third row: topography has been removed from the area shown in figure 3.52 (ERA1.5/2014). The vertical extent of the profiles have been limited to just below the sponge layer. From WRF simulations using ECMWF ERA Interim data.

drostatic dispersion relation (1.15), with $f(55^\circ \text{ N})=1.2 \times 10^{-4}$ s^{-1} and $N \approx 0.02$ s^{-1} in the lower stratosphere. The intrinsic frequency is 4.7×10^{-4} s^{-1} (short λ_h) to 3.5×10^{-4} s^{-1} (long λ_h) and the intrinsic horizontal phase speed, $\hat{c_h}$, is ≈ -19 m/s for both cases.

3.7 The Residual of the Nonlinear Balance Equation

Hydrostatic and geostrophic balance are two states that are commonly found to varying degrees of approximation in atmospheric flows. Synoptic scale motions, for which the horizontal scales greatly exceed the vertical scales, are very close to a hydrostatic state, in which the vertical pressure gradients balance the gravitational force. In this case, vertical motion and accelerations are much smaller than their horizontal counterparts. Low frequency gravity waves are also nearly in a state of hydrostatic balance.

Geostrophic balance is a state in which horizontal Coriolis forces balance horizontal pressure gradients. This form of balance holds only approximately at large horizontal scales in our atmosphere, i.e., at least a 10% departure from geostrophic balance almost always exists even in extratropical latitudes. Since their horizontal wavelengths are much larger than their vertical wavelengths, smaller scale gravity wave motions depart substantially from geostrophic balance. The geostrophic wind is defined by:

$$\boldsymbol{V}_g = \frac{1}{f}\hat{z} \times \nabla\Phi \qquad or \qquad u_g = -\frac{1}{f}\frac{\partial \Phi}{\partial y} \qquad v_g = \frac{1}{f}\frac{\partial \Phi}{\partial x} \tag{3.1}$$

where Φ is the geopotential, $f = 2\Omega \sin\phi$ is the Coriolis parameter and $\hat{z}$ is a unit vector orthogonal to the nearly horizontal isobaric surface. If the variation of f with latitude ϕ is neglected, i.e., $f = f_0 =$ constant, then $\boldsymbol{V}_g$ is exactly nondivergent. In the β-plane approximation we take $f = f_0 + \beta y$, where y is the meridional coordinate and $\beta = df/dy = \frac{2\Omega}{a}\cos\phi$ (a is the radius of the Earth and $y = 0$ at ϕ_0). In this approximation we have:

$$\nabla \cdot \boldsymbol{V}_g = -\frac{\beta v_g}{f} \tag{3.2}$$

which is still small compared to f, since the Earth radius, a, is large (6370 km). The total wind may be divided into geostrophic ($\boldsymbol{V}_g$) and ageostrophic ($\boldsymbol{V}_a$) components. In the quasigeostrophic approximation where $\beta = 0$ in equation 3.2, the ageostrophic wind $\boldsymbol{V}_a$ carries all of the horizontal divergence, i.e., $\nabla \cdot \boldsymbol{V} = \nabla \cdot \boldsymbol{V}_a$. Therefore, the isobaric continuity equation:

$$\nabla \cdot \boldsymbol{V} + \frac{\partial \omega}{\partial p} = 0 \tag{3.3}$$

reduces to:

$$\nabla \cdot \boldsymbol{V}_a + \nabla \cdot \boldsymbol{V}_g + \frac{\partial \omega}{\partial p} = \nabla \cdot \boldsymbol{V}_a - \frac{\beta v_g}{f} + \frac{\partial \omega}{\partial p} \approx \nabla \cdot \boldsymbol{V}_a + \frac{\partial \omega}{\partial p} = 0 \tag{3.4}$$

where $\omega = \frac{dp}{dt}$ is the vertical wind in isobaric coordinates. Equation 3.4 is a diagnostic relationship that shows the ageostrophic horizontal wind is directly associated with vertical motion. Together, $\boldsymbol{V}_a$ and ω form the ageostrophic circulation.

Thermal wind balance is given by differentiating equation 3.1 with respect to pressure:

$$\frac{\partial \boldsymbol{V}_g}{\partial p} = \frac{1}{f_0}\hat{z} \times \nabla(\frac{\partial \Phi}{\partial p}) \tag{3.5}$$

The vertical derivative of geopotential Φ is related to temperature, T, through hydrostatic balance:

$$\frac{\partial \Phi}{\partial p} = -\frac{RT}{p} \tag{3.6}$$

where R is the ideal gas constant. While geostrophic advection of vorticity and temperature tends to destroy geostrophic, hydrostatic and thermal wind balance, the ageostrophic circulation created by that imbalance tends to restore all these types of balance (Holton, 2004). This process is known as geostrophic adjustment.

The details of this process are not fully understood and have been debated for decades. Internal gravity waves are oscillations and are therefore not in a balanced steady state. They also possess horizontal divergence. It is well known that vertical motions provide a generating force for internal gravity waves. Thus the vertical motion and horizontal divergence associated with the ageostrophic circulation lead to the generation of gravity waves that transport excess momentum away from regions of imbalance, thereby tending to reduce the degree of imbalance.

Charney (1955) proposed a nonlinear balance state based on equation for horizontal divergence: $D = \nabla_H \cdot \boldsymbol{V} = \frac{\partial u}{\partial x} + \frac{\partial v}{\partial y}$. In isobaric coordinates, with some approximations to the divergence term, the divergence equation can be written as:

$$\frac{\partial D}{\partial t} + \boldsymbol{V} \cdot \nabla D + \omega \frac{\partial D}{\partial p} = \underbrace{-D^2}_{\text{A}} \underbrace{- \frac{\partial \boldsymbol{V}}{\partial p} \cdot \nabla \omega}_{\text{B}} \underbrace{+ 2J(u,v)}_{\text{C}} \underbrace{- \beta u}_{\text{D}} \underbrace{+ f\zeta}_{\text{E}} \underbrace{- \nabla^2 \Phi}_{\text{F}} \tag{3.7}$$

The terms on the LHS of equation 3.7, represents the material derivative of horizontal divergence D. Term A represents nonlinear divergence effect, while B represents advection of ω by vertical shear of the horizontal wind, $\frac{\partial \boldsymbol{V}}{\partial p}$, which is related to the

thermal wind in equation 3.5. The Jacobian term C:

$$J_{xy}(u,v) = \begin{vmatrix} \frac{\partial u}{\partial x} & \frac{\partial v}{\partial x} \\ \frac{\partial u}{\partial y} & \frac{\partial v}{\partial y} \end{vmatrix} = \frac{\partial u}{\partial x}\frac{\partial v}{\partial y} - \frac{\partial v}{\partial x}\frac{\partial u}{\partial y}$$

is large in regions of strong horizontal wind shear (e.g., jet streaks). Term D represents the β effect, and is often smaller than most of the terms in equation 3.7. Term F is equivalent to $f\zeta_g$, where ζ_g is the quasigeostrophic vorticity, so E+F together represent the effect of the departure of relative vorticity from its quasigeostrophic counterpart.

Charney (1995, 1962) proposed that for synoptic scale motions, the terms in equation 3.7 involving divergence D and vertical velocity ω should be small. By neglecting those terms, he arrived at the equation for nonlinear balance (NBE):

$$2J(u,v) - \beta u + f\zeta - \nabla^2\Phi = 0 \tag{3.8}$$

Since large scale divergence is small, equation 3.8, represents a potential steady state that is presumed to accurately describe the large-scale flow at any given moment. It also reduces to geostrophic balance when the nonlinear Jacobian terms and the β effect are neglected. The quantity:

$$\Delta NBE = 2J(u,v) - \beta u + f\zeta - \nabla^2\Phi \tag{3.9}$$

has been used widely to identify regions in NWP model output where the divergence tendency is large and the generation of divergent internal gravity waves would be expected (e.g. Charney 1955; Hoskins et al. 1985; Davis and Emanuel 1991; McIntyre

and Norton 2000; Zhang et al. 2000 and Zhang, 2004).

Unfortunately there is at present no well-established theory for linking the divergence forcing term ΔNBE to the generation of gravity waves with specific amplitudes wavelengths and frequencies. This is in part because ΔNBE also plays a role in adjusting the large scale divergence field. Some researchers have argued that more accurate balance conditions may be more appropriate than (3.9) (McIntyre, 2015). Such considerations, e.g., the hyperbalance theory of Mohebalhojeh and McIntyre, are beyond the scope of this dissertation.

Figure 3.55 shows contours of ΔNBE at 250 hPa level for the 2003 case at 3 hour intervals from Jan 19, 2003 at 1800 UT to Jan 20, 2003 at 0900 UT. The 250 hPa level ($\sim$ 9.2 km) is used to track the jet stream in the upper troposphere and lower stratosphere, and is expected to be in the source region for gravity waves. It therefore represents a useful level to examine the ΔNBE field for possible regions of imbalance that may lead to spontaneous gravity wave emission. Zhang (2004) has employed a similar approach to correlate ΔNBE with gravity wave emission by an idealized baroclinic jet-front system. Figure 3.55 shows large values of ΔNBE are found along the jet stream off the East Coast of North America. Over the period Jan 19 at 1800 UT to 2100 UT the ΔNBE values remain moderate (less than 0.4×10^{-7} s^{-2}) over a broad region.

One might ask what values of ΔNBE are needed to produce gravity wave emission. Zhang (2004) found values of ΔNBE of 1.8×10^{-9} s^{-2} to 3.8×10^{-9} s^{-2} corresponded to gravity wave emission in an idealized baroclinic jet-front system. Zhang et al., (2001) found much larger maximum values of ΔNBE of $3 - 4 \times 10^{-8}$ s^{-2} were associated with a mesoscale gravity wave event over the East Coast of the US.

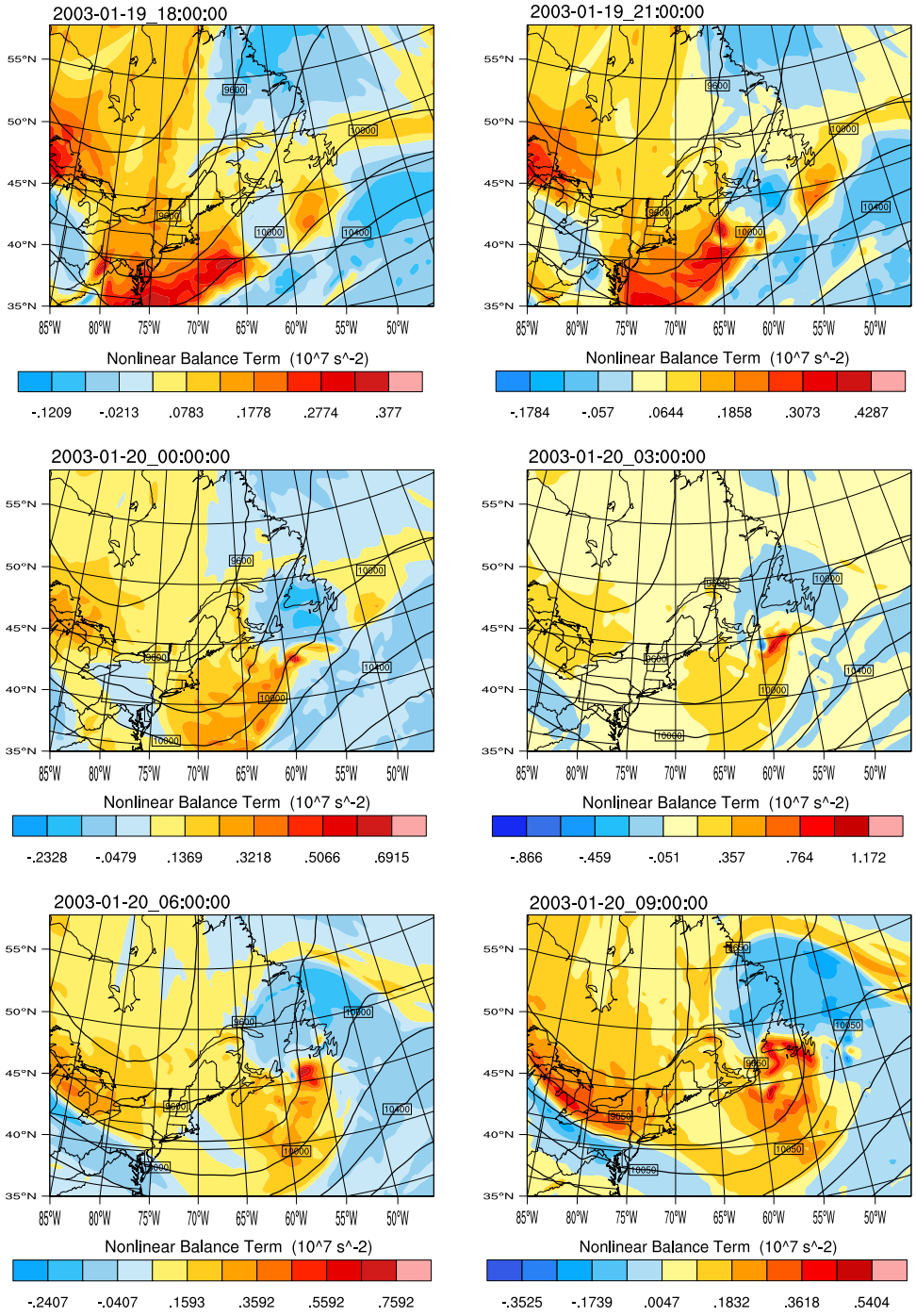

Figure 3.55: The residual of the nonlinear balance equation (ΔNBE, 10^{-7} s^{-2}) and geopotential height contours (m) at 250 hPa, every three hours from January 19, 2003 at 1800 UT to January 20, 2003 at 0900 UT. From WRF simulations using ECMWF ERA Interim data.

In our 2003 case on January 19 at 1800 UT (the first frame in figure 3.55) the strongest values of ΔNBE are around 0.38×10^{-7} s^{-2} and are found just southeast of Cape Cod, in the left exit region of the jet. This 250 hPa ΔNBE forcing lays just below the 80 hPa gravity wave packet shown in figure 3.7 (2003/FNL). This is 12 hours before AIRS detects the peak event, but it should be noted that this packet is well outside the hotspot region and at this time would not be expected to make a large contribution to AIRS measurements shown in figure 3.4.

By January 20 at 0000 UT, the maximum ΔNBE values have risen to a level exceeding 0.5×10^{-7} s^{-2} and have become focused in a small area at the left exit region of the jet (as indicated by the geopotential height contours). Three hours later, the ΔNBE values in the left exit region have climbed to their maximum value of 1.2×10^{-7} s^{-2}. This is just 3 hours before AIRS detects the gravity wave peak event in the stratospheric hotspot region. The ΔNBE maximum continues to track the left exit region of the jet at 0600 UT, with a maximum value near 0.7×10^{-7} s^{-2}. At 0900 UT, maximum ΔNBE values have dropped to around 0.5×10^{-7} s^{-2}.

Note that AIRS measurements are made only once daily at 0600 UT and that a wave packet requires a finite time to travel from the tropopause region into the middle stratosphere. We may therefore conclude that the timing of maximum divergence forcing by ΔNBE corresponds well with the AIRS peak event in the hotspot region.

Figure 3.56 shows the corresponding divergence field at 250 hPa over the same time period as in figure 3.55. On January 20 at 0000 UT and 0300 UT, we see the emerge of strong localized patches of divergence and convergence in precisely the same location as the ΔNBE maxima in figure 3.56. The divergence patches have no wavelike structure, but such structure is not to be expected in the forcing region. We

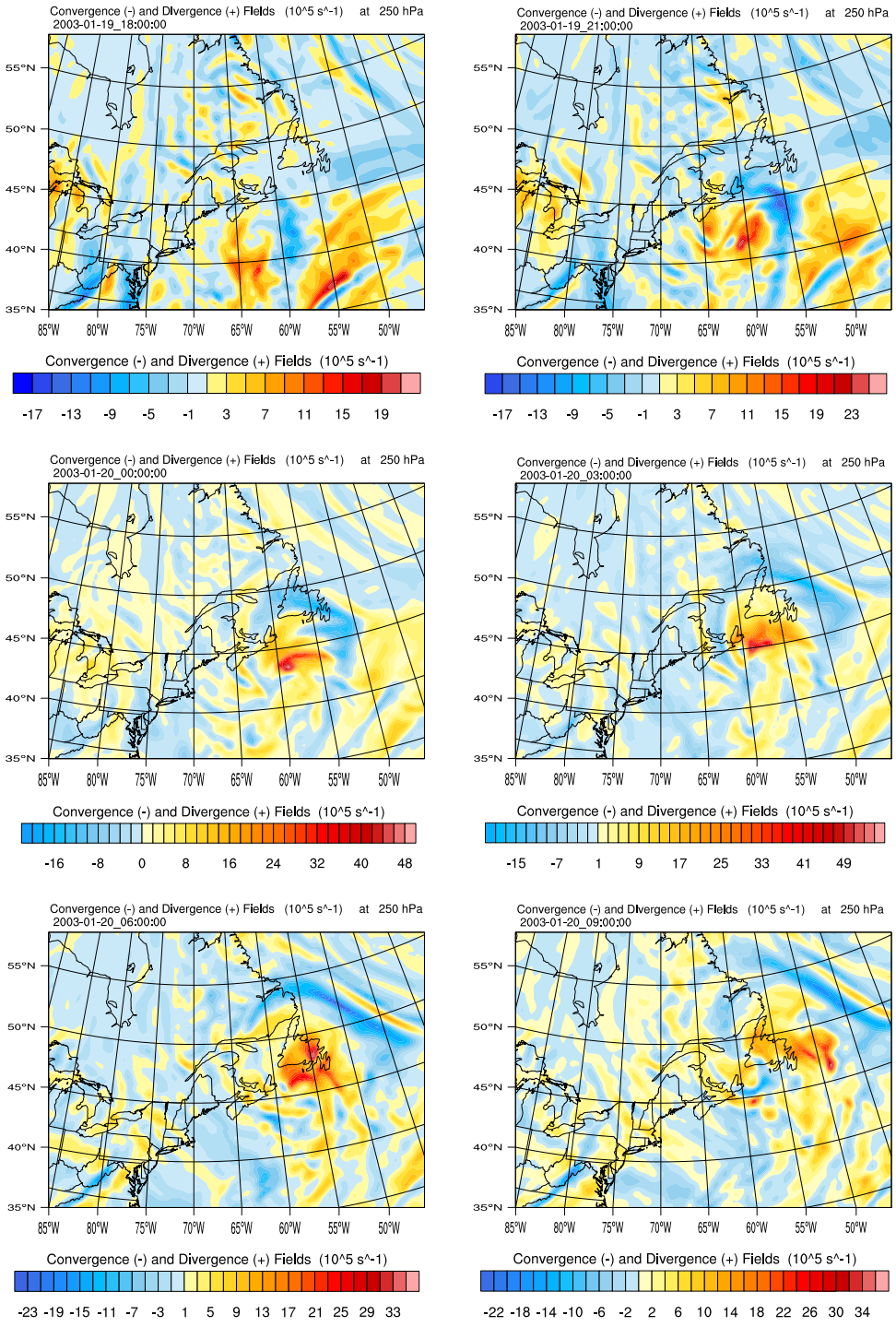

Figure 3.56: Divergence (10^{-5} s^{-1}) at 250 hPa every three hours from January 19, 2003 at 1800 UTC to January 20, 2003 at 0900 UTC. From WRF simulations using ECMWF ERA Interim data.

note that the gravity wave packet at 80 hPa on January 20 at 0600 UT (figure 3.11) lays almost directly above the corresponding 250 hPa divergence patch.

On January 20 at 0600 UT and 0900 UT figure 3.56 also shows a strong band of convergence (blue) to the north of Newfoundland. This band coincides with the warm front associated with the low moving up the East Coast. It does not appear to be associated with the generation of vertically propagating gravity waves.

We conclude that in this case the localized maxima of ΔNBE correspond well with both the location and timing for the gravity wave emission seen in our WRF simulation and the AIRS hotspot measurements.

Figure 3.57 shows the vertical structure of ΔNBE and potential temperature fields in the troposphere every 3 hours for the period of January 19 at 1800 UT to January 20 at 0900 UT, i.e. the sample times as in figures 3.55 and 3.56. The cross-section location is shown in figure 3.58. In order to better follow the jet stream and the tropospheric ΔNBE field, it was taken somewhat to the north and in a slightly different direction than the cross-section used to track gravity wave packets in the stratosphere (See figures 3.9, 3.10 and 3.18).

Over the period of January 19 at 2100 UT to January 20 at 0300 UT, we see very strong values of ΔNBE developing in conjunction with a stratospheric intrusion that is forming in the potential temperature contours. During this period the strongest $|\Delta\text{NBE}|$ values (2.5 to 5.5×10^{-7} s^{-2}) are found near the surface. This stratospheric intrusion and narrow region of imbalance are associated with a developing warm front.

During the period of January 20 at 0000 UT to 0600 UT, ΔNBE values of 1.5 to 2.5×10^{-7} s^{-2} are found in the troposphere region and this imbalance coincides with the localized patches seen in figure 3.55. We conclude that this imbalance provides a

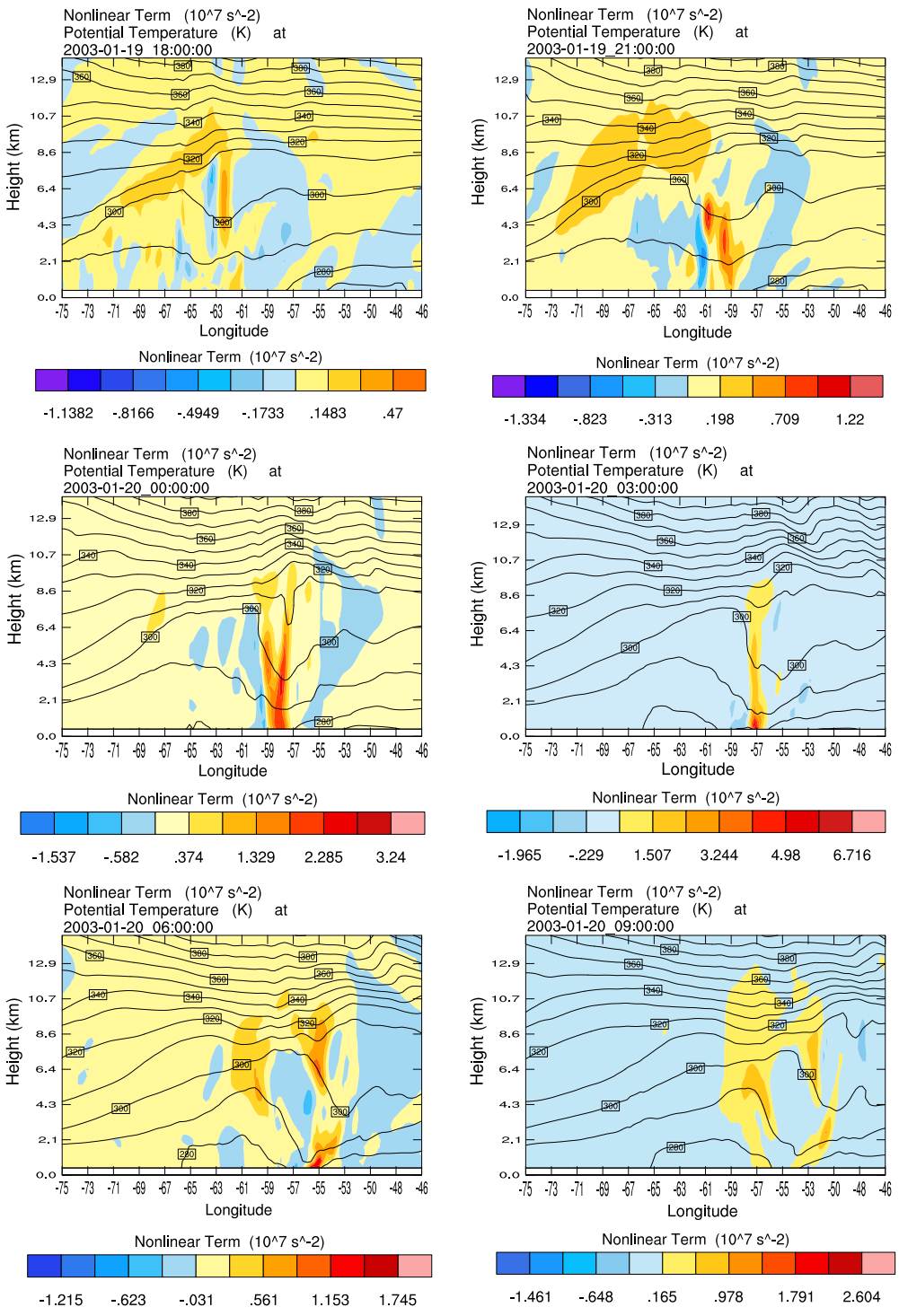

Figure 3.57: Vertical cross section of the residual of the nonlinear balance equation (ΔNBE, 10^{-7} s^{-2}) overlaid with potential temperature contours ($^\circ$ K), every three hours from January 19, 2003 at 1800 UTC to January 20, 2003 at 0900 UTC. From WRF simulations using ECMWF ERA Interim data.

reasonable explanation of the wavepacket seen at higher altitudes.

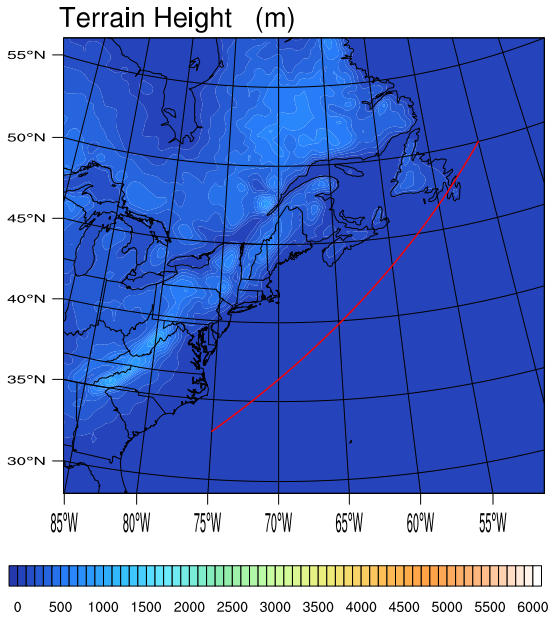

Figure 3.58: The red line on this figure indicates where the cross section on figure 3.57 is plotted.

Figure 3.59 for the 2008/ERA simulation shows only moderate values of ΔNBE (less than 0.45×10^{-7} s^{-2}) spread over a vast area with largest amplitudes on the left side of the jet. The jet is associated with an upper level trough over Eastern Canada, and a strong surface low off the coast (see figure 3.30). Over the time that AIRS finds temperature perturbations in the hotspot region, maximum ΔNBE values fall from 0.45×10^{-7} s^{-2} (December 23 at 0600 UT) to 0.25×10^{-7} s^{-2} (December 24 at 0600 UT).

The corresponding 250 hPa divergence maps in figure 3.60 show there is some response to the ΔNBE associated with the left side of the jet to the northeast of Newfoundland (figure 3.60 December 23 at 0600 UT and 1200 UT), but this response does not generate vertically propagating waves at higher levels, as can be seen from

figure 3.31 (50 hPa) and figure 3.34 (5 hPa).

Evidently the divergence in this region is primarily associated with the secondary circulation and perhaps some horizontally propagating waves (e.g. figure 3.60 Dec 23 at 0000 UT). As expected from the discussion in section 3.5, figure 3.60 shows topographic waves being generated over the Appalachians and being advected northeastward into the hotspot region, as well as topographic waves being generated over the coast of Labrador. None of these topographic wave packets is associated with forcing by the ΔNBE field.

Figure 3.61 shows the 2014 peak event has only moderate maximum values of ΔNBE (less than $\sim 0.43 \times 10^{-7}$ s^{-2}). For the period December 31 at 0000 UT to 1200 UT the strongest values are concentrated in a long band off the Eastern Coast of North America. As shown in figure 3.51 (section 3.6.2), ΔNBE strip corresponds to an intense precipitating squall line. The squall line is also reflected in the 250 hPa divergence field shown in figure 3.62. The long broad strip of divergence is associated with the decelerating updrafts near the tropopause.

We see some vertically propagating waves with phase lines oriented along the direction of the squall line. These correspond to the wave configuration one would expect to be emitted from a squall line. For the most part, these waves lie outside the AIRS hotspot region. Thus they likely make some contribution to the temperature perturbation detected by AIRS, but do not represent a major contribution.

In summary, while the diagnostic ΔNBE field indicates regions of imbalance, it does not distinguish between ageostrophic circulations and gravity wave source regions. The three cases considered here (2003, 2008 and 2014) all exhibit regions with similar values of ΔNBE, yet only the 2003 case shows gravity wave emission from the

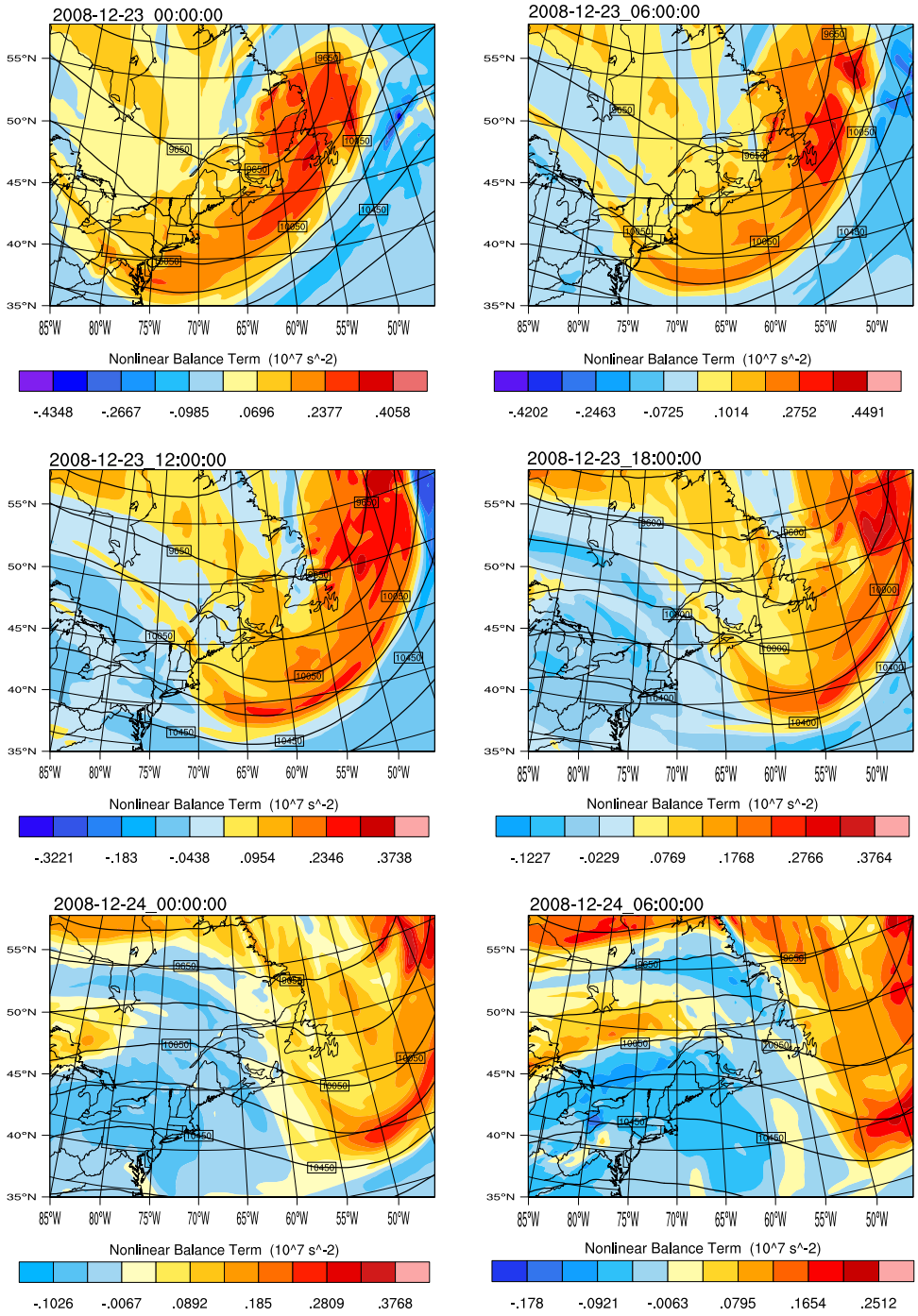

Figure 3.59: The residual of the nonlinear balance equation (ΔNBE, 10^{-7} s^{-2}) and geopotential height contours (m), every 6 hours from December 23, 2008 at 0000 UTC to December 24, 2008 at 0600 UTC. From WRF simulations using ECMWF ERA Interim data.

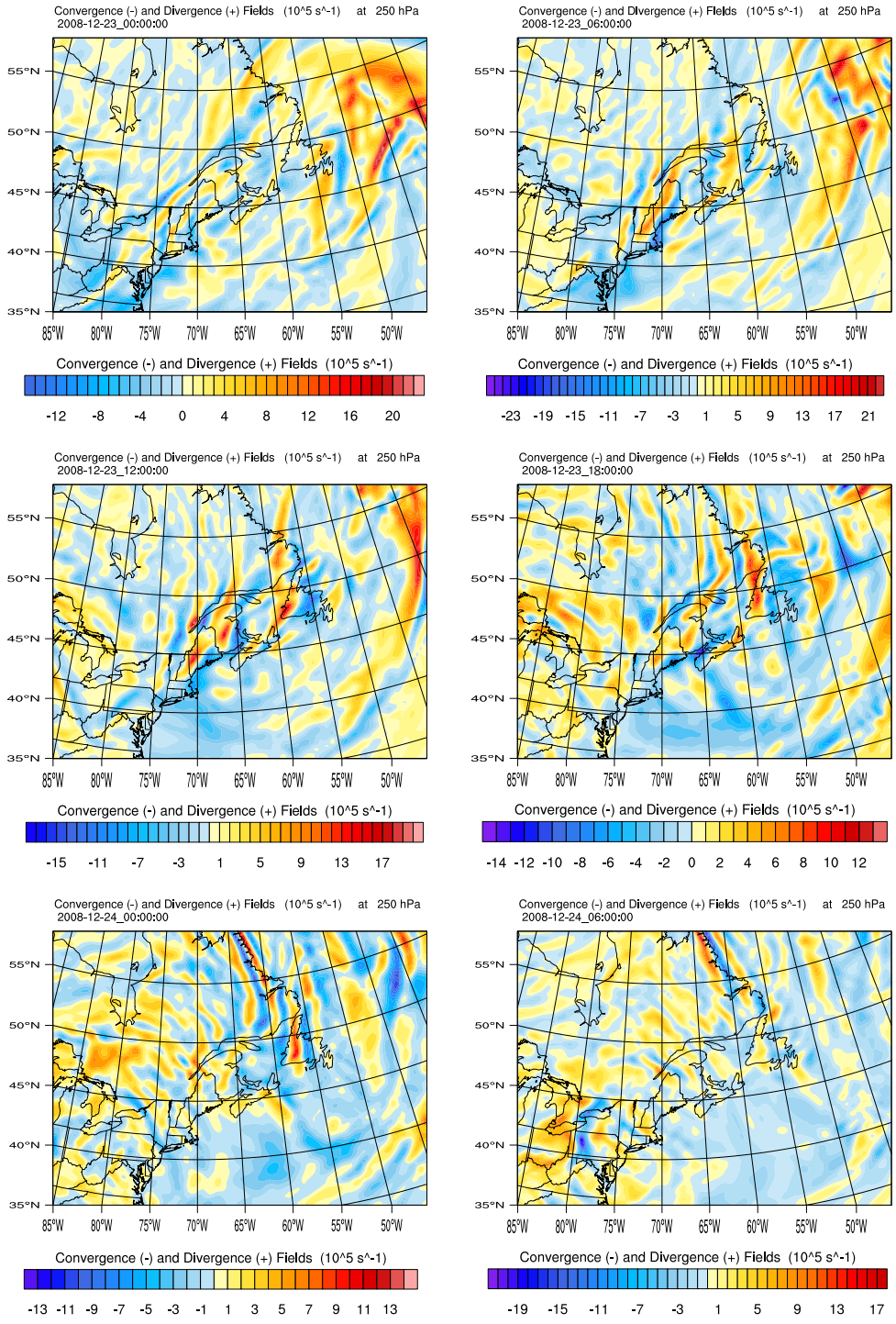

Figure 3.60: Divergence (10^{-5} s^{-1}) at 250 hPa every 6 hours from December 23, 2008 at 0000 UT to December 24, 2008 at 0600 UT. From WRF simulations using ECMWF ERA Interim data.

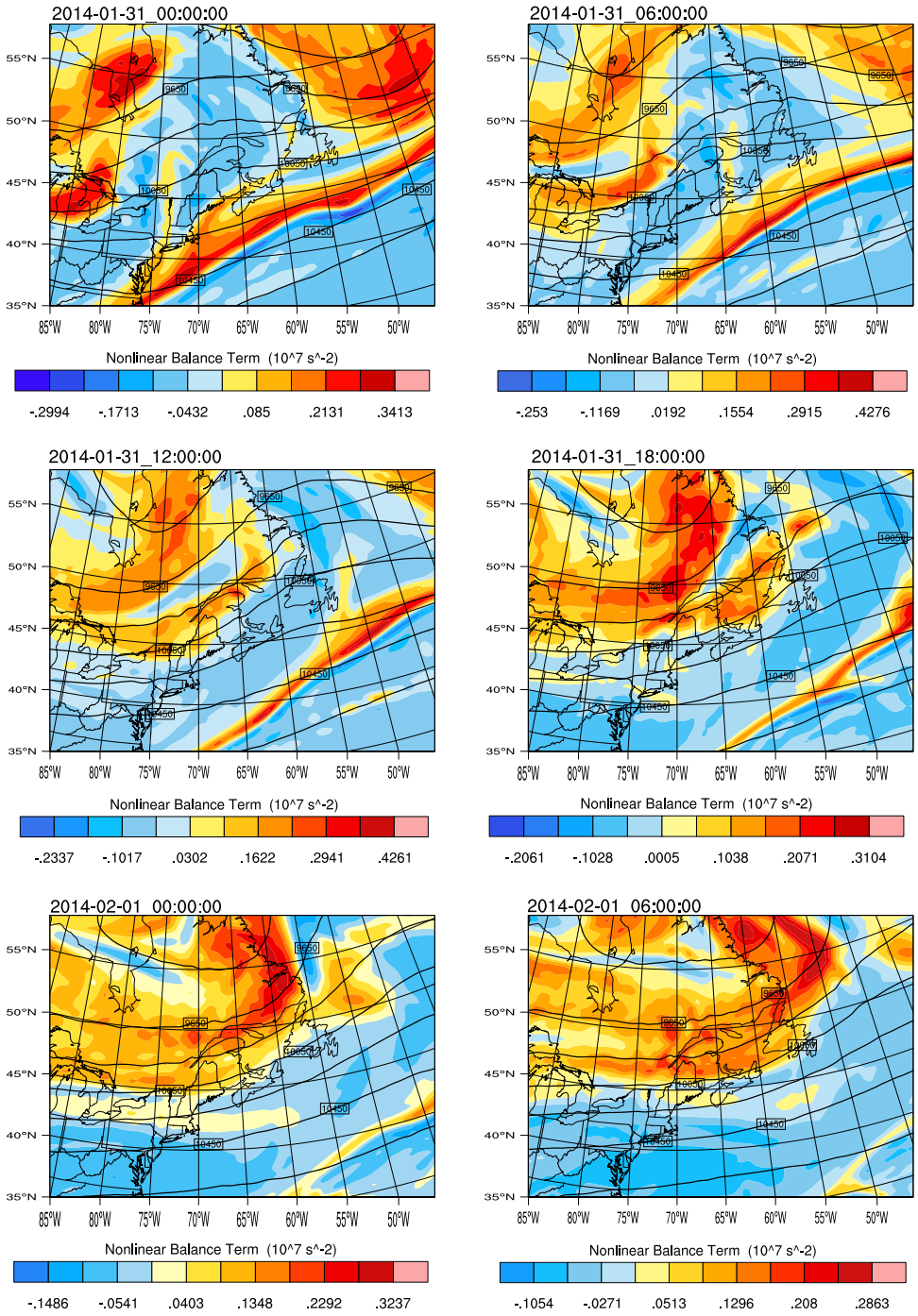

Figure 3.61: The residual of the nonlinear balance equation (ΔNBE, 10^{-7} s^{-2}) and geopotential height contours (m), every 6 hours from January 31, 2014 at 0000 UT to Feb 01, 2014 at 0600. From WRF simulations using ECMWF ERA Interim data.

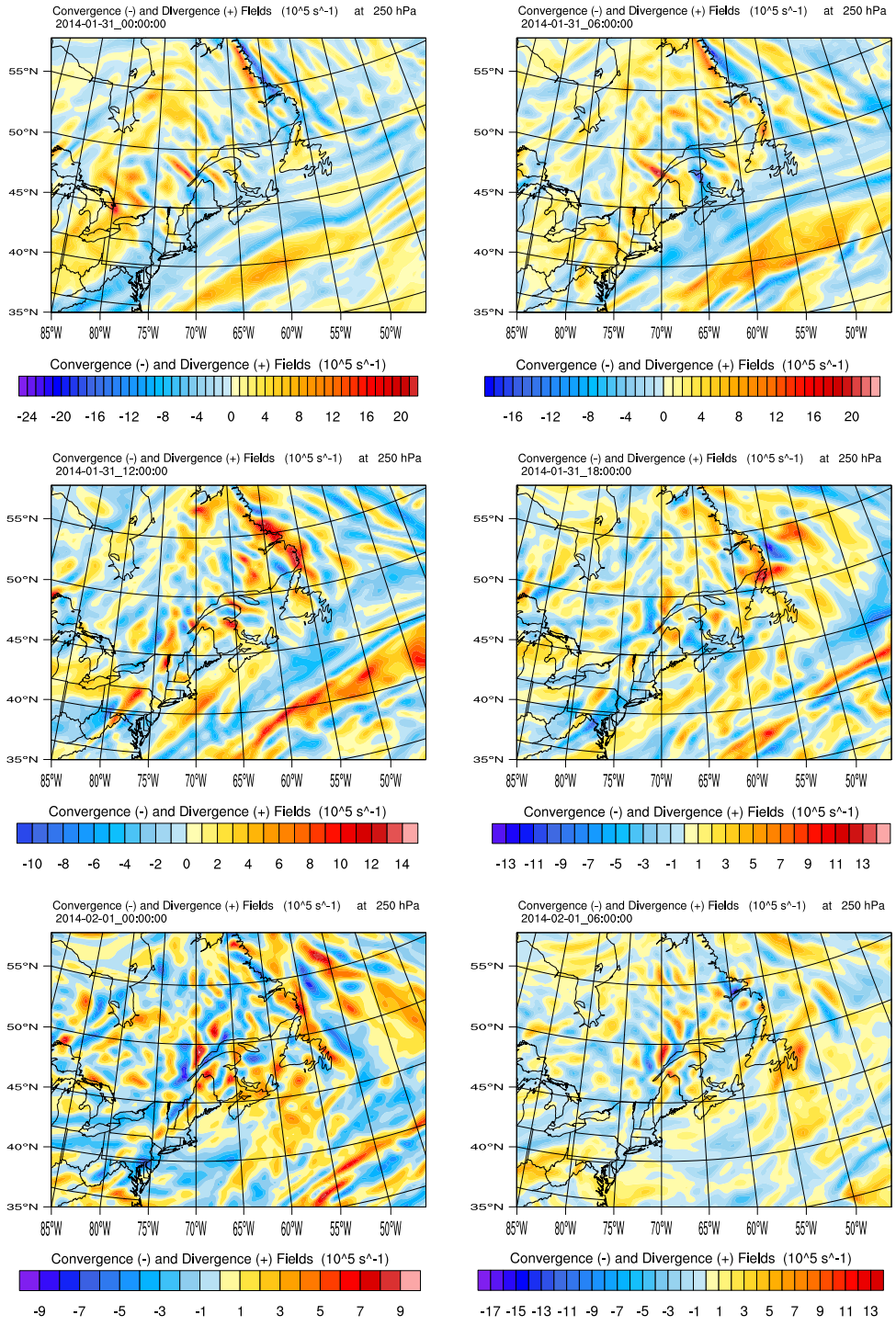

Figure 3.62: Divergence (10^{-5} s^{-1}) at 250 hPa, every 6 hours from January 31, 2014 at 0000 UT to Feb 01, 2014 at 0600. From WRF simulations using ECMWF ERA Interim data.

vicinity of the jet streak. In the 2003 case, the maximum ΔNBE values are roughly 2.5 times larger than in the other cases, and the 2003 maximum values are strongly localized to the left exit region of the jet streak. However it is not clear whether the 2003 case has exceeded some unknown amplitude threshold for gravity wave emission, or whether other aspects of the flow, e.g. the horizontal, vertical or temporal scales are playing a role. It is possible that the ΔNBE field in the 2008 and 2014 cases simply does not project onto propagating gravity wave modes.

Chapter 4

Summary and Conclusion

4.1 Discussion of Nonorographic Gravity Wave Drag Parameterization Schemes

The properties of two nonorographic GWD parameterizations, Hines Doppler-spread and Warner-McIntyre, were examined using a column model based on the gravity-wave drag parameterization code developed by S03 for nonhydrostatic waves. This column model was based on CIRA zonally-averaged middle atmosphere wind data for winter and summer hemispheres and used launch spectra similar to those employed in MS05's GCM study of gravity wave drag. We performed detailed calculations of the evolution of the momentum flux spectra vs. height and used them to examine critical level and nonlinear dissipation. A spectral decomposition of the drag with respect to phase speed plotted vs. altitude, reveals significant differences in the nonlinear dissipation employed by each scheme. The momentum flux spectra were transformed from phase speed to vertical wavenumber m in order to check the ability of the parameterizations to maintain a "universal" m^{-3} shape at large m.

The MS05 variant of Alexander and Dunkerton's (1999) GWD scheme was also briefly considered. This variation (referred to here as AD99) uses the same wave

dissipation threshold as WM, except wave obliteration is imposed instead of wave saturation.

First we demonstrated that most of the middle atmosphere wave drag produced by the original S03 program was confined to launch-relative phase speeds less than 100 m/s, so the original range of 0.25 to 2000 m/s specified in the program was unnecessary. The program was therefore modified to calculate drag for a uniform grid from 0.25 to 100 m/s.

The Hines DSP parameterization is based on a modified form of critical layer absorption. Normal critical levels are enhanced, i.e. large-m waves begin to deposit their momentum before reaching their critical level. Hines DSP also includes spectrum-induced critical levels where the RMS amplitude of the wave spectrum is equal to the wave phase speed. Hines DSP produces an abrupt onset of large net drag at altitudes above the jet maximum. The major drag contribution tends to be confined to a relatively narrow layer, as would be expected from critical layer absorption. It should be noted that such vertically-confined drag is not likely to be representative of non-critical layer events, and the localized strong accelerations resulting from such drag profiles may be problematic in numerical models. Of course the atmospheric response to this strong localized drag would spread to altitudes on the order of a scale height below, according to the downward control theory of Haynes et al. (1991).

In contrast, the WM drag scheme spreads smaller amounts of drag over a much broader range of altitudes. The reason for this is that the WM launch amplitude is set to match the high-m portion of the imposed saturation threshold. Since the WM spectrum is assumed to be saturated at launch, wave dissipation commences immediately as the spectrum grows with increasing altitude. The saturation threshold

(or effectively the launch amplitude) is a free parameter of the WM scheme. It should be noted that in most applications (including S03, MS05, Orr and Scinocca, 2010), it is set to a value well below what one would expect on the basis of observations. MS05 have shown that the amplitude of the WM launch spectrum needs to be increased by a factor of 50 in order to match measurements of saturated atmospheric wave spectra.

In a windless atmosphere, the WM parameterization is the only scheme that reproduces wave saturation. The wave obliteration employed in the Hines and AD schemes prevents the formation of an m^{-3} spectral tail at high m. Obviously neither of these schemes would be expected to produce an appropriate spectral tail in the presence of CIRA zonal winds. Since the WM scheme is based on the imposition of an m^{-3} spectral tail, one would expect it to do so in the presence of CIRA zonal winds. However, it was shown that WM does not produce spectra of saturated form when subjected to wave obliteration by critical levels or when the waves propagate in an azimuth opposite to the background wind.

Medvedev and Klaassen (1995), Klaassen and Sonmor (2006) and Klaassen (2009a,b) have pointed out serious issues with the physical and mathematical foundations of Hines Doppler-spread theory, so it is natural to ask why Hines DSP has been successfully applied to represent the effects of nonorographic gravity wave drag in middle atmosphere climate models. It is clear that this is because the DSP parameterization scheme employs a simplification of Doppler-spread theory that represents the wave drag as an enhanced (or premature) critical layer absorption. MS05 have demonstrated that critical level absorption alone is sufficient to close the jets in the middle atmosphere and provides what looks to be a reasonable zonally-averaged circulation. Given the relationship between Hines DSP and critical layer dissipation, it is not

surprising that Hines DSP works in a similar fashion.

Note that MS05 conclude from their figure 10 that there is little to distinguish between Hines DSP, WM (with launch amplitude adjusted to $C_* = 50$) and critical-level dissipation only, since the zonally-averaged circulations are very similar. However, if one takes into account the highly compressed vertical scale of the figure and examines the momentum deposition in their figure 10 more closely, one finds that the momentum deposition extrema for the critical-level-only and Hines cases are found at an altitude roughly 5 km higher than in the WM case. Although this 5 km distance appears small on middle atmosphere plots, it should be recognized that it corresponds to almost a full scale height and is therefore significant. This demonstrates that the different types of momentum deposition, e.g. strong drag over a narrow layer (in the case of Hines DSP and critical-level-only) vs. weaker drag spread over a deeper layer (in the case of WM) can lead to very similar zonally averaged circulations.

Since there are no measurements of wave momentum deposition to guide the development of gravity wave drag schemes, it may therefore be necessary to find more sensitive indicators of the middle atmosphere circulation in order to constrain gravity wave drag parameterizations. An example of an alternative indicator that has been used in the past is the semi-annual oscillation in the equatorial middle atmosphere (Medvedev et al. 1998).

4.2 Discussion of Gravity-Wave Emission into the Newfoundland-Labrador Hotspot

For the second part of this dissertation, we considered the generation and vertical propagation of gravity waves in the Newfoundland-Labrador region. This study was motivated by Hoffmann et al. (2013) who examined AIRS satellite measurements and identified a wintertime hotspot for gravity wave emission in that region at altitudes between 15 and 65 km. Hoffman et al. left the source for this hotspot unclassified since it did not satisfy their criteria for either topographic or convective gravity wave sources. Given the frequent winter storms traveling up the East Coast storm track and the frequent occurrence of jet streaks along the coast, this hotspot region appeared to be an ideal place to test the hypothesis that jet streaks and developing baroclinic systems could be a significant source of gravity waves in the hotspot region.

From peak events in the AIRS temperature record, we selected two of the strongest events (2008 and 2014), and a third strong event (2003) that had already previously been studied by WZ04. Each of these cases had strong jet streaks traveling along the East Coast of North America. We used the WRF model with ERA-Interim reanalysis data to simulate each of these cases. While earlier studies of gravity waves in this area have relied on other reanalysis datasets, the ERA-Interim data possess the greatest vertical domain of all currently available datasets, and allows the tracking of gravity waves into the upper stratosphere.

Surprisingly, only the 2003 case showed gravity wave emission from a baroclinic jet-front system. The waves were emitted from the left exit region of the jet, consistent with the scenario discussed by WZ04, Koch and Handley (1997) and Uccellini

and Koch (1987). However, during this event, the gravity wave source (the 250 hPa jet streak) was located *outside* the hotspot region, just brushing past its southeast corner. Our simulations show that the wave packet propagates a significant horizontal distance (roughly 500 km) into the hotspot region as it ascends through the stratosphere.

For the extremely strong 2014 event, our simulations indicate the gravity waves originated from the coast of Labrador. This case represents persistent gravity wave generation by topography along that coast when the surface flow is roughly perpendicular to the coast. As the flow tends to increase with height, the stationary waves encounter no critical levels and are able to propagate deep into the stratosphere where they are detected by the AIRS satellite. This wave packet remains local to the region above the source, which is within the hotspot region.

The 2008 event presents a particularly interesting scenario. In the time preceding this event, there is a strong surface flow generating topographic waves over the Appalachian mountains (the flow is roughly perpendicular to the Appalachian ridge). This source is far outside the hotspot region. However, shortly before AIRS detects the gravity wave event, the surface flow shifts into the direction parallel to the Appalachian ridge. This terminates the gravity wave source. What is left of the packet in the middle atmosphere is advected by stratospheric winds into the hotspot region where they can be detected by AIRS.

Two of these cases (2003 and 2008) demonstrate the importance of the background horizontal wind in the advection of gravity wave packets in the middle atmosphere. In particular, it should be noted that all current orographic gravity wave drag parameterizations assume that orographic gravity waves remain stationary with respect to

the source, and deposit their momentum directly above the source. Our simulations of the 2008 event demonstrate that this is not always the case.

Several authors, including Zhang (2004) and Zhang et. al. (2001), have advocated the residual of the nonlinear balance equation, ΔNBE field (see equation 3.9), as a signal of potential gravity wave emission by baroclinic jet-front systems. While the diagnostic ΔNBE field has long been considered to be a useful tool for identifying regions of imbalance in synoptic flow fields, McIntyre (2015) has suggested that higher-order theories may be more appropriate for determining the "true" balanced state. Moreover, there is no theory to readily distinguish which properties of ΔNBE are associated with the ageostrophic circulation that tends to adjust the flow toward a balanced state and which properties are responsible for forcing gravity waves.

All three cases considered in this study (2003, 2008 and 2014) have jet streaks traveling up the East Coast of North America, and the ΔNBE field for all three cases show imbalances exist in the left exit region of those jet streaks. However, it is only the 2003 case that shows gravity wave emission associated with the jet streak. This study showed that a considerably stronger and much more localized maximum of ΔNBE develops in the left exit region of the 2003 jet. The concentrated peak in the 2003 ΔNBE field is roughly 2.5 times stronger than the maximum values found in the 2008 and 2014 cases. It is not clear whether there is some minimum value of ΔNBE required for gravity wave emission, or perhaps other aspects of the flow such as horizontal, vertical and temporal scales are playing a role in forcing gravity waves. More work is required to clarify the connection between the properties of the ΔNBE field and the emission of gravity waves

4.3 Future Work

Many recent publications have focused on connecting nonorographic gravity wave drag schemes to sources such as deep moist convection and baroclinic jet-front systems, as well as considering the effects of horizontal wave packet propagation. The work in chapter 2 has demonstrated that there are still enormous uncertainties in the specification of momentum deposition mechanisms and that much more work in all of these areas needs to be done in order to provide accurate representations of gravity wave drag.

This need is also highlighted by the results of our study of the unclassified winter-time gravity-wave hotspot over Newfoundland and Labrador. Our simulations have demonstrated that there are multiple sources for these gravity waves, which include topography as well as baroclinic jet-front systems traveling along the winter-time storm track off the East Coast of North America. In agreement with Wei and Zhang (2014), we find this baroclinic gravity wave emission is enhanced by deep moist convection. One of the more interesting aspects of the present work is that in two of the three cases the gravity wave sources (including topography) lie outside the hotspot region. As they ascend through the atmosphere, these gravity wave packets propagate into the hotspot region at higher altitudes. Only a few of the gravity wave events detected by AIRS measurements have been considered in this study, so it is certainly possible to learn more from studying other events.

Bibliography

[1] Alexander, M.J. and Pfister L., 1995: Gravity Wave Momentum Flux in the Lower Stratosphere Over Convection, *Geophys. Res. Lett.* **22**, pp. 2029–2032.

[2] Alexander, M.J. and Dunkerton T.J., 1999: A Spectral Parameterization of Mean-Flow Forcing due to Breaking Gravity Waves, *J. Atmos. Sci.* **56**, pp. 4167-4182.

[3] Alexander, M.J., Beres J. H., and Pfister L., 2000: Tropical Stratospheric Gravity Wave Activity and Relationship to Clouds, *J. Geophys. Res.* **105(D17)**, pp. 22299–22309

[4] Alexander, M. J. and Holton, J. R., (2004), On the Spectrum of Vertically Propagating Gravity Waves Generated by a Transient Heat Source, *Atmos. Chem. Phys.*, **4**, pp. 923-932, doi:10.5194/acp-4-923-2004.

[5] Allen K.R., and Joseph, R.I., 1989: A Canonical Statistical Theory of Oceanic Internal Waves *Journal of Fluid Mech.* **204**, pp. 185-228.

[6] Allen, J. S., 1991: Balance Equations Based on Momentum Equations with Global Invariants of Potential Enstrophy and Energy. *J.* Phys. Ocean ogr., **21**, pp. 265–276.

[7] Andrews D.G., Holton J.R., Leovy C.B., 1987: *Middle Atmosphere Dynamics.* Academic Press, 489 pp.

[8] Booker J.R., Bretherton F.P., 1967: The Critical Layer for Internal Gravity Waves in a Shear Flow. *J. Fluid Mech.*, **27**, pp. 513-539.

[9] Broutman D., Alexander J., McConnell J., Semeniuk K., et al., 2009: Gravity Waves in the Middle Atmosphere. *Technical Report to ESA*, 1-83.

[10] Charney J. G., 1955: The Use of Primitive Equations of Motion in Numerical Prediction. *Tellus*, **7**, pp. 22-26.

[11] Charney J. G., Stern M. E., 1962: On the Stability of Internal Baroclinic Jets in a Rotating Atmosphere. *J. Atmos. Sci.*, **19**, pp. 159-172.

[12] Charron M, E. Manzini and C.D. Warner 2002: Intercomparison of Gravity Wave Parameterizations: Hines Doppler- Spread and Warner and McIntyre Ultra-Simple Schemes. *J. Met. Soc. Japan* **80**, pp. 335-345.

[13] Chunchuzov I. 2002: On the High-Wavenumber Form of the Eulerian Internal Wave Spectrum in the Atmosphere. *J. Atmos. Sci.* **59**, pp. 1753-1774.

[14] Davis C. A., Emanuel K. A., 1991: Potential Vorticity Diagnosis of Cyclogenesis. *Mon. Wea. Rev.*, **119**, pp. 1929–1952.

[15] Dutton J. A., 1986: *T*he Ceaseless Wind: An Introduction to the Theory of Atmospheric Motion. Dover Publication, 617 PP.

[16] Eckermann, S., and R. Vincent (1993), VHF Radar Observations of Gravity Wave Production by Cold Fronts over southern Australia, *J. Atmos. Sci.*, **50**, pp. 785-806.

[17] Ern, M., P. Preusse and C.D. Warner 2006: Some Experimental Constraints for Spectral Parameters Used in the Warner and McIntyre Gravity Wave Parameterization Scheme. *Atmos. Chem. Phys.* **6**, pp. 4361-4381.

[18] Evan S., Alexander M.J., Dudhia J., 2012: WRF Simulations of Convectively Generated Gravity Waves in Opposite QBO Phases. *J. Geophys. Res.*, *117*, D12117.

[19] Fleming, E. L., S. Chandra, J. J. Barnett, and M. Corney, 1990: Zonal Mean Temperature, Pressure, Zonal Wind and Geopotential Height as Functions of Latitude. *Adv. Space Res.*, **10(12)**, 119.

[20] Fomichev, V.I., Ward, W.E., Beagley, S.R., McLandress, C., McConnell, J.C., McFarlane, N.A. and T.G. Shepherd 2002: The Extended Canadian Middle Atmosphere Model: Zonal-Mean Climatology and Physical Parameterizations. *J. Geophys. Res.*, **107(D10)**, 4087, doi:10.1029/2001JD000479.

[21] Fritts, D., and G. Nastrom, 1992, Sources of Mesoscale Variability of Gravity Waves. Part II: Frontal, Convective, and Jet Stream Excitation, *J. Atmos. Sci.*, **49(2)**, 111-127

[22] Fritts, D.C. and VanZandt, T.E., 1993: Spectral Estimates of Gravity Wave Energy and Momentum Fluxes. Part I: Energy Dissipation, Acceleration, and Constraints. *J. Atmos. Sci.*, **50**, pp. 3685-3694.

[23] Fritts D.C., Alexander M.J., 2003: Gravity Wave Dynamics and Effects in the Middle Atmosphere. *Reviews of Geophysics*, **41**, pp. 1-64.

[24] Fritts et al., 2009: Gravity Wave Instability Dynamics at High Reynolds Numbers. Part I: Wave Field Evolution at Large Amplitudes and High Frequencies. *J. Atmos. Sci.*, **66**, pp. 1126-1148.

[25] Gardner, C.S., Hostetler, C.A. and Lintelman, S., 1993: The Influence of the Mean Wind Field on the Separability of Atmospheric Perturbation Spectra. *J. Geophys. Res.* **D98**, pp. 8859-8872.

[26] Gent, P., McWilliams J. C., 1982: Intermediate Model Solutions to the Lorenz Equations: Strange Attractors and Other Phenomena. *J.* Atmos. Sci., **39**, pp. 3–13.

[27] Gill A.E., 1982: *Atmosphere Ocean Dynamics.* Academic Press, 662 pp.

[28] Haltiner G.J., Williams R.T., 1980: *N*umerical prediction and dynamic meteorology, Wiley, 477 pp.

[29] Hamilton K., 1996: Comprehensive Meteorological Modelling of the Middle Atmosphere: A Tutorial Review. *J. Atmos. Sol.-Terr. Phys.*, **58**, 1591-1627.

[30] Hamilton K., 1998: Dynamics of the Tropical Middle Atmosphere: A Tutorial Review. *Atmosphere-Ocean*, **36(4)**, 319-354.

[31] Hasha et al., 2008: Gravity Wave Refraction by Three-Dimensionally Varying Winds and the Global Transport of Angular Momentum. *J. Atmos.Sci.* **65**, pp. 2892-2906, doi: 10.1175/2007JAS2561.1

[32] Haynes P.H., Marks C.J., McIntyre M.E., Shepherd T.G. and Shine K.P., 1991: On the Downward Control of Extratropical Diabatic Circulations by Eddy-Induced Mean Zonal Forces. *J. Atmos Sci.* **48**, pp. 651-678.

[33] Hines, C.O., Reddy, C. A., 1967: On the Propagation of Atmospheric Gravity Waves Through Regions of Wind Shear, *J. Geophys. Res.* **72**, pp. 1015–1034, doi: 10.1029/JZ072i003p01015.

[34] Hines, C.O. 1991b: The Saturation of Gravity Waves in the Middle Atmosphere. Part 1: Critique of Linear Instability Theory, *J. Atmos.Sci.* **48**, pp. 1348-1359.

[35] Hines C.O., 1997: Doppler-Spread Parameterization of Gravity Wave Momentum Deposition in the Middle Atmosphere. Part1: Basic Formulation. *J. Atmos. Sol.-Terr. Phys.*, **59(4)**, 371-386.

[36] Hines, C.O. 2001: Theory of the Eulerian Tail in the Spectra of Atmospheric and Oceanic Internal Gravity Waves. *J. Fluid Mech.* **448**, pp. 289-313.

[37] Hodges R., 1967: Generation of Turbulence in the Upper Atmosphere by Internal Gravity Waves. *Journal of Geophysical Research*, **72**, pp. 3455-3458.

[38] Hoffmann, L., and M. J. Alexander, 2009, Retrieval of Stratospheric Temperatures from Atmospheric Infrared Sounder Radiance Measurements for Gravity Wave Studies, *J. Geophys. Res.*, **114**, D07105, doi:10.1029/2008JD011241.

[39] Hoffmann, L., and M. J. Alexander, 2010, Occurrence Frequency of Convective Gravity Waves During the North American Thunderstorm Season, *J. Geophys. Res.*, **115(D20111)**, doi:10.1029/2010JD014401.

[40] Hoffmann, L., X. Xue, and M. J. Alexander, 2013, A Global View of Stratospheric Gravity Wave Hotspots Located with Atmospheric Infrared Sounder Observations, *J. Geophys. Res. Atmos.*, **118**, pp. 416-434, doi: 10.1029/2012JD018658.

[41] Holton J.R., 1982: The Role of Gravity Wave Induced Drag and Diffusion in the Momentum Budget of the Mesosphere. *J. Atmos. Sci.*, **39**, pp. 791-799.

[42] Holton J.R., 1983: The Influence of Gravity Wave Breaking on the General Circulation of the Middle Atmosphere. *J. Atmos. Sci.*, **40**, pp. 2497-2507.

[43] Holton J.R., 2004: *An Introduction to Dynamics Meteorology.* (4th ed) Elsevier Academic Press, 535 pp.

[44] Hong S.Y., Dudhia J., Chen S.H., 2004: A Revised Approach to Ice Microphysical Processes for the Bulk Parameterization of Clouds and Precipitation, *Monthly Weather Report*,**132**, pp. 103-120.

[45] Hoskins, B. J., McIntyre M. E., Robertson A. W., 1985: On the Use and Significance of Isentropic Potential Vorticity Maps. *Q*uart. J. Roy. Meteor. Soc., **111**, pp. 877–946.

[46] Jablonowski C., Williamson D.L., 2006, A Baroclinic Instability Test Case for Atmospheric Model Dynamical Cores. *Q. J.R. Meteorol. Soc.*, **132**, pp. 2943–2975, doi: 10.1256/qj.06.12.

[47] Jockel P., H. Tost, A. Pozzer, et al., 2006: The Atmospheric Chemistry General Circulation Model ECHAM5/MESSy1: Consistent Simulation of Ozone from the Surface to the Mesosphere *Atmos. Chem. Phys.* **6**, pp. 5067-5104.

[48] Kain J. S., Fritsch M., 1990: A One Dimensional Entraining/Detraining Plume Model and Its Application in Convective Parameterization, *J. Atmos.Sci.*,**47(23)**, 2784-2802.

[49] Kain John S., 2004: The Kain–Fritsch Convective Parameterization: An Update, *Journal of Applied Meteorology*,**43**, pp. 170-181.

[50] Kim Y-J., Eckermann S.D., Chun H-Y., 2003: An Overview of the Past, Present and Future of Gravity-Wave Drag Parameterization for Numerical Climate and Weather Prediction Models. *Atmosphere-Ocean*, **41**, pp. 65-98.

[51] Kim, S.Y., and Chun H.Y., 2010, Momentum flux of stratospheric gravity waves generated by Typhoon Ewiniar (2006). *Asia-Pacific Journal of Atmospheric Sciences*, **46**, pp. 199-208.

[52] Kim, Y.H., Y.H Chun, P. Preusse, M. Ern and S.Y. Kim, Gravity Wave Reflection and its Influence on the Consistency of Temperature- and Wind-Based Momentum Fluxes Simulated Above Typhoon Ewiniar, *Atmos. Chem. Phys.* **12**, pp. 10787-10795.

[53] Klaassen, G.P. and Sonmor, L.J., 2006: Does Kinematic Advection by Superimposed Waves Provide an Explanation for Quasi-Universal Gravity-Wave Spectra? *Geophys. Res. Lett.* **33**, L23802, doi:10.1029/2006GL027388.

[54] Klaassen G.P., 2009: Testing Lagrangian Theories of Internal Wave Spectra. Part I: Varying the Amplitude and Wavenumbers. *J. Atmos. Sci.*, **66**, pp. 1077-1100.

[55] Klaassen, G. P., 2009: Testing Lagrangian Theories of Internal Wave Spectra. Part II: Varying the Number of Waves. *J. Atmos. Sci.*, **66**, pp. 1101-1125.

[56] Koch S.E., O'Handley C., 1997, Operational Forecasting and Detection of Mesoscale Gravity Waves. *American Meteorological Society*, **12**, pp. 253-281

[57] Lelong P. and Dunkerton T., 1998a,b: Inertia-Gravity Wave Breaking in Three Dimensions: 1. Convectively Stable Waves, 2. Convectively Unstable Waves. *J. Atmos. Sci.*, **55**, pp. 2473-2488, pp. 2489-2501.

[58] Lindzen R.S., 1973: Wave-Mean Flow Interaction in the Upper Atmosphere. *Boundary Layer Met.*, **4**, pp. 327-343.

[59] Lindzen R.S., 1981: ... Turbulence and Stress Owing to Gravity Wave and Tidal Breakdown. *J. Geophys. Res.*, **86**, pp. 9707-9714.

[60] Lindzen R.S., 1990: *Dynamics in Atmospheric Physics.* Cambridge University Press, 310 pp.

[61] Lubken, F.-J., 1997: Seasonal Variation of Turbulent Energy Dissipation Rates at High Latitudes as Determined by in situ Measurements of Neutral Density Fluctuations, *J. Geophys. Res.* **102(13)**, 441-13,456.

[62] Manzini, E., McFarlane, N.A. and C. McLandress 1997: Impact of the Doppler-Spread Parameterization on the Simulation of the Middle Atmosphere Circulation Using the MA/ECHAM4 General Circulation Model. *J. Geophys. Res.*, **102**, pp. 25751-25762.

[63] Mayr, H.G., R.E. Hartle, and K.L. Chan, 1998a: Equatorial Oscillations Maintained by Gravity Waves as Described with the Doppler Spread Parameterization: II. Numerical Experiments. *J. Atmos. Solar-Terr. Phys.* **60**, pp. 181-199.

[64] Mayr, H.G., R.E. Hartle, and K.L. Chan, 1998b: Equatorial Oscillations Maintained by Gravity waves as described with the Doppler Spread Parameterization: II. Heuristic analysis. *J. Atmos. Solar-Terr. Phys.* **60**, pp. 201-213.

[65] Mayr, H.G., J.G. Mengelb, K.L. Chan, H.S. Porter 2001: Mesosphere Dynamics with Gravity Wave Forcing: Part I. Diurnal and Semi-Diurnal Tides *J. Atmos. Solar-Terr. Phys.* **63**, pp. 1851-1864.

[66] Mayr, H.G., J.G. Mengel, K.L. Chan, and F.T. Huang 2010: Middle Atmosphere Dynamics with Gravity Wave Interactions in the Numerical Spectral Model: Zonal-Mean Variations. *J. Atmos. Solar-Terr. Phys.* **72**, pp. 807-828, doi:10.1016/j.jastp.2010.03.018.

[67] Mayr, H.G., J.G. Mengel, K.L. Chan, and F.T. Huang 2011: Middle Atmosphere Dynamics with Gravity Wave Interactions in the Numerical Spectral Model: Tides and Planetary Waves *J. Atmos. Solar-Terr. Phys.* **73**, pp. 711-730, doi:10.1016/j.jastp.2011.01.019.

[68] McFarlane, N.A., 1987: The Effect of Orographically Excited Gravity Wave Drag on the General Circulation of the Lower Stratosphere and Troposphere, *J. Atmos. Sci.*, **44**, pp. 1775-1800.

[69] McIntyre M. E., Norton W. A., 2000: Potential Vorticity Inversion on a Hemisphere. *J. Atmos. Sci.*, **57**, pp. 1214–1235.

[70] McIntyre, M.E., (2015). Balanced Flow. In: Gerald R. North (editor-in-chief), John Pyle and Fuqing Zhang (editors). *Encyclopedia of Atmospheric Sciences*, 2nd edition, (Vol **2**, pp. 298–303), Elsevier Ltd., Academic Press, ISBN: 9780123822253.

[71] McLandress C., 1998: On the Importance of Gravity Waves in the Middle Atmosphere and their Parameterization in General Circulation Models. *J. Atmos. Sol.-Terr. Phys.*, **60**, pp. 1357-1383.

[72] McLandress, C., Alexander M.J., Wu D.L., 2000: Microwave Limb Sounder Observations of Gravity Waves in the Stratosphere: A Climatology and Interpretation. *J. Geophys. Res.*, **105**, pp. 1194-1967.

[73] McLandress C., Scinocca, J.F., 2005: The GCM Response to Current Parameterizations of Nonorographic Gravity Wave Drag. *J. Atmos. Sci.*, **62**, pp. 2394-2413.

[74] McLandress, C., W.E. Ward, V. I. Fomichev, K. Semeniuk, S.R. Beagley, N.A. McFarlane, and T.G. Shepherd. 2006: Large-scale Dynamics of the Mesosphere and Lower Thermosphere: An Analysis Using the Extended Canadian Middle Atmosphere Model, *J. Geophys. Res.* **111**, D17111, doi:10.1029/2005JD006776.

[75] Medvedev, A.S. and Klaassen, G.P. 1995: Vertical Evolution of Gravity Wave Spectra and the Parameterization of Associated Wave Drag. *J. Geophys. Res.* **100(25)**, 841-25, 853.

[76] Medvedev A.S., Klaassen G.P., 2000: Parameterization of Gravity Wave Momentum Deposition Based on Nonlinear Wave Interactions: Basic Formulation and Sensitivity Tests. *J. Atmos. Sol.-Terr. Phys.*, **62**, pp. 1015-1033.

[77] Mohebalhojeh A.R., McIntyre M.E., 2007: Local Mass Conservation and Velocity Splitting in PV-Based Balanced Models. Part I: The Hyperbalance Equations. *J. Atmos. Sci.*, **64**, pp. 1782–1793. DOI: 10.1175/JAS3933.1

[78] Mohebalhojeh A.R., McIntyre M.E., 2007: Local Mass Conservation and Velocity Splitting in PV-Based Balanced Models. Part II: Numerical Results. *J. Atmos. Sci.*, **64**, pp. 1794–1810. DOI: 10.1175/JAS3934.1

[79] O'Sullivan, D., and T. Dunkerton, 1995, Generation of Inertia Gravity Waves in a Simulated Life Cycle of Baroclinic Instability, *J. Atmos. Sci.*, **52(21)**, 3695-3716.

[80] Orr, A., P. Bechtold, J. Scinocca, M. Ern, M Janiskova 2010: Improved Middle Atmosphere Climate and Forecasts in the ECMWF Model through a Nonorographic Gravity Wave Drag Parameterization. *J. Clim.* **23**, pp. 5905-5926.

[81] Palmer, T.N., Shutts G.J., Swinbank R., 1986: Alleviation of a Systematic Westerly Bias in General Circulation and Numerical Weather Prediction Models Through an Orographic Gravity Wave Drag Parameterization. *Quarterly Journal of the Royal Meteorological Society*, **112**, pp. 1001-1039.

[82] Plougonven R., Teitelbaum H., Zeitlin V., 2003, Inertia Gravity Wave Generation by the Tropospheric Midlatitude Jet as Given by the Fronts and Atlantic Storm-Track Experiment Radio Soundings, *J. Geophys. Res.*, **108(D21)**, 4686, doi: 10.1029/2003JD003535.

[83] Plougonven R., and Snyder C., 2007, Inertia–Gravity Waves Spontaneously Generated by Jets and Fronts. Part I: Different Baroclinic Life Cycles, *J. Atmos. Sci.*, **64**, pp. 2502-2520, DOI: 10.1175/JAS3953.1.

[84] Plougonven, R., and F. Zhang, 2014, Internal Gravity Waves from Atmospheric Jets and Fronts, *Rev. Geophys.*, **52**, doi:10.1002/2012RG000419.

[85] Scaife, A.A., Butchart, N., Warner, C.D. and Swinbank, R. 2002: Impact of a Spectral Gravity Wave Parameterization on the Stratosphere in the Met Office Unified Model, *J. Atmos. Sci.* **59**, pp. 1473-1489.

[86] Schmidt, H., G. P. Brasseur, M. Charron, E. Manzini, M. A. Giorgetta, T. Diehl, V. I. Fomichev, D. Kinnison, D. Marsh, and S. Walters 2006: The HAMMONIA Chemistry Climate Model: Sensitivity of the Mesopause Region to the 11-Year Solar Cycle and CO2 Doubling. *J. Clim.* **19** pp. 3903-3931.

[87] Scinocca, J. F., 2002: The Effect of Back-Reflection in the Parametrization of Non-Orographic Gravity Wave Drag. *.J. Meteorol. Soc. Japan*, **80**, 939–962.

[88] Scinocca, J. F., 2003: An Accurate Spectral Nonorographic Gravity Wave Drag Parameterization for General Circulation Models. *J. Atmos. Sci.*, **60**, pp. 667-682.

[89] Scinocca, J. F., N. A. McFarlane, M. Lazare, J. Li, and D. Plummer, 2008: The CCCma Third Generation AGCM and its Extension into the Middle Atmosphere. *Atmos. Chem. Phys.*, **8**, pp. 7055-7074.

[90] Skamarock, W. C., J. B. Klemp, J. Dudhia, D. O. Gill, D. M. Barker, M. G Duda, X.-Y. Huang, W. Wang, and J. G. Powers, 2008: A Description of the Advanced Research WRF Version 3. *N*CAR Tech. Note NCAR/TN-475+STR, 113 pp. doi:10.5065/D68S4MVH

[91] Smith, S.A., Fritts, D.C., VanZandt, T.E., 1987: Evidence for a Saturated Spectrum of Atmospheric Gravity Waves. *J. Atmos. Sci.* **44**, pp. 1404-1410.

[92] Tan, Z., Zhang F., Rotunno R., and Snyder C., 2004: Mesoscale Predictability of Moist Baroclinic Waves: Experiments With Parameterized Convection. *J.* Atmos. Sci., **61**, pp. 1794–1804; Corrigendum, **65**, pp. 1479.

[93] Uccellini, LW. and S.E. Koch, 1987, The Synoptic Setting and Possible Energy Sources for Mesoscale Wave Disturbances. *Mon. Weather Rev.* **115**, pp. 721-729.

[94] VanZandt, T.E., 1982: A Universal Spectrum of Buoyancy Waves in the Atmosphere. *Geophys. Res. Lett.* **9**, pp. 575-578.

[95] Vincent, R. A., and Alexander M. J., 2000, Gravity Waves in the Tropical Lower Stratosphere: An Observational Study of Seasonal and Interannual Variability, *J.* Geophys. Res., **105**, PP. 17971–17982.

[96] Warner, C.D. and M.E. McIntyre, 1996: On the Propagation and Dissipation of Gravity Wave Spectra through a Realistic Middle Atmosphere. *J. Atmos. Sci.* **53**, pp. 3213-3235.

[97] Warner, C.D. and M.E. McIntyre, 2001: An Ultrasimple Spectral Parameterization for Nonorographic Gravity Waves *J. Atmos. Sci.* **58**, pp. 1837-1857.

[98] Wang, S., F. Zhang, 2007: Sensitivity of Mesoscale Gravity Waves to the Baroclinicity of Jet-Front Systems. *Mon. Wea. Rev.*, **135**, pp. 670–688.

[99] Warner, C.D., A.A. Scaife and N. Butchart, 2005: Filtering of Parameterized Nonorographic Gravity Waves in the Met Office Unified Model, *J. Atmos. Sci.* **62**, pp. 1831-1848.

[100] Wei J., Zhang F., 2014: Mesoscale Gravity Waves in Moist Baroclinic Jet-Front Systems. *J. Atmos. Sci.*, **71**, pp. 929-952.

[101] Whiteway J., 1994: Lidar Observations of Thermal Structure and Gravity Wave Activity in the Middle Atmosphere. (Doctoral Dissertation). York University, Toronto, Ontario.

[102] Whiteway J. A., Carswell A. I., 1994, Rayleigh Lidar Observations of Thermal Structure and Gravity Wave Activity in the High Arctic during a Stratospheric Warming, *J.* Atmos. Sci., **51(21)**, 3122-3136.

[103] Whiteway J. A., Duck T. J., Donovan D. P., Bird J. C., Pal S. R., Carswell A. I., 1997, Measurements of Gravity Wave Activity Within and Around the Arctic Stratospheric Vortex, *G*eophys. Res. Lett., **24(11)**, 1387-1390.

[104] Wu, D. L., 2004, Mesoscale gravity wave variances from AMSU-A radiances, *Geophys. Res. Lett.*, **31**, L12114, doi:10.1029/2004GL019562.

[105] Wu, D. L., and F. Zhang, 2004, A Study of Mesoscale Gravity Waves over the North Atlantic with Satellite Observations and a Mesoscale Model, *J. Geophys. Res.*, **109**, D22104, doi:10.1029/2004JD005090.

[106] Yau K-H., 2002: Stability Properties of Inertio-Gravity Waves with an Investigation of Wave Saturation (Doctoral Dissertation). York University, Toronto, Ontario.

[107] Yau KH., Klaassen G.P. and Sonmor L., 2004: Principal Instabilities of Large Amplitude Inertio-Gravity Waves. *Physics of Fluids*, **16**, pp. 936-951.

[108] Yigit, E., A. D. Aylward, and A. S. Medvedev (2008), Parameterization of the Effects of Vertically Propagating Gravity Waves for Thermosphere General Circulation Models: Sensitivity Study, *J. Geophys. Res.* **113**, D19106, doi:10.1029/2008JD010135.

[109] Zhang, F., Koch S. E., Davis C. A., Kaplan M. L. (2000), A Survey of Unbalanced Flow Diagnostics and their Application., *Adv. Atmos. Sci.*, **17**, PP. 165-183.

[110] Zhang, F., Koch S. E., Davis C. A., Kaplan M. L. (2001), Wavelet Analysis and the Governing Dynamics of a Large-Amplitude Gravity Wave Event Along the East Coast of the United States, *Quart. J. Roy. Meteor. Soc.*, **127**, PP. 2209–2245.

[111] Zhang, F., 2004, Generation of Mesoscale Gravity Waves in Upper Tropospheric Jet-front Systems, *J. Atmos. Sci.*, **61**, pp. 440-457.

[112] Zhang, F., Wang, S. and Plougonven, R., 2004, Uncertainties in Using the Hodograph Method to Retrieve Gravity Wave Characteristics from Individual Soundings, *Geophys. Res. Lett*, **31**, L11110, doi:10.1029/2004GL0.

[113] Zhang, F., Bei N., Rotunno R., Snyder C., and Epifanio C. C., 2007: Mesoscale Predictability of Moist Baroclinic Waves: Convection Permitting Experiments and Multistage Error Growth Dynamics. *J.* Atmos. Sci., **64**, pp. 3579–3594.

Appendix A

Validation of Gravity Waves Simulations vs. Measurements

A.1 introduction

Whiteway and Carswell (1994) and Whiteway et. al. (1997, hereafter JW97), carried out nighttime lidar measurements of gravity wave activity in the polar stratosphere at Eureka on Ellesmere Island (80° N, 86° W). These observations of thermal structure and gravity wave activity in the upper stratosphere and lower mesosphere were performed during winter 1993 at the Arctic Stratospheric Observatory, which is located on a 600 m mountain range, about 20 kilometers from the permanent Canadian Weather Station. The measurements have a vertical resolution of 300m. Figure A.1 shows the temperature (left) and temperature perturbation (right) profiles at 3 A.M. local time (UTC -5hours) on February 14, 1993 at Eureka. For the temperature profile they used half hour averaging. The profile was smoothed in the vertical using a 3 point running average. The temperature perturbation profile shows a dominant wave with a growing amplitude and the vertical wavelength of about 7 km in the upper stratosphere with superimposed shorter wavelengths of 2-4 km. The measured temperature perturbations range from $\pm 2°$ C at 26 km to $\pm 13°$ C at 42 to

55 km. Above altitude 35 km, there are three layers where the lapse rate matches the adiabatic rate $g/c_p \approx 10^\circ$ C/km. These layers likely correspond to wave overturning events that tend to induce saturation.

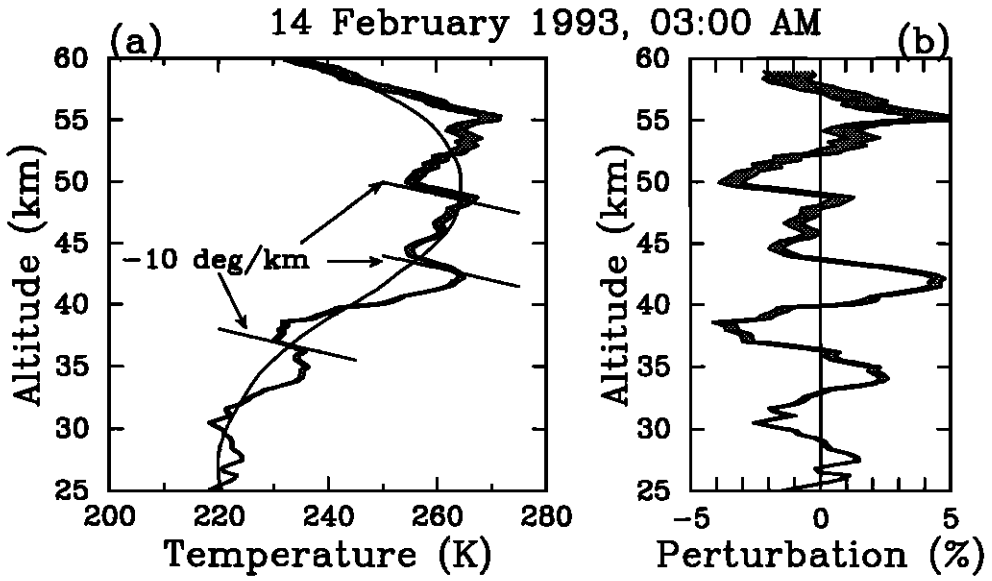

Figure A.1: (a) Temperature profile at Eureka on February 14, 1993 at 3 A.M. local time (8 A.M. UTC). The solid line shows the estimate of unperturbed background state (cubic polynomial fits to the night's mean temperature). (b) The corresponding fractional temperature perturbation profile (After Whiteway et.al., 1997).

A.2 Numerical Simulations Using ECMWF ERA Interim Data

In order to validate the performance of the WRF model, we performed a series of simulations with WRF version 3.8 to study the gravity wave activity on February 14, 1993 at Eureka and compared the wave characteristics with the lidar measurements described above. To initialize WRF and provide boundary conditions, we used ECMWF ERA-Interim data with a resolution of 80 km×80 km on 60 vertical levels

from the surface up to 0.1 hPa. For these simulations we employ 300×250 grid points with 30-km horizontal grid spacing and 90 vertical layers up to 1.5 hPa (≈ 42 km). The model is initialized on 12 February 1993 at 0000 UT and integrated up to 0000 UT on 15 February 1993. The upper 7 km of the model domain contains a wave absorbing layer (with dampcoef = 0.4), so we are unable to compare with the overturning events at $z > 35$ km. The model domain includes all North America, Greenland and Alaska to avoid boundaries over the continent. As we can see in the terrain height plot (figure A.2), Eureka is surrounded by mountains up to 2600 m in height.

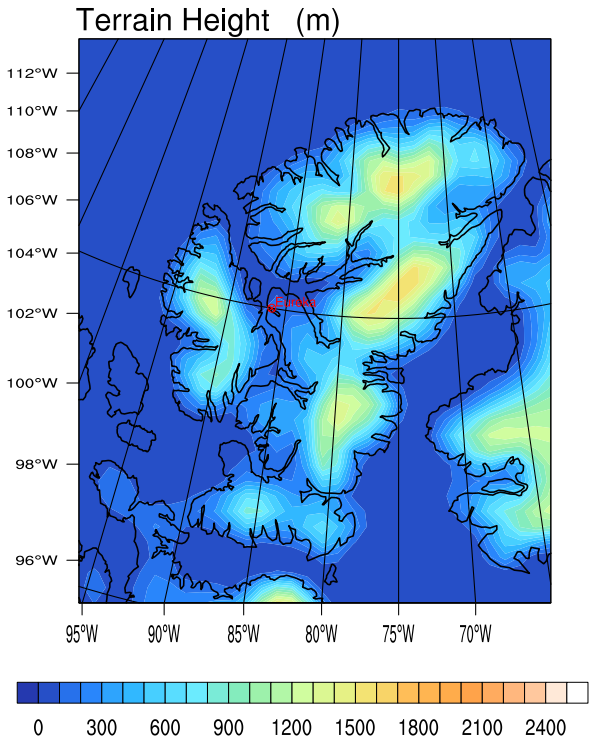

Figure A.2: Ellesmere and Axel Heiberg Islands terrain height map. Eureka is labeled in red. From WRF simulations using ECMWF ERA Interim data.

Figure A.3 shows the surface synoptic flow on Feb 14, 1993 at 0800 UTC. The

white dot marker indicates the location of Eureka. The right plot has been zoomed into an area closer to Eureka. As we can see, Eureka is located between a strong High over the Beaufort sea and a strong Low pressure system over Greenland, and surrounded by mesoscale features over the mountains of Ellesmere and Axel Heiberg Islands. In this case, the northwesterly surface flow from the ocean and over the mountains is ideal for the emission of topographic gravity waves, since it is roughly perpendicular to the coastal topography, which is oriented from the southwest to the northeast.

Geopotential height contour maps overlaid with wind-barbs at 10 hPa ($\approx$ 30 km) on February 14, 1993 at 0800 UT are shown in figure A.4. We can see the low pressure over Greenland extends from the surface all the way into the middle stratosphere, producing a consistent northerly upper level flow over Eureka. The zoomed plot clearly shows the northerly upper level background wind flow near Eureka.

Figure A.5 shows the background temperature profile for February 14, 0800 UT. The profile at the top is plotted on the closest grid point to Eureka 79.93° N, 85.74° W. The bottom left shows the mean temperature contour cross section along the line shown on the bottom right plot. Eureka is nearly at the centre of the cross section horizontal axis (latitude 80° N, figure A.5, bottom right). As we can see, the background temperature profile agrees with the measurements of JW97 (figure A.1, left), allowing for the different vertical range.

Figure A.6 shows the evolution of wave patterns in the perturbation temperature field at 50 hPa (20 km), every four hours from February 13, 2000 UTC to February 14, 1600 UTC. The mean temperature was calculated using a 20 point running average. As shown in figure A.6, timing of the wave activity is consistent with the active

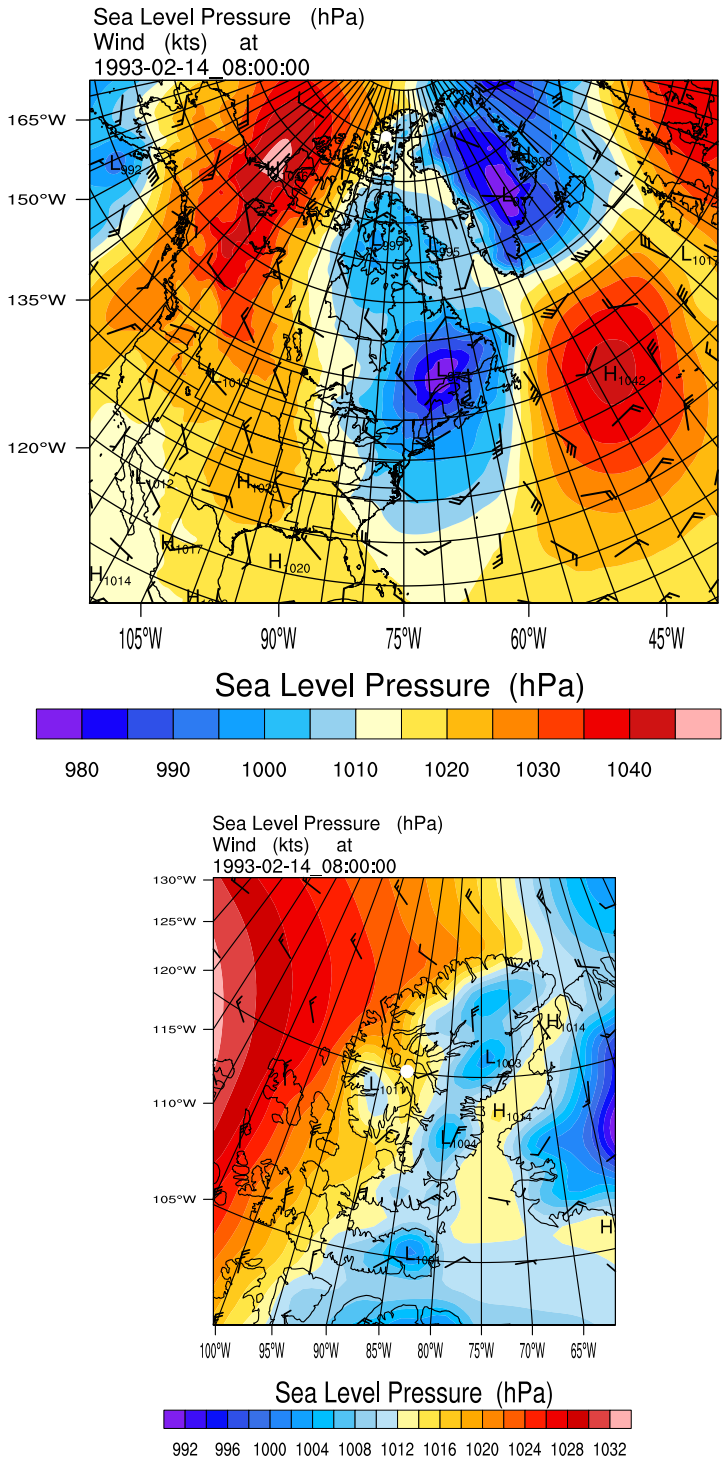

Figure A.3: Sea level pressure contours (hPa) and wind-barbs (kts), on February 14, 1993 at 0800 UT. The top plot shows the full model domain and the plot at the bottom has been zoomed into the area closer to Eureka. From WRF simulations using ECMWF ERA Interim data.

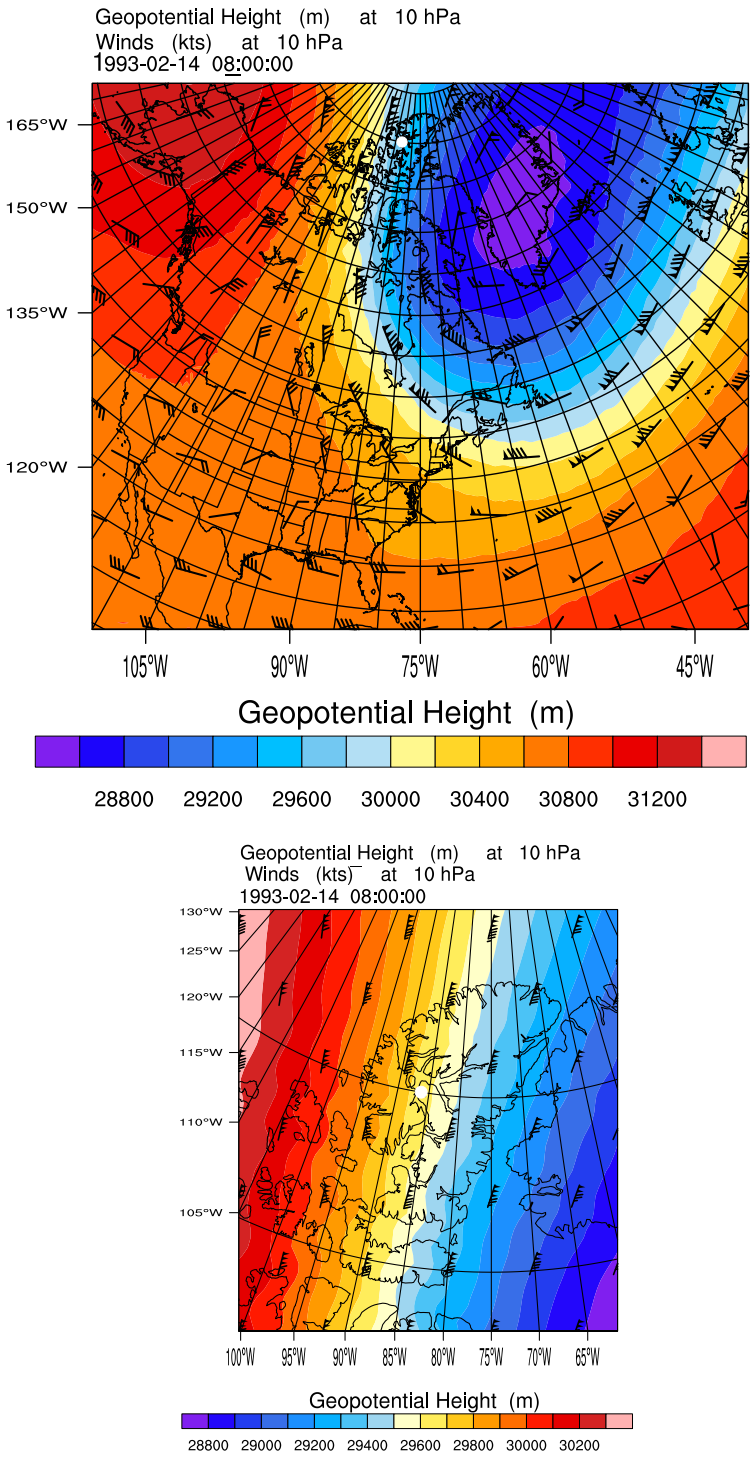

Figure A.4: Geopotential height contours (m) and wind-barbs (kts) at 10 hPa, on February 14, 1993 at 0800 UT. The bottom plot has been zoomed into the area closer to Eureka. From WRF simulations using ECMWF ERA Interim data.

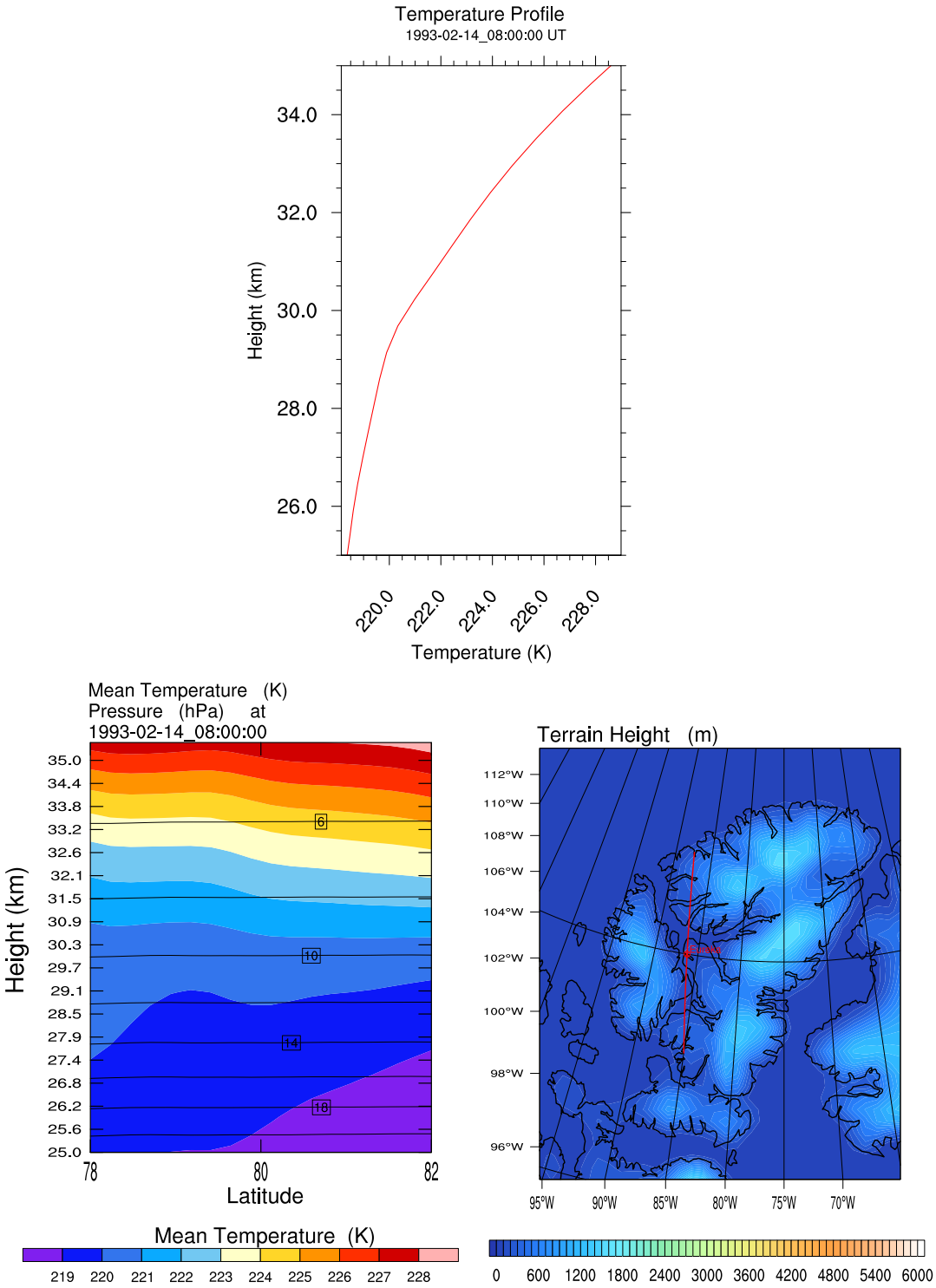

Figure A.5: Top: Background temperature profile (°K). Bottom left: Mean temperature contour cross section. Bottom right: The red line indicates where the cross section is plotted. The vertical extent of the profiles has been limited to 35 km, just below the sponge layer (35 to 42 km). From WRF simulations using ECMWF ERA Interim data.

period measured by JW97 (from 0200 to 0830 UTC). A wave packet forms over southern Ellesmere Island on February 14, 0000 UT. The wave packet then propagates towards the northwest and its eastern edge passes through Eureka. The perturbation temperature varies between $-2°$ K to $2°$ K.

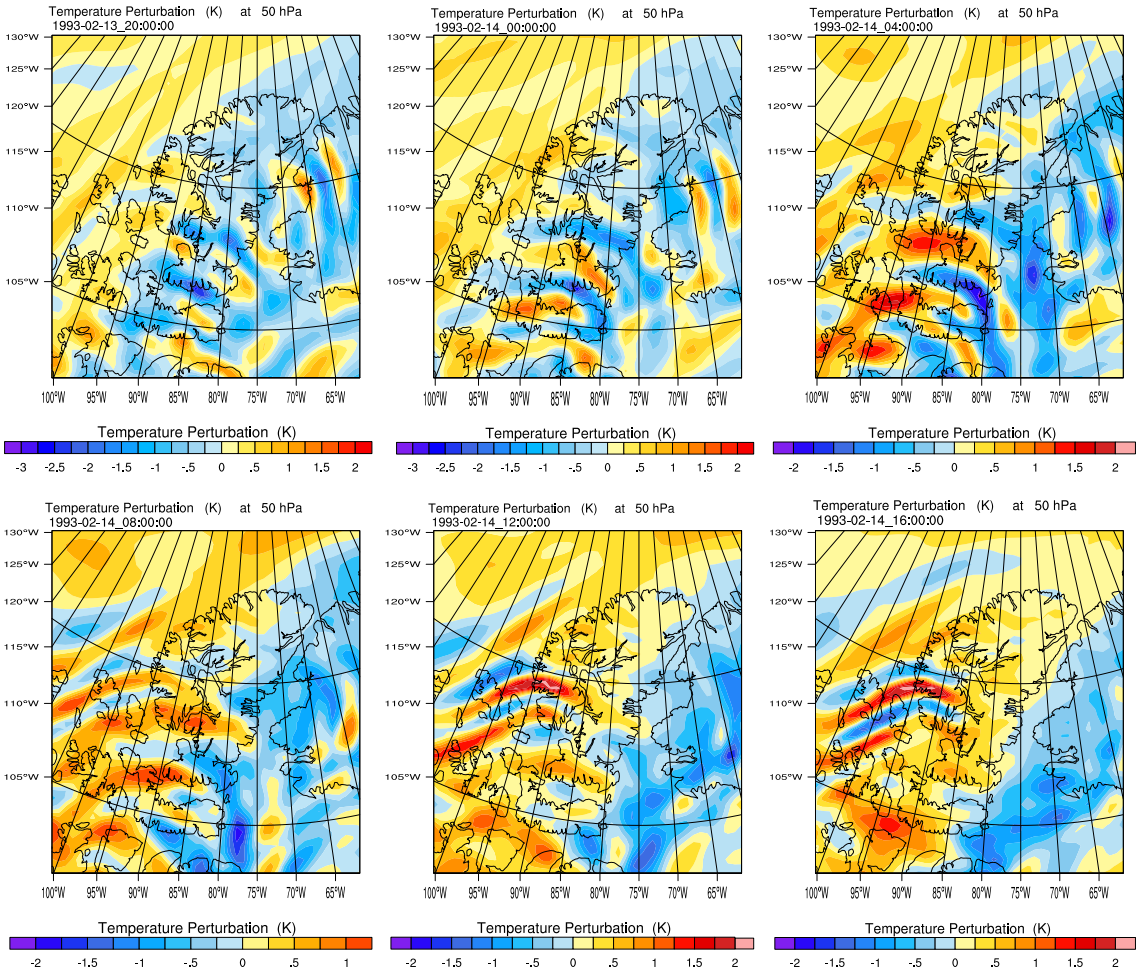

Figure A.6: Temperature perturbation plots at 50 hPa, every four hours from February 13, 2000 UTC to February 14, 1600 UTC. Mean temperature has been removed using running 20 grid point averages. Plots are zoomed into a smaller area close to Eureka. From WRF simulations using ECMWF ERA Interim data.

Figure A.7 shows perturbation temperature (°K) at 250 hPa, 50 hPa and 5 hPa. At 250 hPa, a wave packet is present over Axel Heiberg Islands at the same time

as the lidar measurements in figure A.1. The wave packet is propagating towards southeast as it ascends through the middle atmosphere.

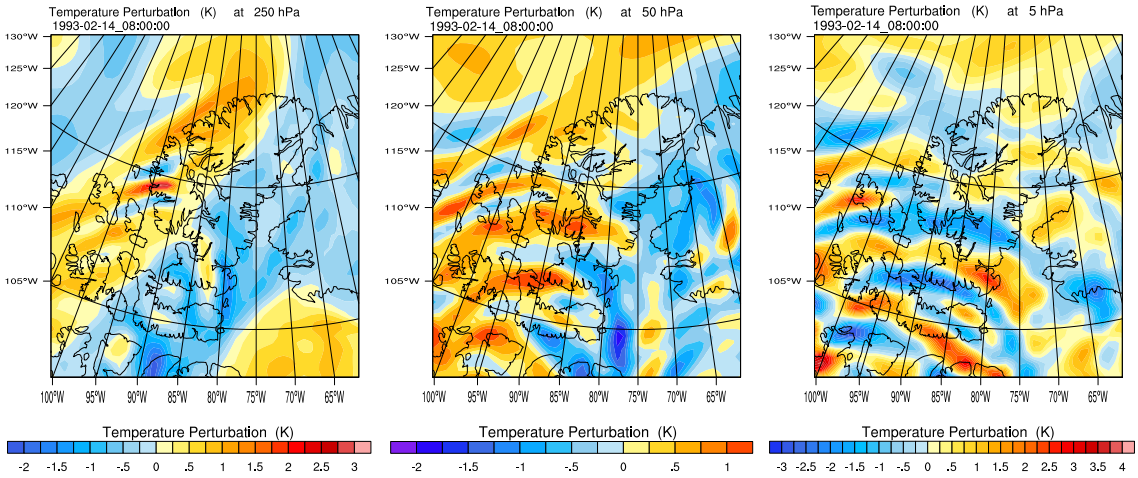

Figure A.7: Temperature perturbation plots at 250 ($\approx$ 10 km), 50 ($\approx$ 20 km) and 5 hPa ($\approx$ 34 km) on February 14, 0800 UTC, using running 20 grid point averages. Plots are zoomed into a smaller area close to Eureka. From WRF simulations using ECMWF ERA Interim data.

Vertical cross sections of temperature perturbation, every four hours from February 13, 1200 UTC to February 14, 2000 UTC, are shown in figure A.8. The cross section has been plotted along the red line shown in figure A.5, bottom right. From February 13 at 1200 UTC to February 14, at 0800 UTC, we can see low frequency gravity waves below 6km with low angle phase lines with respect to the horizontal. From February 13, at 1600 UTC, higher frequency waves with steeper phase lines are present at upper levels. This is due to Doppler shifting by the background wind, which increases with height. The vertical wavelength of these waves are between 4 to 6 km in the troposphere and as large as 17 to 22 km in the stratosphere.

As shown in figure A.8, ΔT at 80° N changes sign around 26 km from negative to positive. Looking at figure A.1, we see $\Delta T < 0$ for $z < 26$ km and $\Delta T > 0$ for $z > 26$ km. This means wave phases are consistent with lidar measurements. However, WRF

simulations show $\Delta T \approx 0.75^\circ$ C at 80.° N and $z = 35$ km, but lidar measurements show $\Delta T \approx 4^\circ$ C at the same height. However, the model does show larger values of ΔT at other locations, e.g. $\Delta T \approx$ -2° C at 78.5° N and $z = 35$ km, so this discrepancy could be explained as a modest spatial and/or temporal displacement in the model, or perhaps the inability to resolve details of the topography.

Since the horizontal wavelengths of these waves are much larger than their vertical wavelengths, we can use the hydrostatic dispersion relation to estimate the intrinsic frequency, $\hat{\omega} = N\frac{\lambda_z}{\lambda_x}$ (N is the Brunt-Väisälä frequency). On February 14, at 0800 UTC, N varies between 0.021 to 0.023 s^{-1}, the horizontal wavelength of these waves are between 110 km $\leq \lambda_x \leq$ 220 km and the vertical wavelengths are between 4 km $\leq \lambda_z \leq$ 22 km. Temperature perturbations vary between -3° K to 3° K. Using equation 1.15 with $N = 0.022$ s^{-1} and $f = 1.4 \times 10^{-4}$ s^{-1}, the calculated wave parameters are shown in Table A.1 for various vertical and horizontal wavelengths.

λ_h (km)	λ_z (km)	$\hat{\omega}$ (s^{-1})	$\lvert\hat{c}_h\rvert$ (m/s)	c_{gz} (m/s)
110	7	4×10^{-3}	70	4.5
220	7	2×10^{-3}	70	2.2
110	20	1.4×10^{-3}	24.5	4.5
220	20	7.2×10^{-4}	25.2	2.2

Table A.1: Wave parameters calculated for February 14, 1993 at Eureka.

Since there is only a 10 km overlap between lidar measurements (starting at 25 km in height) and WRF simulations (upper limit at 35 km), a direct comparison is only partially possible. The appearance of the gravity waves in the simulations corresponds to the same time period as the measurements and the vertical wavelength of the observed waves is consistent with the range seen in the model. WRF results also show that the wave emission in this case is due to topographic sources.

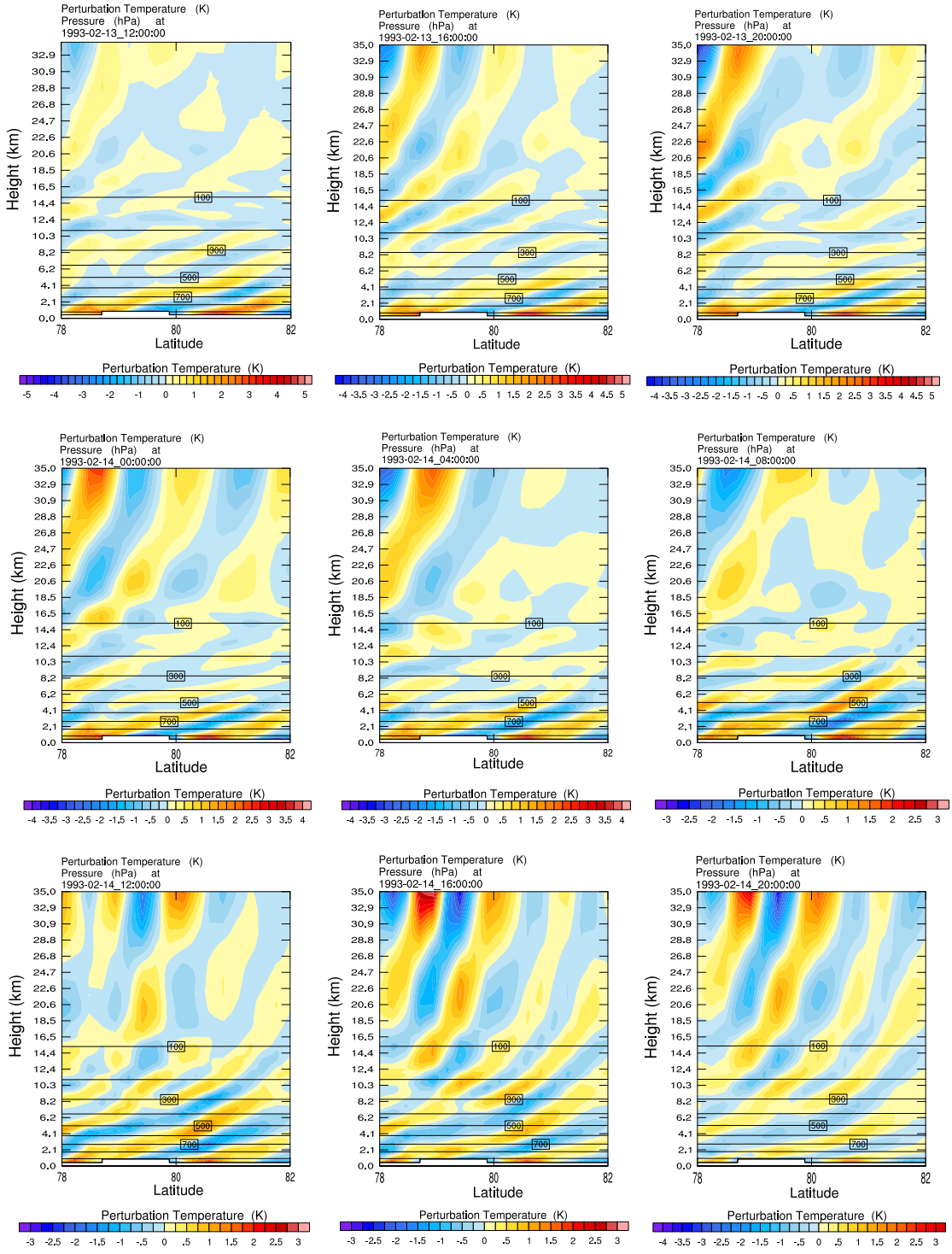

Figure A.8: Temperature perturbation cross section plots, every four hours from February 13, 1200 UTC to February 14, 2000 UTC, using 10 grid point running average. From WRF simulations using ECMWF ERA Interim data.